The Chemistry and CVD of Hydrophobic Surfaces

Colin R. Crick

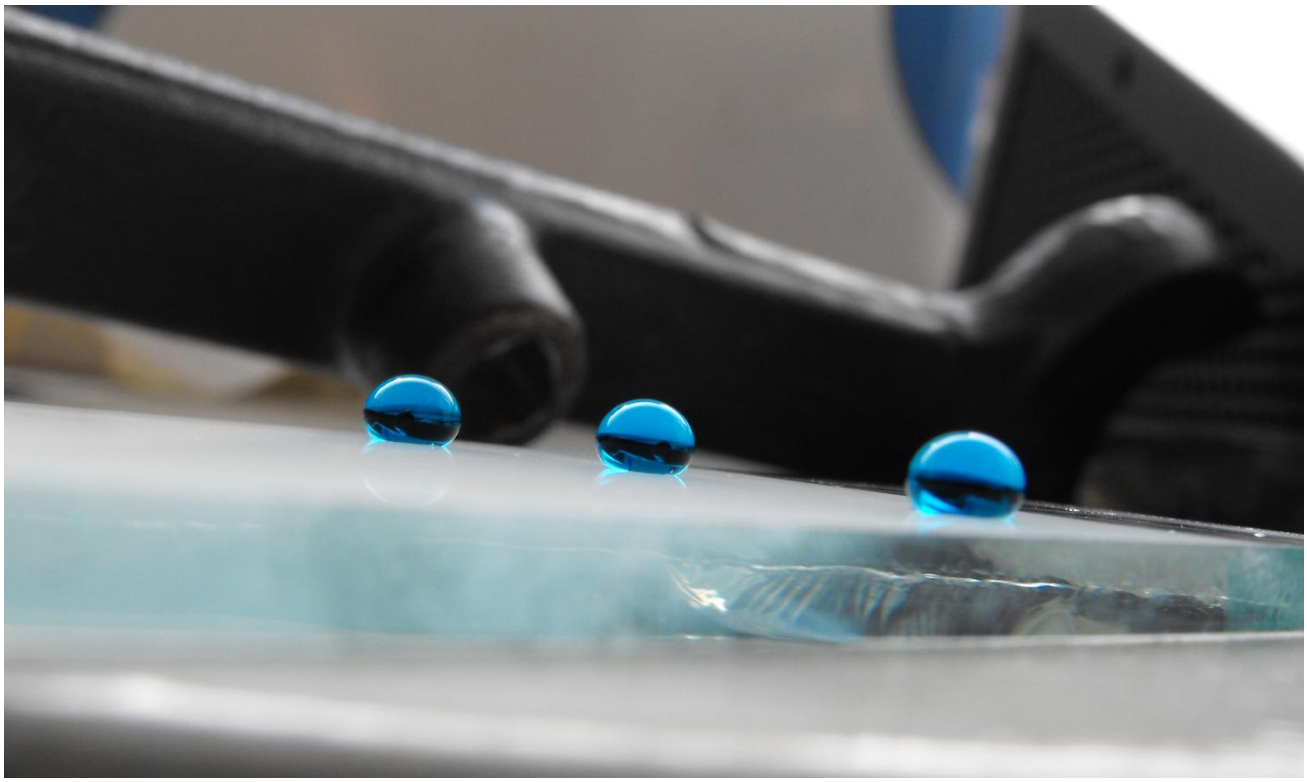

University College London

2011

I, Colin R. Crick, confirm the work presented in this thesis as my own. Where information has been derived from other sources, I confirm that this has been indicated in this thesis.

Abstract

This thesis details the use of chemical vapour deposition (CVD) to deposit hydrophobic surfaces, in addition to this, the functional properties are investigated and further characterisation of the surfaces extreme water repulsion (superhydrophobicity) is made. The design and manufacture of surfaces that repel water (hydrophobic) draws much inspiration from the natural world, including examples of superhydrophobic leaves. The way water can interact with a surface is characterised, with many examples of superhydrophobic surface generation provided from the literature, along with general routes toward their formation. The main aspects of CVD depositions are addressed and examples of hydrophobic surfaces using this technique are cited.

The novel deposition of thermosetting and thermosoftening polymers has been investigated, with the role of the CVD deposition mechanism emphasised. The deposition of the polymer occurs *via* the preformation of polymer particles, which is not typical in CVD, these were then deposited onto the substrate. The result was an easy-to-produce and robust superhydrophobic thin film, constructed from an inherently hydrophobic material. The same principle is then expanded to silica microparticles, films of the particles were deposited on to a substrate with hydrophilic surfaces originally deposited. The silica films were subsequently rendered exceptionally superhydrophobic by a simple post-treatment. The formation of copper films is then reported, using copper nitrate precursors a relatively flat metallic copper film was formed. The films were then roughened by reaction to form copper hydroxide nano-crystals, this hydrophilic surface is again functionalised to render it superhydrophobic. All films deposited were characterised using energy dispersive X-ray analysis, glancing angle X-ray diffraction, UV/Vis spectroscopy, infra-red/Raman spectroscopy and scanning electron and atomic force microscopy were used to study surface morphology, with the hydrophobicities of each surface quantified.

The superhydrophobic elastomer films underwent microbiological testing in order to examine the adhesion of bacteria. A substantial reduction in the ability of bacteria to attach to the superhydrophobic surfaces was observed and rationalised through a reduction in available contact between the media of the bacteria (water) and the surface material.

The dynamic interaction between water and surfaces was examined through water bouncing. The dependence of water bouncing on surface hydrophobicity and microstructure

was studied, in addition to the effect of water droplet volume and impact velocity. A new definition and scale for superhydrophobicity is proposed, through the ability of water droplets to bounce on a surface. Finally the insight gained from previous work carried out is used in developing a device for separating mixtures of oil and water, through the use of superhydrophobic meshes.

Acknowledgements

Firstly, for support and guidance, I thank Prof. Ivan Parkin who has taught me a great deal in the time I have spent within his group, which I very much appreciate. I would also like to thank my secondary supervisor Prof. Claire Carmalt for time taken to discuss the project.

To those who helped me get started in the Parkin Laboratory I thank you; Ms. Gillian Walters, Mr. Paolo Melgari, Dr. Naima Bj and Dr. Caroline Knapp. For constructive discussion and debate I would like to mention; Dr. Geoff Hyett, Dr. Charlie Dunnill and Dr. Russell Binions. Additionally I would like to thank everyone in Lab 308, past and present, who helped to create a wonderful working environment, many of whom I consider to be my close friends.

I thank Kevin Reeves for assistance with SEM imaging and EDX analysis, and Dr. Steve Firth for help with Raman Spectroscopy. For collaboration on bacterial studies I would like to thank Mr. Salim Ismail and Dr. Jonathan Pratten, in addition to Professor David Sheel for constructive dialogue. Mr. Dave Knapp and Mr. Joe Nolan are thanked for technical support and engineering issues. The EPSRC are thanked for providing funding and making the project possible.

I would also like to take this opportunity to thank my parents, brothers Chris and Sam, and friends who helped to support me through my studies. I extend greater thanks to my partner Karolina, who has been there for me throughout my PhD, and who without, the journey would have been much harder.

Contents

List of Figures and Tables

Chapter 4 - The Aerosol Assisted Chemical Vapour Deposition and Functionalisation of Copper (0) and Copper (I) Oxide Thin Films

List of Abbreviations

AACVD	Aerosol Assisted Chemical Vapour Deposition
AAO	Anodic Aluminium Oxide
AFM	Atomic Force Microscopy
AKD	Alkyl Ketene Dimer
APCVD	Atmospheric Pressure Chemical Vapour Deposition
b.p.	Boiling Point
BHI	Brain Heart Infusion
CNT	Carbon Nanotube
CVD	Chemical Vapour Deposition
DAK	Dialkylketone
DMF	Dimethylformamide
E. coli	*Escherichia coli*
EDX	Energy Dispersive X-ray
FAS	Fluoroalkylsilane
HMDS	Hexamethyldisilazane
IR	Infra-Red
MIBK	Methyl Isobutyl Ketone
MWCNT	Multi-walled Carbon Nanotube
PBS	Phosphate Buffered Saline
PDMS	Polydimethylsiloxane
PECVD	Plasma Enhanced Chemical Vapour Deposition
PPG	Polypropylene Glycol
PTFE	Polytetrafluoroethylene
r	Roughness Factor
S. aureus	*Staphylococcus aureus*
SEM	Scanning Electron Microscopy
SPR	Surface Plasmon Resonance
TEOS	Tetraethyl Orthosilicate
THF	Tetrahydrofuran

TMS	Trimethylsiloxane
TOAB	Tetraoctylammonium Bromide
UV/VIS	Ultra-Violet/Visible Light
XRD	X-ray Diffraction
θ	Water Contact Angle
θ_A	Advancing Water Contact Angle
θ_D	Apparent Water Contact Angle
θ_R	Receding Water Contact Angle
θ_t	Water Tilt Angle
Φ_s	Fraction of Solid-liquid Contact

Chapter 1

Introduction

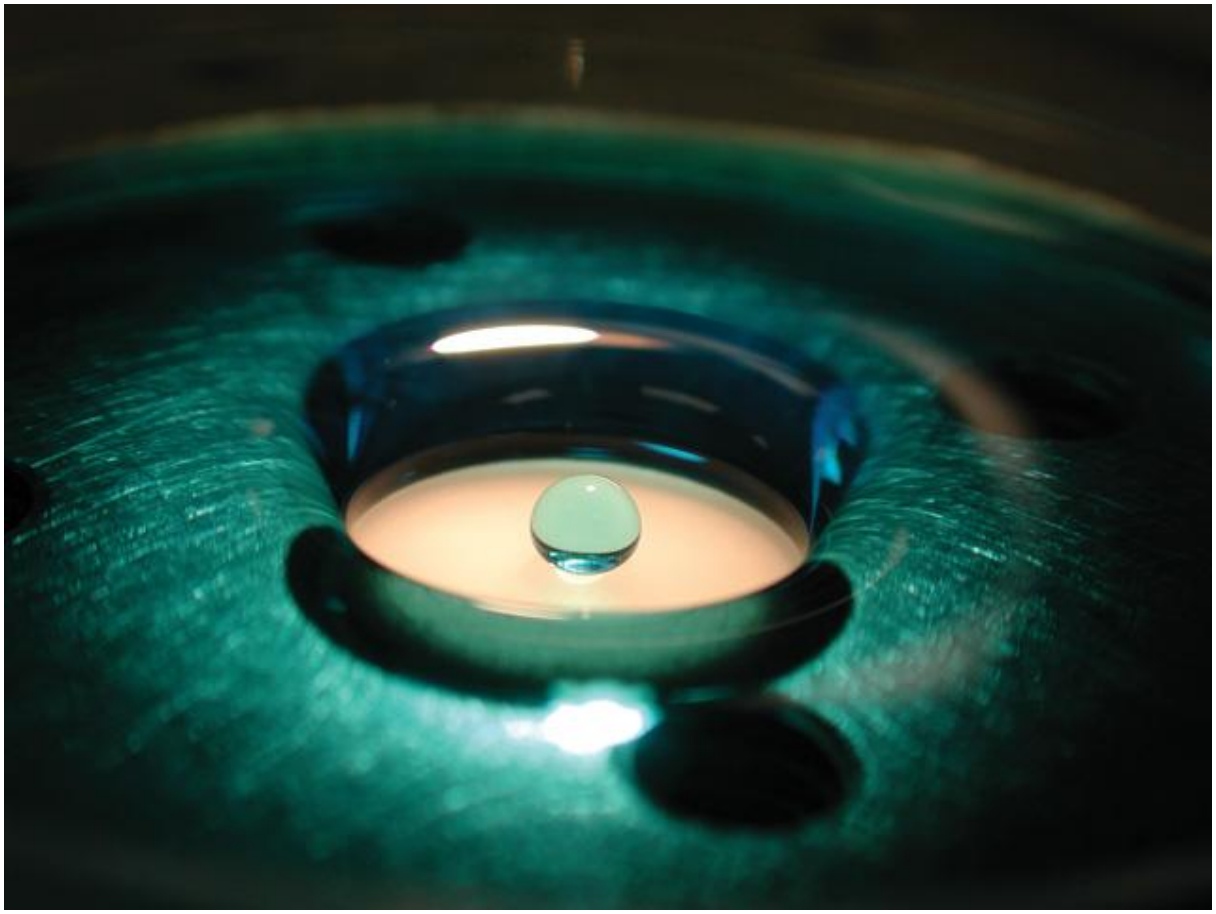

Figure 1.01. A superhydrophobic disk prevents wetting of the surface, a water droplet is placed static in the centre.[1]

1. Introduction

The interaction of water with matter has been the subject of fascination for mankind throughout the ages – from falling rain drops to the flow of rivers and streams. The manner with which water can interact with the extensive array of surfaces in existence is broad and varied[2/3]. The surface characteristics which dictate the mode of contact with water stem from surface composition and structure[4]. This is addressed in the introduction, with examples from the natural world considered in addition to a quantitative characterisation of surfaces. The design and construction of water repellent (hydrophobic) surfaces is an area of huge diversity and innovation[5]. This wide range of surface types will be explored. Chemical vapour deposition (CVD) as the main technique for surface fabrication during this project will be briefly discussed, and its role in hydrophobic surface generation summarised. The fundamental routes toward hydrophobic surfaces are then identified, and the introduction is concluded by investigating their commercial implementation.

The CVD of hydrophobic surfaces is fundamentally challenging. This owes to the requirement for a highly roughened microstructure and the tendency for CVD to provide flat uniform coatings. This work addresses methods in overcoming inherent complications and explores novel routes in doing so. Exploration of superhydrophobic functional properties is also reported, from bacteria adhesion to Lotus effect self-cleaning.

1.1. The Lotus Effect

A water droplet can interact with a surface in a variety of ways. The nature of the contact is related to the energy of water's interaction with the surface. It ranges from superhydrophilic[6], in which the water can fully wet a surface to form a flat puddle due to a strong water–surface interaction, through to superhydrophobic, in which water is effectively repelled from the surface to form a near-spherical droplet[7] and in which there is a weak water–surface interaction.

Superhydrophobic surfaces are observed in nature, the Lotus effect (named after the Lotus plant, *Nelumbo nucifera*), describes the self-cleaning action of some leaf surfaces. If the leaf shows high enough hydrophobicity, water will form near-spherical droplets that roll across the surface instead of sliding (Figure 1.02). The droplets rolling action facilitates foreign bodies to be picked up, with rougher surfaces tending to have a greater self-cleaning action.[8] The Lotus leaf is a surface that demonstrates this mechanism – the leaves themselves have a waxy surface coating which acts to repel water, surface protrusions make the waxy surface highly rough[9] (Figure 1.03). Both of these surface features combine and allow water droplets to roll[10]. The surface features possess rough, nanoscale, hair-like structures (Figure 1.03) which act to trap air underneath the water droplets, further enabling the rolling motion[4]. Those leaves which possess waxy coatings but do not have a highly rough microstructure are less efficient at self-cleaning[6]. Plants both with waxy coatings and rough surfaces

have far superior self-cleaning properties than those with comparable smooth waxy surfaces. Hierarchical micro- and nanoscale roughness has been shown to significantly contribute to Lotus effect self-cleaning in hydrophobic surfaces *via* enabling the rolling mechanism[11].

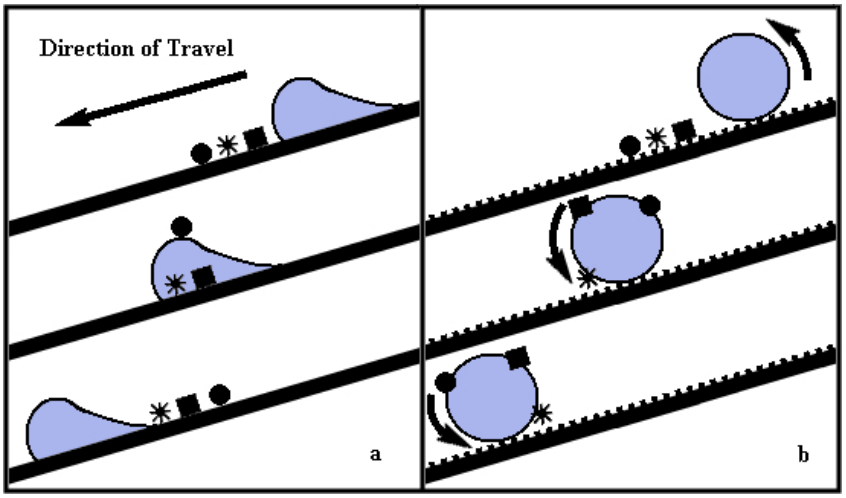

Figure 1.02. Diagram showing the interaction of water droplets with (a) hydrophobic and (b) superhydrophobic surfaces. "Lotus effect" self-cleaning on superhydrophobic surfaces allows for dirt and bacteria to be carried away from the under action of water.

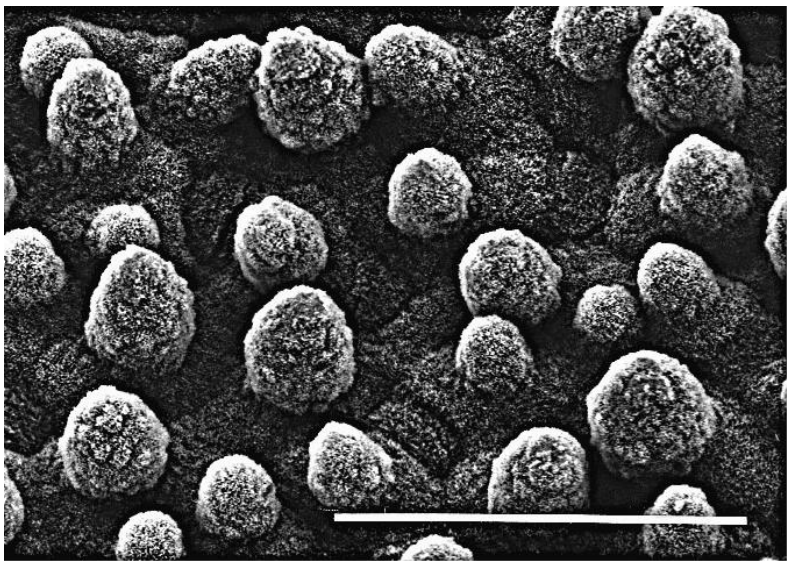

Figure 1.03. Scanning electron microscope (SEM) image of Nelumbo nucifera (Lotus) leaf exhibiting a highly rough surface microstructure, with additional smaller scale roughness on the protrusions. Scale bar shows 50 μm.[12]

Extreme hydrophobicity in nature also includes water strider legs (Figure 1.04), these have a highly defined microstructure and are coated by a layer of secreted wax[13]. The wings of some insects also show hydrophobic properties, brought about by surface microstructure and composition[14]. These include some butterfly wings, which have been observed to employ a network of microstructured scales on the wings surface, this directs rolling of water away from the body of the butterfly keeping it dry[15]. These surface characteristics, in addition to other examples in nature, have provided inspiration for the design of artificial hydrophobic surface. One of the most directly related fabrications of a hydrophobic surface is the direct casting of a Lotus leaf surface by imprinting with polymers[16].

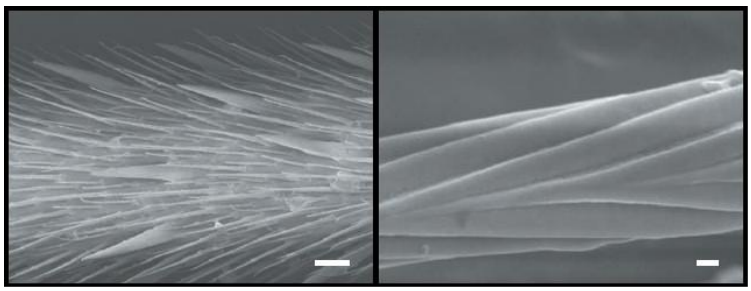

Figure 1.04. SEM images of a water striders leg. Spindle-like structures emanating off the leg have a nano-grooved structure, providing dual-scale roughness to the leg. A secreted wax acts to repel water. Scale bars – *left* = 20 μm and *right* = 200 nm.[13]

1.2. Surface Models and Characterisation

1.2.1 Surface Models

In order to help predict and explain the way water will interact with a surface, models are used. The two most commonly employed are the Wenzel[17] and the Cassie–Baxter[18] models. The measurement used to gauge a surfaces hydrophobicity in both models is the water contact angle (θ) (Figure 1.05), which is the angle subtended by the droplet and the surface. If a surface has a contact angle with water that is greater than 90° it is classed as hydrophobic, if the contact angle is less than 90° the surface is hydrophilic. The higher the contact angle, the more hydrophobic, or water-repellent, a surface is. The maximum contact angle is 180° for which a water droplet would be completely spherical. When water contact angles approaches 0° water would sheet over the whole surface, this is termed a superhydrophilic coating.[19]

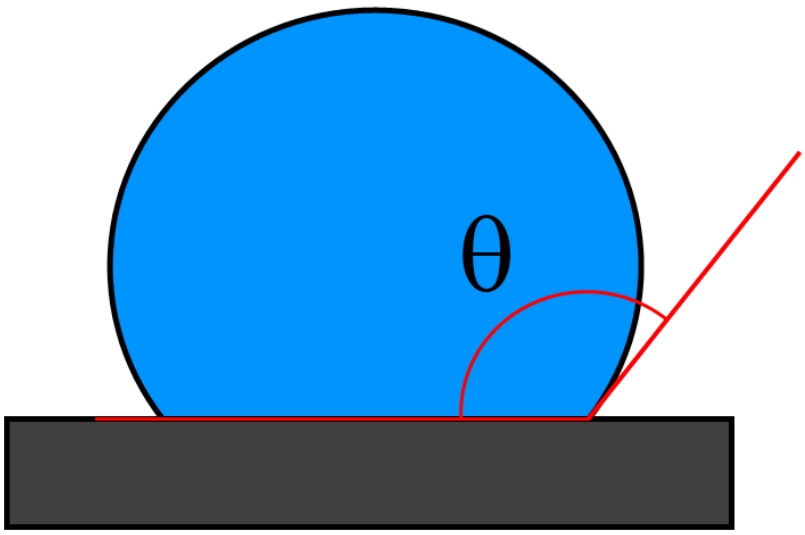

Figure 1.05. The water contact angle (θ) – this is the angle made between the plane of a surface and the tangent from which the droplet makes contact with the surface.

Surface (specific) energy: This is the measurement of how a water droplet will interact with a surface material. If a droplet is in equilibrium, that is, if the contact angle is invariant, then the interfacial tensions (γ_{SL}, γ_{LV} and γ_{SV}) must be balanced. Where γ_{SL}, γ_{LV} and γ_{SV} are the interfacial tensions between the solid and the liquid, the liquid and the vapour, and the solid and the vapour respectively. These tensions can be related by Young's equation; $\gamma_{SL} + \gamma_{LV}\cos\theta = \gamma_{SV}$, where θ is the water contact angle. As γ_{SV} (solid surface energy) decreases the equilibrium θ value must become larger to balance

the interfacial tensions. This change in water contact angle indicates an increase in the hydrophobicity of the surface, which relates directly to the surface energy.[17]

Surface roughness: The roughness of a surface can be defined by looking at the difference between the actual surface area, including peaks and valleys of surface morphology, and the planar or geometric area. The latter is the area of contact the water droplet makes with the surface assuming a totally smooth surface, whereas the actual surface area takes into account the protrusions. Both of these surfaces are used to calculate the roughness factor:

$$\mathbf{r} = \text{roughness factor} = \frac{\text{actual surface}}{\text{planar area}}$$

The roughness factor is incorporated directly into the Wenzel model[17], whereas the Cassie–Baxter model uses a related measurement. The two models are comparable as they contain similar features and deal with the same type of interactions, there are however some fundamental differences.[17]

Advancing (θ_A) and receding (θ_R) water contact angles are used by the Cassie–Baxter model. These measurements describe the dynamic wetting of the surface and are related to the angle of tilt required to move a static water droplet. They can be observed in experiments that use tilted surfaces. An alternate method derives the angles from altering the volume of a water droplet as it rests on a horizontal surface. The receding contact angle is measured by removing some of the water from the droplet and noting the water contact angle at the point where the area of water-surface contact begins to decrease. Advancing contact angles can also be measured by adding to the droplet's volume and noting the water contact angle when the area of contact starts to increase (Figure 1.06).[4]

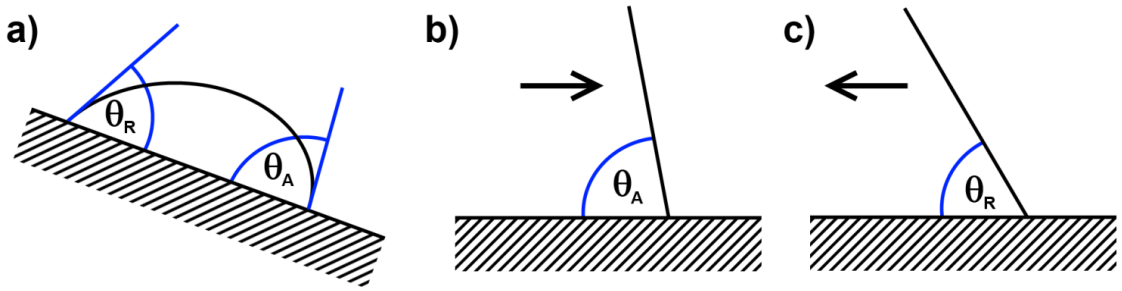

Figure 1.06. Methods for measuring advancing (θ_A) and receding (θ_R) water contact angles. (a) Shows a tilted surface, the water droplet on-top is at the point where it will begin to move across the surface. (b) Volume can also be added (θ_A) or taken away (θ_R) from a droplet at rest on a horizontal surface, the point where the droplet's diameter at the point of contact changes provides the advancing/receding water contact angle.

1.2.1.1 Wenzel Model[17]

The major premise of this model is that the water makes full contact with the surface, with no air trapped underneath a droplet. This model uses the surface tension of the solid and the water–solid

interfacial tension. The roughness of the surface is considered by using the roughness factor (**r**) as described previously, such that if a surface with constant surface tension has its roughness factor doubled, the energy of the surface per unit geometric structure will also double. The Wenzel model uses force vectors to represent the change in surface properties when **r** is incorporated. The force vectors are represented by S_1 and S_{12} and their difference is the adhesion tension A, such that A= S_1 - S_{12} (Figure 1.07). The surface tension of the liquid (S_2), the contact angle (θ) and the adhesion tension (A) can be related by:

$$A = S_2 cos\theta$$

Combining these two equations gives:

$$A = S_1 - S_{12} = S_2 cos\theta$$

Applying surface roughness gives:

$$\boldsymbol{r}A = \boldsymbol{r}(S_1 - S_{12}) = S_2 cos\theta \text{ (Figure 1.07)}$$

Surfaces that adopt a Wenzel-type wetting allow water to make total contact at the solid-liquid interface. The Wenzel model predicts that a surface will have its properties magnified when the roughness factor is increased. This means that a hydrophobic surface (θ > 90°) will have its water contact angle increased when roughened, whereas a hydrophilic surface (θ < 90°) will have its water contact angle reduce upon roughening. Another result of the wetting mechanism is a maximisation of frictional force between the surface and any water that makes contact. The frictional forces render Wenzel-type surfaces relatively sticky as there is no trapped air under a water droplet on the surface.

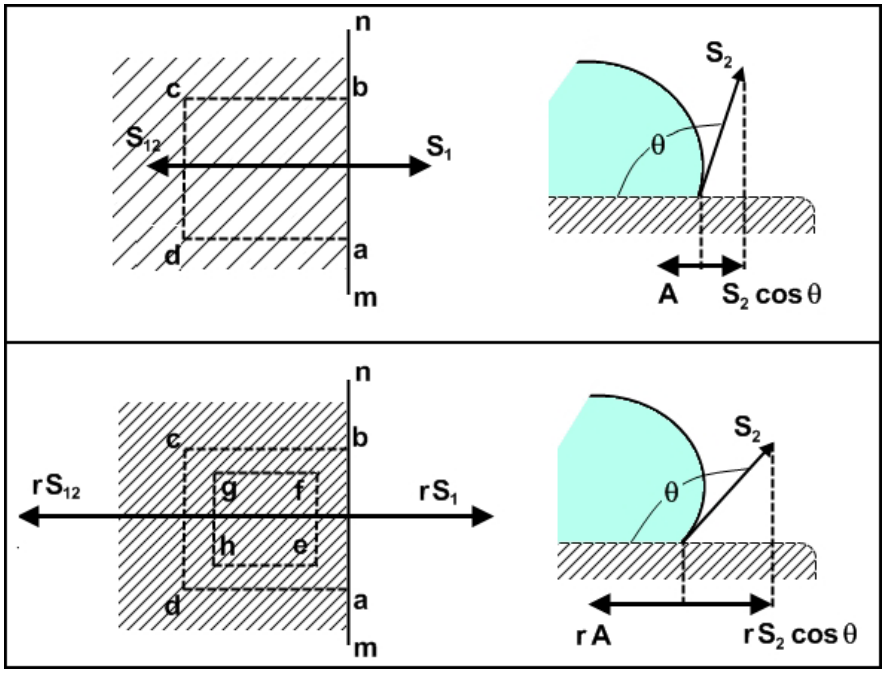

Figure 1.07. Diagram showing forces involved in the Wenzel model; S_1, S_2 and S_{12} represent the force vectors included in the adhesion tensions. The specific energy of the interface is represented by area a,b,c,d. Upon roughening, the area representing the specific energy of the surface is condensed to e,f,g,h.

1.2.1.2 Cassie–Baxter Model[18/20]

This model was developed after the Wenzel model. It considers that the water droplet sits atop any surface protrusions and air is trapped underneath the droplet, residing in the surface porosity (Figure 1.08). This model can be related back to the Wenzel model when considering flat materials. The Cassie–Baxter model considers the interaction with the surface in terms of interface areas and interfacial energies; f_1 is the total solid–liquid interface area, f_2 is the total liquid–air interface area beneath the droplet for a unit geometric area. The energies are represented as γ, in which γ_{LS} is the solid–liquid interfacial energy, γ_{SA} is the solid–air interfacial energy and γ_{LA} is the liquid–air interfacial energy. The products of the area and the energies will give the energy for that area. The net energy, E_D, of the model is expressed as:

$$E_D = f_1(\gamma_{LS} - \gamma_{SA}) + f_2\gamma_{LA}$$

Introducing the contact angle then gives:

$$\cos\theta_D = -\frac{E_D}{\gamma_{LA}} = f_1 cos\theta_E - f_2$$

In which θ_D is the apparent contact angle and θ_E is the static contact angle for the solid–liquid interface. In the same way, equations for the advancing and receding contact angle can be derived[21]. The equation reduces to Wenzel's model when $f_2 = 0$.

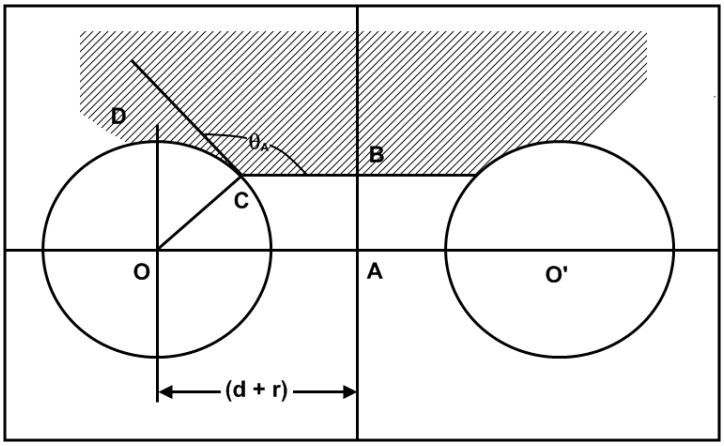

Figure 1.08. Diagram showing the geometries used in the calculations of the Cassie-Baxter model, the calculation uses the cross-section of two fibres, however can be extended to different surfaces. The surfaces can be considered as repeating units of OA, the positions O, A, B, C, D can be used to calculate the interfacial energies (f_1 and f_2). The Cassie-Baxter model has air trapped underneath the water droplet between the surface protrusions.

Both models can be extremely successful in describing the interaction between water and a surface, with neither wholly superior due to the range of behaviours observed on different surfaces. The relative success of each model depends on the nature of wetting observed in each surface considered[22]. The key Cassie-Baxter equation reduces to Wenzel's when looking at rough but not porous surfaces, where $f_2 = 0$ and $f_1 = \mathbf{r}$ [18].

The Cassie-Baxter equation can be simplified further[23]. This is done by considering the area of contact at the liquid-surface interface as flat, with water only wetting the very tops of any surface protrusions. In making this assumption, the total areas of contact $f_1 + f_2 = 1$. These areas can now be regarded as fractions of the total planar contact between water and the surface, where $f_1 = \Phi_s$ and f2 = $1 - \Phi_s$. Φ_s is termed the fraction of solid-liquid contact. The simplified Cassie-Baxter equation then appears as; $\cos\theta_D = \Phi_s\cos\theta_E + \Phi_s - 1$ (Figure 1.09).[23]

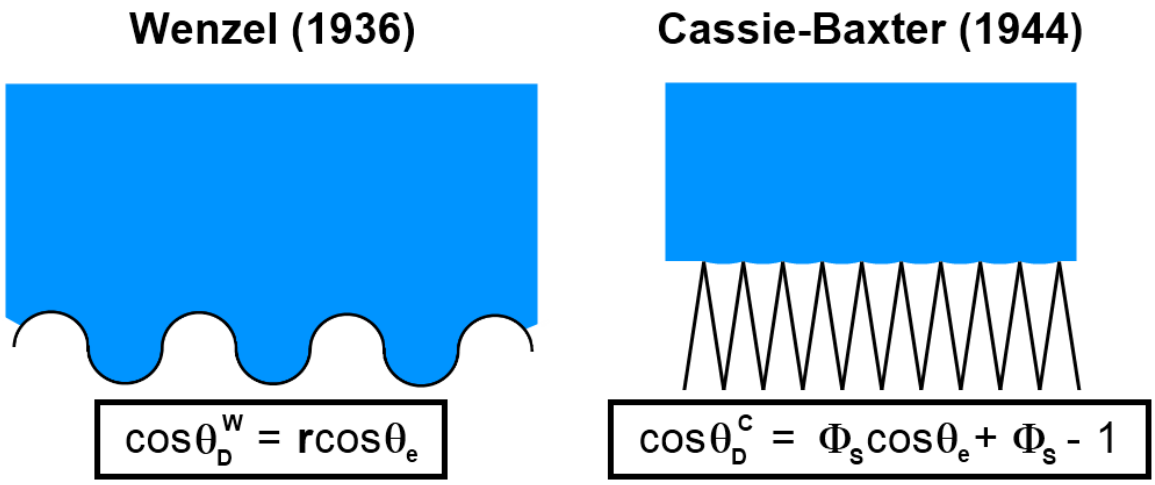

Figure 1.09. Diagram of Wenzel and simplified Cassie-Baxter approaches with key equations, in which $\theta_D^{C/W}$ is the apparent contact angle assuming each theory, θ_e is the equilibrium contact angle on a flat surface, **r** is the roughness factor and Φ_s is the fraction of solid–liquid contact of the total water surface interface (where $1 - \Phi_s$ = fraction of liquid-air contact).

The movement of water across a surface is also affected by the wetting nature of the surface. A Wenzel-type wetting mechanism means that there is complete contact between the surface and water droplet at any point of coverage (Figure 1.09), with no air trapped underneath. The greater area of contact between water and surface renders water movement across the surface relatively hard. A Cassie–Baxter surface, not only has a lesser water-surface contact but air is trapped underneath the water, which makes the surface "slippery" (with respect to water). A Wenzel-type surface is "sticky" a water droplet has a low probability rolling across the surface; Lotus-type self-cleaning is thus less likely on this type of surface. Cassie-Baxter surfaces can allow water droplets to move across them easily, with a rolling action more likely to be observed; it is thus this type of surface that is required for Lotus effect self-cleaning.[4]

1.2.1.3 Intermediate States

The Wenzel model is aimed at surfaces at which the water droplet makes contact with all parts of the surface (Figure 1.09), whereas the simplified Cassie–Baxter model uses a fraction of contact between the droplet and the surface, with flat points of contact. However, a pure form of either model may not

be the case for some surfaces, that is, those that have no flat area of contact with the water droplet (Figure 1.10). If both Wenzel and simplified Cassie-Baxter models are combined, then both the roughness factor (**r**) and the fraction of solid–liquid contact area can be used in an equation to describe such surfaces (Figure 1.10).[24] This approach can also be applied using the full Cassie-Baxter model.[18]

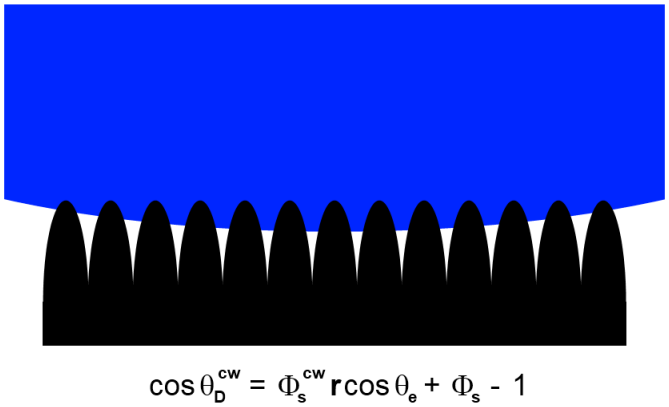

Figure 1.10. Diagram showing a Cassie–Baxter/Wenzel intermediate state with the key equation, in which θ_D^{cw} is the apparent contact angle, θ_e is the equilibrium contact angle on the flat surface and Φ_s^{cw} is the fraction of solid-liquid contact above the total projected surface-water interface plane. The protrusions of the surface only partially penetrate the water droplet. The equation combines the approaches of each surface model.[24]

The transition between the two wetting states is a subject of much study, small changes in the dimensions of surface features (i.e. protrusion height, size and separation) provide large differences in water contact angle, but this can also affect the 'stickiness' of a surface[25/26]. The air trapped under the water drops in the Cassie–Baxter mechanism not only renders the surface slippery but greatly increases water contact angle. Air trapped by the surface remains under the droplets as the penetration of water into the surface porosity is energetically disfavoured. This is either because the water is repelled by the surface material and/or because the air cannot easily flow through the surface microstructure if displaced (i.e., the surface microstructure is not sinusoidal). The introduction of surface microstructure with a particular arrangement of features can render hydrophilic materials (i.e. $\theta < 90°$ with flat surface) hydrophobic. Air trapped under the droplet is maintained by non-sinusoidal surface structure, this air acts to improve the surfaces resultant hydrophobicity[27]. Designing surfaces with these principles in mind can produce interesting results; a directional roughness (e.g., stripes across a surface in one direction) can allow preferential movement (sliding) of water in the direction of the stripes, with water droplet rolling preferred when travelling perpendicular to the stripes. Surfaces demonstrating this property have also been constructed to repel alkanes in a similar way using hexane droplets on a textured surface. Large difference in contact angles were observed depending on the orientation droplet upon measurement.[28]

The evaporation of water on a surface can give an indication of the type of wetting mechanism that occurs[29]. Surfaces that are wetted in a Wenzel fashion are sticky in nature, so when the droplet reduces in volume through evaporation the area of contact remains the same but the contact angle is reduced. On slippery Cassie–Baxter surfaces, the area of contact decreases as the droplet reduces in volume and in consequence the contact angle remains unchanged until a very low droplet volume is

reached (an alternate method for accessing the receding water contact angle). The transition from Cassie–Baxter wetting to Wenzel wetting can be achieved by addition of agents to the surface.[30]

1.2.2 Superhydrophobicity

A superhydrophobic surface is usually classified as one that repels water to such an extent that the water contact angles exceed 150°,[31] but it has also been less commonly adopted as 140°.[32] Superhydrophobic surfaces are formed by successful combination of low surface energy and high surface roughness. The highest water contact angle achieved on smooth low-energy surfaces are around 110° to 120°. Alkyl and fluorinated alkyl groups (in addition to others[21/33]) have very low energies of interaction with water and can be used to construct superhydrophobic surfaces as a strong repulsion to water results in a large water contact angle[34]. Table 1.1 shows the relative hydrophobicities of such surfaces for purely flat surfaces; if surface roughness is introduced these composition types can exhibit superhydrophobic properties dependant on magnitude of roughening. The angle of tilt, from the horizontal, required to move a water droplet may also be considered when categorising a surface as superhydrophobic. This tilt angle is typically less than 10° and also suggests the surface undergoes Lotus effect self-cleaning effect.[35]

Surface Terminal Group	θ (°)
CH_2	94
CH_3	111
CF_2	108
CF_3	120

Table 1.1. Calculated water contact angles (θ) for planar surfaces composed pure arrays of CF_3, CF_2, CH_3 and CH_2 terminal groups. Calculations were made by considering surface energies.[34]

The water contact angle is the most commonly observed property used to gauge the hydrophobicity of a surface. It is however known that the method of measurement used, the water contact angle may appear to differ[2]. It has been shown that Young's law holds when a water droplet is affected by gravity, and so deformation of water droplets due to gravity will not affect this relationship[36]. However if the analysis method does not follow Young's calculations (e.g. spherical fitting by analysis of droplet radius), or the water contact angle is manually assigned then an effect of droplet size may be observed. The method of water droplet analysis also strongly determines the 'observed' contact angle. In one reported case, analysis of an image showing the same 5 μL droplet gave water contact angles varying from 152° to over 179° (Figure 1.11)[2]. The highest water contact angle stems from Laplace-Youngs fitting; this is substantially different from the other calculations as the main component used is the radius of the droplet and this can be subject to greater error. Given this

result, it can be said that only droplets measured using the same analysis system and droplet volume can be directly compared, if either droplet volume and/or analysis techniques varies then a direct comparison between two different surfaces cannot be made with any conviction. These factors must be considered when comparing results from a range of sources, as differences in reported water contact angle may not be due to a variation in surface hydrophobicity, but may be due to the methods implemented to collect the results. Many articles state which apparatus was used to measure the water contact angles but fewer state the computational method used to analyse the droplets. Further complications can also influence the proposed success of a hydrophobic surface measurement, when stating the average[37] or maximum contact angle values is not made clear, with the variation of the results often not provided. The water contact angle values stated in this thesis introduction suffer from the inconsistencies mentioned above, and so must be considered when any comparison is made.

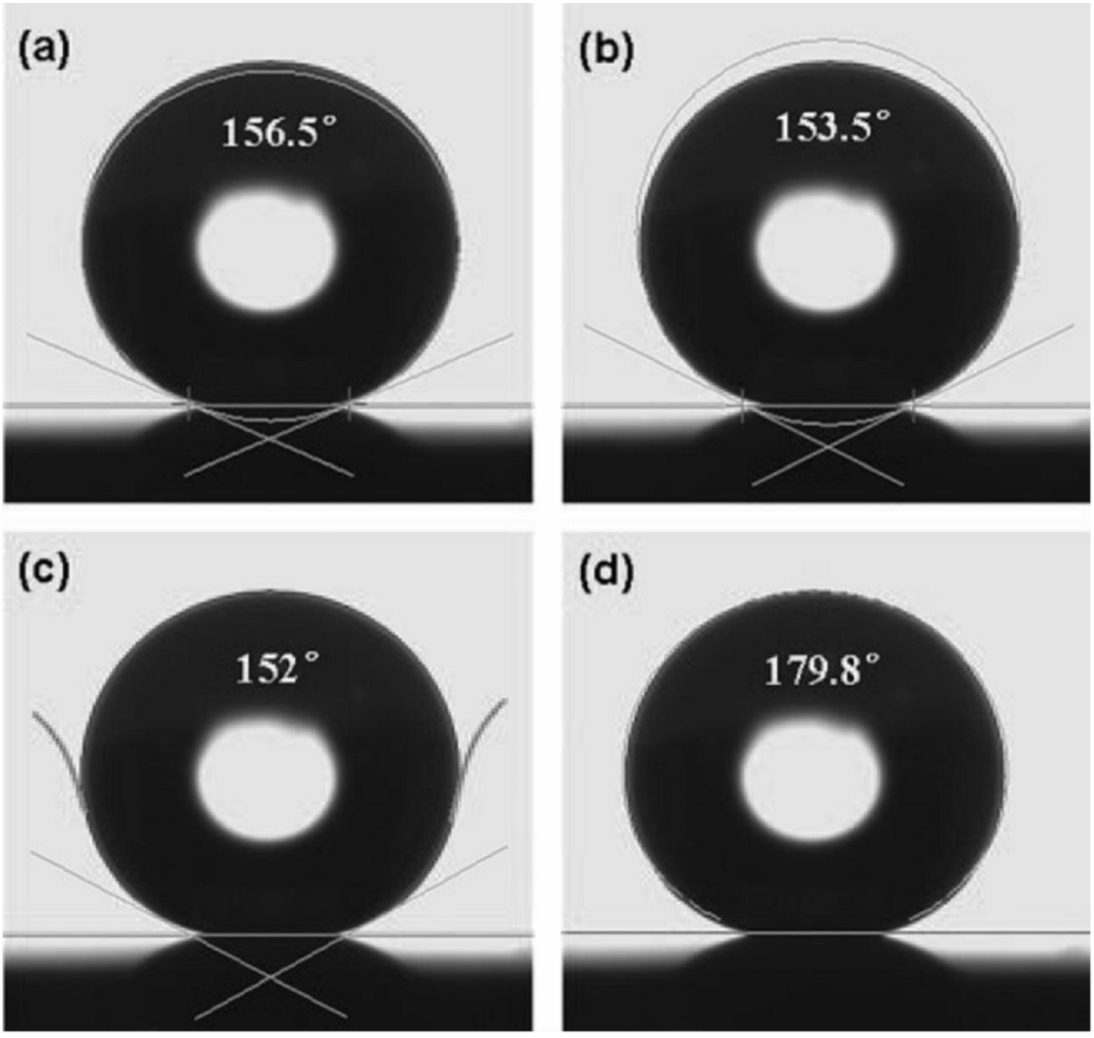

Figure 1.11. Water contact angle measurement disparities – Duplicated images of a 5 μL water droplet on a superhydrophobic surface analysed by using a) ellipse fitting; b) circle fitting; c) tangent searching and d) Laplace–Young fitting (uses radius of the droplet). The result shows that the same water droplet can give a range of results depending on the method of analysis. The overlaid lines show horizontal baselines or shape simulation lines used to calculate the water contact angle.[2]

1.3. The Construction of Hydrophobic Surfaces

This section reviews various methods used in the synthesis of hydrophobic and superhydrophobic surfaces. The key factors responsible for variation in surface hydrophobicities are rationalised in each case.

1.3.1 Fluoroalkylsilane (FAS) coatings

FAS molecules can interact with water in a hydrophobic/non-wetting and a hydrophilic/wetting manner depending on which end of the molecule is considered. Figure 1.12 shows an example of a commercially available FAS molecule; the trichlorosilane part of the molecule is hydrophilic whereas the CF_3-terminated chain is hydrophobic. The trichloro-(tridecafluorooctyl) silane molecule cannot directly form hydrophobic surface as it has both hydrophobic and hydrophilic properties. However, modifying this type of molecule by polymerisation (*via* a hydration reaction) can allow the hydrophilic part of the molecule to react with some surface species[38]. An example of this is shown in Figure 1.13; the hydrated siloxy-chains possess hydroxyl groups which then bind to surface hydroxyls through dehydration reactions. The hydrophilic part of the molecule is bound to the surface and the hydrophobic fluorinated chains exposed on the surface repel water.[39]

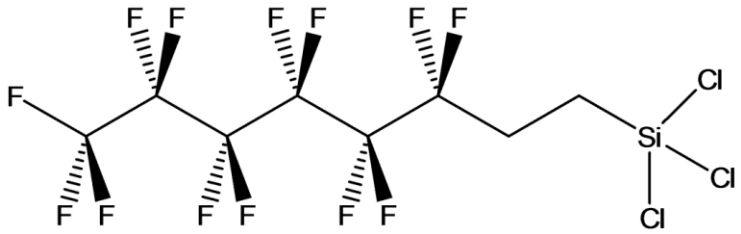

trichloro(tridecafluoro-octyl)silane

Figure 1.12. FAS molecular structure. Fluorinated portions of the molecule shield attractive interactions with water (hydrophobic). The silicon terminated end possesses polarised bonds (Si-Cl) which interact strongly with water (hydrophilic).

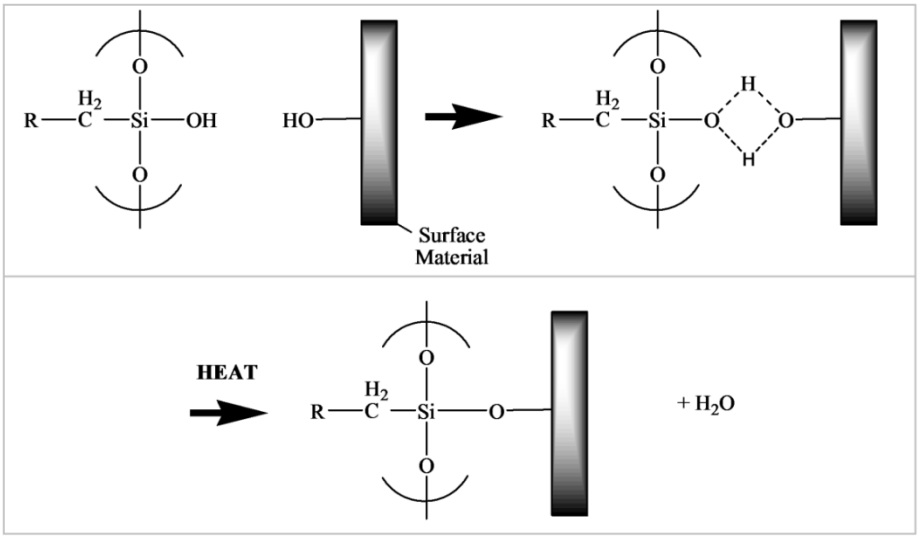

Figure 1.13. Proposed condensation reaction of surface (hydroxyl groups) with a hydroxylated FAS molecule; R represents a hydrophobic alkyl chain.

A study carried out by J. Bico et al. uses silicon wafer substrates and FAS molecules are applied[40]. The FAS ($F(CF_2)_{10}(CH_2)_2SiCl_3$) was put on to the substrate and grafted to it by heating to 1100°C for 2 hours. The results clearly show that a flat FAS coating can be roughened to greatly change the water contact angle, which was increased from less than 118° to 167° on a spiked surface. The surfaces were created by moulding; an image of the created structure is provided in Figure 1.14.[39]

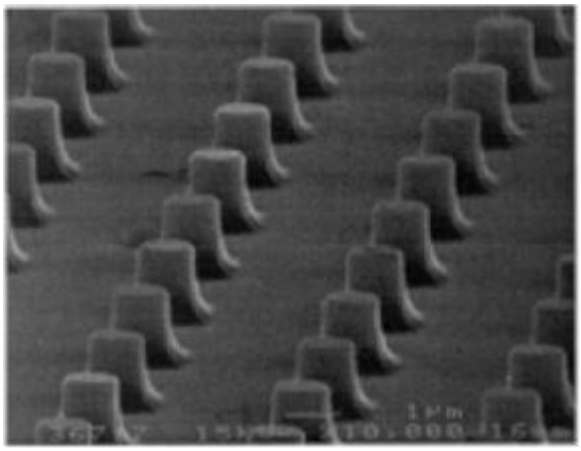

Figure 1.14. SEM image of a spiked FAS surface designed to maximise the attainable contact angle. The surface protrusions allow for less water-surface contact, using the Cassie-Baxter wetting model a water contact angle of 167° is expected, this is achieved by the surface.[40]

Surfaces constructed using similar techniques and following the same synthesis steps have been constructed. This method varies by the addition of an acrylic polymer to the reaction mixture and results in agglomeration of the FAS molecules and a resultant change in the microstructure is observed (Figure 1.15). Water contact angles of up to 152° were achieved on this surface.[41] The use of FAS molecules to coat surfaces has also been carried out by grafting onto already roughened substrates[42].

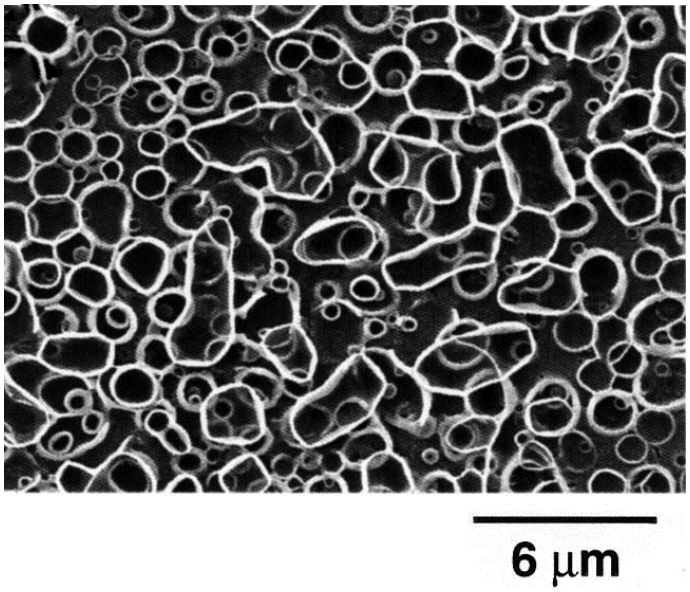

Figure 1.15. SEM image of a surface made from an FAS / acrylic polymer blend; the surface microstructure allows for air to be trapped underneath any water on the surface maximising surface hydrophobicity for large water contact angles.[41]

1.3.2 Poly(tetrafluoroethylene) (PTFE) surfaces:

The chemical composition of PTFE provides an intrinsically very low surface energy, due to a deficiency in favourable orientations for water molecules on the polymers surface (Figure 1.16).[43] PTFE has a high molecular weight, it is a solid at room temperature but can be shaped quite easily by heating, making roughening effective in increasing the hydrophobicity of this surface type. Although there are many strategies imaginable for the modification of PTFE, the basic principles remain the same – to allow the formation of a highly rough surface while maintaining the hydrophobicity of the composite materials.[44]

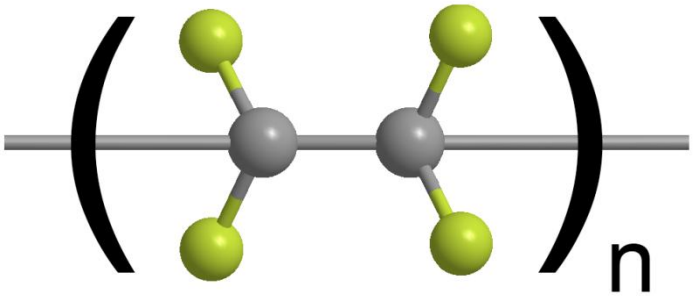

Figure 1.16. Basic chemical structure of a PTFE chain. The polymer molecules are very hydrophobic as they do not interact with water due to no substantial access to the polarised C-F bonds.

The use of plasma has been employed in the alteration of flat PTFE substrates[43]. Oxygen plasma was used to treat flat PTFE, and resultant surfaces showed an increase in water contact angle from 118° to 131°. Addition of a fluorinated molecule (1H, 1H, 2H, 2H-heptadecafluorodecyl acrylate) into the oxygen plasma resulted in a further increase to 148°. The action of the oxygen plasma was shown to have a roughening effect on the flat substrate, confirmed by atomic force microscopy (AFM), however an introduction of foreign particles was also detected. This increased surface energy and lowered water contact angles. When the plasma was combined with the fluorinated acrylate it facilitated the coating of foreign particles with fluorinated material, and enabled a further increase in the hydrophobicity.[43] Recent developments in the plasma treatment of PTFE surface has resulted in controllable roughening of surfaces and increased contact angles to superhydrophobic magnitudes (≈ 162°)[45]. The use of plasma as a surface roughening method can be extended to other polymers, such as poly(L-lactic acid), in which increased hydrophobicity across a substrate has been achieved.[46]

Additionally, silica microspheres have been used to mould highly rough PTFE surfaces (Figure 1.17). The experiment involved sintering silica beads of various diameters onto a flat substrate, gaps between these spheres were subsequently filled with PTFE. Sintering of a microsphere template (diameter 850 nm) at 970°C resulted in a rough PTFE surface with water contact angles of 154° after removal of the silica.[47]

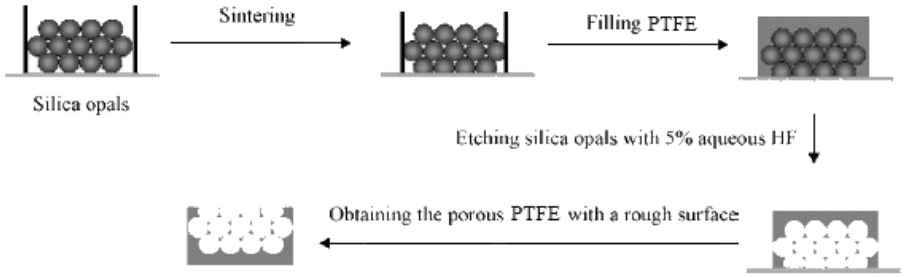

Figure 1.17. Schematic for construction of microporous PTFE surfaces. Surface microstructure was altered by changing the size of silica opals and sintering temperature.[47]

Spray-coating of substrates with mixtures of furfural acetone resin/PTFE has been used to deposit low energy and roughened materials. The droplets in the spray result in agglomerations of PTFE, which form a film of particles on the surface (water contact angle 157°).[48] A variation on this spray-coating example uses a mixture of cellulose nitrate and fluoroacrylic polymer to bring about similar superhydrophobic results, with a water contact angle of 165°.[49] Other methods include the addition of components to molten PTFE to induce surface roughness.[50]

1.3.3 Alkyl–ketene dimers (AKDs)

The chemical structure of an AKD does not make it an obvious candidate for a superhydrophobic surface, in that it has no alkyl or fluoroalkyl chains (Figure 1.18). It is a wax which upon solidification (from its melt) spontaneously forms a fractal surface pattern. Flat non-fractal AKD surfaces prepared by mechanical cutting of the wax, have water contact angles reported as 109°. The fractal surface is highly rough, and it is this extreme roughness that contributes to its hydrophobic properties.[51] The commercial applications of AKD surfaces are relatively limited due to its waxy physical properties and the fact that it must be applied with a certain minimum thickness to allow formation of the fractal surface. Furthermore, its resistance to rubbing is limited.

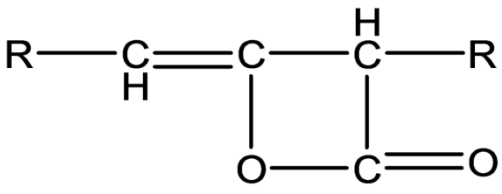

Figure 1.18. The chemical structure of an AKD molecule, R is a long alkyl chain approximately sixteen carbon atoms long. The alkyl chains will repel water due to their non-polar nature, whereas the polarised C=O bonds could potentially interact in a hydrophilic manner.

The transformation from smooth melt to rough fractal form depends on both time and temperature[52]. The surface structure develops naturally as the AKD cures and the fractal structure becomes rougher with time. The temperature at which the surface is cured also affects its hydrophobicity. It takes a shorter time to move to its fractal structure at temperatures close to the melting point of AKD (66°C), and thus develops hydrophobicity faster at higher temperatures.[52]

An example of AKD synthesis uses stearoyl chloride ($CH_3(CH_2)_{16}COCl$) and triethylamine (Figure 1.19).[51] The AKD was isolated from the reaction mixture, then melted and left to solidify on a glass plate. The formation of the fractal surface during solidification occurred in an unprompted process. The AKD is susceptible to hydrolysis and formation of dialkylketone (DAK) impurity (Figure 1.19), and the amount of this impurity could also be used to control the hydrophobicity of the surface. The surface constructed from a 98% AKD melt gives a water contact angle of 174° (Figure 1.20). The change in the water contact angle on flat (109°) compared to a rough surface highlights the huge effect the extreme roughness has on the hydrophobic properties of this material.[50]

Dimerization

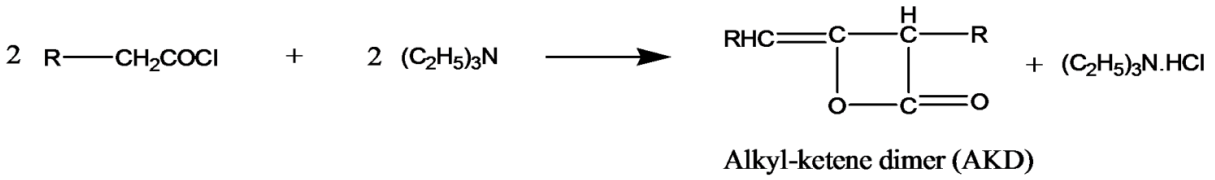

Hydrolysis of AKD

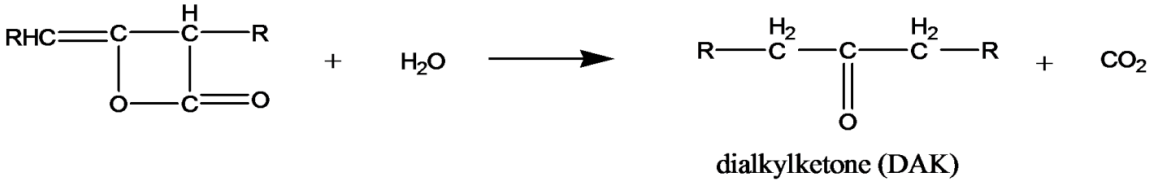

Figure 1.19. The dimerisation of RCH_2COCl reaction gives AKD after removal of HCl. AKDs react with water forms dialkylketone (DAK) impurity after loss of carbon dioxide. R = alkyl group - ($(CH_2)_{15}CH_3$).[51]

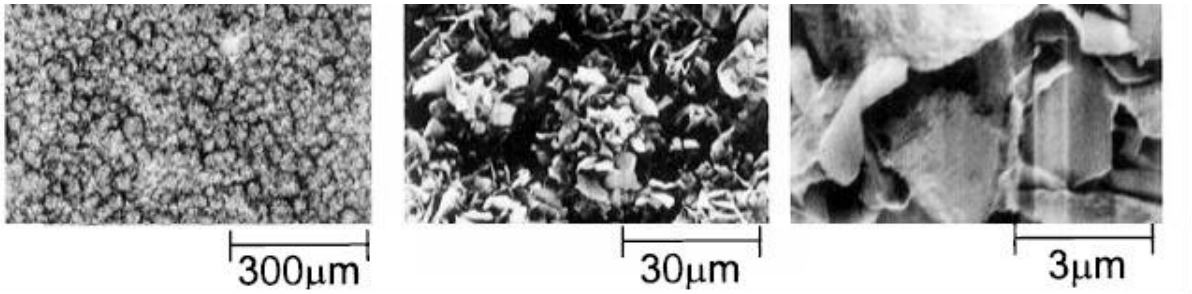

Figure 1.20. AKD surfaces at different magnifications (SEM images). Surfaces were left to solidify for 3 days under an inert nitrogen atmosphere at room temperature.

The addition of surfactants to the AKD melt has also been investigated.[52] It has been shown that, regardless of surfactant polarity, the addition decreased the water contact angle from the maximum achieved value for an unaltered surface. The decrease in hydrophobicity is due to the ionic component of the surfactant interacting with the water, attracting it toward the surface. It was however

shown that small additions of non-polar surfactants could improve the sliding of a water droplet with only a small reduction in contact angle.[52]

1.3.4 Poly(alkylpyrrole)

The structure of the poly(alkylpyrrole) (Figure 1.21) indicates both water repellent components (alkyl (R) group) and also potentially water attracting parts (C-N bond). Steric hindrance of approaching water molecules is provided by the long chain alkyl groups in addition to delocalised electrons on the pyrrole ring. Construction of poly(alkylpyrrole) surfaces show formation of rough fractal structures similar to those observed in the AKD surfaces considered previously.[53] Poly(alkylpyrrole) requires electrochemical synthesis *via* an applied potential difference during a polymerisation reaction. The result is a highly rough surface formed from the growth of microtube structures, directed by the voltage difference, without the need for any templates.[54]

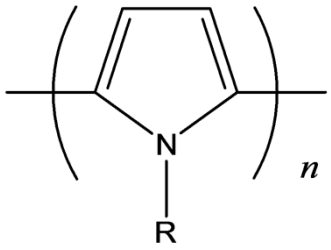

Poly(alkylpyrrole)

Figure 1.21. The chemical structure of poly (alkylpyrrole), contains both water attracting (polar C-N bonds) and repelling components (alkyl R groups). The high surface roughness generated by this material magnifies the material's net hydrophobicity giving the constructed surface superhydrophobic properties.

One known construction for highly rough poly(alkylpyrrole) surfaces uses 1-n-octadecylpyrrole in a polymerisation reaction *via* the addition of sodium p-toluenesulfate (Figure 1.22).[54] A voltage applied to the solution during the reaction results in a build-up of polymer on the plate electrode, this deposition occurs over a 1h period (compared to 3 days for AKD surfaces). The plates were washed and dried, and resulting water contact angles up to 154° were achieved.

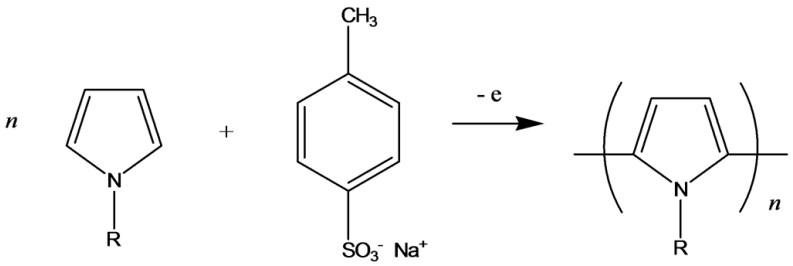

alkylpyrrole sodium *p*-toluenesulfonate poly(alkylpyrrole)

Figure 1.22. The reaction of 1-n-octadecylpyrrole (alkylpyrrole) with sodium p-toluenesulfate, carried out with an applied potential difference, to give the poly(alkylpyrrole); R=$(CH_2)_{17}CH_3$.

The coating exhibited no change in contact angle when treated with organic solvents or oils, due to a particularly high chemical stability and a stable geometric structure (Figure 1.23).

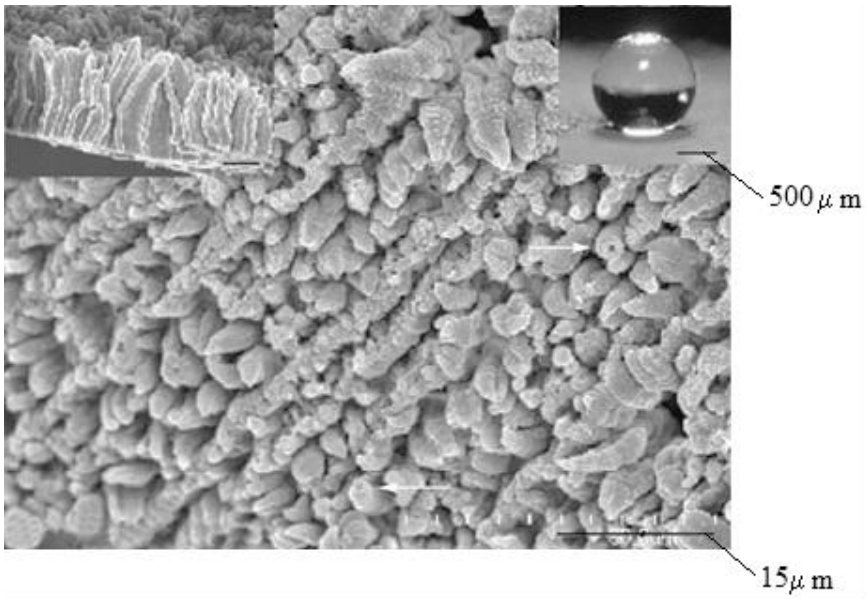

Figure 1.23. SEM image of the electrodeposited poly(alkylpyrrole) surface. The microstructure both acts to magnify the material's hydrophobicity in addition to trapping air underneath any water lying on the surface. *Inset*: A view of a water droplet on the super-hydrophobic surface.[54]

1.3.5 Chemically altered metal surfaces

Unaltered metal surfaces do not generally display hydrophobic characteristics.[55] Most metals can be shaped mechanically, with surface structure design and manufacture carried out with a great deal of accuracy, however due to the inherent hydrophilic nature of most metals the roughening typically brings about enhanced hydrophilicity.[10] Metals must be chemically altered before they can be used in the design of decidedly hydrophobic surfaces. This is usually achieved by roughening the metal and then coating the surface with a hydrophobic material/species.

Copper substrates have been modified to render them superhydrophobic[56]. This process commenced with a pre-treatment of copper metal substrates with an aqueous solution of $K_2S_2O_8$ and KOH, this oxidise the surface to form a thin layer of copper oxide. The resultant surface morphology is highly rough (Figure 1.24), this was coated in a hydrophobic material (polydimethylsiloxane (PDMS)), and the surface was rendered superhydrophobic. The methyl groups on the PDMS provide a low energy interaction with water, flat PDMS has reported contact angles approximately 95°.[57] When applied to a rough surface, the hydrophobic nature of the PDMS is magnified, which allows for a significant increase in water contact angle to 158°. Plain roughened copper had a contact angle of 23°. It is thus the application of the PDMS that makes it hydrophobic. The PDMS coated copper surface is stable over a range of pH values (1–14), with hydrophobicity maintained over these pH values.

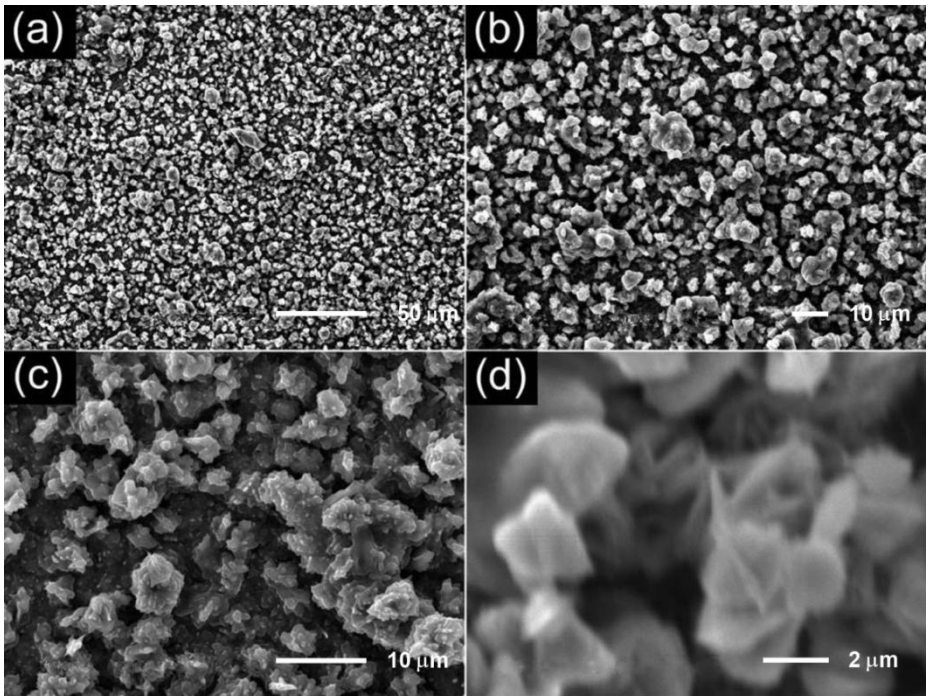

Figure 1.24. SEM images of an oxidised copper surface before the application of PDMS. The high surface roughness of the uncoated hydrophilic surface gives water contact angles of 23°. When the surface is coated with PDMS water contact angles rise to 158°. Scale bars are shown at each magnification.[56]

The use of electrodeposition techniques has been utilised to grow wire-like structures on copper substrates[58]. Deposited copper nanowires were thermally oxidised to form a copper oxide layer, which render them hydrophobic. Flat copper oxide films have been reported to have water contact angles greater than 100°. The nanowire film resulted in a very high water contact angle of 171°. Electrodeposition onto copper has also been used on pre-roughened copper (by etching); in this case electrodeposition of fluorinated polymers was carried out to give superhydrophobic surfaces.[59] Further depositions of copper include the spray-coating on to various substrates with copper alkylcarboxylates. These long-chain molecules act to lower the surface energy with spray-coating process facilitating the fabrication of high surface roughness.[60]

Platinum nanowires have been formed by electrodeposition onto Ti/Si substrates. Chloroplatinic acid (H_2PtCl_6) was used as a platinum source while anodic aluminium oxide (AAO) acted as a porous template.[61] After removal of the template a network of nanowires was formed generating a highly rough surface structure. The nanowires themselves are hydrophilic, with water contact angles below 90°, so functionalisation is required to lower the surface energy. The nanowires were modified by the addition of a FAS molecule ($CF_3(CF_2)_7CH_2CH_2Si(OCH_3)_3$), which lowers surface energy and increases hydrophobicity. The combination of high surface roughness with the low energy FAS gives a contact angle of 158° (Figure 1.25).[61]

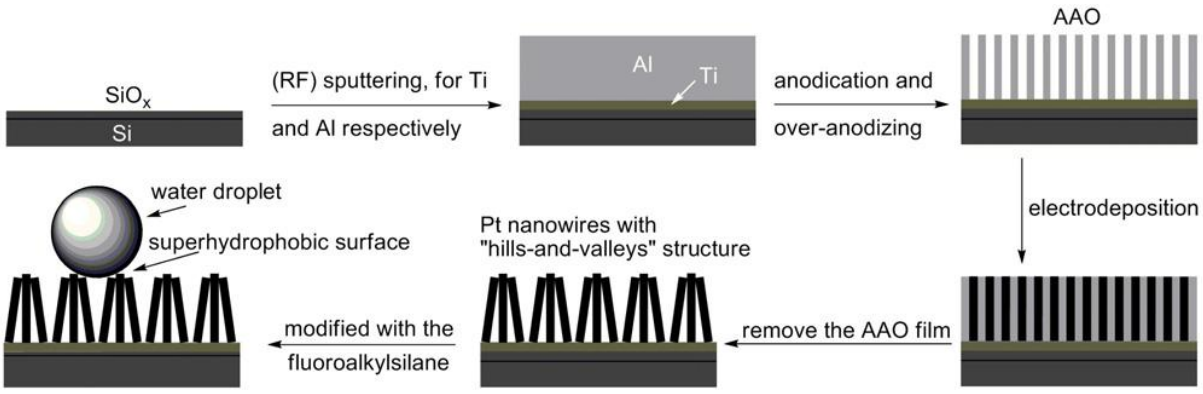

Figure 1.25. Schematic showing the method for generating platinum nanowires on Ti/Si substrates, the roughened surface was subsequently modified with a layer of FAS ((hepta-decafluoro-1,1,2,2,-tetrahydro-decyl)-1-trimethoxysilane) molecules to give water contact angles up to 158°.[61]

A similar surface has been prepared by using ZnO nanowires.[62] The ZnO nanowires were grown hydrothermally in solution by using ZnO nanocrystals embedded in a cotton substrate as seeding points for growth. The nanowires were then coated with a monolayer of FAS molecules to increase the hydrophobicity of the surface. The nanowires roughness combined with the hydrophobicity of the FAS monolayer gave a water contact angle of 161°.[61] FAS molecules can be used to modify other nanorods in a similar way.[63]

Copper mesh has been oxidised by using a solution of NaOH and $K_2S_2O_8$, to form $Cu(OH)_2$ nanoneedles. The needles were 7 μm in length, 150 to 300 nm in diameter and spread evenly over the mesh (Figure 1.26). When treated with a solution of n-dodecanethiol ($CH_3(CH_2)_{11}SH$), the surface $Cu(OH)_2$ nanoneedles are converted to of $Cu(SC_{12}H_{25})_2$. The modification lowers the surface energy by adding C-H bonds, when combined with the intrinsic surface roughness, this generates a surface with a water contact angle of 151°.[64] This superhydrophobic copper mesh was subsequently used to separate solvents from water (Figure 1.27, *left*). Equal ratio mixtures of water and solvent (hexane, petroleum ether, toluene and diesel oil) could be separated with at least 97% efficiency. By tuning the experimental set-up (tilt angle, droplet rolling length and mesh pore size) the separation can be optimised to >99% separation efficiency.[64] Miniature boats have been constructed from a similar superhydrophobic mesh made with n-dodecanoic acid instead of a thiol (Figure 1.27, *right*). Pore sizes of up to 930 μm were constructed, with buoyancy increasing with smaller pore size.[65]

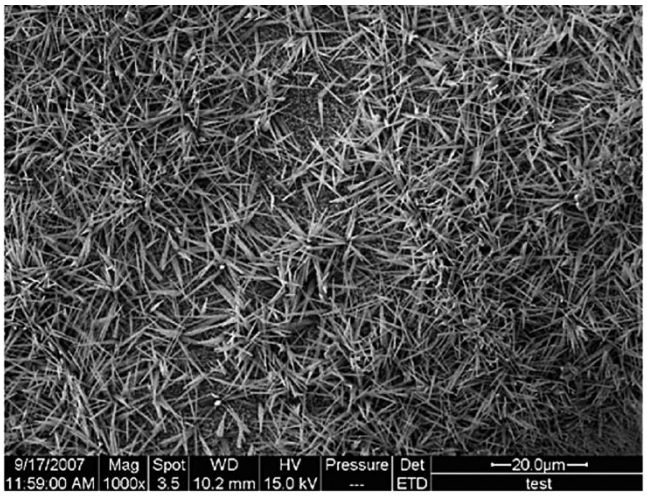

Figure 1.26. SEM image of the uniform coverage of $Cu(OH)_2$ nanoneedles on the copper substrate prior to modification with n-dodecanethiol. The nano-roughness combined with microstructure of the copper mesh, and the low surface energy provided by the C-H bonds of the thiol gave water contact angles of 151°.[64]

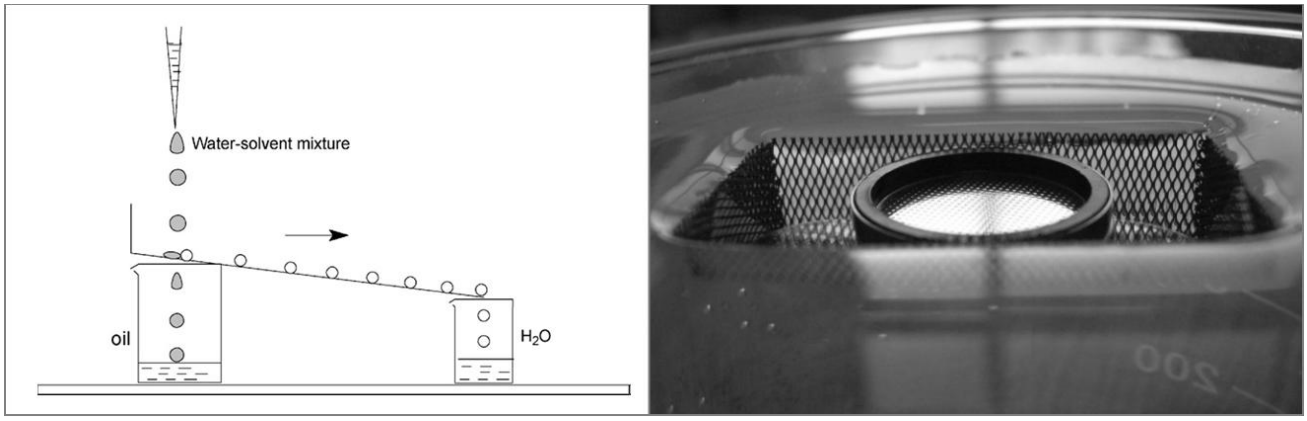

Figure 1.27. *Left*: Experimental set-up of water–solvent mixture separation. The mixtures were added at a rate of 1 drop per second onto the superhydrophobic copper mesh which prevented water falling through the mesh and rolled into a separate vessel, whereas the solvent permeated the mesh and fell through, not travelling down the tilted surface. *Right*: A weighted miniature boat (dimensions: 4 x 2 x 1 cm) constructed from superhydrophobic copper mesh, prevents water from passing through the pores and thus the boat floats on water.[64/65]

Iron–platinum nanoparticles have also been used for surface roughening. The nanoparticles were prepared by using platinum acetylacetonate and $[Fe(CO)_5]$ in the presence of both long-chain carboxylic acids and thiols. The surface-bound ligating groups were then exchanged for hydrophobic molecules through substitution reactions (Figure 1.28). Suspensions of particles were spread onto silicon substrates and the solvent was allowed to evaporate. The resultant surface structure was well developed, combined with the low energy of the fluorinated thiol and carboxylic acids ligating groups, allowed for water contact angles of 160° to be obtained.[66] The use of long-chain molecules is a well-defined method for lowering surface energy.[67] An example of this involves the reaction of a long chain carboxylic acids to Co_3O_4 nanoscale powders modified by using steric acid. These surfaces possess water contact angle up to 155°.[68]

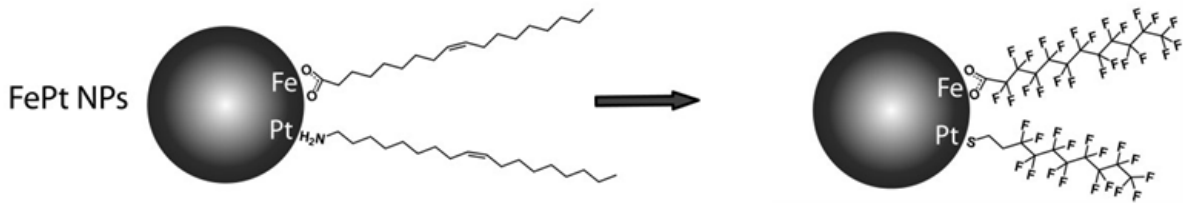

Figure 1.28. A ligand substitution reaction, the fluorinated chain increases the nanoparticles' hydrophobicity.[66]

1.3.6 Carbon nanotubes

Carbon nanotubes can be grown in a variety of ways[69], and this gives rise to the formation of many structures (Figure 1.29)[70]. The rod-shaped conformations of nanotubes can be arranged to provide high surface roughness[71], collections of aligned carbon nanotubes are termed "nanoforests". The hydrophobicity of untreated, vertically aligned nanotube surfaces support water contact angles around 126°. Carbon nanotubes can however compress and collapse when interacting with water, and a reduction in the water contact angle occurs subsequent to this[72/73]. Methods have been developed for constructing resilient carbon nanotube "forests", and combining these robust nanoforests with low energy surface modification can result in superhydrophobic surfaces.[71]

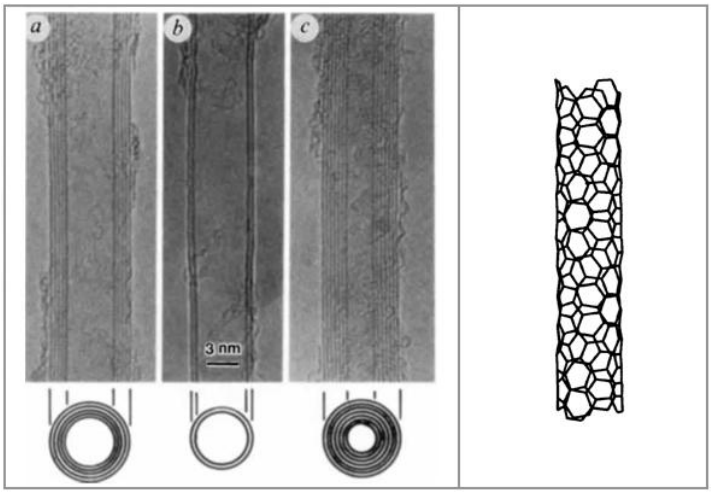

Figure 1.29. *Left*: TEM images of carbon nanotubes with a) five, b) two and c) seven layers. *Right*: diagram depicting the arrangement of carbon atoms in one type of carbon nanotube.[69/73]

To overcome carbon nanotube deformation caused by water, multi-walled carbon nanotubes (MWCNTs) have been anchored to a substrate *via* an amorphous carbon deposition.[71] The adherent MWCNTs have a potentially higher resistance to stress, strain and deformation upon interaction with solvent is consequentially reduced. The nanotubes can be coated with nitrene molecules, introduced as side groups in a UV-initiated process (Figure 1.30). Functionalisation with fluoroalkyl nitrenes formed superhydrophobic films with a water contact angles of 161°. Conversely a hydrophilic hydroxyalkyl nitrene coating gave water contact angles close to 0°. By varying the side chain, the properties of the surface could be altered, with hydrophobicity/hydrophilicity magnified by the high surface roughness of the carbon nanotubes.

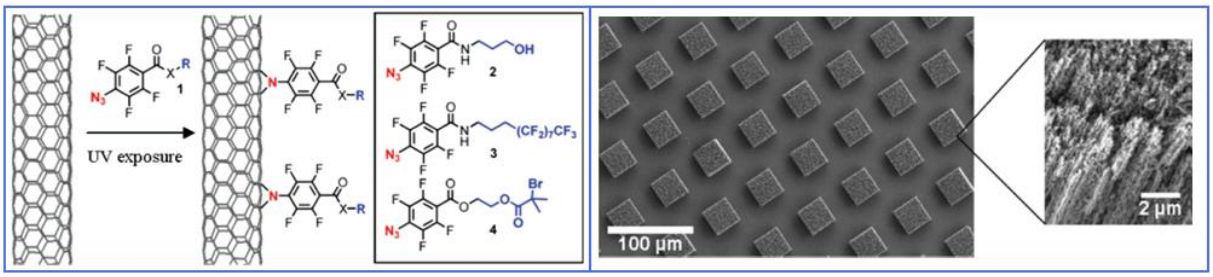

Figure 1.30. *Left*: Attachment of functionalised nitrenes to MWCNTs changes the wetting nature of the surface. *Right*: An etched surface of vertically aligned nanotubes attached to the tops of protrusions.[71]

MWCNTs have also been deposited on pre-patterned surfaces.[75] A silicon substrate was spin-coated with a photoresist, exposed to UV light etching portions of the surface not covered by the photoresist. The remaining photoresist was removed with acetone and the surface pattern developed (Figure 1.31). Electron-beam evaporation was then used to form a layer of Al/Fe catalyst (10 nm Al, 2 nm Fe), used for the carbon nanotube deposition, over the entire surface. MWCNTs were then grown on the catalyst in a water-assisted thermal chemical vapour deposition process carried out at 750–800°C (Figure 1.31).

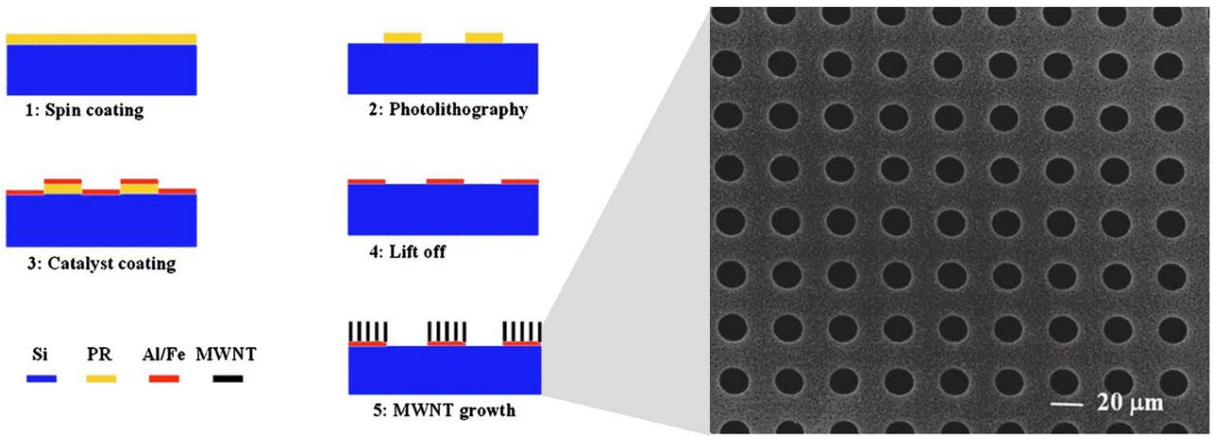

Figure 1.31. *Left*: Summary of the process used to generate the patterned surface and the growth of the MWCNTs. *Right*: An SEM of the patterned, nanotube coated surface.[75]

The water contact angle achieved increased from 163° to 165°, a relatively small change. The angle at which water droplets began to slide on the surface was however significantly altered. Un-patterned MWCNT surfaces were able to hold a 2 µL water droplet at a 90° tilt and even upside-down. Comparing this with the patterned surface, which had an average sliding angle of around 8°, it can be seen that alteration of large scale roughness causes the surfaces to wet in a very different ways. The low sliding angle for the patterned surface suggests a full Cassie–Baxter type wetting mechanism, whereas the sticky nature of the un-patterned surface suggests a Wenzel mechanism. Substantial voids introduced by the large scale roughness of the pattern cause air to be trapped underneath water droplets, and this allows water to move across the surface with less resistive force.[75] Silica

microspheres have also been used to introduce roughness to a substrate, greater than that achievable with solely carbon nanotubes[76]. Plasma action on aligned carbon nanotubes has also been carried out to render the tips of the nanotubes amorphous which increased surface hydrophobicity[77].

1.3.7 Modified silica-based surfaces

Silica materials generally have extensive coverage of hydroxyl (silanol) groups on their surfaces. A favourable interaction of water with these groups occurs through hydrogen bonding which renders most silica surfaces hydrophilic.[78] To decrease this interaction with water, the surface can be heated and hydroxyl groups removed[78]; alternatively the surface groups can be functionalised[79]. Hydrophobic silica is achievable by the lowering of surface energy and lowering the extent of interaction with water (Figure 1.32). In order to greatly enhance the surface hydrophobicity *via* these methods surface roughness must be introduced. Superhydrophobic modification of surface silanol groups is commonly done by using FAS molecules[80-83], in which the functionalisation is combined with roughening.

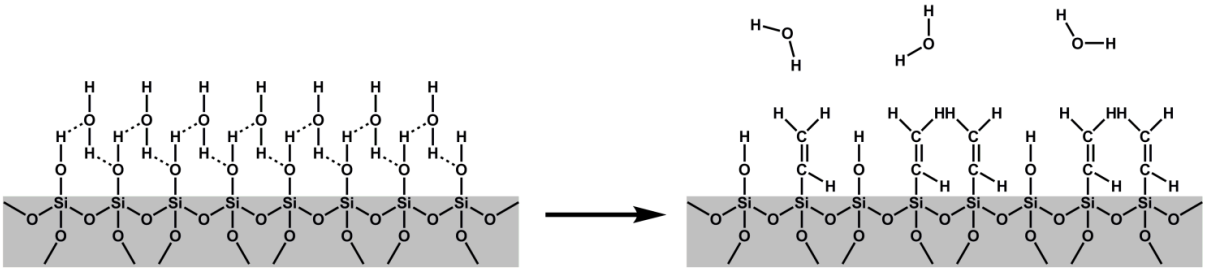

Figure 1.32. Schematic showing the functionalisation of silica surface hydroxyl groups. Treatment of a flat silica substrate with these groups lowers the surface energy and renders the surface hydrophobic.[79]

Fumed silica is made up of nanoparticulate SiO_2 with particle diameters of approximately 10 nm, and is formed by pyrolysis of $SiCl_4$ in the presence of oxygen and hydrogen gas. The nanoparticulate silica agglomerate together at higher temperatures, the small particle size provides a large surface area to mass ratio (> 100 m^2g^{-1}), which can be adjusted by varying the amount of agglomeration.[84] The inherent roughness of agglomerated particles in addition to potential functionalisation of surface silanol groups makes fumed silica an excellent template for superhydrophobic surface generation. Sol-gel techniques have been used to embed silica nanoparticles in an organosilane network *via* spin-coating onto glass[85]. The fumed silica was functionalised by using hexamethyldisilazane (HMDS) to give surface groups of trimethylsiloxane (TMS) (Figure 1.33). The rough and functionalised silica surfaces were extremely water repellent with a maximum water contact angle of 168° reported, and tilt angles of less than 3°. The hydrophobicity of the films degraded after exposure to water as the top layers of the fumed silica were removed. The rate of degradation was slowed by varying the amount of HMDS used in the sol-gel processing. The silica films were also

transparent (optical transmittance of around 92%) providing potential for self-cleaning window coatings.

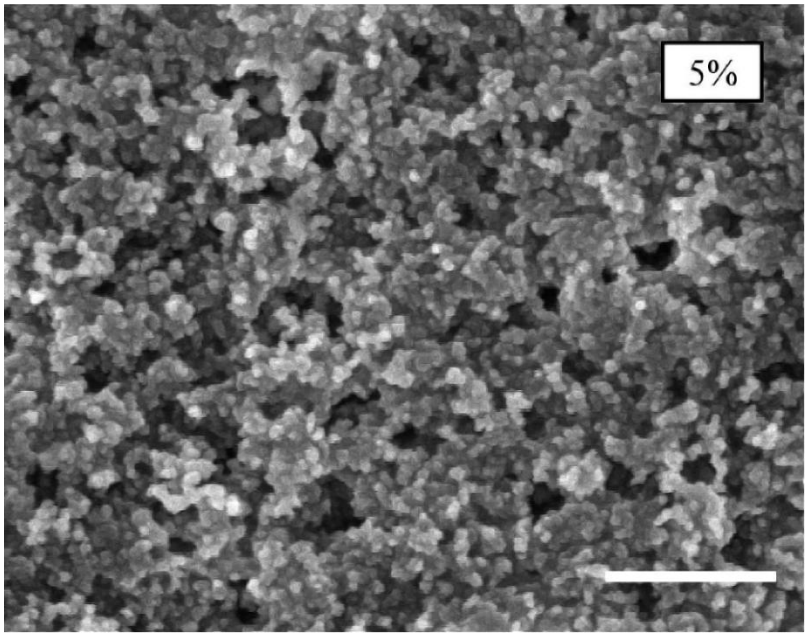

Figure 1.33. SEM image showing a fumed silica film on glass obtained by spin-coating a solution of 5 wt% trimethylsiloxane and silica nanoparticles, in methyl isobutyl ketone solvent. The silica particles diameters are approximately 10 nm; the agglomeration of these particles gives rise to the high surface roughness. The functionalisation with surface trimethylsiloxane groups lowers the surfaces energy. Scale bar shows 200 nm.[85]

The use of agglomerated silica nanoparticles for surface roughening can provide a solid structure that can be altered to lower surface energy[86]. This alteration can be made either by functionalising surface silanol groups[87/88] or by forming a thin layer of hydrophobic material to cover the hydrophilic silica[89]. This method of surface formation can be carried out at low temperature allowing cotton fibres and other temperature sensitive materials to be coated and rendered superhydrophobic[90]. A variation of this method uses colloidal zinc hydroxide, with functionalisation of the surface hydroxyl groups by using bulky stearate groups lowers surface energy. The modified zinc particles were then embedded in a silica network by spray-coating a silica sol-gel. The result is a highly rough surface with a low energy of interaction with water, water contact angle of 165° were achieved.[91]

A technique for the formation of silica is the acid hydrolysis of tetraethylorthosilicate (TEOS).[92] Rough silica surfaces have been constructed by combining the hydrolysed TEOS with polypropylene glycol (PPG). Subsequent pyrolysis of the resulting solid material results in decomposition of the PPG and surface roughening. Varying the amount of PPG in the starting materials network provides a different degree of roughening through differing amounts of decomposing material. Modification of the roughened surfaces was carried out by a reaction with HMDS that resulted in surface TMS groups (Figure 1.34). Water contact angles of around 160° were recorded on the roughest surfaces. Optical transparency could be introduced through changing the pH of the reaction mixture and the ratio of TEOS to PPG, and was raised to higher than 97% (from less than 30%). However, water contact angle were reduced to 156°. Silica formation by using TEOS as a

precursor has also been implemented as a support for silicon carbide nanowires, another route toward a superhydrophobic surface.[93]

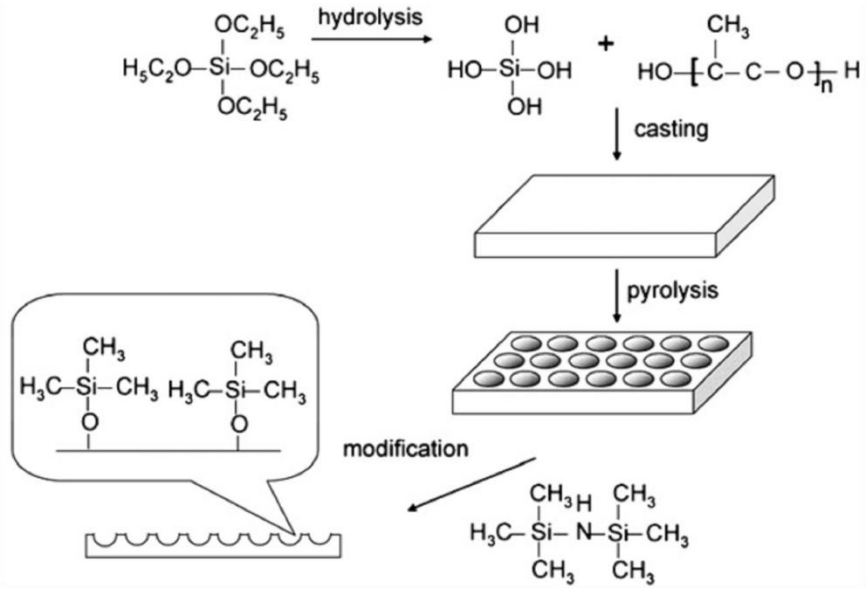

Figure 1.34. Schematic for the preparation of a roughened silica surface. Microstructure is generated by pyrolysis of a surface template material, this is followed by surface functionalisation with TMS groups which lowers surface energy.[92]

1.3.8 Miscellaneous surfaces

1.3.8.1 Lithographic Imprinting

Lithography is a method for depositing material onto a surface by means of a direct or indirect transfer from a mould or template; such a technique has been used using natural Lotus leaves (Figure 1.35). An imprint was made by creating a Lotus leaf cast using PDMS pre-polymer. After the polymer cured it was separated from the leaf giving a negative imprint of the Lotus leaf structure. The cast was then used to mould an ink (Figure 1.35) into the Lotus leaf-type structure, which was then dried in vacuum and remove from the cast. The resultant surface gave a water contact angle of 155°.[94] The ink (BP-AZ-CA) used was a long-chain polymer (Figure 1.35), the structure of which is not completely made up wholly of water-repelling components (i.e., alkyl or fluoroalkyl chains); it is thus the high surface roughness of the Lotus-like surface that contributes to its superhydrophobicity. The ink molecule was required to have some degree of polarity so it could be easily removed from the PDMS cast when stamped.[94]

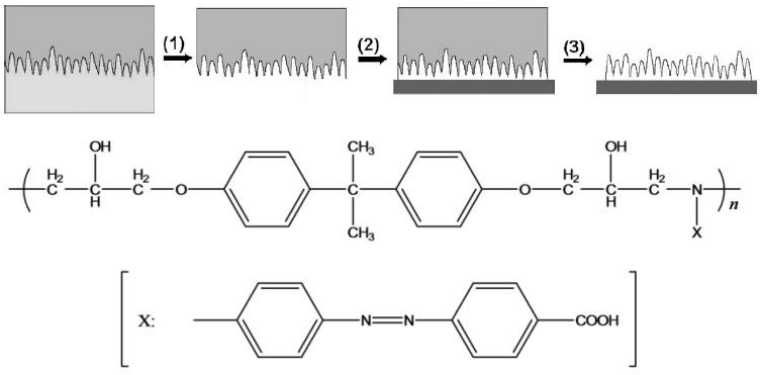

Figure 1.35. Lotus leaf imprinting: 1) A PDMS stamp is prepared by placing it on the surface of the leaf; 2) the stamp is pressed onto the ink; 3) the stamp is peeled off and dried to give an inverse Lotus leaf-type surface. Lower image shows chemical structure of the ink (BP-AZ-CA) used for imprinting.[94]

Low-density polyethylene has also been used to cast the Lotus leaf,[95] the result was the replication of Lotus leaf microstructure, using a low-energy material. The rough polyethylene surface was capable of achieving a 154° water contact angle. Polystyrene is a low energy material that has also been used in casting methods, in this instance a honeycomb structure was formed. The top layer of this honeycomb was then peeled away, leaving a spike where the two layers (top and bottom) were connected. The spiked low energy surface was reported to achieve a water contact angle of 165°.[96]

PDMS is a low-energy material that can be roughened to form superhydrophobic surfaces[97], however it can also be used as a substrate in order to minimise possible substrate interaction with water. Deposition of silica spheres has been carried out by a pressure transfer from a silicon plate (Figure 1.36).[98] In this case there was no mould used, however the silica spheres were used as a template for functionalisation. The silica spheres were coated in silver nanoparticles by action of $[Ag(NH_3)_2]^+$ ions, the silver was then chemically modified with perfluorodecanethiol which lowered the surface energy. The combination of the rough silica spheres and low surface energy allowed for water contact angles of 156° to be achieved. The PDMS substrates remained flexible and somewhat transparent, these superhydrophobic sheets can be applied to other surfaces.

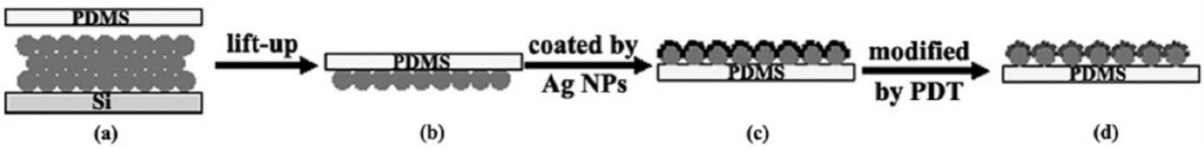

Figure 1.36. Schematic showing the soft lithography of silica spheres, once moulded to the surface the sphere were functionalised with silver nanoparticles which were then treated with perfluorodecanethiol, lowering surface energy.[98]

1.3.8.2 Electro-spinning of Polystyrene

Electro-spinning utilises electrical charge to draw fibres from a liquid. Nature has inspired the generation of extremely rough surfaces. One example uses the silver ragwort leaf[99], as its structure exhibits intricate nanostructured protrusions[100-102]. Application of a voltage to polystyrene solutions produced fibres which were deposited in a collector. The polystyrene solutions contained varying compositions of tetrahydrofuran (THF) and N,N-dimethylformamide (DMF) as solvents. The surface structures generated were extremely rough and porous (Figure 1.37), with the most hydrophobic surface giving a water contact angle of 159.5°.[99]

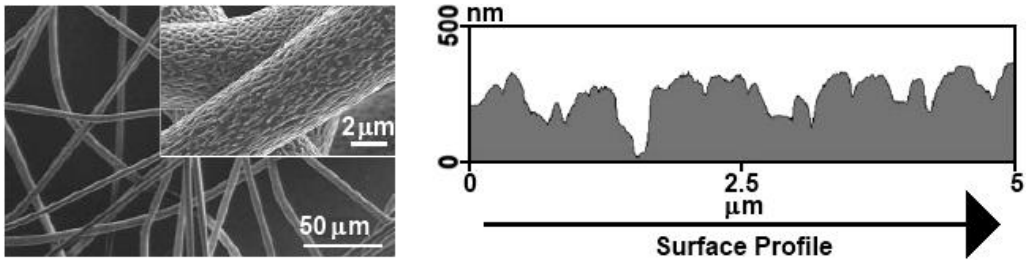

Figure 1.37. Electro-spun polystyrene – *Left*: SEM image of the polystyrene fibres (THF/DMF ratio of 1:3). *Right*: A surface profile cross section gained by atomic force microscopy (AFM).[99]

The surface hydrophobicity was found to be able to be controlled by the solvent ratio used, with a ratio of 1:3 of THF/DMF giving an optimised surface. Air trapped beneath any water droplets on the surface, reduced the amount of liquid–surface contact providing a superhydrophobic Cassie-Baxter type surface. The microstructure (Figure 1.37) was observed to resemble that of the silver ragwort leaf.[99] Electro-spinning of poly(vinylidene fluoride) solutions has also been used in a similar process[103]. The energy of the resultant surfaces could be lowered further by the addition of an FAS compound, which has also been used as a precursor in electro-spinning experiments[104]. This method can be applied to many other hydrophobic compounds[100-102].

This section has covered many of the methods used to form superhydrophobic surfaces. The key principle in superhydrophobic surface construction is the generation of surface roughness, while maintaining a surface chemistry with a low energy of interaction with water. To generate surfaces that demonstrate Lotus effect self-cleaning, a Cassie-Baxter wetting mechanism must be adopted, requiring a porous surface morphology capable of trapping air. The main experimental technique used in this project is chemical vapour deposition (CVD). The following sections will review the facets of this technique and explore examples of hydrophobic surfaces deposited *via* CVD.

1.4. Chemical Vapour Deposition

CVD is a technique used to deposit a solid product onto a substrate by means of a gas phase or surface reaction. There are many forms of CVD each with their own particular reaction routes, however a general mechanism (Figure 1.38) can be described.[105] Primarily the precursors are vaporised, if not already in the gas phase. Vaporisation techniques include; sonic action on a solution[106], thermal heating[107] and reduction of pressure[108]. The reactions can commence in the gas phase, with deposited films usually of high purity and uniformity. After vaporisation the reactants may require some activation to react, this is commonly done by heating[106-108], however other methods include electromagnetic radiation[109] and plasma activation[110]. Once activated, the reactant mixture comes into contact with the substrate a deposition is made onto its surface. Molecules which are not deposited can be lost from the activated complex and extracted as waste gas. The physisorbed atoms left at the substrate move around to chemically bind at favourable positions on the surface. Variation in

vaporisation technique as well as the method of precursor activation determines the category of the CVD taking place.[105]

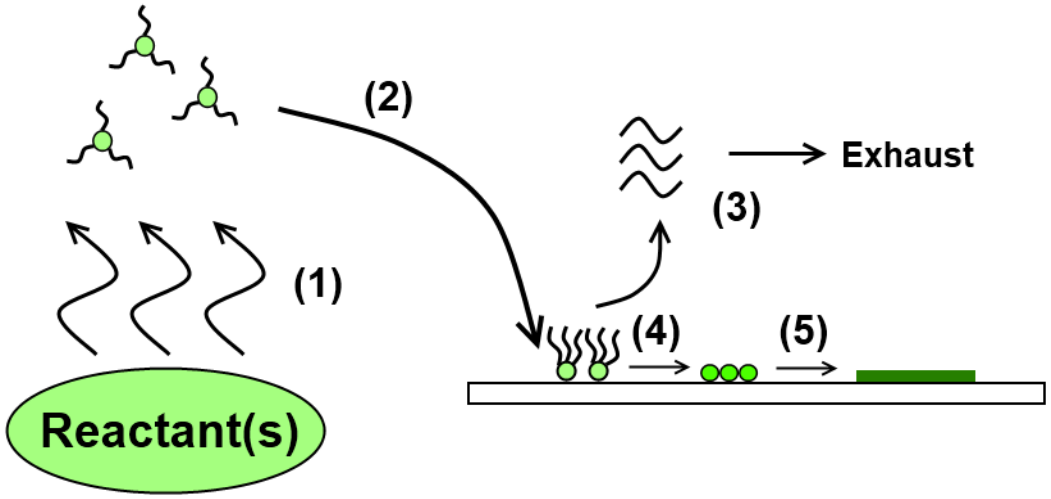

Figure 1.38. Schematic showing a general CVD mechanism – (1) vaporisation of precursors, (2) transfer to substrate where reaction can take place on the surface (some pre-reaction usually takes place at this step), (3) loss of gaseous molecules from reaction that are then transferred to exhaust as waste, (4) physisorption of reaction products onto substrate surface, (5) chemisorption of atoms in ideal surface environment and film formation.

1.5. Hydrophobic Surfaces *via* Chemical Vapour Deposition

The general mechanism for CVD tends to result in flat and chemically homogenous films. The uniformity of the deposited films can allow for a consistently low energy across the surface. The surface based reaction of many CVD processes hinders the growth of a highly rough microstructure in many cases.[105] Surface roughness can be introduced by altering elements of a typical CVD process; this is most commonly done by using precursors that contain preformed particles which then go on to give the deposited film its microstructure[111]. The deposition of hydrophobic films by using CVD is currently an area of great interest[112]. This section gives examples of some of the most successful methods for forming superhydrophobic coatings using CVD.

1.5.1 Carbon Nanotubes (CNTs)

The use of CNTs in CVD depositions can result in a highly rough structure due to the shape of the CNTs themselves[113/114]. Previous examples of CNT functionalisation to lower surface energy enable very hydrophobic surfaces to be constructed[71]. Untreated CNTs are slightly hydrophilic, with water contact angles between 70-80°.[115] Compounds such as CF_4 can be used in a CVD process to allow fluorination of CNTs and results in an increase in hydrophobicity, with water contact angles as large as 165° recorded[116].

1.5.2 Polytetrafluoroethylene (PTFE)

PTFE provides an extremely low surface energy with respect to water, with water contact angles around 118° on a flat substrate (Section 1.3.2). Rendering PTFE superhydrophobic can be accomplished by simple mechanical roughening applied to sheets of PTFE[117]; however CVD can be used to coat a range of substrates. Plasma-enhanced CVD (PECVD) uses plasma energy to activate the PTFE precursors or breakdown solid PTFE[118]. PECVD has been used to deposit flat films of PTFE with water contact angles >100°. Roughened substrates were also used in order to generate superhydrophobic surfaces raising contact angles to 160°.[119] Recent developments have shown that surface roughness can be introduced during the PECVD process.[120] Using pulses of plasma energy through a fluorocarbon source (hexafluorobenzene, C_6F_6), small particles were generated, these then agglomerated to form large features large enough to create a highly rough surface (Figure 1.39), on which water contact angles of over 160° were achieved.[120] Another example fired pulses of electrons at solid PTFE discs, this created PTFE vapours that then deposited onto silicon substrates. These surfaces obtained water contact angles up to 166°.[121]

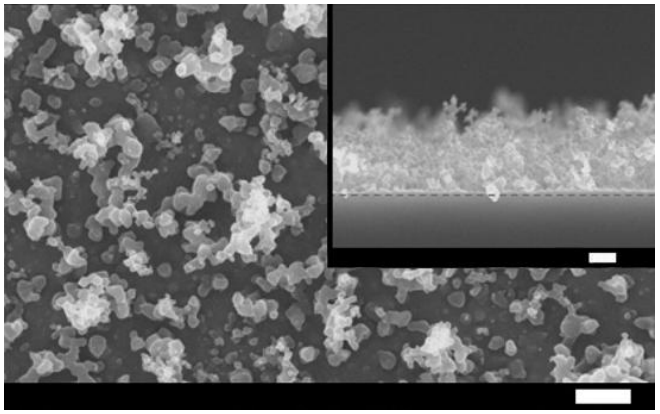

Figure 1.39. SEM of a superhydrophobic PTFE surface constructed by using pulsed PECVD. The pulses of plasma were required for material to agglomerate during the deposition of the film (scale bars = 1 μm).[120]

PECVD has also been used with trimethylmethoxysilane ($(CH_3)_3Si(OCH_3)$) to form hydrophobic surfaces.[122] Microwave energy was used to activate the plasma further, and this caused the subsequent breakdown of trimethylmethoxysilane generating $SiCH_x$, SiH, Si-CH_2-Si, and $SiOCH_3$ surface groups, in addition to a highly developed rough microstructure. The water contact angles for these siloxane surfaces were over 150°.[122] Another precursor used to construct a similar surface is hexamethylcyclotrisiloxane. Upon plasma activation of this molecule, chains and rings of methylated siloxanes were formed. The result was a range of superhydrophobic surfaces with water contact angles up to 162°.[123]

1.5.3 Thermally Activated Deposition

This type of deposition vaporises solid or liquid precursors by heating, and can be carried out at atmospheric pressure or reduced pressures[107/108]. The atmospheric pressure CVD (APCVD) of tungsten diselenide (WSe_2) onto glass has been carried out by reaction of tungsten hexachloride and diethyl

selenide[124]. Water contact angles up to 145° were achieved (Figure 1.40), and the surface structures were found to be made up of thin needles oriented predominantly perpendicular to the plane of the substrate. The high roughness of the film facilitated the maximisation of the water contact angle. The films did not exhibit Cassie-Baxter wetting, since water droplets on the surface did not roll or slide even at high tipping angles. This suggests a Wenzel wetting type with no air trapped beneath the droplet. Water droplets of up to 100 mg were stationary at a 90° tip angle. Other diselenide systems did not show similar wetting behaviours ($TiSe_2$[125], VSe_2[126], $NbSe_2$[127], $MoSe_2$[128]).

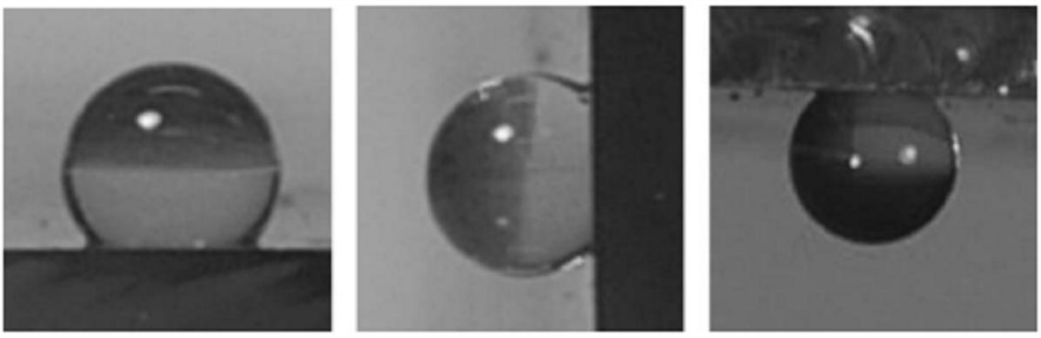

Figure 1.40. Shows water droplets (1 mg) sitting on a tungsten–selenide film deposited via APCVD, tip angles of 0° (left), 90° (centre) and even suspended upside down (right) could not remove the water droplet. This clearly demonstrates the effect of Wenzel-type surface wetting on the nature of interaction between water and a surface.

The formation of poly-p-xylylenes is a contrasting example that did form a Cassie–Baxter wetting surface. These films were formed by the evaporation of aromatic and fluorinated precursors that gave a gas-phase reaction which formed a poly-p-xylylene surface with a water contact angle of 153°.[129]

1.6. Routes to Hydrophobicity

The techniques explored in superhydrophobic surface formation have led to the development of four main routes to construct extremely hydrophobic surfaces. In the design of superhydrophobic surfaces, there are two main features that must be focussed on: a low surface energy so a flat surface has a contact angle above 90° and a high surface roughness to amplify the hydrophobicity of the surface and trap air in the surface porosity. Surface roughness can be introduced while depositing a low-energy material[120] or each can be introduced separately[40], the result of which is a one-step construction (laying down a rough and low energy surface) or a two-step construction (introducing surface roughness and then lowering the surface energy), see Figure 1.41. Surface roughness can also be introduced to a low-energy material, such as PTFE[40], or a low-energy material can be applied to a substrate and roughening performed subsequently (e.g. AKD application).[130]

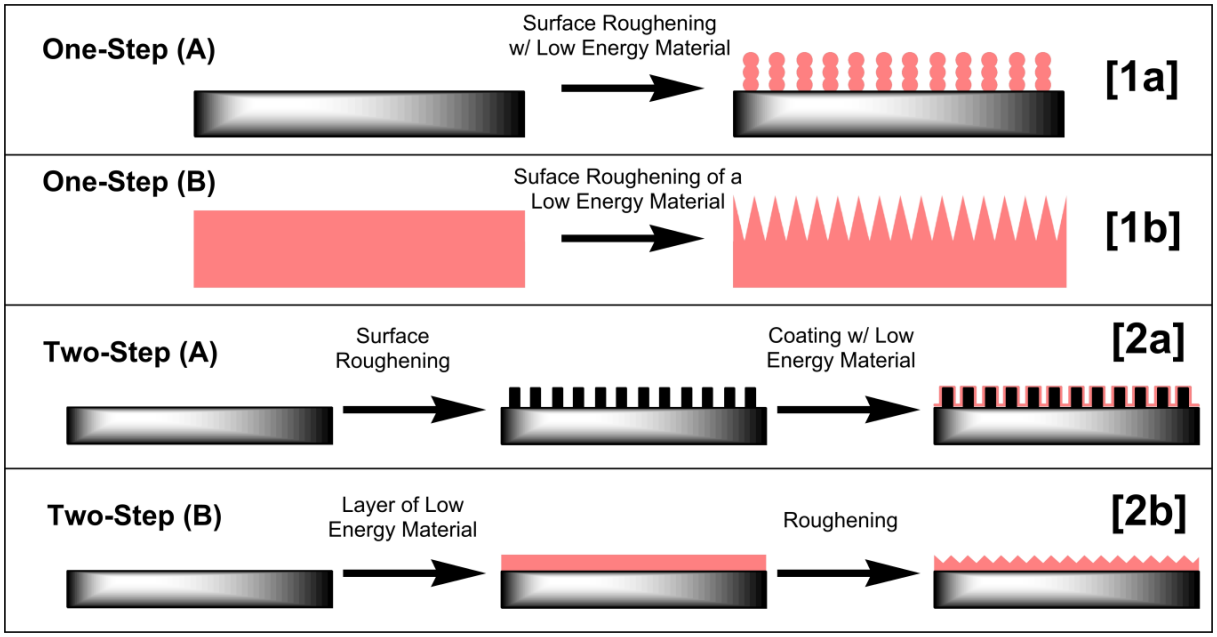

Figure 1.41. Schematic showing four main mechanisms (**1a**, **1b**, **2a**, **2b**) for the construction of a hydrophobic surface.

In order to carry out each route different issues must be considered. Route **1a** requires the use of low-energy material that has good adherence to the substrate. If it has no adherence, the film will be powdery and would have limited use. Route **1b** requires only the use of a low-energy material that can be roughened with the material's hydrophobicity maintained after the roughening process has taken place. The two-step formation, **2a**, needs a strong attraction force between the material used for roughening and the hydrophobic reagent. If there is no adherence, the hydrophobic coating would degrade and the surface's hydrophobicity is reduced. A variation of the two-step technique, **2b**, has the deposition of a substantial amount of hydrophobic material first which is then followed by roughening. This route (analogous with **1b**) requires the low energy to be maintained upon roughening, in addition to a constant adherence to the original substrate.

Hydrophobic surfaces can be constructed from inherently hydrophilic materials.[131] This is brought about by forming highly rough surfaces that trap air with a lot of force, forming a Cassie-Baxter surface from a high-energy material. Although this can be achieved, the most hydrophobic surfaces use low energy materials for construction or a low-energy functionalisation.[2-5]

1.7. Commercial Application of Hydrophobic Surfaces

The Lotus effect can allow the self-cleaning of surfaces. However hydrophobic surfaces have many other applications in a wide number of fields. The following section will focus on the range of uses of such surfaces, including self-cleaning.

1.7.1 Lotus Effect Self-cleaning (Anti-biofouling)

It has been demonstrated that surface coatings can be designed to remove particles when treated with water, by duplicating the Lotus effect. Figure 1.42 shows a Formica sheet, one side was unaltered and the other coated with superhydrophobic PTFE, both sides were dusted with soot particles. Upon action of water, the particles were completely removed from the PTFE-treated side, whereas the untreated sheet did not demonstrate the Lotus effect and did not self-clean.[132] Commercial paints have been developed (Sto AG) which dries to form a superhydrophobic coating and possesses significant self-cleaning attributes.[132]

Figure 1.42. Soot-coated Formica plates. The side of the left plate is untreated and shows no Lotus-effect self-cleaning and soot removal with action of water is inefficient. The right side of the plate is coated with micropowdered PTFE giving the surface superhydrophobic properties, from which soot is easily removed with water.[132]

A substantial area of research is currently focussed toward transparent superhydrophobic self-cleaning coatings. Transparent films applied to optically transmitting glasses and plastics could be utilised in many industries including automotive developments, buildings and solar panels. Superhydrophobicity would insure transparency is maintained due to self-cleaning under the action of water. Superhydrophobic surfaces require a rough microstructure.[133] To generate a transparent coating the light which passes through must not interact the coating itself or the substrate used to deposit onto, to ensure this the features of the surfaces microstructure must have dimensions less than the wavelength of visible light (< 380 nm).[134] In constructing transparent films the surface microstructure must be carefully considered.

Despite these factors, there is a wide range of products on the market aimed toward transparent hydrophobic applications developed by Pilkington, Saint-Gobain and PPG Industries in addition to others.[135-137] Hydrophobic surfaces can prevent adhesion of bacteria to surfaces[138]. An example of this is a commercially available spray for ship hulls limits biofouling by reducing the

ability of bacteria to stick to the surface[139]. Hydrophobic coatings for windows (domestic and vehicular) are also available[135/140]. The coatings act to keep the glass free of water marks by preventing water droplet adhesion with self-cleaning properties also apparent. With respect to car windscreens, products aim to make the glass slippery and allow the fast removal of water so windscreen wipers may not have to be operated.[141/142] Spectacles are also an area of commercial exploitation for hydrophobic coatings.[143]

1.7.2 Surface protection

A superhydrophobic surface limits the contact between water and a surface, this principle can be applied to a metal surface which would reduce possible corrosion. Copper surfaces oxidised then post-treated with a functionalisation gave rise to superhydrophobic properties, and corrosion was shown to be hugely reduced.[144] This technology could be applied to other surfaces in order to protect against water. Hydrophobic surfaces not only repel water droplets but also show resistance to humidity. Fluorinated silanes have been used to coat paper, and as the paper was already rough the surface was rendered superhydrophobic and resistant to humidity, with tensile strength maintained up to extremely high humidity.[145]

1.7.3 Textiles

Natural fibres and textiles such as cotton have an inherently rough microstructure, the lowering of surface energy could render them superhydrophobic. Treatments on cotton fibre[146/147] in addition to paper sheets[145] have been carried out to create water repellent materials. Transforming textiles from a natural hydrophilic state to superhydrophobic not only keeps the fabric dry, but there is also a chance for the flexibility and insulating properties of the original material to be maintained. Figure 1.43 shows cotton fibres that have been coated by using a sol–gel method. Nanoparticulate silver was also incorporated into the coating to give a potential antimicrobial activity. The inherent roughness of the fibres used in textile design means that water-repellent fibres can be treated with a low energy material in order to magnify the surfaces hydrophobicity. The development of hydrophobic textiles is a widely explored area, and countless products are available commercially.[148/149]

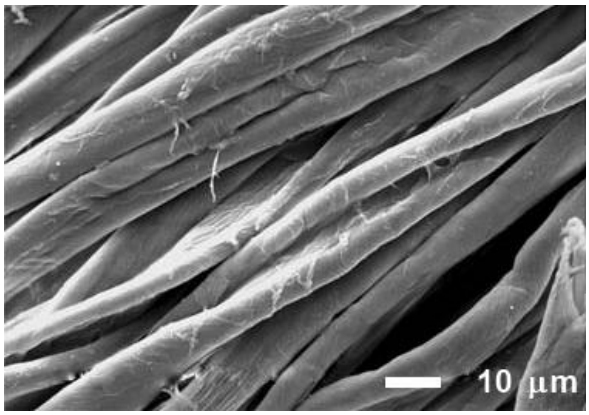

Figure 1.43. An SEM image of superhydrophobic cotton fabric coated with a fluoroalkyl siloxane. The cotton fibres provide an inherent surface roughness, and coating the fabric with a low energy material increases hydrophobicity.[147]

1.7.4 Movement of water

The manner in which water wets a surface dictates the ease of movement across it, a Cassie–Baxter model suggests a slippery surface, whereas a Wenzel-type surface would be more resistant to water movement. This reduction in drag force, for a Cassie–Baxter surface, results from a layer of gas at the liquid–solid interface which limits contact between the water and surface material. Flow dynamic experiments carried out inside copper pipes demonstrate this point. The insides of the pipes are coated so that they are superhydrophobic, these pipes show significant reduction in water drag through them (see Figure 1.44 for the experimental setup).[150] The superhydrophobic tube allows a greater rate of flow through it, relative to an untreated pipe when put under the same pressure. Commercially available treatments for boat hulls can reduce drag in the water and allow the craft to travel more easily through the water[139]. Another effect of the layer of gas at the water–solid interface stems from the buoyancy of air under water. Objects with a Cassie–Baxter wetting mechanism will have a volume of air between the surface and the water when floating on a body of water. This air could act as a buoyancy force, supporting floating of previously non-buoyant objects.[151/152]

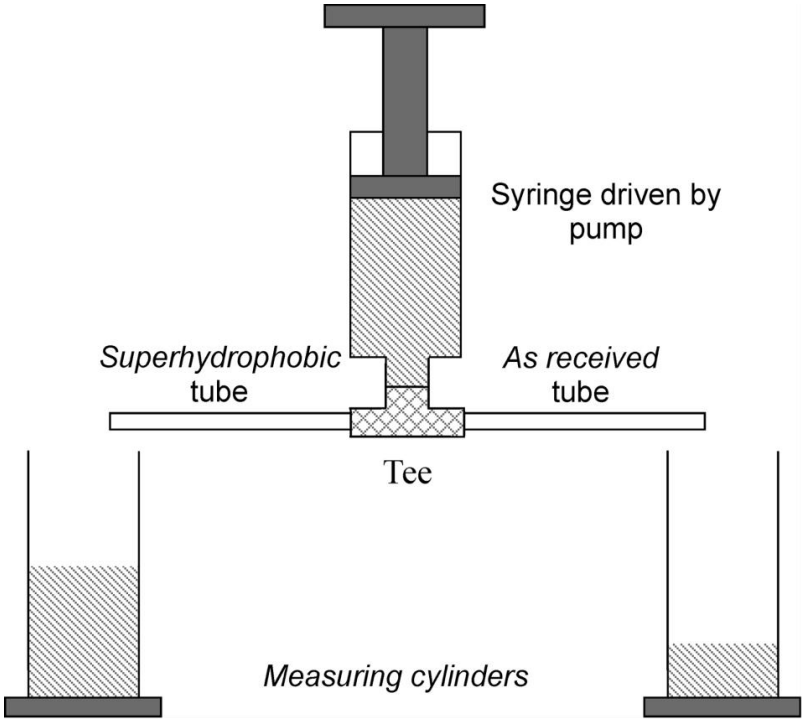

Figure 1.44. Schematic showing the experimental setup to show a difference in flow though pipes. The movement of water through superhydrophobic tubing is a lot faster relative to unaltered tubing. This more rapid movement is due to a reduction in drag force between the water and the walls of the superhydrophobic tubes.[150]

The repulsion of water from a superhydrophobic surface also has the effect of limiting contact of any components in the water with the surface. This can be important in areas such as artificial organ implantation, in which the adhesion of platelets to blood-containing vessels can cause coagulation or thrombosis.[153]

1.7.5 Microfluidics

Recent developments in superhydrophobic surface construction allows for movement of water on a microscale. It has been shown that by altering the wetting properties of a surface on an incredibly small scale, allows for water droplets to be moved by controlling a surfaces microstructure.[154/155] Water movement at the microscale is important in areas such as biofluid transport[156], in which wetting behaviour and water movement can be controlled by small external forces such as application of a voltage or change in temperature.[154]

1.7.6 Oil–water separation

Water-repellent molecules such as long alkyl chains are oleophilic. Their use to coat a rough surface to render them superhydrophobic could also give superoleophilic properties to that surface.[64] A copper mesh modified to be superhydrophobic would support water and prevent it from passing through the pores in the mesh, and water droplets would also roll off when the surface was tilted. Substances such as hexane, petroleum ether, toluene and diesel oil were not repelled like the water and slip through the mesh upon contact. Mixtures of water and oily substances were then separated up to and above 99% efficiency. Superhydrophobic nanoporous polymers have been investigated and have been found to be very effective absorbers of organic compounds.[157] These materials could act to absorb any oil-like products and leave water behind; these materials could be implemented in the clean-up of oil spillages at sea.

1.8 Summary

A large number of methods have been used to make hydrophobic surfaces as shown in this introduction. The use of CVD to construct a superhydrophobic surface is inherently difficult due to the flat-uniform structures observed in most CVD reactions. Exceptionally hydrophobic surfaces not only need to be constructed from low energy materials, they require a highly developed surface microstructure which acts to magnify surface hydrophobicity, in addition to trapping air in the porosity of the surface in order to increase hydrophobicity further. Examples of hydrophobic surfaces made *via* CVD, explored within this introduction, suggest that preformation of potential surface features must be accomplished (or commenced) prior to contact with a substrate.

The following work in this thesis details novel routes toward hydrophobic surfaces *via* CVD, and methods for overcoming inherent complications in generating surface roughness. Other issues handled will include the interaction of bacteria with superhydrophobic surfaces, in addition to investigating new methods for assessing surface hydrophobicity. The early chapters focus on synthesising new hydrophobic surfaces, and chapter 2 starts this by detailing the aerosol assisted chemical vapour deposition (AACVD) of polymers, in which highly rough and water-repellent

surfaces are deposited in a one-step process. The hybrid CVD and functionalisation of silica microparticles is covered in Chapter 3; this is a two-step deposition in which rough surfaces are subsequently functionalised to render them extremely hydrophobic. Chapter 4 deals with the AACVD of copper and copper oxide films, these are flat uniform coatings that can be roughened and functionalised in post-treatments. The bacterial adhesion to superhydrophobic surfaces is discussed in Chapter 5, with potential future developments in anti-microbial surface design identified. Chapter 6 covers the dynamic behaviour of water when interacting with a surface, which also leads to a new definition of superhydrophobicity through water bouncing. The design of a device to separate mixtures of oil and water is the last experimental chapter (Chapter 7). Chapter 8 concludes the main points addressed in the thesis.

1.9 References

1. B. D'Urso and J. T. Simpson, *Appl. Phys. Lett.*, 2007, **90**, 044102.
2. X. Zhang, F. Shi, J. Niu, Y. Jiang and Z. Wang, *J. Mater. Chem.*, 2008, **18**, 621.
3. X. Li, D. Reinhoudt and M. Crego-Calama, *Chem. Soc. Rev.*, 2007, **36**, 1350.
4. G. McHale, N. J. Shirtcliffe and M. I. Newton, *Langmuir*, 2004, **20**, 10146.
5. M. L. Ma and R. M. Hill, *Curr. Opin. Colloid Interface Sci.*, 2006, **11**, 193.
6. W. Att, N. Hori, F. Iwasa, M. Yamada, T. Ueno and T. Ogawa, *Biomaterials*, 2009, **30**, 4268.
7. Z. Cui, L. Yin, Q. Wanga, J. Ding and Q. Chen, *J. Colloid Interface Sci.*, 2009, **337**, 531.
8. W. Barthlott and C. Neinhuis, *Planta*, 1997, **202**, 1.
9. Y. Cheng and D. E. Rodak, *Appl. Phys. Lett.*, 2005, **86**, 144101.
10. Z. Burton and B. Bhushan, *Ultramicroscopy*, 2006, **106**, 709.
11. B. Bhushan, Y. C. Jung, *Prog. Mater. Sci.*, 2011, **56**, 1–108.
12. C. Neinhuis and W. Barthlott, *Ann. Bot.*, 1997, **79**, 667.
13. X. Gao and L. Jiang, *Nature*, 2004, **432**, 36.
14. M. Sun, G. S. Watson, Y. Zheng, J. A. Watson and A. Liang, *J. Exp. Biol.*, 2009, **212**, 3148.
15. Y. Zheng, X. Gao and L. Jiang, *Soft Matter*, 2007, **3**, 178.
16. S. Lee and T. H. Kwon, *Nanotechnology*, 2006, **17**, 3189.
17. R. N. Wenzel, *Ind. Eng. Chem.*, 1936, **28**, 988.
18. A. B. D. Cassie and S. Baxter, *Trans. Faraday Soc.*, 1944, **40**, 546.
19. V. Rico, P. Romero, J. L. Hueso, J. P. Espinós and A. R. González-Elipe, *Catal. Today*, 2009, **143**, 347.
20. A. B. D. Cassie, *Discuss. Faraday Soc.*, 1948, **3**, 11.
21. J. Kim, H. Sugimura and O. Takai, *Vacuum*, 2002, **66**, 379.
22. A. Marmur, *Langmuir*, 2003, **19**, 8343.
23. D. Quéré and M. Reyssat, *Phil. Trans. R. Soc. A*, 2008, **366**, 1539.
24. P. Roach, N. J. Shirtcliffe and M. I. Newton, *Soft Matter*, 2008, **4**, 224.
25. A. M. Peters, C. Pirat, M. Sbragaglia, B. M. Borkent, M. Wessling, D. Lohse and R. G. H. Lammertink, *Eur. Phys. J. E*, 2009, **29**, 391.
26. S. M. Lee, C. Y. Park, S. Bae, J. S. Go, B. Shin and J. S. Ko, *Jpn. J. Appl. Phys.*, 2009, **48**, 095504.

27. J. Liu, X. Feng, G. Wang and S. Yu, *J. Phys. Condens. Matter*, 2007, **19**, 356002.
28. W. Choi, A. Tuteja, J. M. Mabry, R. E. Cohen and G. H. McKinley, *J. Colloid Interface Sci.*, 2009, **339**, 208.
29. S. A. Kulinich and M. Farzaneh, *Appl. Surface Sci.*, 2009, **255**, 4056.
30. F. Chang, S. Hong, Y. Sheng and H. Tsao, *Appl. Phys. Lett.*, 2009, **95**, 064102.
31. S. Wang and L. Jiang, *Adv. Mater.*, 2007, **19**, 3423.
32. G. J. Toes, K. W. van Muiswinkel, W. van Oeveren, A. J. H. Suurmeijer, W. Timens, I. Stokroos and J. J. A. M. van den Dungen, *Biomaterials*, 2002, **23**, 255.
33. A. M. Almanza-Workman, S. Raghavan, S. Petrovic, B. Gogoi, P. Deymier, D. J. Monk and R. Roop, *Thin Solid Films*, 2003, **423**, 77.
34. E. L. Decker and S. Garoff, *Langmuir*, 1997, **13**, 6321.
35. K. Koch, B Bhushan, Y. C. Jung and W. Barthlott, *Soft Matter*, 2009, **5**, 1386.
36. E. M. Blockhuis, Y. Shilkrot and B. Widom, *Mol. Phys.*, 1995, **86**, 891.
37. W. Wu, X. Wang, X. Liu and F. Zhou, *Appl. Mater. Interfaces*, 2009, **1**, 1656.
38. Y. Akamatsu, K. Makita, H. Inaba and T. Minami, *Thin Solid Films*, 2001, **389**, 138.
39. M. Mostefa, Y. Auriac, M. E. R. Shanahan, J. Bressan and A. Meslif, *Int. J. Adhes. Adhes.*, 2000, **20**, 257.
40. J. Bico, C. Marzolin and D. Quere, *Europhys. Lett.*, 1999, **47**, 220.
41. A. Nakajima, K. Abe, K. Hashimoto and T. Watanabe, *Thin Solid Films*, 2000, **376**, 140.
42. J. Lu, Y. Yu, J. Zhou, L. Song, X. Hub and A. Larbot, *Appl. Surface Sci.*, 2009, **255**, 9092.
43. S. R. Coulson, I. Woodward, J. P. S. Badyal, S. A. Brewer and C. Willis, *J. Phys. Chem. A*, 2000, **104**, 8836.
44. E. Bormashenko, V. Goldshtein, R. Barayev, T. Stein, G. Whyman, R. Pogreb, Z. Barkay and D. Aurbach, *Polym. Adv. Technol.*, 2009, **20**, 650.
45. A. Milella, R. Di Mundo, F. Palumbo, P. Favia, F. Fracassi and R. d'Agostino, *Plasma Processes Polym.*, 2009, **6**, 460.
46. W. Song, D. D. Veiga, C. A. Custdio and J. F. Mano, *Adv. Mater.*, 2009, **21**, 1830.
47. J. Li, J. Fu, Y. Cong, Y. Wu, L. Xue and Y. Han, *Appl. Surface Sci.*, 2006, **252**, 2229.
48. J. Yang, Z. Zhang, X. Men and X. Xu, *J. Macromol. Sci. Part A*, 2009, **46**, 997.
49. I. S. Bayer, A. Steele, P. J. Martorana, E. Loth and L. Miller, *Appl. Phys. Lett.*, 2009, **94**, 163902.
50. L. Yan, K. Wang and L. Ye, *J. Mater. Sci. Lett.*, 2003, **22**, 1713.
51. S. Shibuichi, T. Onda, N. Satoh and K. Tsujii, *J. Phys. Chem.*, 1996, **100**, 19512.
52. R. Mohammadi, J. Wassink and A. Amirfazli, *Langmuir*, 2004, **20**, 9657.
53. H. Yan, H. Shiga, E. Ito, T. Nakagaki, S. Takagi, T. Ueda and K. Tsujii, *Colloids Surf.*, 2006, **284**, 490.
54. H. Yan, K. Kurogi, H. Mayama and K. Tsujii, *Angew. Chem.*, 2005, **117**, 3519; *Angew. Chem. Int. Ed.*, 2005, **44**, 3453.
55. R. Wang, L. Cong and M. Kido, *Appl. Surface Sci.*, 2002, **191**, 74.
56. Z. Guo, W. Liu and B. Su, *Appl. Phys. Lett.*, 2008, **92**, 063104.
57. M. Jin, X. Feng, J. Xi, J. Zhai, K. Cho, L. Feng and L. Jiang, *Macromol. Rapid Commun.*, 2005, **26**, 1805.
58. F. Mumm, A. T. J. van Helvoort and P. Sikorski, *ACS Nano*, 2009, **3**, 2647.
59. Z. Kang, Q. Ye, J. Sang and Y. Li, *J. Mater. Process. Technol.*, 2009, **209**, 4543.

60. W. Wu, X. Wang, X. Liu and F. Zhou, *Appl. Mater. Interfaces*, 2009, **1**, 1656.
61. M. Qu, G. Zhao, Q. Wang, X. Cao and J. Zhang, *Nanotechnology*, 2008, **19**, 055707.
62. B. Xu and Z. Cai, *Appl. Surface Sci.*, 2008, **254**, 5899.
63. D. Tian, Q. Chen, F. Nie, J. Xu, Y. Song and L. Jiang, *Adv. Mater.*, 2009, **21**, 3744.
64. Q. M. Pan, M. Wang and H. B. Wang, *Appl. Surface Sci.*, 2008, **254**, 6002.
65. Q. M. Pan and M. Wang, *ACS Appl. Mater. Interfaces*, 2009, **1**, 420.
66. Y. Ofir, B. Samanta, P. Arumugam and V. M. Rotello, *Adv. Mater.*, 2007, **19**, 4075.
67. F. Zhang, L. Zhao, H. Chen, S. Xu, D. G. Evans and X. Duan, *Angew. Chem.*, 2008, **120**, 2500; *Angew. Chem. Int. Ed.*, 2008, **47**, 2466.
68. Z. Yuan, H. Chen, C. Li, L. Huang, X. Fu, D. Zhao and J. Tang, *Appl. Surface Sci.*, 2009, **255**, 9493.
69. S. Iijima, *Nature*, 1991, **354**, 56.
70. M. Paradise and T. Goswami, *Mater. Des.*, 2007, **28**, 1477.
71. S. J. Pastine, D. Okawa, B. Kessler, M. Rolandi, M. Llorente, A. Zettl and J. M. J. Frchet, *J. Am. Chem. Soc.*, 2008, **130**, 4238.
72. C. T. Wirth, S. Hofmann and J. Robertson, *Diamond Relat. Mater.*, 2008, **17**, 1518.
73. J. S. Lee, J. Ryu and C. B. Park, *Soft Matter*, 2009, **5**, 2717.
74. M. S. Dresselhaus, G. Dresselhaus, J. C. Charlier and E. Hernandez, *Philos. Trans. R. Soc. A*, 2004, **362**, 2065.
75. Z. Wang, N. Koratkara, L. Ci and P. M. Ajayan, *Appl. Phys. Lett.*, 2007, **90**, 143117.
76. L. Zhang and D. E. Resasco, *Langmuir*, 2009, **25**, 4792.
77. M. Shakerzadeh, H. E. Teo, C. Tan and B. K. Tay, *Diamond Relat. Mater.*, 2009, **18**, 1235.
78. J. Laskowski and J. A. Kitchener, *J. Colloid Interface Sci.*, 1969, **29**, 670.
79. Q. Wei, Y. Wang, Z. Nie, C. Yu, Q. Li, J. Zou and C. Li, *Microporous Mesoporous Mater.*, 2008, **111**, 97.
80. X. Liu and J. He, *Langmuir*, 2009, **25**, 11822.
81. Q. F. Xu, J. N. Wang, I. H. Smith and K. D. Sanderson, *J. Mater. Chem.*, 2009, **19**, 655.
82. T. Saison, C. Peroz, V. Chauveau, S. Berthier, E. Sondergard and H. Arribart, *Bioinspiration Biomimetics*, 2008, **3**, 046004.
83. Q. F. Xua and J. N. Wang, *New J. Chem.*, 2009, **33**, 734.
84. N. Auner and J. Weis, *Organosilicon Chemistry II: From Molecules to Materials, Wiley, New York*, 1996, p. 761.
85. M. Manca, A. Cannavale, L. De Marco, A. S. Aricò, R. Cingolani and G. Gigli, *Langmuir*, 2009, **25**, 6357.
86. C. Liao, C. Wang, H. Lin, H. Chou and F. Chang, *Langmuir*, 2009, **25**, 3359.
87. P. N. Manoudis, A. Tsakalof, I. Karapanagiotis, I. Zuburtikudis and C. Panayiotou, *Surf. Coat. Technol.*, 2009, **203**, 1322.
88. Z. Qian, Z. Zhang, L. Song and H. Liu, *J. Mater. Chem.*, 2009, **19**, 1297.
89. Z. Cui, L. Yin, Q. Wanga, J. Ding and Q. Chen, *J. Colloid Interface Sci.*, 2009, **337**, 531.
90. G. Y. Bae, B. G. Min, Y. G. Jeong, S. C. Lee, J. H. Jang and G. H. Koo, *J. Colloid Interface Sci.*, 2009, **337**, 170.
91. R. V. Lakshmi and B. J. Basu, *J. Colloid Interface Sci.*, 2009, **339**, 454.
92. K. Chang, Y. Chen, H. Chen, *Surf. Coat. Tech.*, 2008, **202**, 3822.

93. J. J. Niu and J. N. Wang, *J. Phys. Chem. B*, 2009, **113**, 2909.
94. B. Liu, Y. He, Y. Fan and X. Wang, *Macromol. Rapid Commun.*, 2006, **27**, 1859.
95. J. Feng, M. Huang and X. Qian, *Macromol. Mater. Eng.*, 2009, **294**, 295.
96. W. Ting, C. Chen, S. A. Dai, S. Suen, I. Yang, Y. Liu, F. M. C. Chenad and R. Jeng, *J. Mater. Chem.*, 2009, **19**, 4819.
97. S. J. Hwang, D. J. Oh, P. Gu Jung, S. M. Lee, J. S. Go, J. Kim, K. Hwang and J. S. Ko, *J. Micromech. Microeng.*, 2009, **19**, 095010.
98. T. Yao, C. Wang, Q. Lin, X. Li, X. Chen, J Wu, J. Zhang, K. Yu and B. Yang, *Nanotechnology*, 2009, **20**, 065304.
99. Y. Miyauchi, B. Ding and S. Shiratori, *Nanotechnology*, 2006, **17**, 5151.
100. D. Reneker and I. Chun, *Nanotechnology*, 1996, **7**, 216.
101. D. Li and Y. N. Xia Y, *Nano. Lett.*, 2004, **4**, 933.
102. H. Q. Liu and Y. L. Hsieh, *J. Polym. Sci. Part B*, 2002, **40**, 2119.
103. Y. Chen and H. Kim, *Appl. Surface Sci.*, 2009, **255**, 7073.
104. T. Ogawa, B. Ding, Y. Sone and S. Shiratori, *Nanotechnology*, 2007, **18**, 165607.
105. R. Gordon, *J. Non-Cryst. Solids.*, 1997, **218**, 81.
106. S. O'Brien, M. G. Nolan, M. Çopuroglu, J. A. Hamilton, I. Povey, l. Pereira, R. Martins, E. Fortunato and M. Pemble, *Thin Solid Films*, 2010, **518**, 4515.
107. G. Shi, T. Franzke, W. Xia, M. D. Sanchez and M. Muhler, *Chem. Vap. Deposition*, 2011, **17**, 162.
108. N. Licausi, S. Rao and I. Bhat, *J. Electron. Mater.*, 2011, **40**, 1668.
109. V. Santucci, F. Maury and F. Senocq, *Thin Solid Films*, 2010, **518**, 1675.
110. Z. Wang, M. Shoji and H. Ogata, *Appl. Surf. Sci.*, 2011, **257**, 9082.
111. S. Wang, Y. Li, X. Fei, M. Sun, C. Zhang, Y. Li, Q. Yang and X. Hong, *J. Colloid Interface Sci.*, 2011, **359**, 380.
112. Z. Guo, W. Liu and B. Su, *J. Colloid Interface Sci.*, 2011, **353**, 335.
113. S. A. Miller, V. Y. Young and C. R. Martin, *J. Am. Chem. Soc.*, 2001, **123**, 12335.
114. T. Kyotani, L. Tsai and A. Tomita, *Chem. Mater.*, 1995, **7**, 1427.
115. D. Mattia, M. P. Rossi, B. M. Kim, G. Korneva, H. H. Bau and Y. Gogotsi, *J. Phys. Chem. B*, 2006, **110**, 9850.
116. Y. C. Hong, D. H. Shin and H. S. Uhm, *Surf. Coat. Technol.*, 2007, **201**, 5025.
117. M. A. Nilsson, R. J. Daniello and J. P. Rothstein, *J. Phys. D: Appl. Phys.*, 2010, **43**, 045301.
118. J. Wang, F. Liu, H. Chen and D. Chen, *Appl. Phys. Lett.*, 2009, **95**, 084104.
119. D. J. Balazs, C. Hollenstein and H. J. Mathieu, *Plasma Processes Polym.*, 2005, **2**, 104.
120. S. H. Yang, C. Liu, W. Hsu and H. Chen, *Surf. Coat. Technol.*, 2009, **203**, 1379.
121. S. Gupta, A. C. Arjunan, S. Deshpande, S. Seal, D. Singh and R. K. Singh, *Thin Solid Films*, 2009, **517**, 4555.
122. Y. Wu, M. Kouno, N. Saito, F. A. Nae, Y. Inoue and O. Takai, *Thin Solid Films*, 2007, **515**, 4203.
123. M. C. Kim and C.-P. Klages, *Surf. Coat. Technol.*, 2009, **204**, 428.
124. N. D. Boscher, C. J. Carmalt and I. P. Parkin, *J. Mater. Chem.*, 2006, **16**, 122.
125. N. D. Boscher, C. J. Carmalt and I. P. Parkin, *Chem. Vap. Deposition*, 2006, **12**, 54.

126. N. D. Boscher, C. S. Blackman, C. J. Carmalt, I. P. Parkin and A. G. Prieto, *Appl. Surface Sci.*, 2007, **253**, 6041.

127. N. D. Boscher, C. J. Carmalt and I. P. Parkin, *Eur. J. Inorg. Chem.*, 2006, 1255.

128. N. D. Boscher, C. J. Carmalt, R. G. Palgrave, J. J. Gil-Tomas and I. P. Parkin, *Chem. Vap. Deposition*, 2006, **12**, 692.

129. Y. Elkasabi, H. Nandivada, H. Chen, S. Bhaskar, J. D'Arcy, L. Bondarenko and J. Lahann, *Chem. Vap. Deposition*, 2009, **15**, 142.

130. T. Minami, H. Mayama and K. Tsujii, *J. Phys. Chem. B*, 2008, **112**, 14620.

131. C. Guo, L. Feng, J. Zhai, G. Wang, Y. Song and L. Jiang and D. Zhu, *Chem. Phys. Chem.*, 2004, **5**, 750.

132. A. Solga, Z. Cerman, B. F. Striffler, M. Spaeth and W. Barthlott, *Bioinspiration Biomimetics*, 2007, **2**, S126.

133. J. Fresnais, J. P. Chapel and F. Poncin-Epaillard, *Surf. Coat. Technol.*, 2006, **200**, 5296.

134. A. Nakajima, *J. Ceram. Soc. Jpn.*, 2004, **112**, 533.

135. http://www.saint-gobain-sekurit.com/EN/?nav1=PR&id=360. (*Date accessed: 31/08/2011*)

136. http://www.opticalcoatings.com/processes/hydrophobic.html. (*Date accessed: 31/08/2011*)

137. http://www.diamonfusion.com/en/products/applications.aspx. (*Date accessed: 31/08/2011*)

138. D. P. Bakker, F. M. Huijs, J. de Vries, J. W. Klijnstra, H. J. Busscher and H. C. van der Mei, *Colloids Surf. B*, 2003, **32**, 179.

139. http://www.auroramarine.com/aurora/catalog/01250/. (*Date accessed: 31/08/2011*)

140. http://www.nanoprotect.co.uk/nanofor-car.html. (*Date accessed: 31/08/2011*)

141. http://www.rainx.co.uk/. (*Date accessed: 31/08/2011*)

142. http://www.aquapel.com/. (*Date accessed: 31/08/2011*)

143. http://www.mayerandmayer.com/more_info.asp?current_id=84. (*Date accessed: 31/08/2011*)

144. X. H. Chen, G. B. Yang, L. H. Kong, D. Dong, L. G Yu, J. M. Chen and P. Y. Zhang, *Cryst. Growth Des.*, 2009, **9**, 2656.

145. H. Yang and Y. Deng, *J. Colloid. Interface Sci.*, 2008, **325**, 588.

146. S. C. Cho, Y. C. Hong, S. G. Cho, Y. Y. Ji, C. S. Han and H. S. Uhm, *Curr. Appl. Phys.*, 2009, **9**, 1223.

147. B. Tomšič, B. Simončič, B. Orel, L. Černe, P. F. Tavčer, M. Zorko, I. Jerman, A. Vilčnik and J. Kovac, *J. Sol-Gel Sci.*, Technol. 2008, **47**, 44.

148. http://www.velouk.com/. (*Date accessed: 31/08/2011*)

149. http://www.salclear.com/DWR.htm. (*Date accessed: 31/08/2011*)

150. N. J. Shirtcliffe, G. McHale, M. I. Newton and Y. Zhang, *App. Mater. Inter.*, 2009, **1**, 1316.

151. Y. Zhou, M. Li, B. Su and Q. Lu, *J. Mater. Chem.*, 2009, **19**, 3301.

152. M. S. Żbik, J. Du, R. A. Pushkarova and R. St. C. Smart, *J. Colloid Interface Sci.*, 2009, **336**, 616.

153. T. Sun, H. Tan, D. Han, Q. Fu and L. Jiang, *Small*, 2005, **1**, 959.

154. T. Saitoh, A. Sekino and M. Hiraide, *Anal. Chim. Acta*, 2005, **536**, 179.

155. J. Yang, J. C. Chen, K. Huang and J. A. Yeh, *J. Microelectromech. Syst.*, 2006, **15**, 697.

156. P. Bayiati, A. Tserepi, P. S. Petrou, K. Misiakos, S. E. Kakabakos, E. Gogolides and C. Cardinaud, *Microelectron. Eng.*, 2007, **84**, 1677.

157. Y. Zhang, S. Wei, F. Liu, Y. Du, S. Liu, Y. Ji, T. Yokoi, T. Tatsumi and F. Xiao, *Nano Today*, 2009, **4**, 135.

Chapter 2

The Aerosol Assisted Chemical Vapour Deposition of Polymers

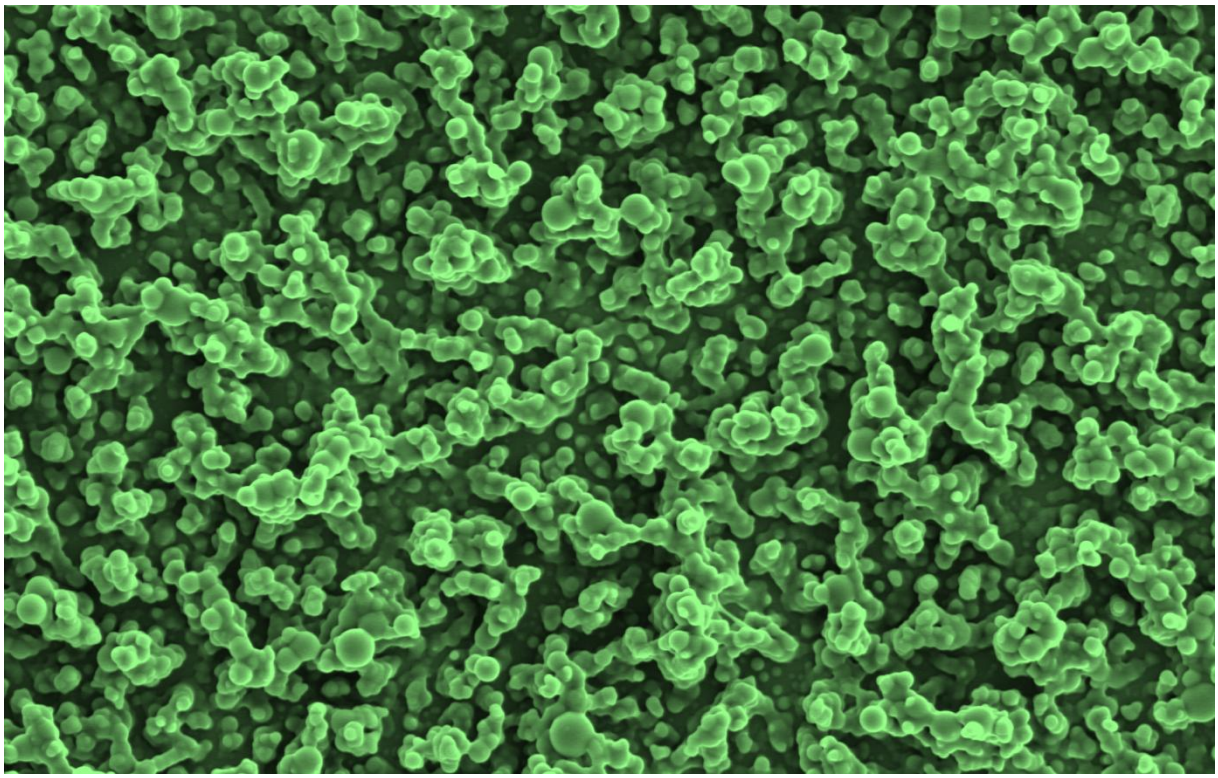

Figure 2.01. SEM image of silicone elastomer film deposited *via* CVD.

2. The Aerosol Assisted Chemical Vapour Deposition of Polymers

2.1. Introduction

Polymers are one of the most widely implemented materials used to construct hydrophobic surfaces[1]. Polymers are large molecular chains, formed from repeating structural units. The species able to form polymeric molecules are wide and varied[2], and the majority of materials used in hydrophobic surface generation are based on organic or silicone units[3-6]. These types of polymer materials are highly suitable for the assembly of superhydrophobic surfaces as the two main features required in a superhydrophobic surface can easily be generated:

- **Low Surface Energy** – Repeating units of polymer molecules provide a regular chemical structure which interacts with water in a similar manner along the whole length of the polymer chain. Hydrophobic units can provide a uniformly low energy surface, with no areas of attraction across the polymer surface.[7]
- **High Surface Roughness** – Many polymers are flexible and/or mouldable, and can be manipulated into shape and permanently fixed into position. Highly rough microstructures can easily be produced by means of very basic etching or moulding techniques.[8]

Low energy polymers such as PTFE[9], polyethylene[10] and PDMS[11] exhibit a high-level of surface hydrophobicity, with water contact angles of 110°, 100°, and 95° achieved respectively on flat solid surfaces of each polymer. When the inherently hydrophobic material is roughened the hydrophobicity of the material magnified greatly[12]. With the construction of surfaces wetting with a Cassie-Baxter mechanism is easily accomplished given the ease of manipulation of the polymer materials[13].

2.1.1 Thermosoftening vs. Thermosetting Polymers

Polymers can be placed into two main groups – thermosoftening (thermoplastic/non-curing)[14] and thermosetting (curing)[15] polymers. Amorphous thermosoftening polymers begin to melt when their temperature is increased, and resolidify when cooled sufficiently. Softening of polymers in this class occurs as the molecular chains making up the material are attracted by relatively weak forces, which are interrupted by heating and so melting occurs (Figure 2.02).[14] Thermosetting polymers are those that cure irreversibly and are usually liquids prior to a curing process. The polymer chains within the starting material contain reactive species which can be activated by heat, addition of a catalyst or electromagnetic irradiation, in addition to other methods. Reaction of the species on the precursor chains binds them together in a cross-linking reaction. Propagation of the cross-linking reaction greatly increases the molecular weight throughout the material and results in solidification. This solidification is permanent as much of the structure is interlinked with strong covalent bonds (Figure 2.02); any further heating may lead to decomposition of the material.[15]

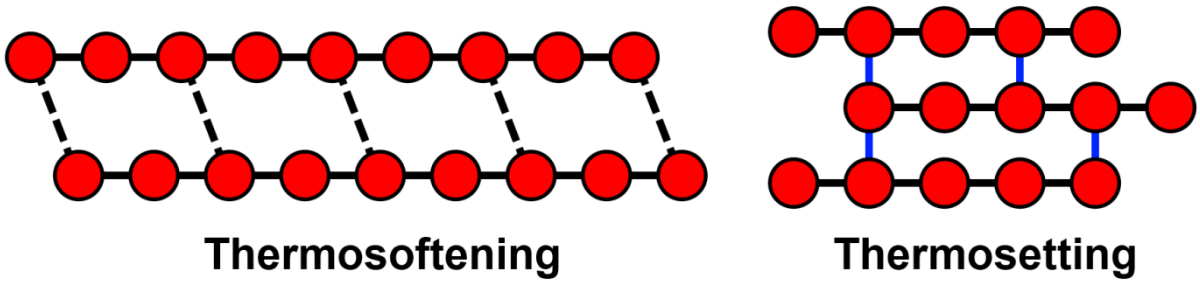

Figure 2.02. Schematic showing a representation of inter-chain bonding in thermosoftening and thermosetting polymers. Thermosoftening polymer chains have weak attractions, mainly electrostatic, which are lessened by high temperatures and so the polymers melt upon heating. The covalently bonded chains in thermosetting polymers are not readily broken, and excessive heating may cause decomposition.

2.1.2 Aerosol Assisted Chemical Vapour Deposition

Aerosol assisted chemical vapour deposition (AACVD), uses solutions of precursors as starting materials for thin films. The precursor solutions are vaporised by transforming them into an aerosol. This can be carried out by an ultra-sonic vibration and atomiser devices.[16-18] The resulting aerosol of the precursor solution is made up of microdroplets of the starting solution small enough to be suspended in air for a given period. The diameter of the aerosol microdroplets depends on the method of vaporisation and solution used. For example there is an indirect relationship between the diameter of droplet and frequency of ultrasonic aerosol generation. Once aerosols are formed they are passed into a heater reactor, the AACVD reaction chamber.[16-18]

Forming solutions of CVD precursors affords many advantages over the use of the same precursor in its pure form, especially in the case of polymers. In other CVD processes vaporisation of precursors is carried out by heating or a reduction in pressure[19], and these methods require reactants to have relatively high vapour pressures; with the most successful precursors existing as liquids at room temperature. Polymers (both thermosoftening and thermosetting) consist of very large molecular units, and so ambient vapour pressures are typically extremely low[20]. This, in addition to the susceptibility of polymers, such as PTFE, polyethylene and PDMS, toward degradation at high temperatures means most hydrophobic polymers would be poorly suited to a vapour pressure driven precursor delivery. The aerosol droplets of precursor solutions are able to transport the large polymer molecules to a reaction chamber, and this negates the need for a volatile CVD precursor[19]. This chapter details the AACVD of hydrophobic polymers and explains the need for curing agents during the reactions through a rationalisation of the deposition mechanism. The microstructure of films deposited is analysed, with changes in hydrophobicities related back to the surface structure and type of polymer used. Some of the deposited films are enhanced by incorporation of light activated antimicrobial agents, in addition to routes for improving the hydrophobicity and adhesion of the deposited films. The deposition of a hydrophilic curing polymer (melamine-formaldehyde resin) resulted in films of

similar microstructures, giving Cassie-Baxter wetting surfaces that were hydrophobic. The work covered in this chapter was the first reported use of polymers to form superhydrophobic surfaces.

2.2. Experimental Details

2.2.1 Materials

With the exception of Sylgard 184 Silicone Elastomer which was purchased from R. W. Greeff, NuSil Med-4850 which was obtained from UCL Eastman Dental Institute and Dyneon FC-2120 Fluoroelastomer which was provided by Dyneon™ UK office, all chemicals used in this investigation were purchased from Sigma-Aldrich Chemical Co; including chloroform, methylene blue, ethanol, acetone, 4-methyl-2-pentanone (MIBK), butan-2-one, melamine, 37 wt.% formaldehyde aqueous solution and triethanolamine.

Sylgard 184 and NuSil Med-4850 are both two-part silicone elastomers consisting of base and curing agent, and their main components are dimethyl siloxanes. The curing process for both polymers uses a platinum catalyst cross-linker:

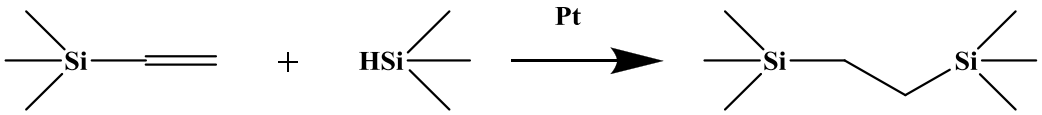

With variations in the viscosity of precursor material and the base:curing agent ratios. The Dyneon FC-2120 fluoroelastomer's main component is a mixture of polyvinylidene fluoride and polyhexafluoropropylene, there is also a presence of bisphenol AF. Bisphenol AF acts as a curing agent in the presence of an acid acceptor (e.g. MgO). However the sample provided did not contain any acid acceptor thus no curing occurred.

2.2.2 AACVD Precursor Solutions

The two components of Sylgard 184 (0.5 g) were dissolved in chloroform (50 mL) with rapid stirring for 5 min. NuSil Med-4850 (0.50 g, two components) was also dissolved in chloroform (80 mL) with rapid stirring for 10 min. Concentration and stirring time was chosen to ensure the highest solubility. To prevent premature curing, the mixtures were used immediately after stirring for deposition studies.

Dyneon FC-2120 Fluoroelastomer (0.125 g) was cut into small portions with a scalpel and placed into a ketone (MIBK, butan-2-one and acetone):ethanol mixture (19:1 ratio, 50 mL) and stirred rapidly until the polymer completely dissolved (approximately 45 min).

2.2.2.1 Melamine Precursors

Spin/Dip-coating solution. 0.5 g of melamine and 1.28 g formaldehyde solution were added to 50 ml of deionised water. The mixture was adjusted to pH 8.5 using triethanolamine and stirred at 70°C.

When the solution appeared transparent it was left stirring/heating for a further 10 min, and then the solution was cooled and filtered. The filtered solution was subsequently used in dip-coating.

AACVD solution. 0.25 g of melamine and 0.64 g formaldehyde solution were added to 50 ml of deionised water. The same steps were followed as above (spin/dip-coating solution). The filtered solution was subsequently used in the AACVD deposition.

2.2.3 Dip-coating/Spin-coating of Polymer Solutions

Concentrated solutions of each polymer were prepared to dip-coat substrates. One volume equivalent of Sylgard 184 was diluted with two equivalents of chloroform. NuSil Med-4850 dip-coat solutions were made from a 1:3 polymer:chloroform mixture. Solutions of Dyneon FC-2120 were prepared by dissolving one mass equivalent of polymer into four equivalents of a MIBK: ethanol mixture (19:1) (solvent mixture was determined as optimum by the polymer supplier).

Coupons of SiO_2 coated barrier glass (dimensions: 45 x 45 x 5 mm; barrier thickness 50 nm) supplied by Pilkington NSG were used to form dip-coated films of polymers. The glass portions were submerged in a solvent: polymer mixture and withdrawn at an arbitrary rate (*ca*. 0.5 mm/s). The coated substrates were laid horizontally in a vacuum desiccator kept at room temperature and left to cure for 48 hours. The upward-facing side of the coated glass was subsequently used in any further analysis.

2.2.3.1 Dip-coating/Spin-coating of Melamine-formaldehyde Resin

VWR cut edged glass microscope slides (dimensions: 76 x 25 x 1 mm) were used for spin/dip-coating. The slides to be spin-coated were placed on a centrifuge stage (NE-010G Clifton Centrifuge), a film of pre-polymer solution was added over the whole surface of the slide. The centrifuge was then spun for 5 seconds at 2800 rpm. The spin-coating process was repeated 5 times on each slide to achieve a consistent film. Dip-coated slides were prepared by immersing the pre-polymer solution and withdrawing at a constant speed of 0.2 cm/s. After full withdrawal the slides were held horizontally until the excess liquid had flowed down the glass. Both sets of slides were then cured at 250°C for 1 h.

A third evaporation method for coating the microscope slides was also carried out, this involved coating a horizontal microscope slide in a film of the pre-polymer solution.

2.2.4 Spray-Coating

Only Sylgard 184 was used in spray coating experiments. The depositions were carried out on SiO_2 coated barrier glass (dimensions: 95 x 130 x 5 mm). Substrate temperature was set to 300°C on a horizontal flat carbon block heater. A spray head was passed up and down the substrate 210 mm above

the glass. A spray nozzle pressurised by air at 3 bar was used to spray 60 mL of chloroform containing 2 g of Sylgard 184 toward the substrate, over a 20 min period (i.e. ~3 mL/min).

2.2.5 Aerosol Assisted Chemical Vapour Deposition of Polymer Solutions

The depositions were carried out in a cold-walled horizontal-bed CVD reactor. The reactor contained top and bottom plates for deposition to occur, both composed of SiO_2 coated barrier glass (dimensions: 145 x 45 x 5 mm). The SiO_2 barrier glass prevents possible ion transfer from the bulk glass and possible contamination of the films deposited. The bottom plate was placed on a carbon block which was used to heat the CVD reactor chamber. The top plate was positioned 8 mm above and parallel to the bottom plate, with the complete assembly enclosed inside a quartz tube. The aerosol of the precursor solution was generated using a PIFCOHEALTH ultrasonic humidifier, the device had an operating frequency of 40 kHz and 25W of power. The aerosol generated was moved to the reactor using a nitrogen gas flow via PTFE and glass tubing, where it entered between the top and bottom plates. Any gaseous by-products left *via* an exhaust (Figure 2.03).

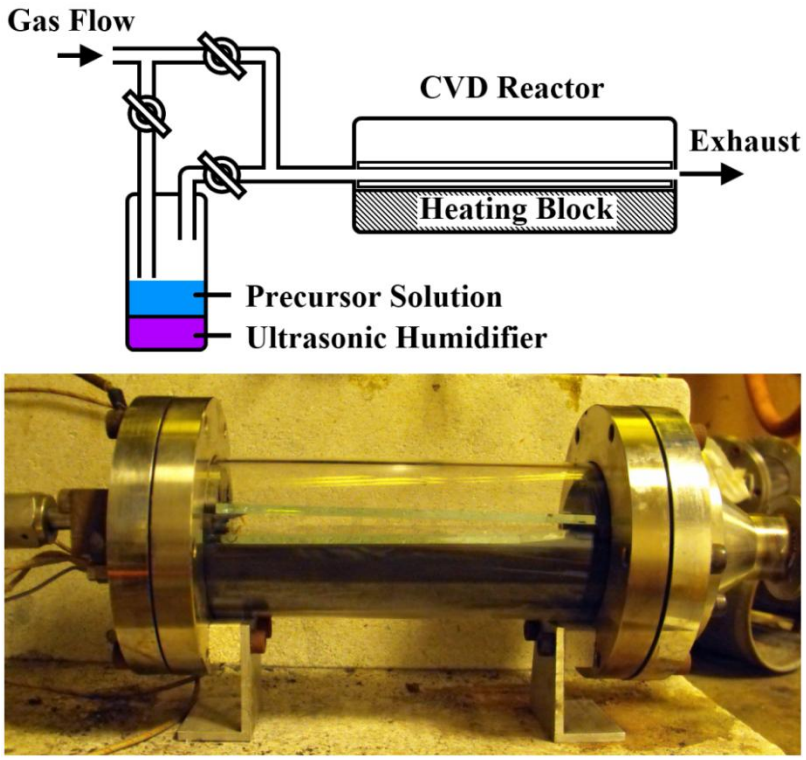

Figure 2.03. (*upper*) Experimental set-up for the AACVD deposition of polymer films. (*lower*) Photograph of CVD reactor, with glass slides inserted.

The carrier gas (nitrogen) flow through the flask was continued until all liquid was gone, this took typically 30–35 min for the Sylgard depositions, 60 min for the NuSil depositions and 90 – 100 min for the Dyneon depositions. Depositions of melamine-formaldehyde resin also took 90-100 minutes for the complete transfer of precursor solution. After all liquid was transferred to the reactor the heater was then turned off and allowed to cool to room temperature, and the nitrogen flow was left on for a further 10 min. The cooled plates were removed and handled in air. The films were deposited on the top plate (due to thermophoresis — see results). The reactor temperature (as measured by a

thermocouple in the carbon heater block) was varied between 90°C and 420°C to find the optimum deposition temperatures.

2.2.5.1 Modifications and Enhancements of AACVD Process

The following treatments were only carried out on the Sylgard 184 elastomer.

Dip-coating of CVD Substrates Prior to Deposition. Silica glass, used in the AACVD process, was dip-coated in a similar fashion as discussed in Section 2.2.3. The coated glass was then used in the AACVD process as a top-plate substrate. All other AACVD parameters were kept the same.

Swell Encapsulation of Methylene Blue. Swell encapsulation of methylene blue was carried out by submerging the films, still attached to glass, in a solution of methylene blue (8 mM) dissolved in an equal part water-acetone mixture (v/v) for 2 hours. The films were subsequently removed from the solution rinsed well with water and left to dry in air for 24 hours.

Incorporation of Gold Nanoparticles. The AACVD deposition of gold nanoparticles was carried out prior to that of Sylgard elastomer. Precursor solutions of gold nanoparticles were synthesised using a Brust two-phase chemical reduction method carried out in toluene. Two solutions were prepared; $HAuCl_4.3H_2O$ (99%, 0.17 g) dissolved in distilled water (15 mL) and tetraoctylammonium bromide (TOAB) (99%, 1.04 g) dissolved in toluene (40 mL). These two solutions were stirred together. A $NaBH_4$ (0.19 g) solution in distilled water (25 mL) was added drop-wise over a 30 min period with rapid stirring; yielding a dark red organic layer. The dark red organic layer was separated and washed with dilute aqueous H_2SO_4 and water, dried using Na_2SO_4 and diluted to 100 mL with toluene. Each solution was prepared the same day it was used for AACVD deposition.

The gold nanoparticles were deposited using the same AACVD method as described in this section onto silica barrier glass. The volume of precursor solution used was 30 mL and a deposition time of 55 min was typical. The flow rate of 1.0 L/min was used. The deposition of nanoparticles always occurred on the top plate; the substrate temperature was kept constant at 450ºC. The deposition of Sylgard was carried out immediately after the deposition of nanoparticles without cooling the reactor to room temperature.

Atomiser Assisted Deposition of Sylgard 184. Solutions of silicone elastomer were made using 400 mL of Chloroform and varying amounts of Sylgard 184 (10 g, 20 g and 30 g). Upon addition of the elastomer to chloroform, the mixture was stirred vigorously for 5 minutes and used immediately for deposition. The depositions were carried out in the same CVD reactor, using the same glass substrates. The precursor aerosol was generated using a Model 2076 Constant Output Atomiser, in which sub-micrometre aerosols were used to atomise the solution. Compressed air was expanded through an orifice to form a high velocity jet. The solvent was drawn into the atomising section of the apparatus

where it was atomised by the jet. The aerosol generated was moved to the reactor using the air flow generated from the atomiser *via* PTFE and steel tubing, where it entered between the top and bottom plates. The reactor waste gas left *via* an exhaust.

The air flow carried the vapour from the flask for 1 hour once the reactor reached the deposition temperature. The heater was then turned off after this period and allowed to cool to room temperature. The cooled plates were removed and handled in air, with the top plate having the deposited film. The reactor temperature, as measured by a thermocouple in the carbon heater block, was maintained at 360°C.

2.2.6 Film Characterisation

The films were analysed as deposited onto the SiO_2 barrier glass substrate unless otherwise stated. Subsections (*ca* 1 x 1 cm) of the samples were gold-sputtered and analysed using field emission scanning electron microscopy (SEM) using a Jeol JSM-6301F operating at 5 kV. Energy dispersive X-ray (EDX) analyses of carbon-sputtered samples were measured using the same machine. Powder X-ray diffraction (XRD) patterns were measured on a Brucker D8 discovery instrument using monochromated Cu Kα radiation (λ = 1.5406 Å) in the reflection mode. Atomic force microscopy (AFM) measurements were performed in air on a Veeco Dimension 3100 in a contact operating mode (cantilever model; Veeco MSNL-10). Infrared (IR) spectroscopy was employed over the range of 2200–4000 cm^{-1} using a Perkin Elmer FT-IR (Fourier transform infrared) Spectrum RX1 instrument. Raman measurements were made using a Renishaw 1000 spectrometer which used a 632.8 nm laser. UV–visible absorption spectra were taken using a Perkin Elmer Lambda 25 UV/VIS Spectrometer single beam instrument over a range of 300–1000 nm. Elemental analysis experiments were carried out using an EA-440 horizontal load analyser supplied by Exeter Analytical. For analysis the dip/spin-coated samples were easily delaminated and the AACVD films scraped off the glass substrates using a scalpel. Adherence tests were carried out by applying Scotch Home and Office masking tape to the deposited films with even pressure applied by hand, followed by removal in one swift motion. Any difference in the film appearance was noted. Scratch tests were also carried out by observing the action of a metal scalpel being dragged across a surface.

2.2.7 Surface Hydrophobicity Measurements

Water contact angle measurements were carried out using an FTA-1000 drop shape instrument; 3 μL water droplets were used to minimise any gravitational effects. The water droplet images were analysed using a digital protractor to obtain the water contact angles on the surface. A range of points across the substrates were tested, with 12 measurements made on each film. Water slip angles were also measured, noting the angle to the horizontal at which 3 μL water droplets moved on the surface. Many positions across the substrates were tested.

2.3. Results and Discussion

2.3.1 The Deposition of Thermosoftening Polymers

The following section details the dip-coating and AACVD of the ketone soluble Dyneon FC-2120 Fluoroelastomer (structure shown below, Figure 2.04).

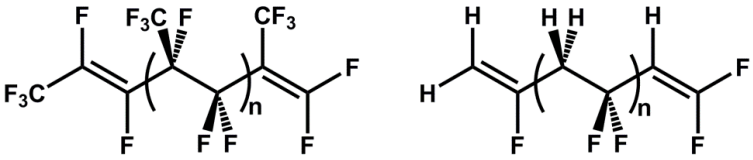

Figure 2.04. Component molecules of the Dyneon FC-2120 Co-polymer. Both the C-F and C-H bonds act to lower the surface energy by their strong repulsion of water.

2.3.1.1 Dip-coated Films of Dyneon FC-2120 on Glass

The as-received Dyneon polymer was a solid off-white block of material. Once portions of the polymer were dissolved, the solutions appeared clear in colour. After the dip-coating treatment, the dried films were hazy. They did however allow approximately 75% visible light to be transmitted. The coatings were well adhered to the glass substrate but delamination of the polymer was possible by action with a scalpel. Images of the dip-coated surfaces (Figure 2.05) show a very flat microstructure, with AFM measurements confirming no surface features over 40 nm in height. The flat dip-coated fluoroelastomer surface gave hydrophobic water contact angles of 99°, with this relatively high angle for a flat surface stemming form the presence of C-F/C-H bonds (verified by Raman measurements). Introducing surface roughness would magnify the low energy of the elastomer and increase the water contact angle achieved.

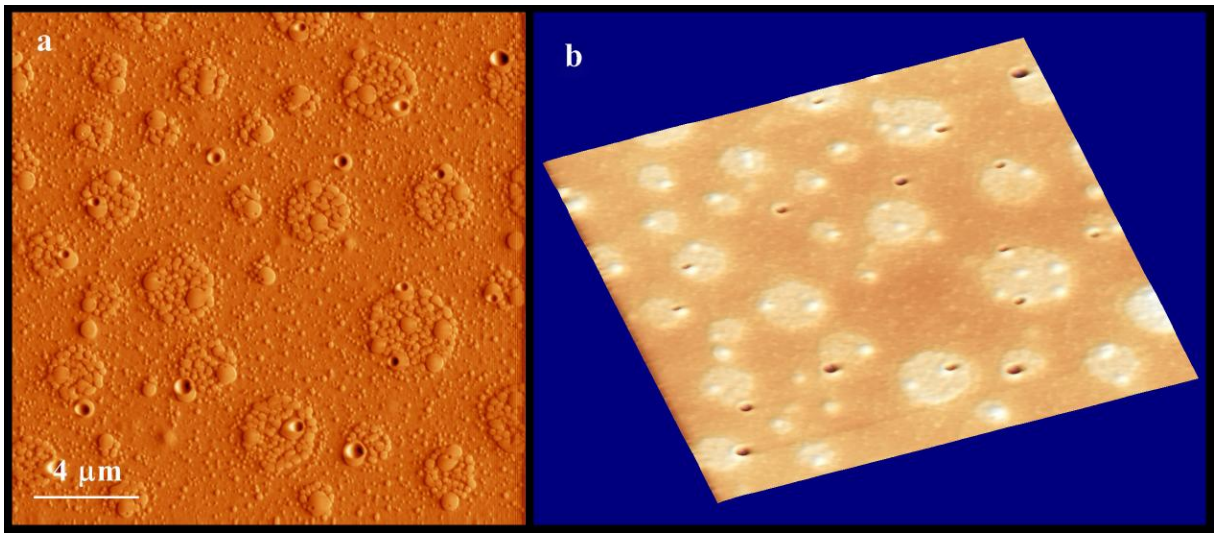

Figure 2.05. AFM image of a dip-coated film of Dyneon FC-2120 fluoroelastomer on glass, (a) 2D and (b) 3D. Surface feature height confirmed as less than 40 nm by AFM measurements. Scale bar is shown. Viewing area is 25 x 25 µm.

2.3.1.2 AACVD Films of Dyneon FC-2120 on Glass

All depositions in this section, unless otherwise stated, were carried out using MIBK solvent.

The depositions occurred to the top plate in the reactor. This is commonly observed in CVD reactors where there are preformed particles in the gas phase. The temperature of the bottom plate was approximately the same as the stated deposition temperature, however the non-heated top plate was measured to be 40-50°C below this due to a thermal gradient extending from the carbon block within the reactor. This temperature gradient causes a movement of air away from the bottom plate toward the top, forcing top plate deposition of any gas-phase particles. Substantial amounts of material were not deposited until reaction temperatures were raised above 240°C. Films deposited at and above this temperature were white and opaque, able to transmit approximately 40% of visible light. Decomposition signified by heavy discolouration was observed at substrate temperature at and above 330°C. The films were resistant to removal with Scotch tape. However they could be scraped off with a metal scalpel and substantial force. All polymer films were shown to be amorphous by XRD with no discernable diffraction peaks. The presence of C–F bonds was verified by Raman measurements (Figure 2.06). EDX analysis suggested > 25 atomic% fluorine film composition.

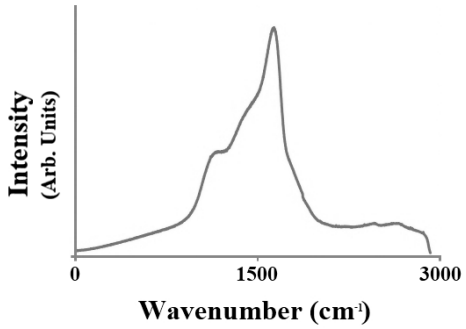

Figure 2.06. Raman spectrum from 0 to 3000 cm^{-1} of a Dyneon FC-2120 film deposited by AACVD showing the expected C-F Raman shift[21].

The AACVD films of Dyneon gave water contact angle values as high as 118°, with average measurement of 104° at a 330°C deposition temperature. The surface roughness increased the water contact angles from those seen on dip-coated films. The coverage of the substrate by the elastomer increased up to this temperature, thus enhancing the surface hydrophobicity (Table 2.1, p84). Increasing the amount of elastomer deposited (by using more precursor solution in a deposition) gave a thicker film but did not increase the water contact angle and there was no change in surface morphology (confirmed by SEM/AFM). The features seen were *ca* 1 μm in height and as large as 10 μm across (Figure 2.07).

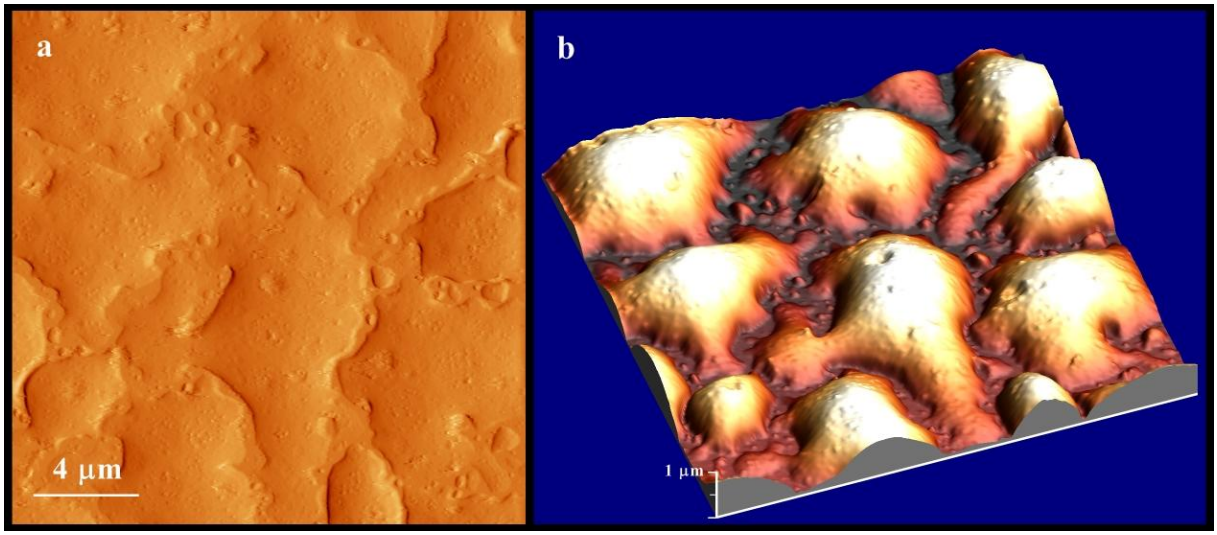

Figure 2.07. AFM image of Dyneon FC-2120 deposited by AACVD onto glass substrate carried out at 300°C, (a) 2D and (b) 3D. Viewing area is 25 x 25 µm, scale bars are shown.

Dyneon FC-2120 was confirmed to be soluble in 3 ketones (acetone, butan-2-one and MIBK). Using acetone as a carrier solvent (b.p. - 56-57°C) resulted in a very volatile aerosol, the solvent evaporated before reaching the CVD reactor, and no deposition was observed over a range of temperatures. The use of butan-2-one (b.p. - 80°C) did not result in any detectable change in the surface structure compared to using MIBK (b.p. - 117-118°C) (SEM) or the observed water contact angles. This suggests a similar mechanism for deposition while using MIBK or butan-2-one, and was not noticeably affected by the boiling point of the solvent.

2.3.2 The Deposition of Thermosetting Polymers

The following section details the dip-coating and AACVD of two chloroform soluble silicone polymers Sylgard 184 and NuSil Med-4850. Sylgard 184 is a two part silicone elastomer which comprises a 10:1 ratio of silicone base: curing agent. Both parts are viscous liquids, and when combined they cure into a rubber-like solid. The curing process is accelerated by increased temperature. The silicone chain comprises alkylated side chains that act to repel water (Figure 2.08). NuSil Med-4850 is also a two part silicone elastomer (1:1, silicone base: curing agent) which is also thermally cured. The latter polymer had a more viscous pre-reactive consistency and also required a greater amount of solvent to facilitate the formation of an aerosol.

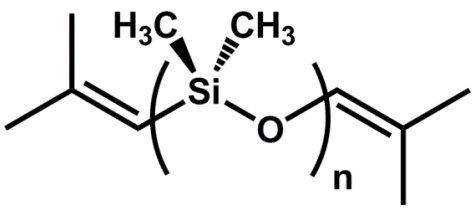

Figure 2.08. Chemical structure of the main component used in the silicone base portion of Sylgard 184. Chain cross-linking is accomplished through a platinum based cure system which links the unsaturated ends of the chains. Hydrophobic methyl side chains repel water and lower the surface energy of the material.

2.3.2.1 Dip-coated Films of Sylgard 184 and NuSil Med-4850 on Glass

Both silicone polymers were transparent prior to curing, with solutions of the polymers also clear. The dip-coated films were also transparent letting more than 90% of visible light (λ = 380-760 nm) to transmit through the films. The adhesion of the coating was similar to that observed for the Dyneon fluoroelastomer as they were well adhered to the glass substrate. The surfaces were near featureless with an observed microstructure similar to that seen in figure 2.05. Both flat elastomer films were hydrophobic with water contact angles of 95° in each case, brought about by water repelling C-H groups on the surface (verified by infra-red measurements). The 95° water contact angle was less than the 94° - 111° expected for a surface constructed from $-CH_2/-CH_3$ groups (Section 1.2.2), due to possible surface rearrangement of dangling C-H bonds.

2.3.2.2 AACVD Films of Sylgard 184 and NuSil Med-4850 on Glass

Aerosol assisted deposition of the Sylgard elastomer resulted in substantial deposition between 240 and 360°C, with decomposition occurring at temperatures above this temperature. Depositions of NuSil elastomer were observed up to 420°C without discolouration of the films. The thickest films, indicated by UV–visible spectroscopy, were observed at 360°C (Sylgard) and 420°C (NuSil) with visible light transmission as low as 12% and 8% respectively. The opaque-white thin films were well adhered to the substrate with the polymer material no longer having a tacky consistency as in the pre-set form. Both film sets showed the presence of C-H bonds in the IR spectra which matched spectra taken of dip-coated films of the appropriate polymer (Figure 2.09). EDX analysis gave a 2:1 (O:Si) ratio for the thickest part of the film, with no presence of chlorine detected - ruling out contamination by chloroform. Both film sets were not removed by Scotch tape and were difficult to rub-off, the films could however be readily marked with a steel scalpel. However the highest temperature depositions using NuSil Med-4850 were noticeably more resistant to the scalpel scratching but were still able to be removed.

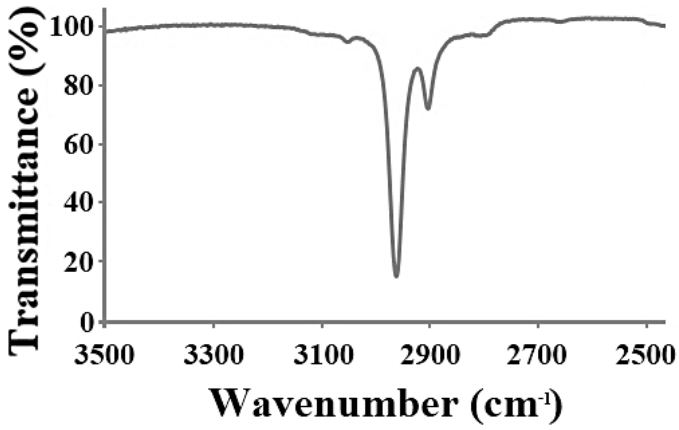

Figure 2.09. Infra-red spectrum across a range of 3500 to 2500 cm^{-1} of Sylgard 184 deposited by AACVD showing the expected C-H vibrations.

Film morphology, analysed by SEM, showed that the films deposited over the range of temperatures from both Sylgard and NuSil polymers consisted of agglomerates on the glass substrate. Low temperature depositions (at and below 240°C) showed some surface roughness, which consisted of globules with some agglomeration (Figure 2.10) which increased with temperature. Raising the temperature above 270°C resulted in very rough surfaces made up of interlocking spheres, Figure 2.11.These spheres formed a network across the surface and contained a high degree of porosity (side-on SEM, Figure 2.11). The size of the spheres was around 0.5–1 μm. Both film roughness and deformation of the spheres increased as the deposition temperature was raised. AFM of the high temperature films could not be successfully completed as intense surface roughness meant the limitations of the instrument were met and exceeded. These factors indicate the mechanism by which spherical particles of the polymer is deposited (Figure 2.12). The microdroplets of polymer precursor solution enter the reactor where the solvent is evaporated leaving spheres of liquid elastomer, the polymer curing is accelerated by the elevated temperature of the reactor and the particles begin to cure. The spherical particles are deposited onto the top plate, a result of thermophoresis (caused by the temperature gradient across the reactor), which forces the partially cured polymer particles toward the top plate. The particles land on the top plate where they stack up onto of each other forming the observed surface roughness. This mechanism was not observed with the Dyneon polymer as there was no curing taking place and thus no formation of spherical particles.

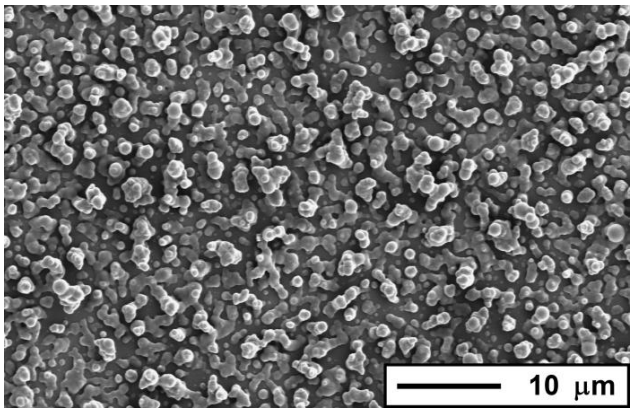

Figure 2.10. SEM image of a Sylgard 184 film deposited by deposited by AACVD onto glass substrate at a 240°C substrate temperature. Scale bar shown.

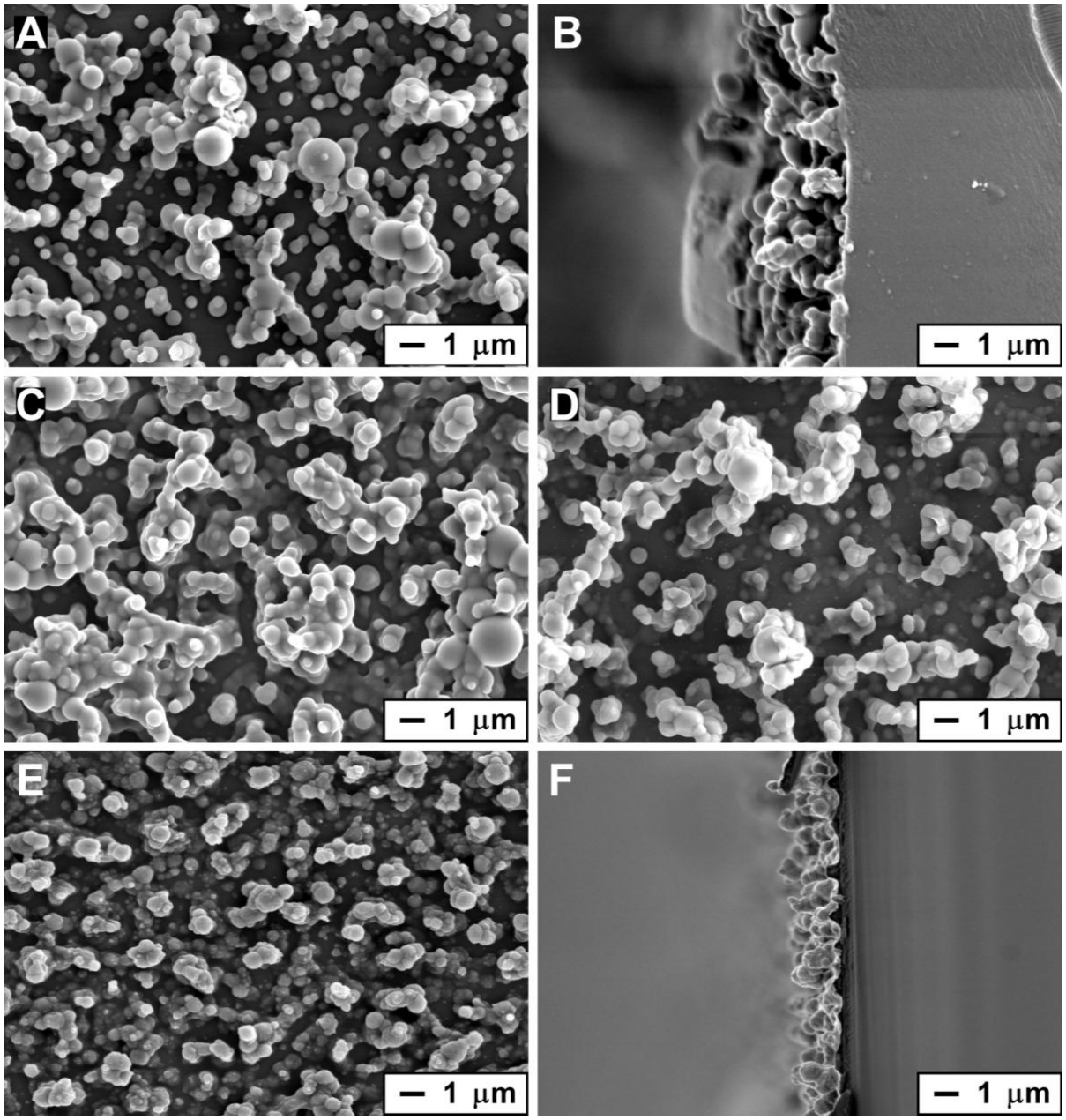

Figure 2.11. SEM images of films deposited by AACVD using Sylgard 184 using a deposition temperature of (A/$B_{Side\text{-}on}$) 270°C, (C) 300°C and (D) 360°C, and NuSil Med-4850 deposited at (E/$F_{Side\text{-}on}$) 420°C. The particle agglomeration increased with deposition temperatures (A > C > D), with deformation of the spherical elastomer particles also increasing (probably due to increased decomposition). The NuSil particles have a smaller average diameter (~0.5 μm) in comparison to the Sylgard particles (~1 μm). Side-on SEM images (B/F) show the porosity of the polymer thin films. The thickness of the highest temperature depositions for Sylgard/NuSil are 3.2/1.5 μm respectively.

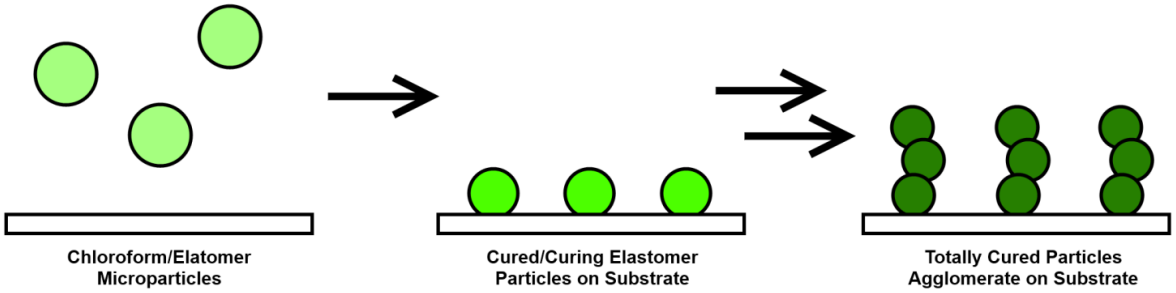

Figure 2.12. Schematic representation of the deposition mechanism of thermosetting polymers *via* AACVD.

The water droplet contact angles for the films are shown in Table 1. It was noted that the Sylgard films started to decompose at 360°C, however NuSil was resistant up to 420°C. The NuSil films did not demonstrate superhydrophobic water contact angles (> 150°) unless substrate deposition temperatures greater than 360°C were used. The maximum water contact angle observed for the NuSil elastomer was 170° (Figure 2.13) at a deposition temperature of 420°C. This was greater than the maximum water contact angle achieved by the Sylgard elastomer of 167° at 360°C. The higher temperature required for superhydrophobic films formation using NuSil is most likely due to the slower curing rate of the polymer, in addition to the greater proportion of solvent required to make the precursor solution. An observable pattern in both cases was that the average and maximum water contact angles increased with deposition temperature, with the spread in θ decreasing.

Deposition Method	**Water Contact Angle (°)**								
	Dyneon FC-2120			Sylgard 184			NuSil Med-4850		
	Average	*Maximum*	±	**Average**	*Maximum*	±	**Average**	*Maximum*	±
Dip-Coated	99	-	0.9	95	-	0.9	95	-	0.8
AACVD (240°C)	99	*107*	3.2	156	*162*	3.9	110	*125*	4.2
AACVD (270°C)	101	*110*	3.3	158	*165*	3.6	118	*133*	4.8
AACVD (300°C)	104	*116*	4.0	160	*166*	3.4	126	*143*	4.2
AACVD (330°C)	104*	*118**	4.8	160	*167*	3.0	140	*156*	3.9
AACVD (360°C)	-	-	-	160*	*167**	3.0	152	*160*	3.4
AACVD (390°C)	-	-	-	-	-	-	160	*167*	2.8
AACVD (420°C)	-	-	-	-	-	-	162*	*170**	2.7

Table 2.1. Water contact angles (at least ten separate measurements) for Dyneon FC-2120, Sylgard 184 and NuSil Med-4850 films deposited on glass substrates by AACVD. (*) Indicates films with significant discolouration, (–) indicates films with decomposition of the polymer. Temperatures indicated are those of the carbon block used while the AACVD deposition was carried out. All films were deposited onto the top plate which was measure to be *ca* 50°C lower. (±) Presents 95% confidence intervals using Student's t-test distributions)

Figure 2.13. Images showing 10 µL water droplets on Dyneon, Sylgard and NuSil surfaces (from left to right) deposited *via* AACVD 330, 360 and 420°C respectively. Images chosen represent average water contact angles on each surface (104°, 160° and 162°).

The water droplet slip angles for the most hydrophobic NuSil deposition were recorded, the average being 6°, with some points on the surface only requiring a tilt angle of 2° for the water droplet to slip off. Sylgard films deposited at 360°C had water droplet slip angles averaging 9°, and a lowest result of 5°. Both of the highest temperature depositions for Sylgard and NuSil films showed the lowest slipping angles. The generally low slip angles indicate classical Cassie–Baxter type wetting, analogous in properties to those reported for the Lotus effect.

2.3.2.3 Spray-coating of Sylgard 184

The spray-coating process has many of the facets of AACVD, such as precursor solutions, droplet formation, transport through air and delivery to a heated substrate. The spray coating system however creates larger droplets and the substrate is not enclosed inside a CVD reactor.

The spray-coated films were more transparent than the Sylgard films formed by AACVD, letting approximately 60% of visible light transmit through them. SEM images of the deposited films show very wide surface features (approximately 10 – 20 µm across, Figure 2.14), where individual polymer agglomerations are spread over the substrate and not upward in tower like structures (AACVD). The surface feature heights (confirmed by AFM measurements) average between 2 – 3 µm; however this is not as rough as AACVD films. The hydrophobicity of the surfaces was measured with a maximum water contact angle of 115° and an average of 102°.

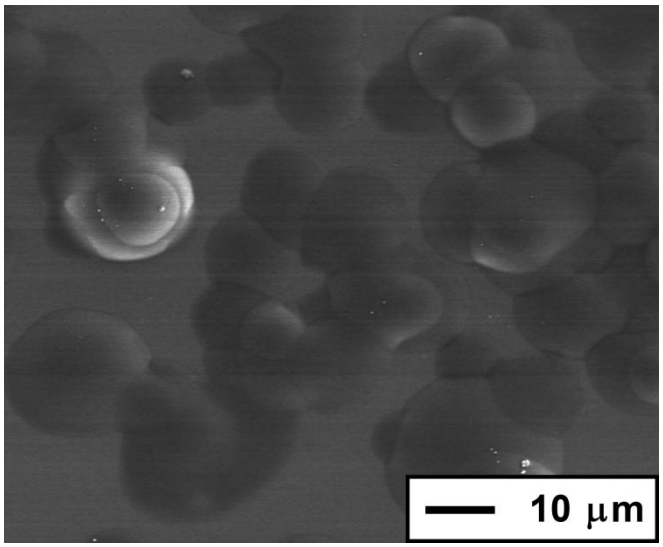

Figure 2.14. SEM image of a Sylgard 184 spray-coated glass surface. The substrate temperature during coating was 300°C. Feature heights were confirmed as 2 – 3 μm high with the surface achieving an average water contact angle of 102°.

The feature shape indicates the deposition mechanism of the polymer. The spray process creates large solvent droplets (> 200 μm in diameter, compared to those in the aerosol ~ 35 μm)[22] which fall on the heated substrate, and not carried across it by a gas. The large droplets contain more solvent and need more energy in order to evaporate this. There is also a greater amount of polymer, which requires a greater amount of energy to fully cure. The process from diluted polymer to cured product takes more time in the spray process, with a smaller area for the evaporation to take place. This leads to the smoother microstructure (with respect to AACVD), and thus the resultant water contact angle is reduced.

2.3.3 Comparing the AACVD of Thermosoftening and Thermosetting Elastomers

2.3.3.1 Substrate Adhesion

The greatest adherence to the substrates was observed on the Dyneon fluoroelastomer films. This is due to a greater area of contact between elastomer agglomerates and substrate, brought about by melting of the polymer particles on the hot glass. The second most adherent films were found when NuSil elastomer was deposited at 420°C; the high temperature of the deposition and partial decomposition of the polymer allowed for a strong connection between polymer and substrate. Sylgard depositions had a faster curing rate which allowed for the formation of spherical particles more rapidly. The spheres of cured/curing elastomer made the least effective bind with the surface due to their shape and the likelihood that they were almost fully hardened by the time they made contact with the surface. The most adhesive Sylgard films were seen at 360°C, when partial decomposition was observed.

2.3.3.2 Film Appearance and Microstructure

Decomposition of the Dyneon elastomer started to occur at a deposition temperature of 330°C (~290°C top-plate temperature). Sylgard and NuSil depositions showed signs of decomposition at 360°C and 420°C (~310°C and ~370°C top-plate temperature) deposition temperatures. The average deposition times must also be considered as this determined the length of time the films were left heated these; were 95, 33 and 60 mins for the Dyneon, Sylgard and NuSil depositions respectively. Dyneon films were left at temperature for the longest time, exposing the polymer to the greatest amount of thermal damage. The NuSil depositions were higher in temperature than the Sylgard depositions, due to a higher energy required to drive the reaction and a slower curing rate. The NuSil films were also left for a greater amount of time, with the polymers resilience also explained through the slower curing rate.

Dyneon films were the most transparent with the thickest films allowing approximately 40% of visible light to transmit, although being the only material which was opaque before deposition. This opacity was caused by additives mixed into the polymer. The Dyneon films had a very high surface coverage. However the films were the thinnest and the surface microstructure was the least developed (due to no curing agent present). Sylgard films allowed 12% of visible light to transmit through, while NuSil films let 8% of light through. The cured material is transparent to light when dip-coated or cured in a mould, thus it is the change in microstructure that causes the reduction in transmitted visible light. The scattering of light by surface features with similar dimensions to the wavelength of light, can reduce the observed amount of light passing through a surface. The surface protrusions on NuSil and Sylgard surfaces have average dimension of 0.5 μm (or 500 nm) and 1 μm (or 1000 nm) respectively. The similarity to that of the wavelength of light (390-750 nm), suggests that diffraction of visible light would be expected. The NuSil films (1.5 μm) are not as thick as the Sylgard films (3.2 μm), but the less transparent NuSil films can however be explained through a greater similarity between the surface features and wavelength of visible light, in addition to the slightly greater surface coverage achieved in the NuSil depositions.

Depositions of Sylgard 184 carried out at 360°C (with 0.5 g in 80 mL chloroform) gave surface protrusions with similar dimensions to these observed in the 420°C NuSil Deposition. An increase in the amount of elastomer deposited during the Dyneon depositions introduced a thicker film but did not increase the water contact angle and there was no change in surface morphology (confirmed by SEM/AFM).

2.3.3.3 Hydrophobicity

The presence of C–F (Dyneon) and C–H (Sylgard and NuSil) stretching vibrations were verified by Raman and infrared measurements respectively. The Dyneon elastomer has the lowest inherent

hydrophobicity, with water contact angles averaging 99°. Both Sylgard and NuSil had water contact angles of 95° on dip-coated samples. Films formed *via* AACVD had highest water contact angles of 118° (330°C), 167° (360°C) and 170° (420°C) for Dyneon, Sylgard and NuSil elastomers respectively. The low change in water contact angle observed in the Dyneon elastomer was due to a slight increase in surface roughness, caused by melting of the polymer on the substrate and not curing. This magnified the surfaces hydrophobicity but did not render it superhydrophobic. Superhydrophobic surfaces formed by Sylgard and NuSil polymers were made possible by the formation of extreme surface roughness. Low tilt angles confirmed a Cassie-Baxter wetting mechanism on these surfaces with the successful trapping of air underneath water droplets within the film porosity. The higher surface hydrophobicity seen in the NuSil depositions was a result of grater deformation of silicone particles on the substrate, in addition to a smaller scale of surface roughness which was more efficient at trapping air underneath the surface – this was shown not only by the higher water contact angles but also the lowest slip angles were found on the NuSil surfaces.

2.3.4 Surface Modifications and Enhancements

The polymeric materials used in CVD depositions discussed in this section can be altered or added to in order to change their functional properties. This section details the variation or modification of AACVD depositions of Sylgard 184.

2.3.4.1 Dip-coating of CVD Substrates Prior to the AACVD of Sylgard 184

As the highly rough elastomer surfaces formed by AACVD facilitate a Cassie-Baxter wetting mechanism, there should be no contact with the underlying substrate. The random nature of the AACVD deposition mechanism however leaves opportunity for small regions of the film to have less coverage, relative to a machined surface with regular patterned microstructure. An area of lower surface coverage, even in the smallest area would result in water making contact with a hydrophilic glass substrate. This contact would have two major local effects – a reduction in water contact angle and an area of Wenzel-like wetting causing water to stick to that region, in-turn raising the slip angle. Coating the hydrophilic glass with hydrophobic Sylgard 184 elastomer prior to AACVD deposition could minimise the effect of that contact and the surface hydrophobicity on the deposited surface would be maximised.

The physical appearance of the polymer coated substrates was very similar to glass substrates, except for a slight rubber-like texture when handled. The surface morphology of the dip-coated glass was extremely flat (no surface features larger than 50 nm, AFM), with the films observed to be 60 μm thick with SEM imaging. When Sylgard 184 was deposited on top of the dip-coated films using AACVD the films appeared very similar showing no observable differences upon visible inspection. On closer examination the deposited elastomer particles were observed to agglomerate to the

underlying substrate (Figure 2.15). The coating's physical robustness was also greatly improved on previous work using an ultrasonic aerosol, surviving the application of Scotch tape and only being removed with a scalpel when the underlying polymer film was cut from the glass.

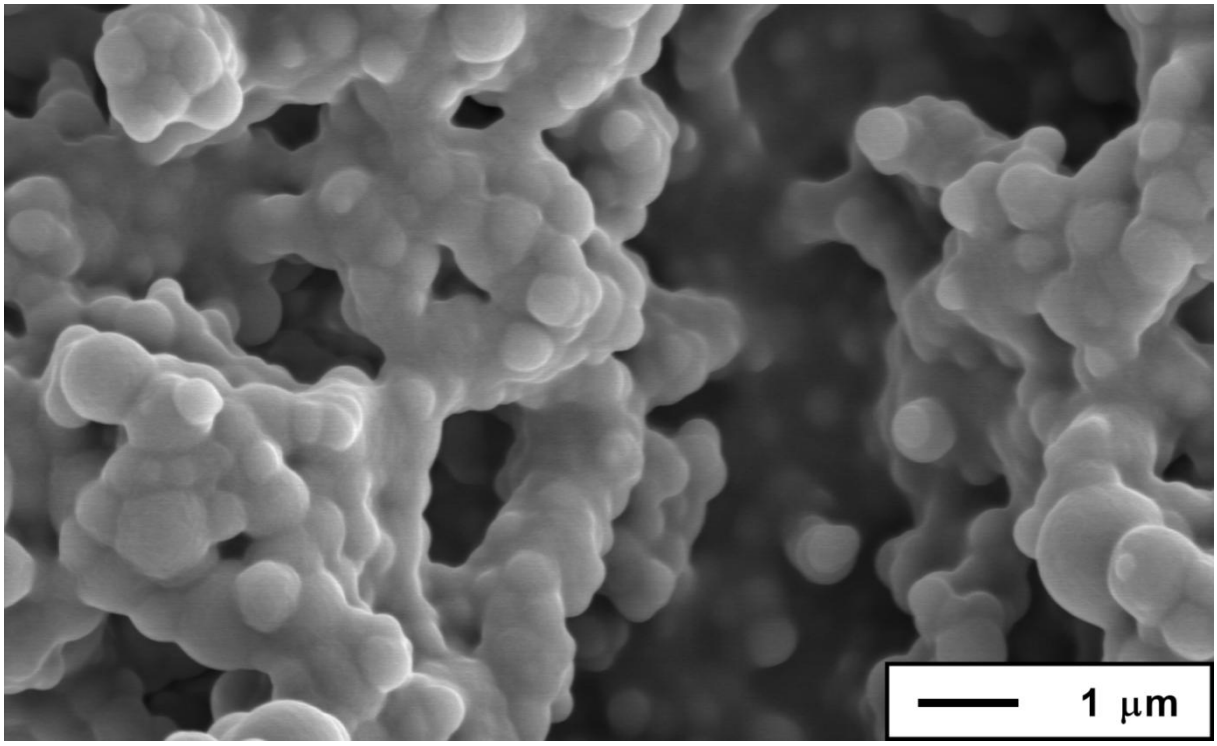

Figure 2.15. SEM image of a Sylgard 184 surface deposited via AACVD onto a glass substrate dip-coated with a layer of the same elastomer. Image shows agglomeration between deposited material and the dip-coated under-layer. Deposition was carried out at 360°C. Scale bar inset.

The water contact angle measurements on the films gave significantly consistent results, with angles averaging 169° and showing less than 1° of variation over the substrate (Figure 2.16). The major factor for this improvement was reducing the effect made by regions of lower surface coverage, which would previously result in contact with the hydrophilic glass substrate.

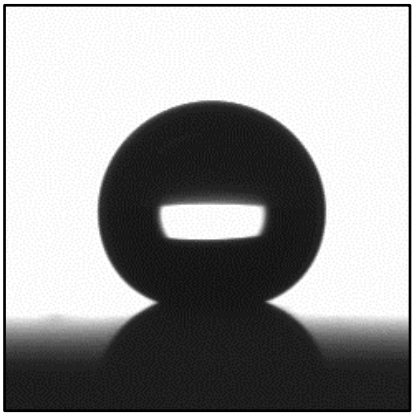

Figure 2.16. Photograph showing a 3 μL water droplet in a Sylgard 184 surface deposited *via* AACVD onto a glass substrate dip-coated with a layer of the same elastomer. The elastomer coated substrate provides highly consistent water contact angle measurement (average 169°).

2.3.4.2 Swell Encapsulation of Methylene Blue

The films adopted a blue shade upon the swell encapsulation treatment. This was observed as an absorption peak *via* UV-Vis at a wavelength of 630 nm (Figure 2.17).[23] The water contact angles were not altered after the treatment was applied, suggesting no significant change in surface morphology or composition. SEM images showed no observable change in microstructure.

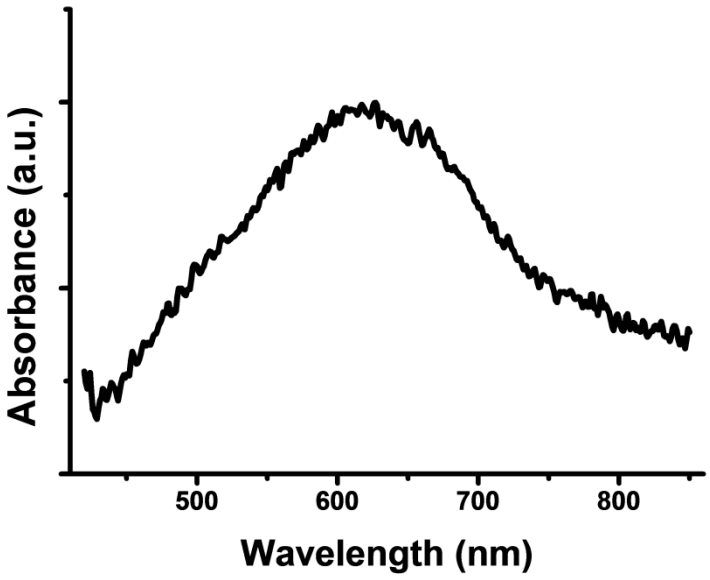

Figure 2.17. UV-vis spectrum of Sylgard 184 film deposited via AACVD using an atomiser aerosol generator, post-treated by incorporation of methylene blue dye. Absorption observed at 630 nm relates to an absorption by the dye molecule embedded in the polymer.

The surface morphology allows for Lotus effect-self-cleaning, however given the uptake of methylene blue with no change to the hydrophobicity provides excellent potential for additional anti-microbial properties. Methylene blue can act as a light activated anti-microbial agent, killing bacteria upon irradiation with a laser or visible light source by generation of singlet oxygen species[24]. The superhydrophobic elastomer surfaces with methylene blue incorporated could significantly reduce the ability of bacteria surviving on a surface, given that activation of the dye by irradiation with visible light forms species which are toxic to bacteria.[24]

2.3.4.3 Incorporation of Gold Nanoparticles

Gold nanoparticles, typically with diameters between 1 and 100 nm, have been a matter for extensive research in recent years.[25] This is mainly due to the vast array of applications these particles can be employed in, from use in labelling in electron microscopy to their utilisation in biomedical areas. The huge interest for gold nanoparticles stems from their chemical properties which bring about observed phenomena, such as surface plasmon resonance (SPR).[26] The use of gold nanoparticles in combination with the superhydrophobic elastomer surfaces, was geared toward the incorporation of a species that could aid the killing of bacteria.[24]

The deposition of gold nanoparticles prior to the AACVD of elastomer gave films a purple shade. The hydrophobicity of the Sylgard films was unaffected by pre-treatment of the substrate with gold nanoparticles with water contact angles averaging 160°. SEM images of the films showed the presence of the nanoparticles underneath the deposited elastomer (Figure 2.18). The gold particles were typically 50-100 nm in diameter and were weakly adhered to a surface when not coated with polymer, however most particles were now embedded under the surface protrusions. The presence of the nanoparticles was also observed in UV-Vis spectroscopy. The particles undergo surface plasmon resonance, and this is observed in the spectra as an absorption band around 538 nm. This method of embedding particles has possible application as a light activated antimicrobial agent, akin to methylene blue.

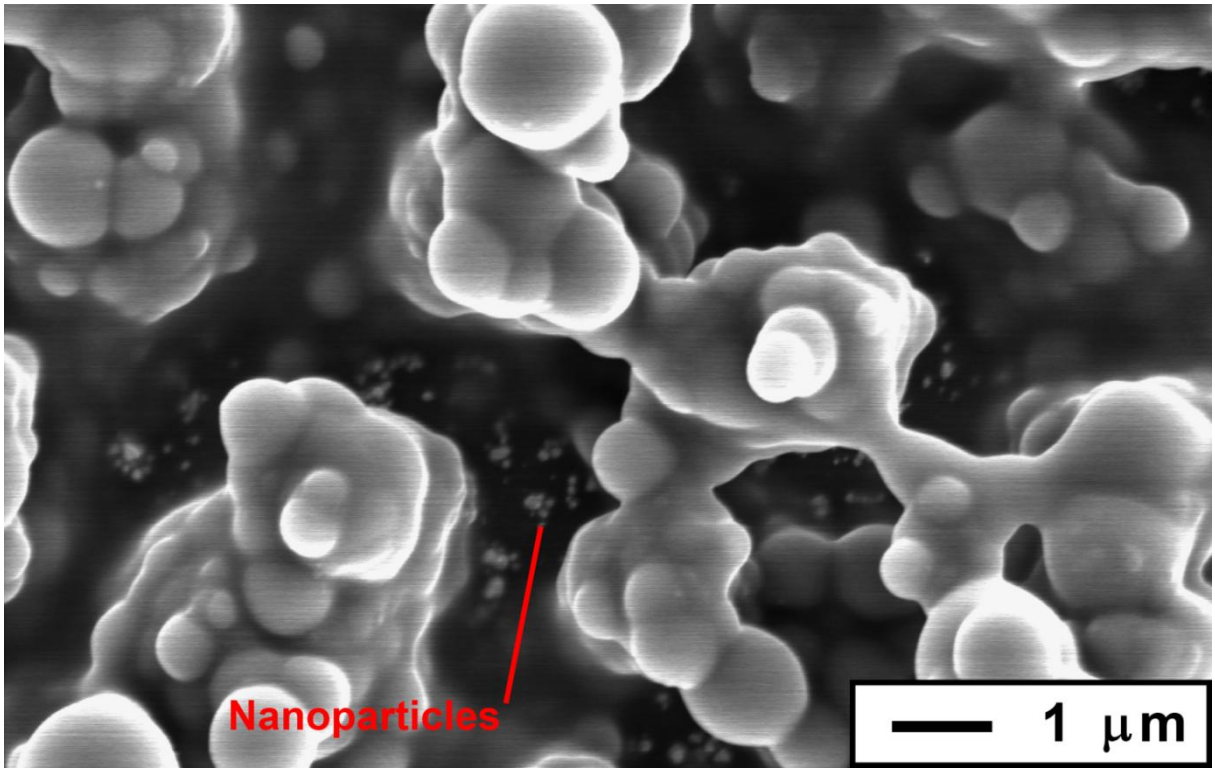

Figure 2.18. SEM image showing gold nanoparticles (50-100 nm diameter) deposited by AACVD at 450°C, the nanoparticles are embedded in a Sylgard 184 polymer also deposited by AACVD but at 360°C.

2.3.4.4 Atomiser Assisted Deposition of Sylgard 184

Depositions took place on the top plate inside the reactor similar to AACVD depositions, with the deposition temperature maintained at 360°C. The films deposited at all concentrations appeared white and opaque, with the most transparent films formed using the lowest concentration of elastomer (above 65% visible light transmission, observed by UV-Vis spectroscopy). The films were very physically robust (more robust than the AACVD Sylgard films), remaining intact after action with Scotch tape and requiring a substantial amount of pressure to be removed with a scalpel. Infra-red

spectroscopy showed typical absorption frequencies associated with C-H bonds (2950-2860 cm^{-1}). EDX analysis showed a 2:1 O/Si ratio, with no other contaminants detected.

The surface microstructure (shown in Figure 2.19) was highly developed for depositions of all concentrations of precursor, however roughness did increase with elastomer concentration. The surface protrusions were made up of agglomerations of elastomer particles akin to AACVD depositions, originating from the spherical nature of the atomised aerosol droplets. All depositions formed similar microstructures with varying magnitudes, with average feature size increasing with concentration. Average agglomerate protrusion diameter was 2.6 μm, 3.1 μm and 3.5 μm for depositions using 10 g, 20 g and 30 g of the precursor Sylgard 184 dissolved in 400 mL chloroform, with the average size for individual polymer particles smaller than 1 μm. A greater surface coverage could also be observed at higher concentration suggesting that an increased amount of precursor reached the substrate. The surface protrusions appear very similar to those deposited AACVD, albeit on a smaller scale. Surface roughness analysis was attempted by AFM; however the surfaces extreme roughness meant instrumental limitations were exceeded and substantial surface analysis could not be made.

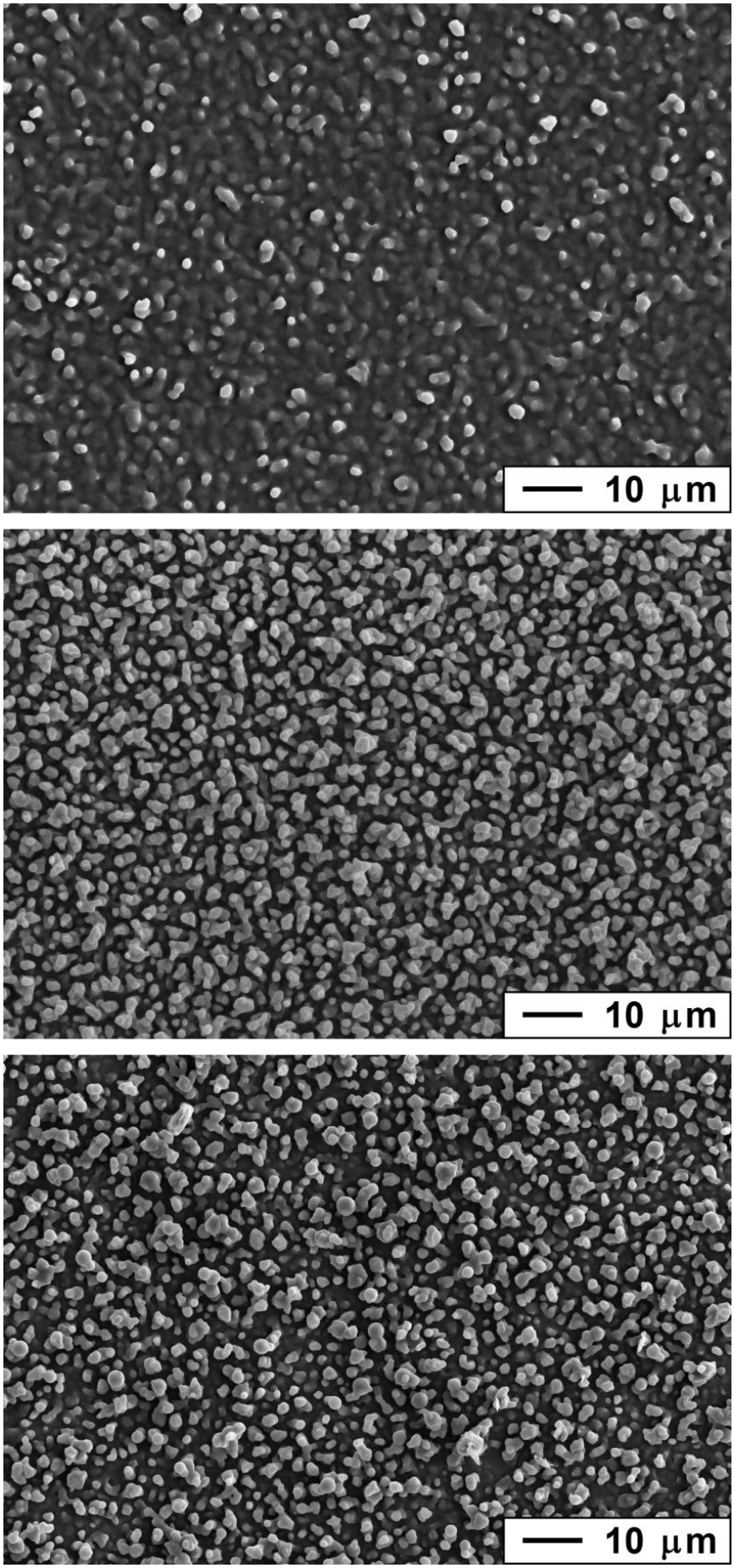

Figure 2.19. SEM images showing the atomiser assisted depositions of Sylgard 184 elastomer, with precursor solutions of (top) 10 g in 400 mL chloroform, (middle) 20 g in 400 mL chloroform and (bottom) 30 g in 400 mL chloroform. A substrate temperature of 360°C was used in all depositions. Scale bars inset.

The relatively small feature size, in comparison to AACVD, is a result of the diameter of droplets in the aerosol and solution concentrations in each method. The concentrations used in this atomiser technique are substantially higher than concentrations used in humidifier depositions, however particles deposited using the former method are much smaller. This suggests that aerosol droplets formed by the atomiser (calculated to be ~ 5 μm) must be very much smaller than those created by ultrasonic humidification (calculated to be ~ 35 μm)[22] leading to the smaller feature sizes[27].

The water contact angles of the films formed was highly dependent on precursor concentration. The resultant films deposited form the lowest concentration of elastomer (10 g in 400 mL of chloroform) had water contact angles averaging 119°. The average water contact angles increased to 165° and 167° for depositions with 20 g and 30 g respectively in the starting solution. The high contact angles stem from a substantial increase in the roughness of the surfaces microstructure. The protrusions act to trap air under a water droplet as surface roughness is increased, resulting in a Cassie-Baxter wetting mechanism in the same way as the AACVD films. The water contact angle values were consistent showing only 2° of variation across all of the films.

2.3.5 The Deposition of Hydrophilic Melamine-formaldehyde Resin

2.3.5.1 Spin/Dip-coated Films

The polymerisation reaction of melamine with formaldehyde occurs as follows (Figure 2.20):

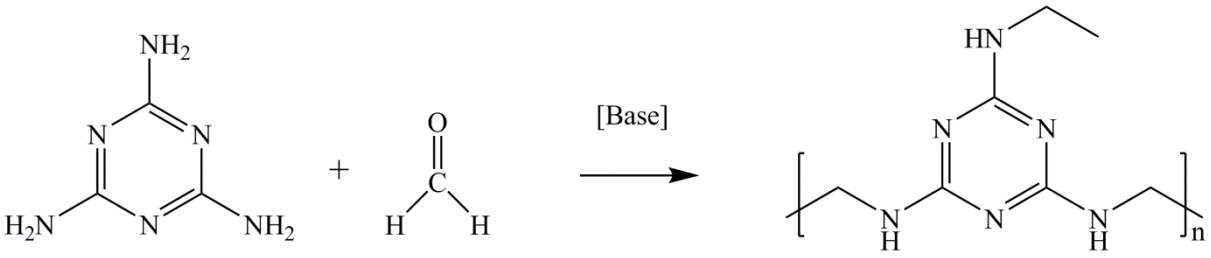

Figure 2.20. Polymerisation reaction between melamine and formaldehyde under alkaline conditions.

The pre-polymer solution of melamine-formaldehyde resin gave a film that transmitted visible light upon both the spin- and dip-coating process. The transparent films were confirmed to be relatively flat by SEM images (Figure 2.21), showing only small sparsely distributed features on the surface. Analysis of these films *via* IR spectroscopy suggested the presence of C–H, N–H (or O–H) bonds with no peaks indicating the presence of C=O bonds. Elemental analysis of the delaminated films gave a consistent composition for both spin-coated and dip-coated films. The result also shows that polymerisation of melamine was extensive with low levels of contaminant.

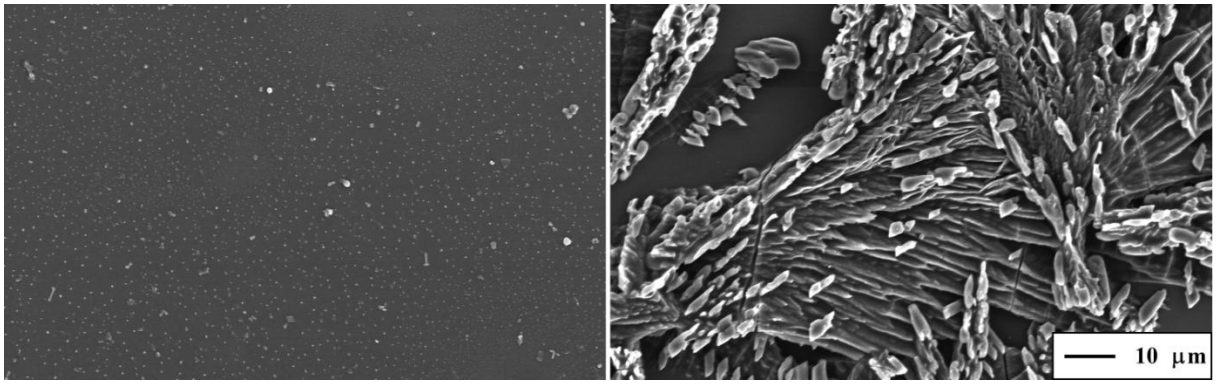

Figure 2.21. SEM images of melamine-formaldehyde resin films formed via; (left) spin-coating and (right) evaporation of the pre-polymer material. Both films were heated at 250°C for 1 hour for evaporation/curing. Scale bar shown is consistent for both images.

The water contact angles achieved on the dip/spin-coated melamine-formaldehyde resin films averaged 34°. The SEM images of these films show a flat surface, this suggests that the resultant melamine-formaldehyde surface is a high-energy material for water, i.e. it is hydrophilic when flat. The film produced by evaporation of the pre-polymer solution on a microscope slide gave a roughened film of the same material (Figure 2.21). These roughened surfaces gave a higher contact angle upon addition of the water droplet, and an average contact angle of approximately 50° was obtained in the first moments after addition. When left for approximately 5 seconds the droplet further wets the surface reducing the water contact angle to between 15 and 20°. This shows that the wetting of the surface porosity is gradual and that the roughened surface does decrease the water contact angle, which corresponds to the intrinsic hydrophilicity of the melamine-formaldehyde resin.

2.3.5.2 AACVD Deposited Films

All the films in this section were deposited onto the top plate in the CVD reactor. Deposition on the top plate in a CVD process indicates that the thermophoretic effect is prevalent. The melamine-formaldehyde films were most adherent at a 250°C deposition temperature. The film were scratched by a scalpel, however they were resistant to Scotch tape.

Combustion elemental analysis of a delaminated portion of the film gave a very similar composition of films deposited *via* AACVD to those using spin/dip-coating. XRD measurements gave no definable sharp peaks, suggesting an amorphous film. Raman measurements gave similar peaks to the IR spectra of the spin/dip-coated films, with peaks in C–H, N–H (or O–H) regions present, and no presence of C=O stretches (Figure 2.22). The spectrum is identical to those for the polymer resin.

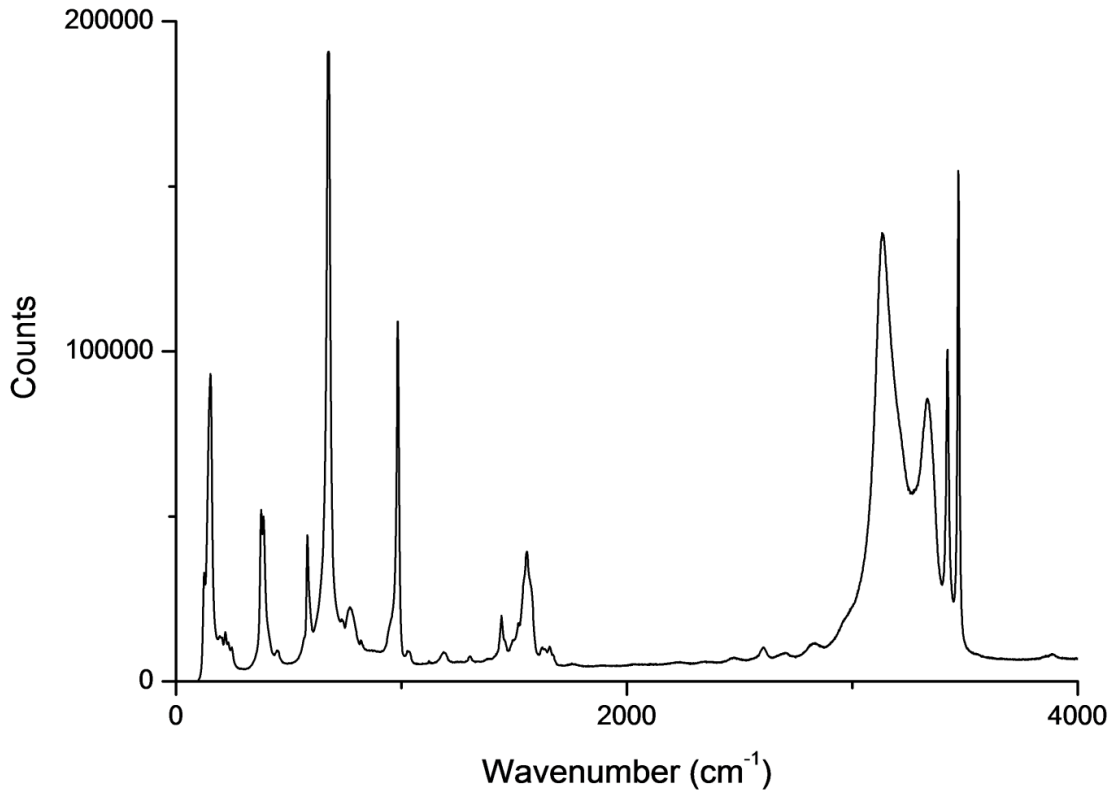

Figure 2.22. Raman spectrum of melamine-formaldehyde resin film deposited *via* AACVD at 250°C.

SEM images of the melamine-formaldehyde resin surfaces deposited by AACVD revealed a highly developed surface microstructure (Figure 2.23). Spherical particles of melamine-formaldehyde resin, ranging from 200 to 800 nm diameter were seen agglomerated into tower-like configurations up to 5 μm thick. The particles deposit as spheres because the AACVD process involves the formation of aerosol droplets of the precursor solution, when the solvent is evaporated in the CVD reactor the polymer precursor reacts and cures at the elevated temperatures. The spherical aerosol droplets (calculated to be approximately 35 μm in diameter[22]) thus become smaller spherical polymer particles (~ 300 nm diameter) which are subsequently deposited onto the substrate. The surface microstructure extends across the whole substrate. However the films were thinner closest to the reactor inlet and the coating was incomplete. For the same set of conditions the film thickness was maximised at 200°C. At a deposition temperature of 250°C the amount of the material deposited decreased due to an increase in the thermophoretic repulsion from the bottom plate which forced the particles around the top plate onto the top of the reactor. The deposited films showed signs of decomposition at 350°C, denoted by a yellow/brown tint on the film, with almost complete decomposition at 400°C.

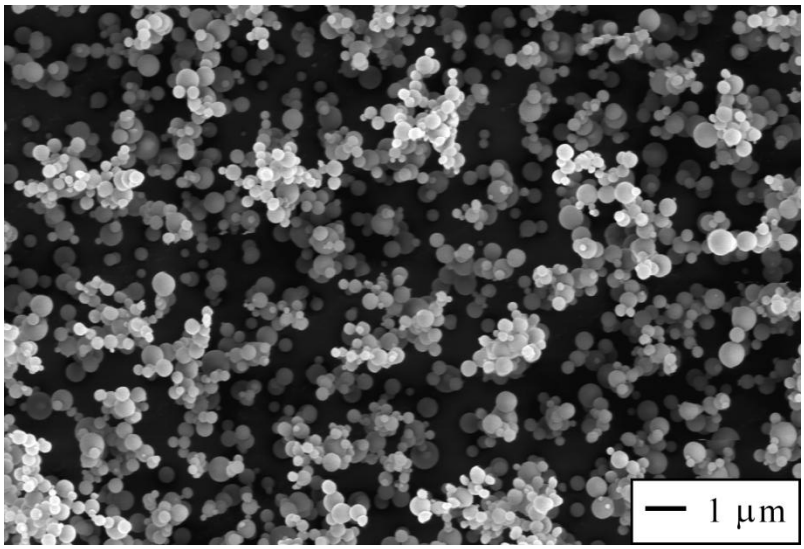

Figure 2.23. Top-down SEM image of melamine-formaldehyde resin, deposited using AACVD at a reactor temperature of 250°C, showing a highly developed microstructure. Scale bar shown.

The high-energy material and the highly developed surface microstructure suggest that there should be a decrease in the contact angle, relative to the flat melamine-formaldehyde surface. However the AACVD deposition at 250°C, gave an average water contact angle of 115° (standard deviation (σ) = 16.1°). Most of the contact angles values however occurred between 120° and 135°, for over 90% of the film area, the average water contact angle for this region was 124° (σ = 5.9°). Regions of lower polymer surface coverage, in the region closest to the reactor inlet (less than 10% of the total substrate), gave the lower contact angles below 90° for some droplets, shown in Figure 2.24. The water droplets in this region gradually wet the surface, taking approximately 2–3 s to come to the equilibrium contact angle, reducing from an initially higher angle. The water contact angle results suggest a Cassie–Baxter wetting mechanism, as the roughening of a Wenzel type wetting surface would lower the contact angle (from 34° achieved on a flat surface).

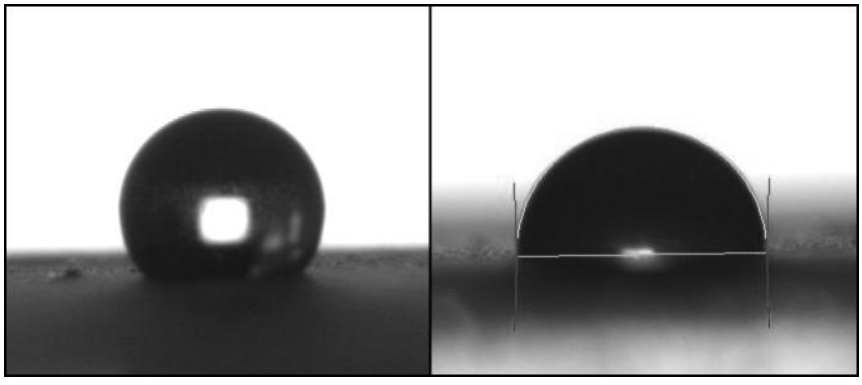

Figure 2.24. Contact angle images used in the analysis of wetting properties on a film deposited using AACVD at a deposition temperature of 250°C. Images show droplets on the surface on a; (left) a region of the highest surface coverage (water contact angle = 133°), (right) a region of low surface coverage (water contact angle = 92°).

A hydrophobic Wenzel type surface must be constructed from a material which when flat gives a contact angle greater than 90°. The same is not true however for Cassie–Baxter wetting surfaces. A few studies have been carried out to show that superhydrophobic surfaces can indeed be generated from using high-energy materials using multi-step and mechanical roughening routes. The work reported in this paper gives an example of a Cassie–Baxter wetting mechanism constructed using a high-energy material. It indicates that the air under the water droplet between the surface protrusions, increases surface hydrophobicity. The air underneath the droplet cannot flow through the surface porosity due to the arrangement of the surface protrusions, thus the air is trapped and the water sits on top of this air.[28] A water droplet sitting on air would in theory have a contact angle of 180° (if wind distortion is negated), so the high energy melamine-formaldehyde resin film reported in this paper is rendered hydrophobic because parts of the water droplet are "sitting on air", increasing the contact angle of a flat surface from 34° to above 120°. The theoretical area fraction of solid–liquid contact made (Φ_s) can be calculated from these results, for a simplified Cassie–Baxter model:

$$\cos\theta_e^c = \Phi_s cos\theta_e + \Phi_s - 1$$

$$\text{Rearranges to: } \Phi_s = \frac{(\cos\theta_e^c + 1)}{(cos\theta_e + 1)}$$

$$\text{Where } \theta_e^c = 135° \text{ and } \theta_e = 34°$$

$$\text{Gives: } \Phi_s = 0.160$$

θ_e is the equilibrium water contact angle for the flat surface, θ^c_e is the equilibrium water contact angle for the Cassie–Baxter surface and Φ_s is the area fraction of solid–liquid contact.

This indicates that if a pure Cassie–Baxter model is supposed then 16% of the water droplet is calculated to be in contact with the film protrusions and the remaining 84% in contact with air trapped under the water droplet. Penetration of the surface by water droplets was observed in regions of low surface coverage, thus a wholly Cassie–Baxter wetting mechanism is unlikely, however the magnitude of contact between the surface and water droplets can be envisaged using this calculation.

Side-on SEM images show the variation in the surface coverage (Figure 2.25). Areas of low surface coverage (close to the reactor inlet) are confirmed to have a thickness around 1.5 μm; these areas gave water contact angles below 90°. Areas where water contact angles were around 120°–135°, were shown to be 2–3 μm thick. Longer AACVD deposition times led to the generation of very hydrophilic portions of the deposited films (water contact angles less than 10°); these areas were shown to be over 4 μm thick. The areas of low coverage can allow the water droplet to touch the substrate and result in further wetting of the surface, which reduces the proportion of air trapped underneath the water droplet and thus reduces hydrophobicity. Regions of medium coverage, allow for

air to be trapped and little contact with the substrate occurs. This means that the fraction of the solid–liquid contact area is minimised resulting in a maximisation of surface hydrophobicity. An increase in the material (areas of heavy deposition) should not affect the solid–liquid contact area if air is trapped beneath the water, as the tops of the surface protrusions remain relatively similar in shape, regardless of film thickness. However the large reduction in water contact angle (< 10°) can be explained by examining the air located beneath the water droplet.

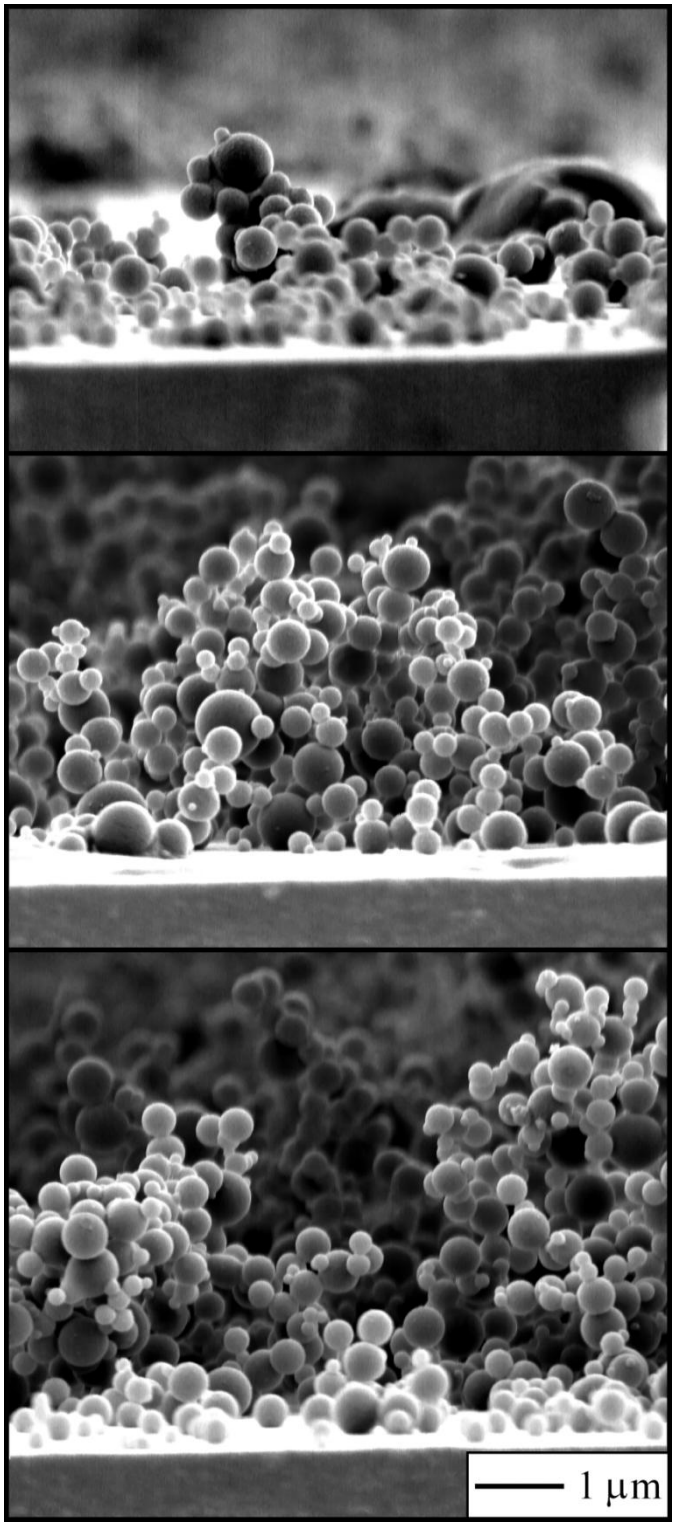

Figure 2.25. Side-on SEM images of melamine-formaldehyde resin, all deposited using AACVD (deposition temperature 250°C). Showing; (Top) a region of low substrate coverage (film thickness ~ 1.5 μm, average water contact angle ~ 80°), (Middle) a region of medium substrate coverage (film thickness ~ 2–3 μm, average water contact angle 120–135°), (Bottom) a region of heavy substrate coverage (film thickness ~ 4 μm, average water contact angle ~ 10°).

2.3.5.3 Comparison with Low Surface Energy Materials

The deposition mechanism of the AACVD process is similar to that for the deposition of silicone elastomers, described throughout this chapter. The silicone elastomers had a water contact angle of 95° when flat, which increase to 167° when deposited *via* AACVD. The surface microstructure formed in both the silicone elastomer and the melamine polymer reported in this section is very similar, a greater amount of particle agglomeration is seen in the AACVD of silicone elastomers. An increase in the material deposited in the AACVD process resulted in no observed change in the silicone elastomers contact angle. However upon increasing the deposition amount, the melamine-formaldehyde resin film became very hydrophilic in the area of thickest deposition, giving a contact angle as low as 5°. This change can be rationalised by considering air underneath a water droplet; in areas where there is a 2–3 μm film thickness, there is a smaller volume of 'trapped air', Figure 2.26. The very low contact angles achieved in thicker areas of deposition (film thickness ~ 4 μm) are explained through a change in the wetting mechanism, from a Cassie–Baxter to a Wenzel mechanism. The greater film thicknesses allow a greater volume of air underneath the droplet which is not only more easily compressed but also facilitates movement through the film porosity. The water droplet could thus not be supported by the air beneath it and the water will penetrate the microstructure. This mechanism would result in water becoming exposed to more of the high-energy melamine-formaldehyde resin instead of resting on air, reducing the surface hydrophobicity severely. The silicone elastomer equivalent would not be affected by this due to the greater agglomeration of particles and the elastomer's inherently high water repellence.

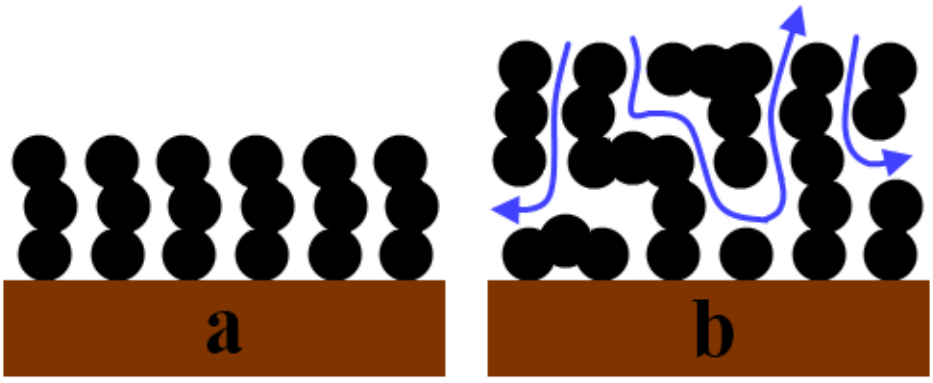

Figure 2.26. Schematic representation of a cross-section through; (a) a normal deposition with air trapped between the surface protrusions and glass, and (b) a heavier deposition showing more space for air to travel and so the air is not trapped beneath a water droplet.

The movement of water across the surface is a good indication of the surface wetting mechanism. Films of melamine-formaldehyde resin formed by AACVD had a high water droplet slip angle, the parts of the films with the highest contact angle were able to hold 30 μL water droplets at 90° tilt. If water droplets were dropped onto a surface already tilted (~45°) the water droplets bounce

on the surface, this indicates an immediate repulsion from air trapped in the film. Advancing/receding contact angle measurements showed a large difference (large angle of hysteresis), and water droplets that spent a longer time on the surface gave a larger difference. These results points toward a progressive wetting mechanism which begins as a slippery Cassie–Baxter mechanism which moves toward an intermediate state as a water droplet is left on the surface, thus becoming stickier. The intermediate state will give points on the films where there is strong attraction between water and the surface material, resulting in parts of the water droplet remaining after the bulk of the droplet is removed (i.e. low receding contact angle)[29]. This contrasts with the silicone elastomer AACVD depositions where there is a low slip angle, which is due to the low energy material preventing any penetration of surface protrusions in to the water droplet.

2.4. Conclusions

The deposition of polymers *via* an aerosol route is a successful method for forming exceptionally rough-superhydrophobic surfaces. The key factors of the process are:

- **Microdroplets of polymer precursor solution**. These are small enough to be transferred in the gas phase to a heated reactor. Evaporation of the solvent in the droplets results in spherical particles of polymers, preformed in the gas phase.
- **Thermosetting polymer**. Once the microparticles of polymer have entered the heated reactor, they can either be cured or melted. Thermosoftening polymers melt and contact with a substrates results in molten mounds of the material. Thermosetting polymers begin to harden with heat, subsequent contact with the substrate allows for assembling of microparticle agglomerated which form networks of intense microstructure.
- **Process Enhancements**. The hydrophobicity of the highly rough polymer films can be subject to enhancement. This has been done by varying the type of polymer used (Sylgard vs. NuSil), Changing the aerosol generation method and pre-treating the substrates with a flat film of elastomer. Photo active species have also been embedded into the films, either by swell encapsulation (methylene blue) or forming an intermediate layer between substrate and elastomer (gold nanoparticles).
- **Surface Wetting Mechanism**. The deposition route resulted in a highly rough microstructure for all curing polymers. The wetting of the polymer surfaces occurred with air becoming trapped under water on the surface (a Cassie-Baxter mechanism). Depositions of a hydrophilic polymer ($\theta = 34°$ for a flat surface) allowed the formation of a Cassie-Baxter wetting surface. By control of the deposition conditions it was shown that changes in surface microstructure and material coverage could enable the same material to be tailored between superhydrophilic, hydrophilic, hydrophobic to near superhydrophobic.

The methods used to form superhydrophobic films from polymers can entail expensive and time consuming apparatus or procedure. The AACVD polymers explored in this chapter is an inexpensive, fast and versatile one-step method for forming superhydrophobic surfaces that was previously unexplored.

2.5. References

1. Z. Guo, W. Liu, B. Su, *J. Colloid Interface Sci.*, 2011, **353**, 335.
2. D. J. Crisp, *J. Colloid Sci.*, 1946, **1**, 161.
3. X. Zhang, F. Shi, J. Niu, Y. Jiang and Z. Wang, *J. Mater. Chem.*, 2008, **18**, 621.
4. X. Li, D. Reinhoudt and M. Crego-Calama, *Chem. Soc. Rev.*, 2007, **36**, 1350.
5. G. McHale, N. J. Shirtcliffe and M. I. Newton, *Langmuir*, 2004, **20**, 10146.
6. M. L. Ma and R. M. Hill, *Curr. Opin. Colloid Interface Sci.*, 2006, **11**, 193.
7. E. L. Decker and S. Garoff, *Langmuir*, 1997, **13**, 6321.
8. J. Bico, C. Marzolin and D. Quere, *Europhys. Lett.*, 1999, **47**, 220.
9. Z. J. Yu, E. T. Kang, K. G. Neoh, C. Q. Cui and T. B. Lim, *J. Adhesion*, 2000, **73**, 417.
10. K. M. Forward, A. L. Moster, D. K. Schwartz and D. J. Lacks, *Langmuir*, 2007, **23**, 5255.
11. R. A. Lawton, C. R. Price, A. F. Runge, W. J. Doherty III, S. S. Saavedra, *Colloid. Surface. A*, 2005, **253**, 213.
12. R. N. Wenzel, *Ind. Eng. Chem.*, 1936, **28**, 988.
13. A. B. D. Cassie and S. Baxter, *Trans. Faraday Soc.*, 1944, **40**, 546.
14. M. Heckele and W. K. Schomburg, *J. Micromech. Microeng.*, 2004, **14**, R1.
15. B. S. Hayes and J. C. Seferis, *Polym. Compos.*, 2001, **22**, 451.
16. S. Basharat, C. J. Carmalt, R. Binions, R. Palgrave and I. P. Parkin, *Dalton Trans.*, 2008, 591.
17. J. Akhtar, M. A. Malik, P. O'Brien and M. Helliwell, *J. Mater. Chem.*, 2010, **20**, 6116.
18. T. Ogi, D. Hidayat, F. Iskandar, A. Purwanto and K. Okuyama, *Adv. Powder Technol.*, 2009, **20**, 203.
19. R. Gordon, *J. Non-Cryst. Solids.*, 1997, **218**, 81.
20. M. R. Zaghloul, *J. Appl. Phys.*, 2004, **95**, 3339.
21. D. S. Kummli, H.-M. Frey and S. Leutwyler, *Chem. Phys.*, 2010, **367**, 36.
22. R. J. Lang, *J. Acoust. Soc. Am.*, 1961, **34**, 6.
23. G. J. Smith, A. Harriman, A. D. Woolhouse, T. G. Haskelll and T. H. Barnes, *Photochem. Photobiol.*, 1998, **67**, 101.
24. S. Noimark, C. W. Dunnill, M. Wilson and I. P. Parkin, *Chem. Soc. Rev.*, 2009, **38**, 3435.
25. T. K. Sau, A. Pal, N. R. Jana, Z. L. Wang and T. Pal, *J. Nanopart. Res.*, 2001, **3**, 257.
26. J. Jung, K. Na, J. Lee, K. Kim and J. Hyun, *Anal. Chim. Acta.*, 2009, **651**, 91.
27. G. G. Nasr, A. J. Yule and L. Bending, *Industrial Sprays and Atomization*, Springer, 2002.
28. J. Liu, X. Feng, G. Wang and S. Yu, *J. Phys. Condens. Matter*, 2007, **19**, 356002.
29. P. S. H. Forsberg, C. Priest, M. Brinkmann, R. Sedev and J. Ralston, *Langmuir*, 2010, **26**, 860.

Chapter 3

The Hybrid CVD and Functionalisation of Silica Microparticles

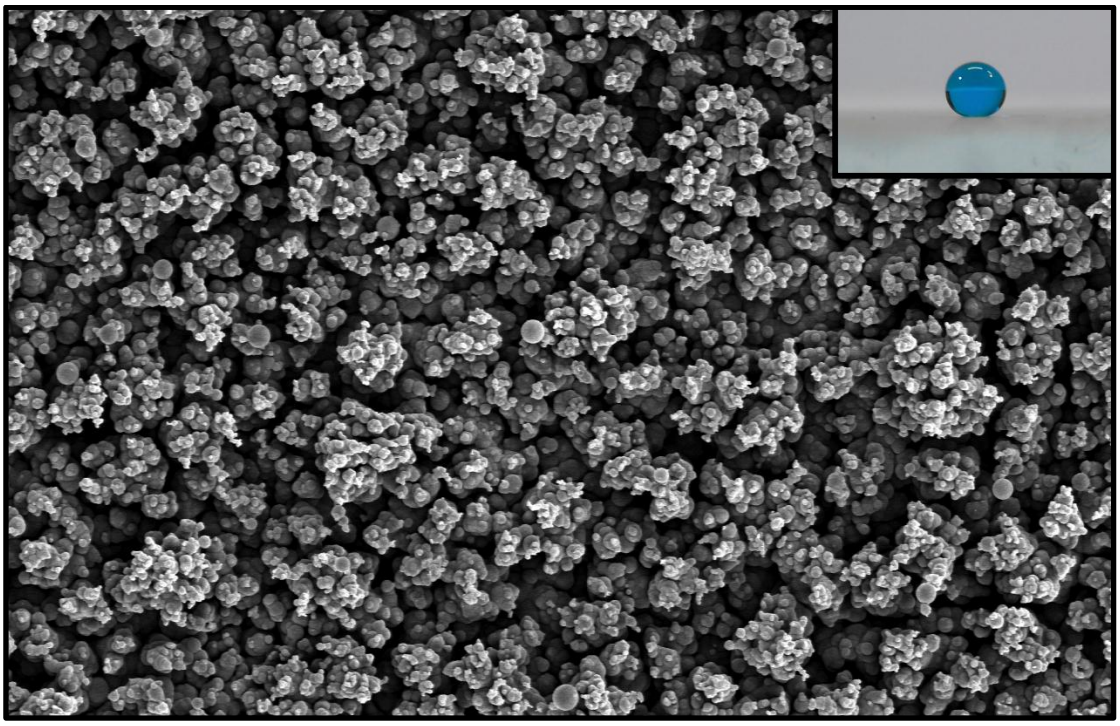

Figure 3.01. SEM image of a silica microparticle surface deposited using CVD, with an image of a water droplet on the surface subsequent to functionalisation.

3. The Hybrid CVD and Functionalisation of Silica Microparticles

3.1. Introduction

Silicon dioxide (silica) is found in both crystalline structures and amorphous phases[1]. It is the structural versatility and malleability of silica that render it a popular choice to construct structured and subsequently superhydrophobic surfaces[2/3].

3.1.1 The Hydrophobicity of Silica

The surface of silica materials is readily hydrolysed in ambient conditions (Figure 3.02)[4]. It is the extent of this hydrolysis and the resulting amount of surface silanol groups which dictate the hydrophobicity of a silica surface[4], with water contact angles of around 45° for silica glass stored at room temperature. The surface silanol groups form hydrogen bounds with water, the more of these groups present the more hydrophilic a surface will become. The silanol groups are removed upon heating[4], with hydrophobic water contact angles achieved when the same silica sample is heated.

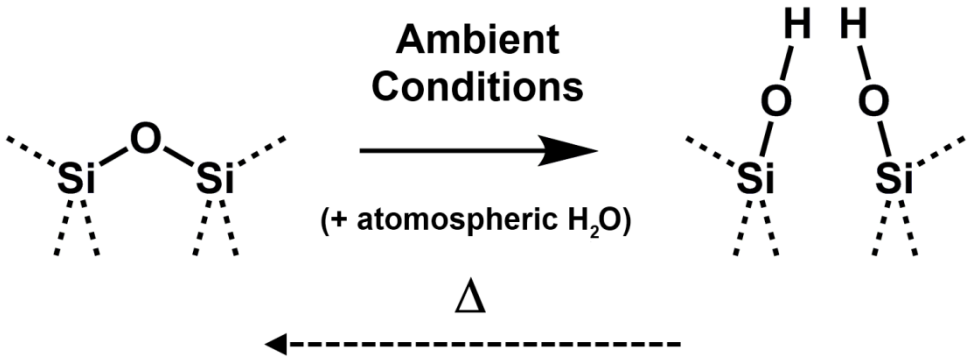

Figure 3.02. The hydrolysis of a silica surface when left at room temperature in ambient conditions, leads to the production of water attracting surface silanol groups. The reverse transformation occurs upon heating.

The surface silanol groups attract water, and so their presence is unfavourable when considering the construction of hydrophobic surfaces. These groups can be functionalised in order to lower the energy of interaction with water and thus surface energy[5/6]. The most common routes for silanol functionalisation is the use of alkylsilanes[7] and FAS[8] with the addition of these molecules resulting in water contact angles up to 100° being reported for flat surfaces. The roughening of surface microstructure can be readily accomplished through use of silica beads[9] or high temperature sintering of silica surfaces[6]. These steps fulfil the requirements for extreme hydrophobicity (low surface energy and high surface roughness).

3.1.2 The CVD of Silica-based Thin Films

CVD requires gaseous or soluble precursors in order to form thin films[10]. One of the most commonly used precursors used to construct silica films is tetraethylorthosilicate (TEOS)[11], in addition to tetramethylorthosilicate and other similarly structured compounds.[12] The frequent application of this compound type is a result of their ease of activation toward forming silica products and also their relatively high volatilities. TEOS is quite thermally stable, requiring temperatures above 700°C to begin decomposition.[10] Existing CVD routes must reach temperatures exceeding this or incorporate another form of activation, which include exposure to plasma energy[13] and ultra-violet light[14]. The molecular nature of these CVD reactions means that relatively flat and uniform films are formed[10], with roughened silica usually obtained by further etching[15].

The previous chapter discussed using AACVD to generate high surface roughness. This chapter utilises a similar deposition process to form rough silica textured surfaces. The deposition of silica microparticles *via* a hybrid CVD is detailed in this chapter, and the key aspects of the deposition route will be discussed with important factors in particle formation identified. The microstructure of the surfaces deposited will be characterised, showing that the size and amount of particles deposited can be varied by the reaction conditions used. A post-treatment was used to functionalise surface groups and lower surface energy. This allows for the superhydrophilic silica surface to be converted to a superhydrophobic one. The hydrophobicities of both unmodified and modified films were analysed.

3.2. Experimental Details

3.2.1 Materials

All chemicals used in this investigation were purchased from Sigma-Aldrich Chemical Co; including TEOS, hydrochloric acid, toluene and hexamethyldisilazane (HMDS).

3.2.2 Hybrid CVD of Silica Microparticles

The form of hybrid CVD used is a combination of AACVD and atmospheric pressure CVD (APCVD) and is best represented in a schematic (Figure 3.03). The depositions were carried out in a cold-walled horizontal CVD reactor. The reactor contained a top and bottom silica barrier layer glass for deposition (dimensions: 145 x 45 x 5 mm; barrier thickness 50 nm), provided by Pilkington NSG. The barrier layer prevented any ion transfer from the bulk glass. The CVD reactor was heated using a carbon block, which the bottom plate was placed on. The top plate was positioned 8 mm above and parallel to the bottom plate, the complete assembly was enclosed in a quartz tube. The aerosol of aqueous acid (1 M HCl) was formed using a PIFCOHEALTH ultrasonic humidifier, operating at a frequency of 40 kHz and 25 W of power. The generated aerosol was moved into a cylindrical mixing chamber (length: 180 mm diameter: 35 mm) using a nitrogen gas flow via PTFE

(polytetrafluoroethylene) and glass tubing. The aerosol then passed through the mixing chamber and subsequently into the CVD reactor. TEOS was carried from a heated bubbler using preheated nitrogen (passed through a 300°C tube furnace), brought together in the mixing chamber, mixing with the aerosol and passed into the heated reactor (over a range of temperatures, 450–600°C). The bubbler temperature was maintained at 80°C to keep the vapour pressures constant. All of the lines to and from the bubblers were maintained at 150°C, including the mixing chamber. The nitrogen flow rate from the bubblers and aerosol was maintained at 0.5 L/min. Depositions were carried out for a logged period of time and nitrogen flow was left on for a further 10 min (at heated temperature, including line heaters), the reactor's heater was also switched off after 10 min and was allowed to cool. The cooled plates were removed from the reactor and handled in air.

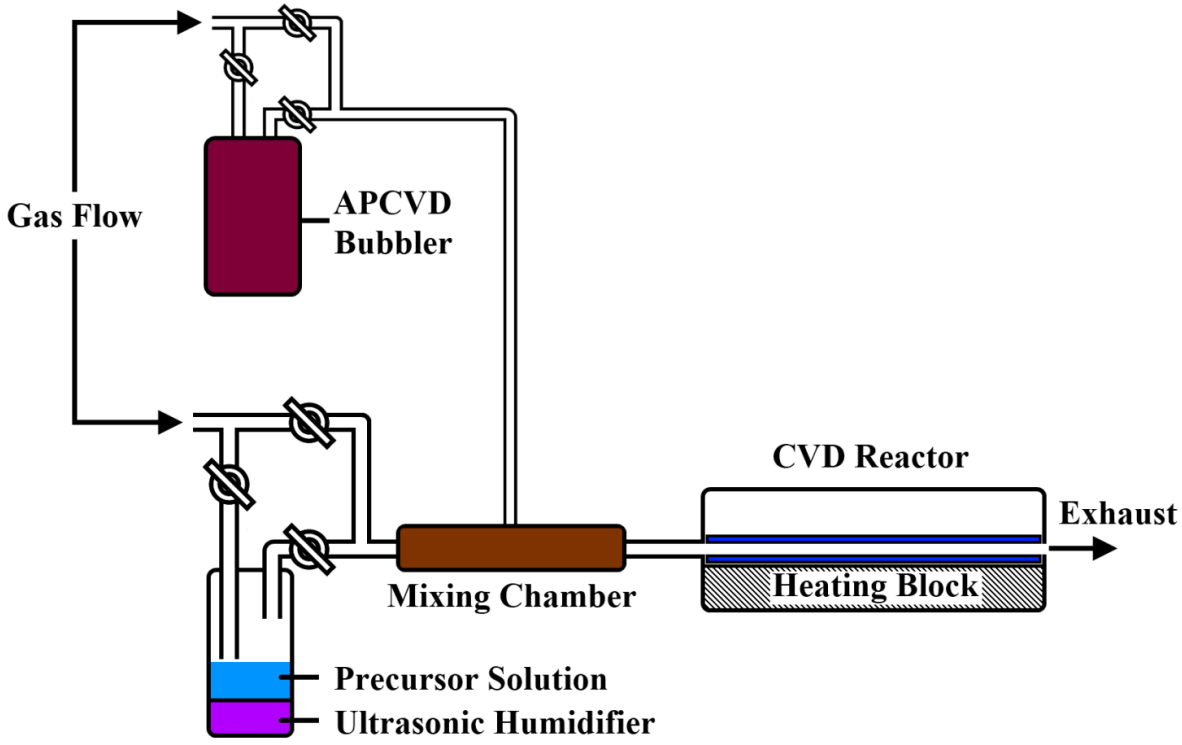

Figure 3.03. Schematic of the hybrid CVD setup.

3.2.3 Functionalisation of Silica Microparticle Surface

Portions of the deposited films were totally immersed in a solution of HMDS (10% v/v in toluene) inside a large crystallisation dish. The solution was stirred at 40°C for 24 h. The plates were removed from the solution and then placed in a 100°C oven for an hour to dry. Once cooled the films were stored in air.

3.2.4 Films Characterisation

The films were analysed as coatings on the barrier glass substrate. SEM images were taken from gold-sputtered small subsections (ca. 1 x 1 cm) cut from the substrates. Analysis was carried out using a field emission scanning electron microscope (SEM), a Jeol JSM-6301F operating at 5 kV. Energy Dispersive X-ray (EDX) analysis was also carried out on the same machine using an operating frequency of 10 kV. Powder X-ray diffraction (XRD) patterns were measured on a Bruker D8 discovery instrument using monochromated Cu-Kα radiation (λ = 1.5406 Å) in the reflection mode. Raman measurements were made using a Renishaw 1000 spectrometer which used a 632.8 nm laser. UV–visible absorption spectra were taken using a Perkin Elmer Lambda 25 UV/VIS Spectrometer single beam instrument over a range of 300–1000 nm. Adherence tests were carried out, done by applying Scotch Home and Office masking tape to the surface followed by its removal. Scratch tests were also carried out by observing the action of a metal scalpel being dragged across a surface.

3.2.5 Surface Hydrophobicity Measurements

Water contact angle measurements were carried out using an FTA-1000 drop shape instrument; 3 μL water droplets were used to minimise any gravitational effects. The water droplet images were analysed using a digital protractor to obtain the water contact angles on the surface. A range of points across the substrates were tested, with 12 measurements made on each film. Water slip angles were also measured, noting the angle to the horizontal at which 3 μL water droplets moved on the surface. Many positions across the substrates were tested.

3.3. Results and Discussion

3.3.1 The Deposition of Silica Microparticles via Hybrid CVD

3.3.1.1 Preliminary Depositions

Preliminary hybrid CVD depositions were carried out over a 5 minute period. It was found that substantial deposition of material only occurred at and above a deposition temperature of 450°C, these depositions occurred to the top substrate plate. The highest deposition temperature used was 600°C, limited by the melting of the glass substrates. The films were white and hazy in appearance with the thickest deposition found to occur at 550°C. It was also found (confirmed by SEM) that the average deposited particle size varied with deposition temperature: 450°C (300 nm), 500°C (500 nm), 550°C (650 nm) and 600°C (750 nm) (Table 3.1, p113), with a variation in particle sizes exhibited at all temperatures (Figure 3.04). A Si:O ratio of 1:2 was also obtained from EDX analysis. The pre-mixing of the reactants in the mixing chamber was found to be vital to a deposition taking place. Depositions with no mixing chamber, where reactants entered and mixed in the heated reactor, gave no deposition at any temperature used. The necessity to pre-mix TEOS and aerosol, and the fact that depositions

occur to the top plate indicates that the formation of particles occurs around the acidic aerosol droplets which results in silica precursors being generated inside the individual droplet particles. This in turn leads to aerosol solutions of silica precursors, which then upon entering the reactor, will have the water evaporated leaving pre-formed microparticles in the gas phase. These microparticles are then forced toward the top plate due to the thermophoretic effect, repelling the particle away from the heated bottom plate. The solidifying particles are thus deposited on the top plate (Figure 3.04).[16]

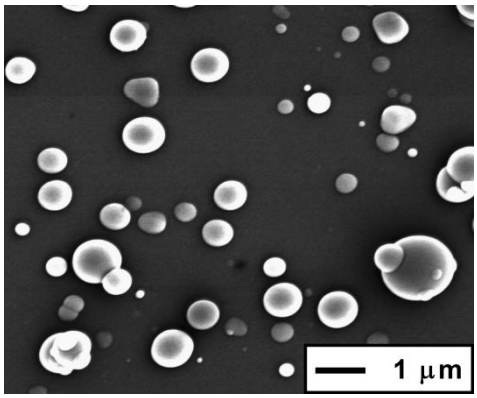

Figure 3.04. SEM image showing an area of low coverage of silica microparticles deposited *via* hybrid CVD at a deposition temperature of 600°C for a period of 5 minutes. The variation in particle size can be observed in this image. Scale bar shown.

3.3.1.2 Film Appearance and Substrate Adhesion

To generate an optimised surface roughness the deposition time was increased to 30 min, resulting in complete substrate coverage. The microparticulate films appear as a white hazy film, with film transparency lowering with film thickness. The thickest film which was deposited at a 550°C substrate temperature, appeared white and let very little light transmit through it (3%). The films were not affected by Scotch tape. However films deposited below 550°C had a low resistance to the action of a steel scalpel, with resistance improving at and above a 550°C deposition temperature. The reduced adherence in the low temperature experiments could be due to the speed at which the particles reach the top plate as the thermophoretic effect increases with temperature and so the higher temperature depositions result in particles reaching the top plate faster and in an earlier state of solidification. This, combined with potential partial melting or condensation reactions between surface silanol groups at higher temperatures, may explain the greater adhesion between microparticles themselves and to the substrate at higher deposition temperatures. The adherence of microparticles could also be improved by a post heat sintering with a Bunsen burner.

3.3.1.3 Film Microstructure

SEM images of the deposited film showed an extremely rough microstructure (Figure 3.05). The surface was made up of clusters of spherical particles that were agglomerated and fused together. The largest individual particles were *ca.* 1 μm but these often had attached a large number of smaller particles (100 nm) – giving a surface roughness on at least two length scales. AFM was attempted on the microparticle films however the extreme roughness made any valid measurement impossible due

to instrument limitations. Films deposited at lower substrate temperatures gave similar surface features, however they were made up of different sized particles. The thicker films of microparticles were also subjected to EDX analysis which gave a 1:2 (Si:O) ratio, confirming a composition consistent with that of silica. The crystal structure of the particles was also confirmed to have no long range order with XRD patterns showing only very broad peaks.

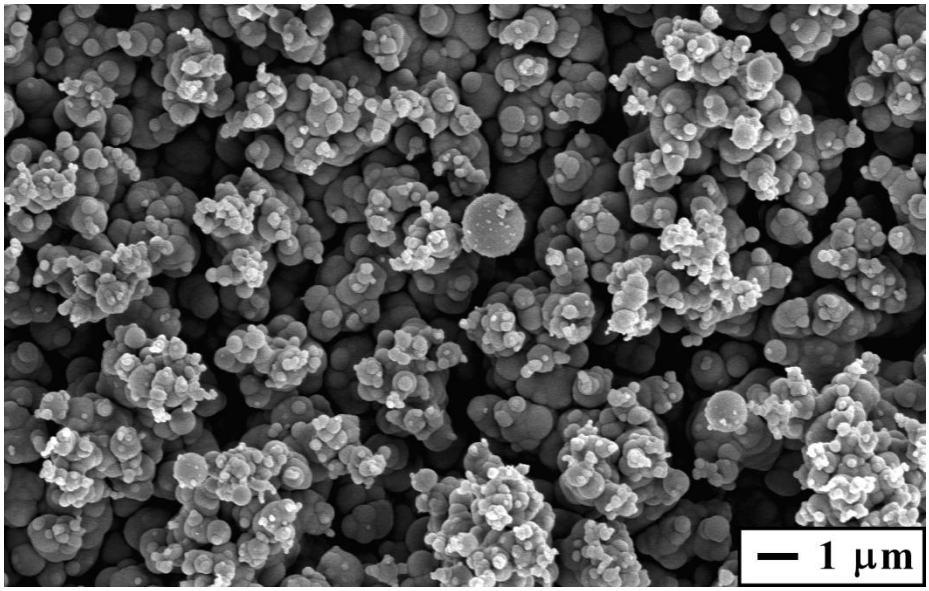

Figure 3.05. SEM image of a silica microparticle film deposited via hybrid CVD, using a substrate temperature of 550°C over a period of 30 min. The particles are of similar size to those deposited over a shorter period. Scale bar shown.

The deposition mechanism, described for preliminary depositions, supports the microstructure observed in the extended runs. This is seen more clearly from side-on SEM images by the formation of particle towers (Figure 3.06), a result of the solidifying particles landing on-top of those already on the surface. Similar microstructures were observed for films deposited at other deposition temperature, albeit with their respective particle sizes and film thicknesses (Table 3.1, p113).

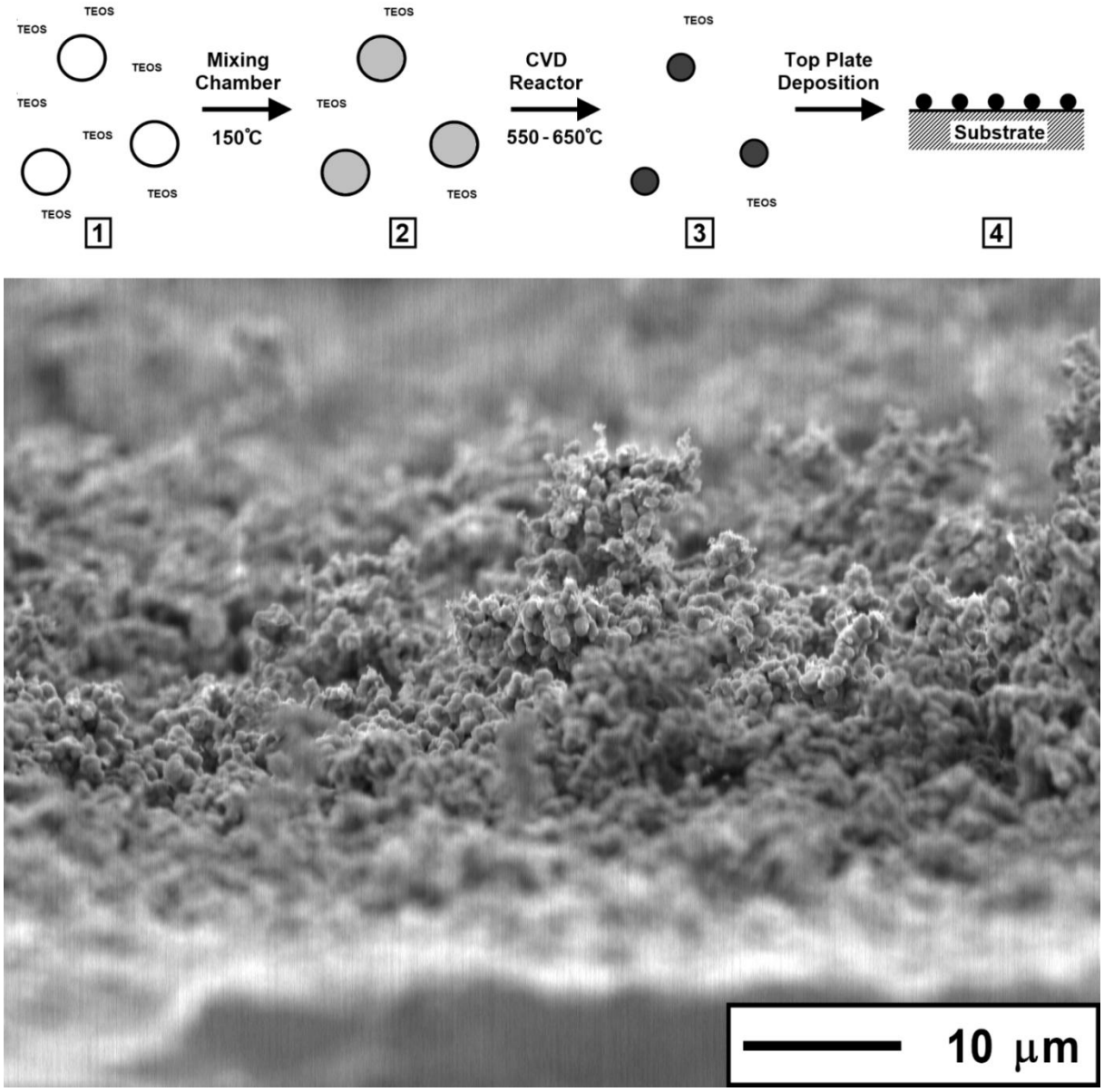

Figure 3.06. (Top) Proposed hybrid CVD deposition mechanism for the formation of silica microparticles – (1) Initial mixing of TEOS and aerosol, (2) TEOS interacts with the acidic aerosol forming aqueous silica precursors, (3) As the aerosol enters the CVD reactor, evaporation of water takes place resulting in solidifying silica particles, (4) The solidifying particles make contact with the substrate were they are then deposited. (Bottom) Side-on SEM image of a silica microparticle film deposited via hybrid CVD, using a substrate temperature of 550°C over a period of 30 min. Scale bar shown.

3.3.1.4 Hydrophobicity

Water contact angle tests were carried out on the as-formed highly rough silica film. The application of water droplets to the film resulted in an immediate spreading of the water, contact angles were always below 5° for films deposition at all temperatures used (Figure 3.07). The superhydrophilic

nature of the film confirms a Wenzel-type wetting mechanism, where water penetrates all of the surface porosity resulting in a strong attraction to the surface.

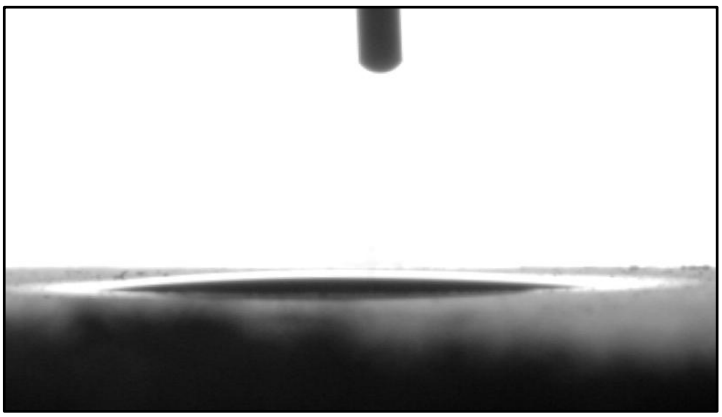

Figure 3.07. Image of a 3 μL droplet on a silica microparticle film deposited via hybrid CVD, using a substrate temperature of 550°C. The high roughness of the microparticle surface magnifies the intrinsic hydrophilicity of the silica material deposited resulting in a water contact angle around 4°.

3.3.2 Functionalisation of Silica Microparticle Surface

The surface of the silica microparticle film as formed is markedly hydrophilic; the presence of surface silanol groups is directly linked to its attraction to water (i.e. more silanol groups leads to a greatly amount of hydrogen bonding to water). The superhydrophilic films were treated with HMDS, with the aims of forming trimethylsiloxane (TMS) groups in place of silanol bonds, rendering them hydrophobic (Figure 3.08)[17]. The treatment was also carried out on the flat silica barrier layer CVD substrates, whose ordinary water contact angle is 45°; this was increased to 84° upon treatment with HMDS. The surface microstructure, as well as other physical properties of any the films treated was not noticeably altered by the functionalisation process. TMS groups were not observed by Raman or EDX analysis, this could be due to TMS being present only present as a monolayer on the surface after functionalisation and so cannot be detected above any background readings.

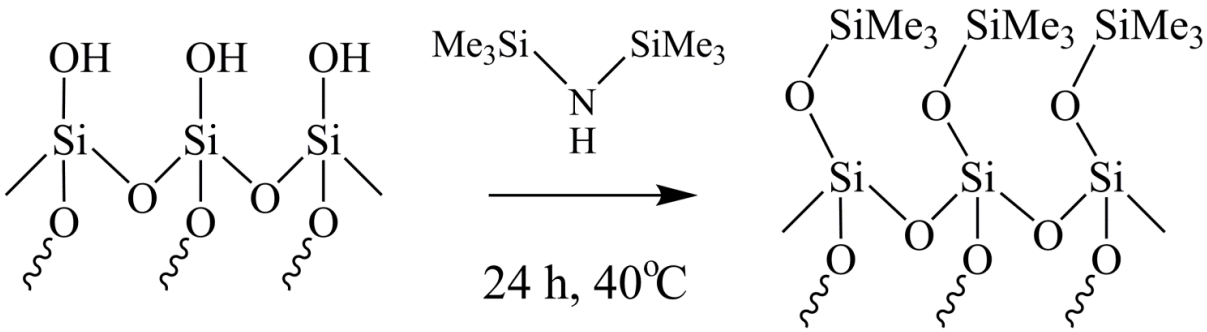

Figure 3.08. Scheme shows surface functionalisation of silanol groups, exchanging for low energy TMS groups. The reaction was carried out in toluene solvent, the conditions are also shown.

3.3.2.1 Hydrophobicity of Functionalised Silica Film

All of the silica microparticle films were rendered extremely superhydrophobic after functionalisation, with all achieving water contact angles that approached 180° (Figure 3.09). There was very little variation of water contact angles exhibited by the films deposited at different temperatures (Table 3.1). Calculation of the fraction of solid-liquid contact of water (Φ_s) using the Cassie-Baxter model could not be carried-out because the hydrophobicity of an equivalent flat functionalised surface not being able to be attained, as the silica particles were formed during the CVD process. The films were also extremely slippery relative to water, requiring tilt angles less than 1° for even very small water droplets (3 μL). Advancing/receding contact angles (θ_A/θ_R) were measured, no variation was observed showing $\theta_A = \theta_R \approx 180°$. The high water contact angles, as well as the low slip angles, suggests a Cassie-Baxter type wetting mechanism. As a water droplet moved across the surface it would roll and spin giving this surface an ideal Lotus effect self-cleaning mechanism. The microparticles are rounded, and allow for a reduction in contact pinning with sharp edges; this facilitates smooth travel of water over the surface[18]. Any tilt of the surface, even minuscule and virtually undetectable tilt, resulted in lateral movement in the direction of surface tilt.

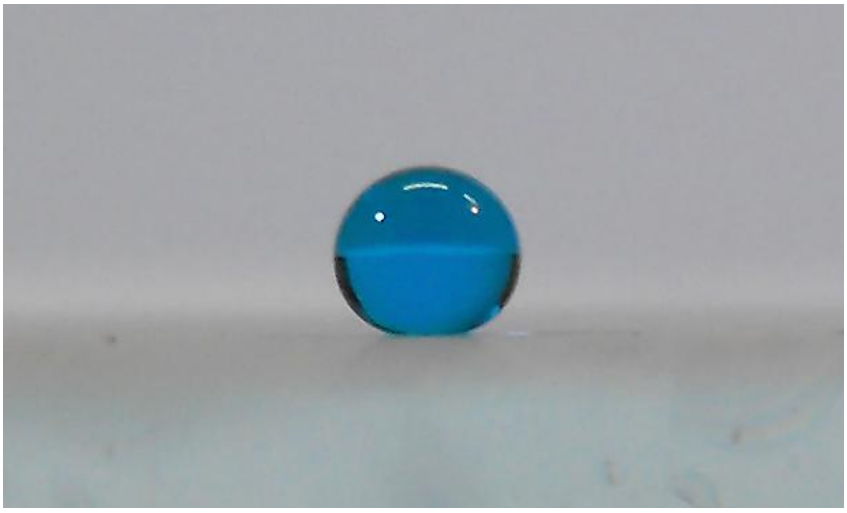

Figure 3.09. Photograph showing a 5 μL droplet of water on the modified silica microparticle film, deposited by hybrid CVD at a substrate temperature of 550°C. The water droplets would roll on the surface, even at very low tilt angles.

Deposition Temperature (°C)	Average Particle Size (nm)	Average Water Contact Angle (°)	±	Average Water Contact Angle (TMS-Functionalised) (°)	±
450	300	5	0.8	**172**	1.3
500	500	4	0.9	**174**	1.3
550	650	4	0.6	**175**	1.0
600	750	5	0.6	**173**	1.1

Table 3.1. Properties of films deposited at different temperatures using the hybrid CVD of TEOS and an acidic aerosol, over a 30 minute deposition time. (±) Presents 95% confidence intervals using Student's t-test distributions)

The method reported in this chapter is a novel one-step technique for forming silica microparticles, which allows for variation in microparticle size. The hybrid CVD system is also an inexpensive technique for forming silica particles, with readily available reactants used. The silica microparticle surface can be converted from superhydrophilic to superhydrophobic with a post-treatment. Other examples of superhydrophobic silica surfaces usually involve expensive precursors or elaborate processes these include: sol–gel[9], pyrolysis[6] and sintering procedures[19].

The extreme hydrophobicity of the microparticle films formed in this chapter provides a potential application in many fields including: Lotus effect self-cleaning[20], surface protection[21] and microfluidics[22]. The unmodified silica particles possess densely packed surface silanol groups, which allow the films to display hydrophilicity similar to that of superhydrophilic photocatalysts, also formed using CVD[23/24]. The physical robustness limit the applications of many films in the literature, and this can be directly linked to the scale of the surface features required for superhydrophobicity; the fragility comes with the microscale surface protrusions. The assembly of surfaces that possess similar superhydrophobicity to the reported surface (i.e. near 180° water contact angles, very low slip angles or near zero contact angle hysteresis) has focused on methods that produce fibrous[25] or pin like structures[26], as this can result in the lowest proportion of surface-water contact in superhydrophobic surfaces[27]. Films constructed from fibrous organosilanes have demonstrated near 180° water contact angles[28/29]. These surfaces allow for a high proportion of air to be trapped underneath the nanofibres, without need for a higher magnitude microroughness. A surface made up of pin-like structures could support a water droplet with minimal surface-water contact, resulting in maximisation of the droplets possible contact with air. The very nature of the highly developed surface roughness required to

achieve a near 180° contact angle results in many of the techniques involving complex reaction steps[30] or surface etching[31]. The technique reported in this chapter utilises an inexpensive and facile method for producing highly robust films of silica microparticles – facilitated by the aerosol directed deposition mechanism, with a straightforward post treatment which renders the particles extremely hydrophobic.

3.4. Conclusions

The acid catalysed hydrolysis of TEOS was carried out using hybrid CVD, a combination of an acidic aerosol and thermally vaporised precursors. The result was formation of silica microparticles in the gas phase, the particles were then deposited onto a glass substrate where they undergo further condensation to form a rugged film. The surface microstructure observed in the silica depositions (stacks of microparticles) show similarities to that observed in the AACVD depositions described in chapter 2. It is the common aerosol component of each deposition that allows for the production of intense surface roughness. The size of particles deposited could be varied with deposition temperature, with largest particle forming at the higher deposition temperatures. The greatest amount of material deposited at 550°C. Upon extended depositions the particles piled on together forming a film with a highly developed microstructure, higher temperature depositions also cause partial melting of microparticles, providing increased physical robustness. The unmodified films were superhydrophilic with water contact angles less than 5° achieved. Functionalisation of surface silanol groups with hydrophobic TMS groups rendered the microparticle film extremely hydrophobic with water contact angles approaching 180°. A tilt of less than 1° was required to move even very small water droplets, with droplets rolling as they moved across the surface. Water contact angle hysteresis was near zero, showing advancing/receding contact angles that were indistinguishable from static water droplets. This extreme hydrophobicity as well as the variability of surface features provides potential applications in Lotus effect type self-cleaning.

3.5. References

1. W. B. Fowler and A. H. Edwards, *Radiat. Eff. Defects Solids*, 1998, **146**, 11.
2. X. Yao, Y. Song and L. Jiang, *Adv. Mater.*, 2011, **23**, 719.
3. C. Xue, S. Jia, J. Zhang and J. Ma, *Sci. Technol. Adv. Mater.*, 2010, **11**, 033002.
4. A. S. D'Souza, C. G. Pantan and K. M. R. Kallur, *J. Vac. Sci. Technol. A*, 1997, **15**, 526.
5. Q. Wei, Y. Wang, Z. Nie, C. Yu, Q. Li, J. Zou and C. Li, *Microporous Mesoporous Mater.*, 2008, **111**, 97.
6. K. Chang, Y. Chen, H. Chen, *Surf. Coat. Tech.*, 2008, **202**, 3822.
7. A. B. Gurav, S. S. Latthe, C. Kappenstein, S. K. Mukherjee, A. V. Rao and R. S. Vhatkar, *J. Porous. Mater.*, 2011, **18**, 361.
8. X. Liu and J. He, *Langmuir*, 2009, **25**, 11822.
9. M. Manca, A. Cannavale, L. De Marco, A. S. Aricò, R. Cingolani and G. Gigli, *Langmuir*, 2009, **25**, 6357.

10. R. Gordon, *J. Non-Cryst. Solids.*, 1997, **218**, 81.
11. K. G. Sharp, *J. Mater. Chem.*, 2005, **15**, 3812.
12. H. Guo, B. N. Nguyen, L. S. McCorkle, B. Shonkwiler and M. B. Meador, *J. Mater. Chem.*, 2009, **19**, 9054.
13. C. Vallée, A. Goullet, A. Granier, A. van der Lee, J. Durand and C. Marliére, *J. Non-Cryst. Solids*, 2000, **272**, 163.
14. J. Lin, X. Zeng and Y. Hou, Polym. Plast. Technol., 2008, **47**, 1297.
15. M. Zhu, H. Gao, H. Li, J. Xu and Y. Chen, *J. Solid State Chem.*, 2010, **183**, 595.
16. S. Ashraf, C. S. Blackman, G. Hyett and I. P. Parkin, *J. Mater. Chem.*, 2006, **16**, 3575.
17. Q. F. Xu, J. N. Wang, I. H. Smith and K. D. Sanderson, *J. Mater. Chem.*, 2009, **19**, 655.
18. M. Nosonovsky and B. Bhushan, *Microsyst. Technol.*, 2005, **11**, 535.
19. J. Li, J. Fu, Y. Cong, Y. Wu, L. Xue and Y. Han, *Appl. Surf. Sci.*, 2006, **252**, 2229.
20. D. Kim, J. Kim, H. C. Park, K. Lee and W. Hwang, *J. Micromech. Microeng.*, 2008, **18**, 015019.
21. P. N. Manoudis, A. Tsakalof, I. Karapanagiotis, I. Zuburtikudis and C. Panayiotou, *Surf. Coat. Technol.*, 2009, 203, 1322.
22. C. J. Teo and B. C. Khoo, *Microfluid. Nanofluid.*, 2010, **9**, 499.
23. A. Kafizas, S. Kellici, J. A. Darr and I. P. Parkin, *J. Photochem. Photobiol. A*, 2009, **204**, 183.
24. A. Kafizas and I. P. Parkin, *J. Mater. Chem.*, 2010, **20**, 2157.
25. T. Wang, X. Hu and S. Dong, *Chem. Commun.*, 2007, 1849.
26. E. Hosono, S. Fujihara, I. Honma and H. Zhou, *J. Am. Chem. Soc.*, 2005, **127**, 13458.
27. S. M. Lee, C. Y. Park, S. I. Bae, J. S. Go, B. Shin and J. S. Ko, *Jpn. J. Appl. Phys.*, 2009, **48**, 095504.
28. L. Gao and T. J. McCarthy, *J. Am. Chem. Soc.*, 2006, **128**, 9052.
29. L. Gao and T. J. McCarthy, *Langmuir*, 2008, **24**, 362.
30. A. Borras and P. Gröning, *Langmuir*, 2010, **26**, 1487.
31. S. Hsu and W. M. Sigmund, *Langmuir*, 2010, **26**, 1504.

Chapter 4

The Aerosol Assisted Chemical Vapour Deposition and Functionalisation of Copper (0) and Copper (I) Oxide Thin Films

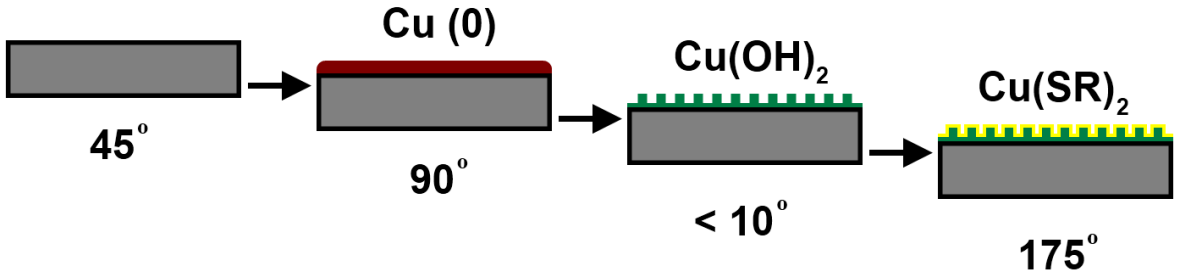

Figure 4.01. Scheme showing the deposition of copper onto a glass substrate and subsequent functionalisation, with resultant water contact angles also shown.

4. The Aerosol Assisted Chemical Vapour Deposition and Functionalisation of Copper (0) and Copper (I) Oxide Thin Films

4.1. Introduction

The fabrication of metallic thin films has been of great technological importance in microelectronics and related areas[1], with thin coatings of copper metal acting as interconnecting material within current circuit boards. Deposition of the copper films has been carried out *via* decomposition of copper containing compounds, such as copper acetylacetonates[2] in addition to others[3]. The relatively high temperatures required for these decompositions result in many routes resulting in oxide formation,[2/4] with pure copper metal acquired after a reductive post treatment[5]. In-situ prevention of copper oxide formation usually involves incorporating hydrogen gas or other reducing agent into the decomposition process[6]. The production of Cu_2O and CuO thin films is an area of huge significance due to their semiconducting properties, Cu_2O and CuO are both p-type semiconductors with a 2.0 eV and 1.21-1.51 eV band gaps with cubic and monoclinic crystal structures respectively.[7] Methods for the generation of Cu_2O and CuO thin films include – thermal oxidation[3], CVD[8], sputtering[9], electrolysis[10], as well as others[11/12]. Most of these techniques result in a mixture of copper metal and oxides with only a limited amount of control over what copper species is formed.

4.1.1 Thin Films of Copper via CVD

Many forms of CVD have been used to deposit metal oxide films[13/14] – including atmospheric pressure CVD[15], aerosol assisted CVD (AACVD)[16], plasma assisted CVD[17] and hybrid CVD[18]. The CVD of metal oxide films is readily achieved as the activation of precursors is usually a thermal process, with the high temperatures directing the synthesis toward the thermodynamically stable oxidised films.[19] Metallic films can be formed via similar CVD methods with the use of less reactive metal species[20/21], the use of low temperatures[22/23] or the introduction of reducing agents during depositions[5/6]. Copper organometallics such as copper acetylacetonates are among the most commonly used CVD precursors to deposit copper films. These types of precursors are frequently utilised as they are readily available, easy to handle and relatively volatile.[24-31] The use of these precursors can result in the deposition of copper films with mixed or hard to control oxidation states[32/33]. Copper salts, including CuI_2 and $[Cu(NO_3)_2]$, have been used for CVD depositions (as volatile precursors). However due to the high temperatures required for vaporisation or decomposition copper oxides were readily formed.[34/35]

4.1.2 Copper in Hydrophobic Surfaces

The modification of copper substrates with oxidising reagents is an established route to forming highly rough surfaces. The post treatment of these modified surfaces with long-chain thiols renders the surfaces exceptionally hydrophobic by lowering the surface energy.[36-38] It is the combination of the

surface roughness and lowering of surface energy (with respect to water) that result in the extremely high water repellency.[39/40]

This chapter describes the deposition of copper metal and cuprous oxide *via* a single step AACVD process, with thin film composition able to be altered by varying reaction conditions. The thin films morphology, phase and deposition route were all investigated. The metallic copper films generated were also rendered superhydrophobic after they were roughened and functionalised via a post-treatment with reducing agent and fluorinated thiol. In essence a three-step variation of two-step routes discussed in Chapter 1.

4.2. Experimental Details

4.2.1 Materials

All chemicals used in this investigation were purchased from Sigma-Aldrich Chemical Co; including copper nitrate trihydrate, potassium persulfate, sulphuric acid, methanol and ethanol.

4.2.2 Precursor Solutions

Copper nitrate trihydrate ($[Cu(NO_3)_2.3H_2O]$, 0.5 g) was added to 50 mL of solvent (methanol, ethanol or water). Upon addition, the mixture was left to stir for 5 minutes and used immediately for the AACVD deposition.

4.2.3 AACVD of $[Cu(NO_3)_2.3H_2O]$ Solutions

The depositions were carried out in a cold-walled horizontal-bed CVD reactor. The reactor contained a top and bottom plate for deposition to occur, both composed of SiO_2 barrier glass (dimensions: 145 x 45 x 5 mm) supplied by Pilkington NSG. Deposition was carried out on the barrier layer to prevent possible ion transfer from the bulk glass. A carbon block under the bottom plate heated the CVD reactor. The top plate was positioned 8 mm above and parallel to the bottom plate, the complete assembly was enclosed within a quartz tube. The aerosol of the precursor solution was generated using a PIFCOHEALTH ultrasonic humidifier with an operating frequency of 40 kHz and 25 W of power. The aerosol generated was moved to the reactor using a nitrogen gas flow *via* PTFE and glass tubing, where it entered between the top and bottom plate. The reactor waste gas left *via* an exhaust.

The flow of nitrogen carrier gas transported the vapour from the flask until all liquid was spent; this took typically 60 min. The flow of nitrogen was maintained at 1.0 L/min. The reactor's heating was continued for a further 10 min after the deposition and then switched off, the flow of nitrogen was continued until cool. The cooled plates were removed and handled in air. The film deposition occurred on the bottom plate. The temperature of the bottom plate was varied between 300–550°C with corresponding changes in film composition determined.

4.2.4 Film Characterisation

The films were analysed while adhered to the glass substrate. Field emission SEM analysis of the films was carried out using a Jeol JSM- 6301F operating at 5kV. EDX analysis was also carried out on the same machine using an operating frequency of 10 kV. Powder X-ray diffraction (XRD) patterns were measured on a Brucker D8 discovery instrument using monochromated Cu Kα radiation (λ = 1.5406 Å) in the reflection mode. Raman spectra were taken over the range 400-4000 cm^{-1} on a Renishaw Raman System 1000 using a helium-neon laser (λ = 532 nm) calibrated against the emission lines of neon. UV-vis spectra were taken using a Perkin Elmer Lambda 25 UV/VIS Spectrometer single beam instrument over a range of 300-1000 nm. Adherence/Scratch tests were carried out using Scotch Home and Office masking tape and a metal scalpel.

4.2.5 Functionalisation of Copper Metal Films

Copper films were submerged in dilute HCl for 2 mins. The samples were then immersed in an aqueous solution of potassium persulfate (0.06 M) and sulphuric acid (1.2 M) for 20 mins and then washed with water and air dried. The resulting films were then submerged in a solution of perfluorodecanethiol (0.025 M) in toluene. This thiol was chosen as it is a fluorinated equivalent of a widely used species to modify similar copper surfaces[36]. The samples were removed from the solution, washed with toluene and air dried. This process was also carried out on 2 mm thick copper plate for comparison.

4.2.6 Surface Hydrophobicity Measurements

Water contact angles were measured using an FTA-100-B Automated Drop Shape Analyzer, 3 μL water droplets were used to minimise any gravitational effects. The water droplet images were analysed using a digital protractor to obtain the contact angles on the surface. The surfaces were tested from a range of areas over the substrate plate. Water slip angles were also measured by noting the angle to the horizontal at which a water droplet of known volume moved on the surface. Spots from many positions were measured from each surface.

4.3. Results and Discussion

4.3.1 AACVD of $[Cu(NO_3)_2.3H_2O]$ in Methanol

4.3.1.1 Film Appearance and Substrate Adhesion

All films were uniformly deposited over the bottom substrate, and all were well adhered to the substrate remaining attached after the action of Scotch tape, with minimal damage observed after the use of a scalpel on films deposited at 300°C and 350°C. Films deposited at 300°C and 350°C appeared

red/brown in reflected light (Figure 4.02). Transmitted light passing through the films transmitted green. The deposition carried out at 350°C reflected more light and appeared less transparent and was also less green in transmittance (relative to that deposited at 300°C). Films deposited at and above 400°C were transparent and appeared yellow/brown in reflected light (Figure 4.02).

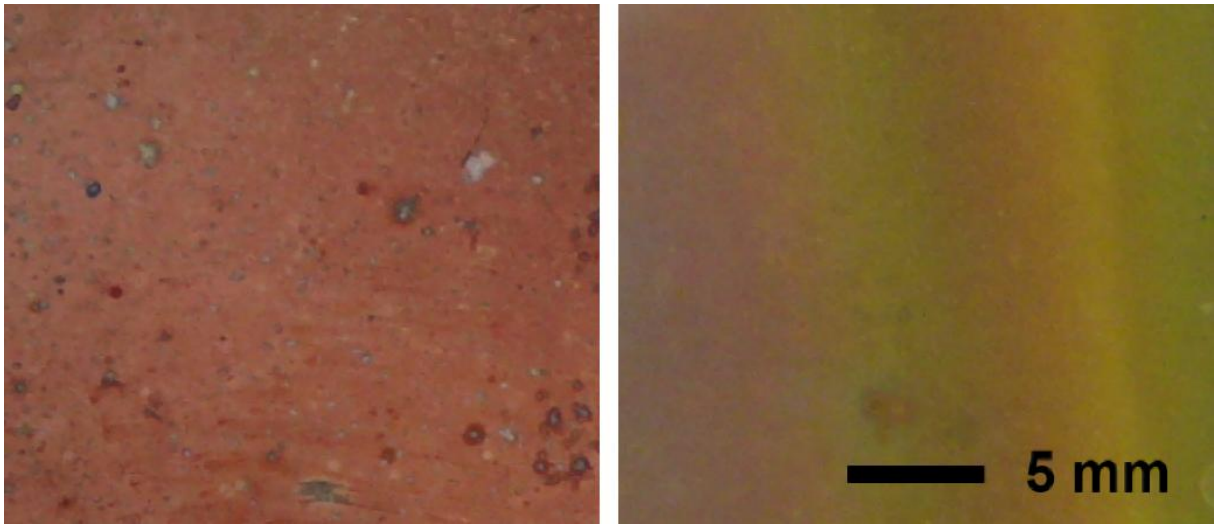

Figure 4.02. Photograph showing films deposited using [$Cu(NO_3)_2.3H_2O$] in methanol at a deposition temperature of 350°C (left) and 450°C (right). Scale bar shown.

4.3.1.2 Surface Microstructure

SEM was used to image the films (Figure 4.03), the surface structure depended strongly on the deposition temperature. The low temperature (300°C /350°C) depositions showed large surface features indicating an island growth mechanism in these conditions. At higher deposition temperatures the surface features became smaller in size and these particles were less distinct. This change in surface morphology may be due to the deposited material having a different crystal structure (*vide infra*).

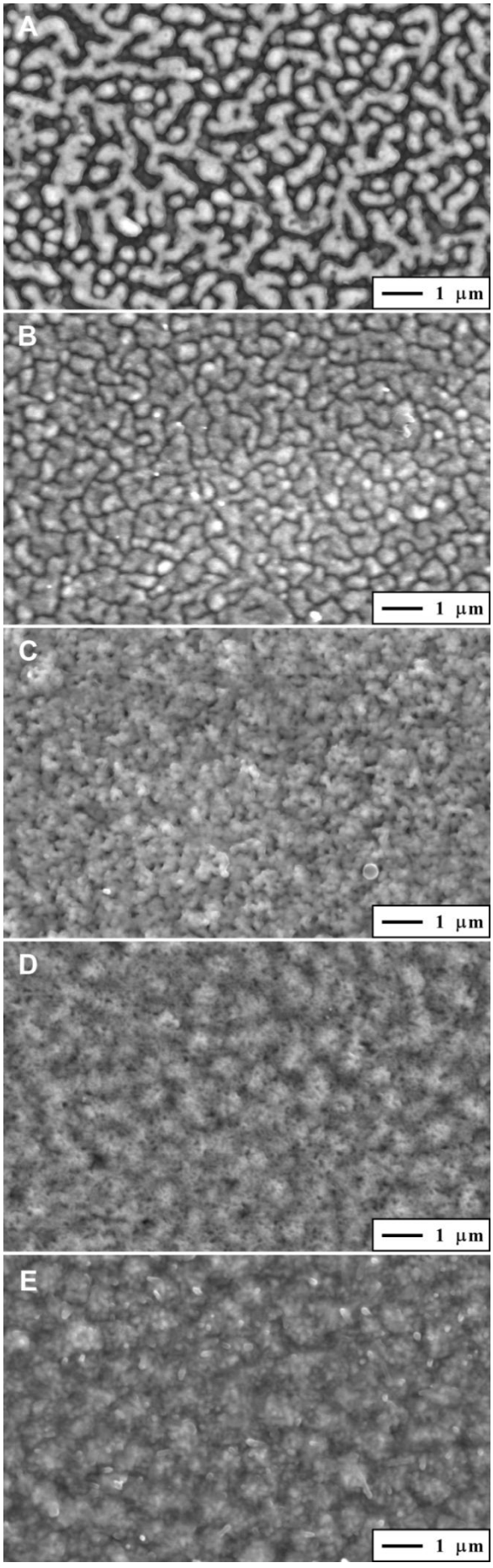

Figure 4.03. SEM images of films deposited via the AACVD of $[Cu(NO_3)_2.3H_2O]$ in methanol using substrate temperatures of (A) 300°C, (B) 350°C, (C) 400°C, (D) 450°C and (E) 500°C.

4.3.1.3 Phases Deposited

The elemental composition of the films deposited could be controlled by simply varying the substrate temperature (Figure 4.04). Substantial deposition only occurred above 300°C, with a mixture of copper metal and Cu_2O being formed at this temperature. A film of copper metal was obtained at a temperature of 350°C, and was also shown to be electrically conductive (less than 2Ω resistance registered on an ammeter). A slight presence of Cu_2O was observed using XRD, but this could however be due to reaction at the boundary with the glass substrate[41]. EDX analysis confirmed copper metal and a very low proportion of Cu_2O, less than 2%. The Cu_2O character of the film increased with deposition temperature, CuO did not appear in any depositions. Reflections relating to copper metal were not apparent in the depositions at 450°C and 500°C.

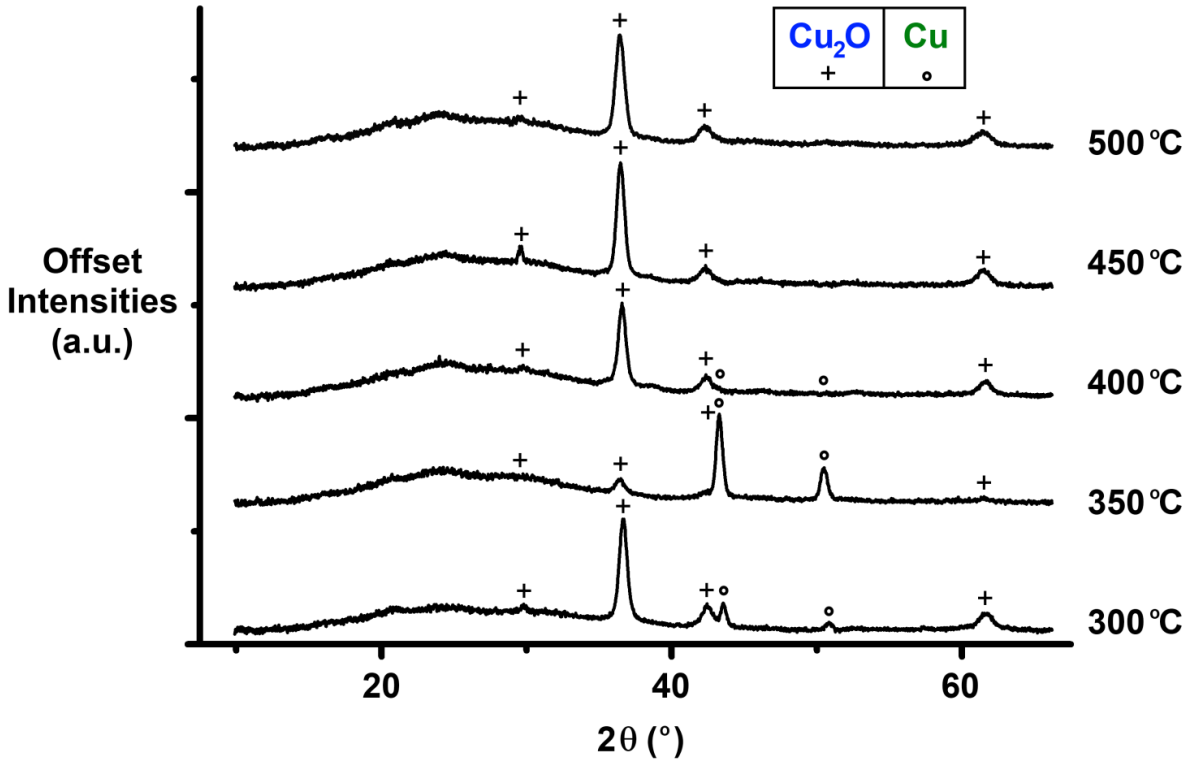

Figure 4.04. XRD of films deposited *via* the AACVD of $[Cu(NO_3)_2.3H_2O]$ in methanol at the associated substrate temperatures. Peaks positions relating to Cu and Cu_2O are marked.

The deposition of metallic copper films usually takes place at lower temperature than those achieved *via* the method described in this chapter[42], with elevated temperature resulting in oxide formation (Cu_2O/ CuO).[35/43] The formation of Cu_2O at 350°C was prevented by the flow of nitrogen through the reactor during substrate cooling, when nitrogen flow was terminated prior to cool-down Cu_2O films would result due to the heated copper film oxidising once exposed to air (Figure 4.05). The hydrophobicities of the films were also tested with copper metal surfaces formed at 350°C, the water

contact angles averaged 87° prior to any alteration. All other films gave more hydrophilic water contact angles; between 30-75°.

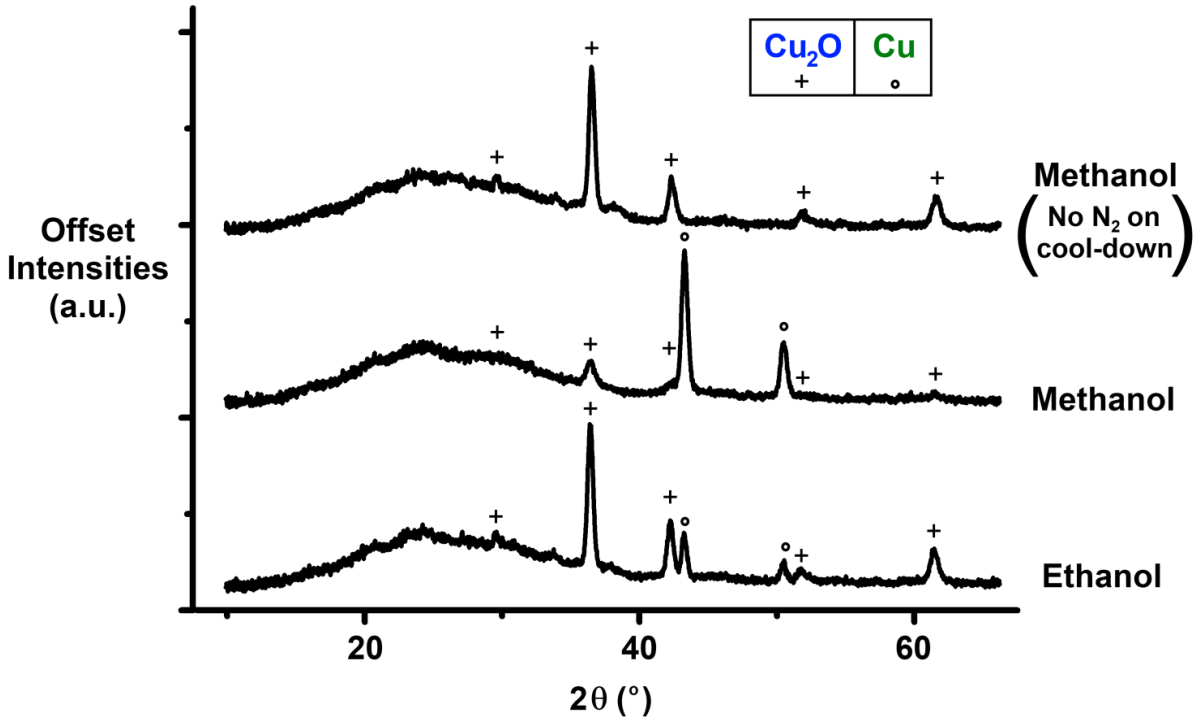

Figure 4.05. XRD of films deposited via the AACVD of $[Cu(NO_3)_2.3H_2O]$ using a 350°C substrate temperatures, (lower) in ethanol with nitrogen (middle), in methanol with nitrogen and (upper) in methanol with no nitrogen gas flowing through the reactor during cooling of the substrates.

4.3.2 AACVD of $[Cu(NO_3)_2.3H_2O]$ in Ethanol and Water

The films deposited using ethanol as a solvent were carried out using exactly the same conditions as the methanol CVD experiments. All films generated appeared brown/yellow in appearance; films showed a partial redness for films deposited at 300°C/350°C. The adherence of the films was relatively poor compared to the methanol depositions, surviving action by Scotch tape. However the films were removed with the action of the scalpel. The surface morphologies (examined by SEM) were similar to those observed in the depositions that used methanol. The glancing angle XRD of the films confirmed them to be Cu_2O. The presence of copper metal was observed for depositions taking place at 300°C/350°C (Figure 4.05).

The generation of copper metal films at 350°C substrate temperature suggests a reducing environment. *In-situ* hydrogen generation has been reported *via* decomposition of methanol over copper[44]:

$$CH_3OH \leftrightarrow C + H_2 + H_2O \qquad \Delta H^0_{298} = -42\ \text{kJ mol}^{-1}$$

$$CH_3OH \leftrightarrow CO + H_2 \qquad \Delta H^0_{298} = 49\ \text{kJ mol}^{-1}$$

Formation of copper metal was highly unexpected, as methanol is commonly used as a solvent in AACVD depositions as a successful oxygen source for many depositions.[45-47] The expected thermodynamic product of copper nitrate decomposition would be Cu_xO. The combination of a low temperature deposition and a potentially reducing atmosphere allows for the formation of copper metal. The failure to generate metallic copper in great abundance at 350°C while using ethanol suggests a less reducing atmosphere. The catalytic breakdown of ethanol to form hydrogen has been shown to be less efficient than that of methanol.[48] A more reducing atmosphere during the reactions occurs while using methanol solvent, due to a more efficient production of hydrogen, as a result predominantly copper metal films are formed.

4.3.3 Functionalisation of Copper (0) Films

4.3.3.1 Film Properties

The treatment of copper metal films formed by AACVD with the $NaOH/K_2S_2O_8$ solution resulted in uniform coverage of the coatings with nanoscale crystals, approximately 200 nm in length and 50 nm in diameter (Figure 4.06). The crystals were confirmed to be $Cu(OH)_2$ by XRD. The formation of the nano-crystal films had an effect on the films robustness, as they survived Scotch tape; however they were removed by the action of a scalpel. The surfaces reflected green light upon oxidation, and showed no further visible change upon functionalisation with perfluorodecanethiol. The surface features are relatively small when compared to the same treatment when applied to 2 mm thick copper plates (Figure 4.06). The causes of differences observed in surface structures stem from the thickness of the deposited material, confirmed to be approximately 400 nm at the thickest part of the metallic films (cross-sectional SEM), in addition to the microstructure of copper film deposited driving small crystallite growth. The treatment of copper plates provided a substantial amount of material and no grain boundaries which facilitated the formation of large surface features. However the lack of material and microstructure of the films on the AACVD substrates limited the growth of $Cu(OH)_2$ crystals and thus surface features are relatively small.

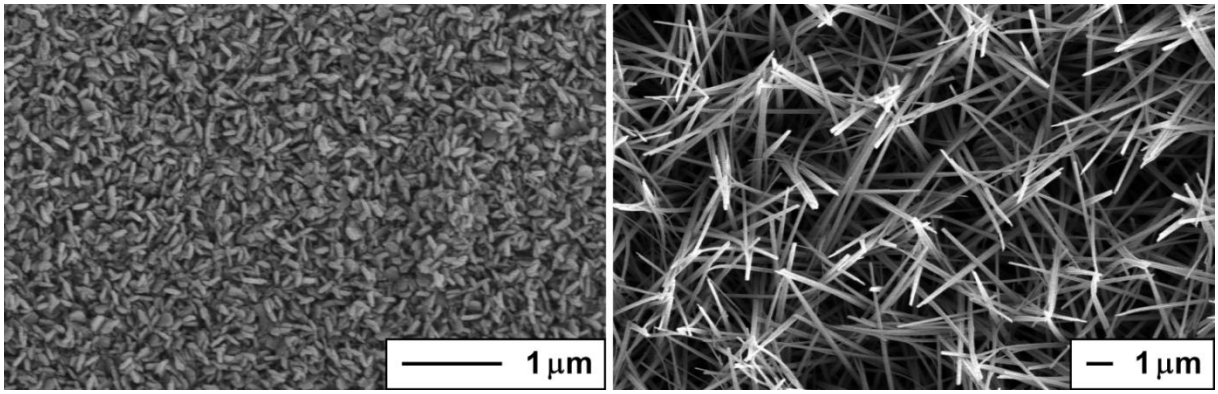

Figure 4.06. SEM image of $Cu(OH)_2$ nano-crystals formed by immersing copper metal surfaces in $NaOH/K_2S_2O_8$ solution for 20 mins – (left) copper deposited by AACVD and (right) copper plate. Scale bars inset.

4.3.3.2 Hydrophobicity

Upon formation of $Cu(OH)_2$ nano-crystals the water contact angle decreased to approximately 10°, from the 87° observed on the copper metal films. Functionalisation of the nano-crystals with thiol resulted in a surface that demonstrated near perfect hydrophobicity – water contact angles approached 180° (Figure 4.07) and tilt angles were less than 1°. The highly rough nano-structure of the coating allows air to be trapped under the water droplet as it lies on the surface; this minimises any water-surface contact. The perfluorodecanethiol lowers the energy of interaction at any points where contact is made (Figure 4.08). The combination of highly rough surface and very low energy of interaction results in a surface that is highly water repellent, requiring a particularly level surface to support a static water droplet. The surface facilitates elastic bouncing of water droplets which is exhibited by extremely hydrophobic surfaces. Depositions on substrates *via* CVD usually occur in a conformal manner, coating all the substrate uniformly; the deposition route discussed in this chapter demonstrates an island growth pattern (Figure 4.03). Subsequent functionalisation of copper films could be employed on substrates with pre-existing microscale roughness, and would provide dual-scale roughness upon nano-crystal synthesis which would elevate surface hydrophobicity even further.[49]

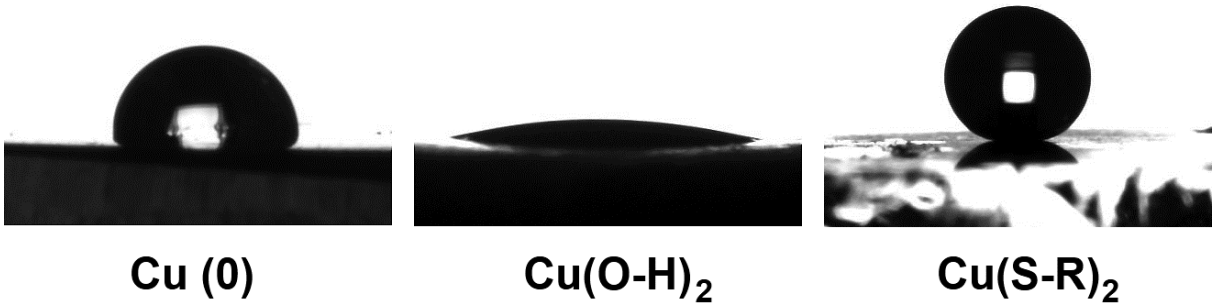

Figure 4.07. Water droplets (3μL) on copper deposited by AACVD, $Cu(OH)_2$ nano-crystals formed by oxidising copper and thiol-functionalised $Cu(OH)_2$ nano-crystal films.

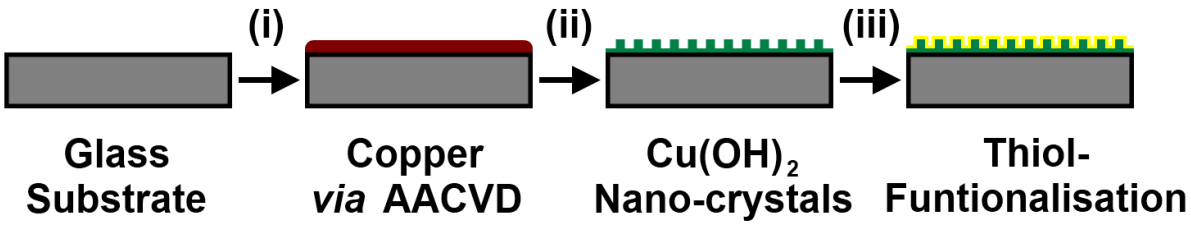

Figure 4.08. Schematic showing the deposition and functionalisation steps of copper coating. (i) AACVD of $[Cu(NO_3)_2.3H_2O]$ using a substrate temperature of 350°C, (ii) Oxidation of copper with potassium persulfate and sulphuric acid solution and (iii) functionalisation of surface using a toluene solution of perfluorodecanethiol.

4.4. Conclusions

Near perfect superhydrophobic films were synthesised *via* a simple solution-based functionalisation of copper metal films deposited using AACVD. *In-situ* decomposition of alcohols during the CVD process provided a reducing atmosphere facilitating the formation of copper metal films from copper nitrate precursors. The compositions of copper films could be controlled by the substrate temperature and solvent used, with copper metal or Cu_2O films deposited. The employed technique is a facile method for generating copper films with potential applications in metallic of semiconductor coatings, dependant on deposition conditions. The conformal coverage of CVD depositions combined with depositions on roughened substrates would provide a dual-scale roughness and improved hydrophobicity.

4.5. References

1. R. Becker, A. Devi, J. Weiß, U. Weckenmann, M. Winter, C. Kiener, H. Becker and R. A. Fischer, *Chem. Vap. Deposition*, 2003, **9**, 149.
2. B. Wisniewski, J. Durand and L. Cot, *J. Phys. II*, 1991, **1**, 389.
3. B. T. Collins, W. Desisto, R. Kershaw, K. Dwight and A. Wold, *J. Less Common Met.*, 1989, **156**, 341.
4. Z.H. Gan, G. Q. Yu, B. K. Tay, C. M. Tan, Z. W. Zhao and Y. Q. Fu, *J. Phys. D: Appl. Phys.*, 2004, **37**, 81.
5. D. R. Sparks and G. M. Vest, *Thin Solid Films*, 2001, **200**, 77.
6. H. Ko, J. Jhin, D. Byun, J. Lee and D. Park, *IEEE Trans. Compon. Packag. Technol.*, 2005, **28**, 781.
7. G. Papadimitropoulos, N. Vourdas, V. Em Vamvakas and D. Davazoglou, *J. Phys. Conf. Ser.*, 2005, **10**, 182.
8. X. Lin, Q. Wang, S. Wu and Z. Liu, *J. Electrochem. Soc.*, 2006, **153**, C142.
9. G. Correa and R. Almanza, *Sol. Energy*, 2004, **76**, 111.
10. M. R. Madjidi, K. Asadpour-Zeynali and B. Hafezi, *Int. Electrochem. Sci.*, 2011, **6**, 162.
11. H. Y. H. Chan, C. G. Takoudis and M. J. Weaver, *J. Phys. Chem. B*, 1999, **103**, 357.
12. S. W. Ko, T. Dechakupt, C. A. Randall, S. Trolier-McKinstry, M. Randall and A. Tajuddin, *J. Electroceram.*, 2010, **24**, 161.
13. R. Gordon, *J. Non-Cryst. Solids*, 1997, **218**, 81.

14. K. L. Choy, *Prog. Mater. Sci.*, 2003, **48**, 57.
15. A. Kafizas and I. P. Parkin, *J. Mater. Chem.*, 2010, **20**, 2157.
16. M. R. Waugh, G. Hyett and I. P. Parkin, *Chem. Vap. Deposition*, 2008, **14**, 366.
17. J. A. Babcock, S. G. Balster, A. Pinto, C. Dirnecker, P. Steinmann, R. Jumpertz and B. El-Kareh, *IEEE Electron Device Lett.*, 2001, **22**, 230.
18. R. Binions, C. Piccirillo, R. G. Palgrave and I. P. Parkin, *Chem. Vap. Deposition*, 2008, **14**, 33.
19. P. A. Williams, A. C. Jones, N. L. Tobin, P. R. Chalker, S. Taylor, P. A. Marshall, J. F. Bickley, L. M. Smith, H. O. Davies and G. W. Critchlow, *Chem. Vap. Deposition*, 2003, **9**, 309.
20. R. G. Palgrave and I. P. Parkin, *Chem. Mater.*, 2007, **19**, 4639.
21. A. Grodzicki, I. Łakomska, P. Piszczek, I. Szymańska and E. Szłyk, *Coord. Chem. Rev.*, 2005, **249**, 2232.
22. D. W. Sheel and J. L. Hodgkinson, *Plasma Processes Polym.*, 2007, **4**, 537.
23. N. Bahlawane, P. A. Premkumar, Z. Tian, X. Hong, F. Qi and K. Kohse-Höinghaus, *Chem. Mater.*, 2010, **22**, 92.
24. P. Piszczek, I. Szymańska, W. Bała, K. Bartkiewicz, E. Talik and J. Heiman, *Thin Solid Films*, 2008, **516**, 3924.
25. P. A. Premkumar, N. Bahlawane and K. Kohse-Höinghaus, *Chem. Vap. Deposition*, 2007, **13**, 219.
26. P. A. Premkumar, N. Bahlawane, G. Reiss and K. Kohse-Höinghaus, *Chem. Vap. Deposition*, 2007, **13**, 227.
27. F. Maury, S. Vidal and A. Gleizes, *Adv. Mater. Opt. Electron.*, 2000, **10**, 123.
28. W. Zhuang, L. J. Charneski, D. R. Evans, S. T. Zhu, Z. Tang and A. M. Guloy, *J. Phys. IV*, 2001, **11**, 553.
29. J. A. T. Norman, *J. Phys. IV*, 2001, **11**, 497.
30. R. Becker, J. Weiß, A. Devi and R. A. Fischer, *J. Phys. IV*, 2001, **11**, 569.
31. R. Becker, A. Devi, J. Weiß, U. Weckenmann, M.Winter, C. Kiener, H. Becker and R. A. Fischer, *Chem. Vap. Deposition*, 2003, **9**, 149.
32. D. Barreca, A. Gasparotto, C. Maccato, E. Tondello, O. I. Lebedev and G. Van Tondello, *Cryst. Growth Des.*, 2009, **9**, 2470.
33. J. Medina-Valtierra, J. Ramírez-Ortiz, V. M. Arroyo-Rojas, P. Bosch and J. A. de los Reyes, *Thin Solid Films*, 2002, **405**, 23.
34. M. Ottosson and J. Carlsson, *Surf. Coat. Technol.*, 1996, **78**, 263.
35. H. M. Yates, L. A. Brook, D. W. Sheel, I. B. Ditta, A. Steele and H. A. Foster, *Thin Solid Films*, 2008, **517**, 517.
36. Q. Pan, M. Wang and H. Wang, *Appl. Surf. Sci.*, 2008, **254**, 6002.
37. C. Wang, T. Yao, J. Wu, C. Ma, Z. Fan, Z. Wang, Y. Cheng, Q. Lin and B. Yang, *ACS Appl. Mater. Interfaces*, 2009, **1**, 2613.
38. X. Wu and G. Shi, *J. Phys. Chem. B*, 2006, **110**, 11247.
39. R. N. Wenzel, *Ind. Eng. Chem.*, 1936, **28**, 988.
40. A. B. D. Cassie and S. Baxter, *Trans. Faraday Soc.*, 1944, **40**, 546.
41. G. P. Schwartz, J. E. Griffiths and G. J. Gualtier, *Thin Solid Films*, 1982, **94**, 213.

42. W. Xu, J. S. Yang and T. J. Lu, *Mater. Des.*, 2011, **32**, 154.
43. A. Y. Oral, E. Menşur, M. H. Aslan and E. Başaran, *Mater. Chem. Phys.*, 2004, **83**, 140.
44. S. D. Jackson, D. S. Anderson, G. J. Kelly, T. Lear, D. Lennon and S. R. Watson, *Top. Catal.*, 2003, **22**, 173.
45. C. Edusi, G. Hyett, G. Sankar and I. P. Parkin, *Chem. Vap. Deposition*, 2011, **17**, 30.
46. S. Ashraf, C. S. Blackman, R. G. Palgrave, S. C. Naisbitt and I. P. Parkin, *J. Mater. Chem.*, 2007, **17**, 3708.
47. A. A. Tahir, K. G. U. Wijayantha, M. Mazhar and V. McKee, *Thin Solid Films*, 2010, **518**, 3664.
48. S. R. Segal, K. A. Carrado, C. L. Marshall and K. B. Anderson, *Appl. Catal., A*, 2003, **248**, 33.
49. B. Cortese, S. D'Amone, M. Manca, I. Viola, R. Cingolani and G. Gigli, *Langmuir*, 2008, **24**, 2712.

Chapter 5

Bacterial Adhesion to Superhydrophobic Polymer Surfaces

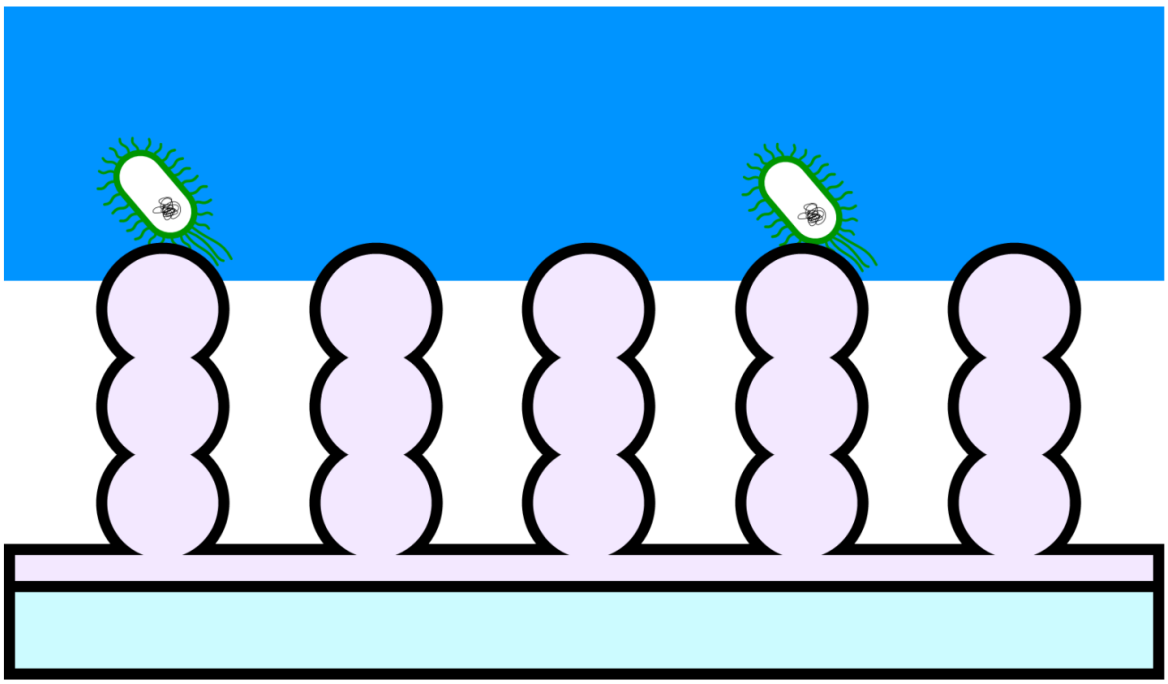

Figure 5.01. Schematic showing the interaction of a bacterial suspension and a superhydrophobic surface.

5. Bacterial Adhesion to Superhydrophobic Polymer Surfaces

5.1. Introduction

The prevention of bacterial adherence to surfaces is of the upmost importance to many industries, especially in healthcare and food production.[1] The ease of bacterial attachment, colony growth and biofilm formation is directly linked to surface acquired infections.[2] Recent developments in the area of preventing surface acquired infection include incorporating antimicrobial agents[3] and species that promote irradiative killing of bacteria into surface materials[4/5]. These materials are aimed toward killing any bacteria on a surface. This approach could result in a coating of dead bacteria which would inhibiting further killing while providing a favourable platform for subsequent bacterial attachment[6] (Figure 5.02).

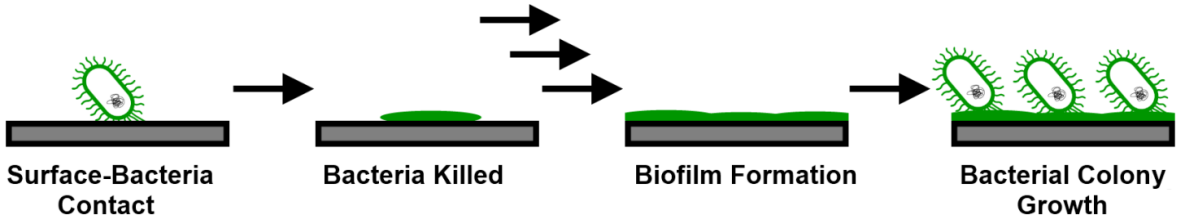

Figure 5.02. Schematic showing the action of an anti-microbial surface on bacteria. The repeated killing of bacteria leads to a coating of dead bacteria ideal for the growth of bacterial colonies.

There is therefore a considerable scientific interest in manufacturing a surface which prevents bacteria coming into contact with it, and stopping any bacterial adherence. These types of surfaces can be found in nature[7]. The Lotus plant, *Nelumbo nucifera*, as well as other plant species has specially adapted leaves that repel water, so much so that they are superhydrophobic, with water forming balls and not spreading. These leaves are very rough incorporating their roughness over two different length scales (large surface protrusions with smaller hairs emanating from them), and also have a waxy film which is naturally hydrophobic. These two factors act to trap air underneath a water droplet as it lies on the surface, which increases surface hydrophobicity and also renders the surface "slippery"[8/9]. The balls of water on the leaves thus roll and spin across the surface. As this occurs, dirt and bacteria particles are picked up by the droplet, which moves off from the leaf taking the bacteria with it, thus this effect is termed the "Lotus Effect"[8]. A surface with similar properties could thus prevent any contact with bacteria in an aqueous environment. Bacterial adhesion to plant leaves including the Lotus plant as well as others is well known[10/11]. However many manufactured superhydrophobic surfaces are yet to undergo microbiological investigation.

Surfaces manufactured in this area are aimed toward biomimetics; surfaces that are designed to replicate Lotus effect self-cleaning by forming materials similar to that of the Lotus leaf and/or other superhydrophobic surfaces in nature[12]. The most basic examples of this are moulds taken of the

leaves which are then used to cast replica surfaces from hydrophobic (low energy) materials[13]. Most manufactured materials take only the main principles from examples found in nature[14/15], making surfaces from a low energy material with a highly developed microstructure, and some incorporating two different length scales in roughness[16/17].

The previous chapters describe the synthesis of hydrophobic surfaces. The surfaces investigated in this chapter were constructed from the curable silicone elastomer (Sylgard 184) as described in Chapter 2 using AACVD (Section 2.1). The elastomer is inherently hydrophobic, with a water contact angle of 95° being achieved on a flat surface. The AACVD depositions allow the formation of a network of polymer surface protrusions approximate 3 μm in height. The surface protrusions allow water to sit on them, thus trapping air underneath, resulting in a surface that mimics the Lotus leaf surface and Lotus effect self-cleaning. This investigation looks specifically at bacterial adhesion on the surface compared to control materials.

5.2. Experimental Details

5.2.1 Materials

The chemicals used in this investigation were acquired as follows; purchased from Sigma-Aldrich Chemical Co; chloroform and phosphate buffered saline (PBS). Columbia Blood Agar Base and Brain Heart Infusion (BHI) Broth were both purchased from Oxoid Ltd. BacLight Bacterial Viability Stain was purchased from Invitrogen Ltd. Sylgard 184 Silicone Elastomer was purchased from R. W. Greeff.

5.2.2 Sylgard 184 Precursor Solutions

Sylgard 184 (0.50 g) was dissolved in chloroform (50 mL) with rapid stirring for 5 min. In order to prevent premature curing the mixture was used immediately after stirring for deposition studies.

5.2.3 Dip-coating of Microscope Slides

Cut-edged microscope slides purchased from VWR International (71 x 21 x 1 mm) were cut into three equally sized portions (23.6 x 21 x 1 mm). Each of these glass slide portions was submerged in a chloroform: Sylgard 184 mixture (2:1) and withdrawn at an arbitrary rate (*ca*. 0.5 mm/s). The coated substrates were laid horizontally in a vacuum desiccator kept at room temperature and left to cure for 48 h. The upward-facing side of the coated glass was subsequently used in the AACVD process or underwent bacterial adherence tests.

5.2.4 AACVD of Sylgard 184 onto Polymer-Coated Microscope Slides

The AACVD depositions were carried out in a cold-walled horizontal-bed CVD reactor. The reactor contained top and bottom glass plates, both with SiO_2 coated barrier glass (dimensions: 145 x 45 x 5 mm; barrier thickness 50 nm) supplied by Pilkington NSG. A carbon block on which the bottom plate was placed heated the CVD reactor. The top plate was positioned 8 mm above and parallel to the bottom plate, the complete assembly was enclosed within a quartz tube. Dip-coated glass slides were pressed onto the top plate, placed 35 mm away from the reactor inlet to ensure conformal coverage of all portions, the slides were held in place by the natural adhesiveness of the cured elastomer (schematic shown in Figure. 5.03). The aerosol of the precursor solution was generated using a PIFCO HEALTH ultrasonic humidifier operating with a frequency of 40 kHz and with 25 W of power. The generated aerosol was moved to the reactor using a nitrogen gas flow *via* PTFE and glass tubing, where it entered between the top and bottom plates. The reactor waste gas left *via* an exhaust.

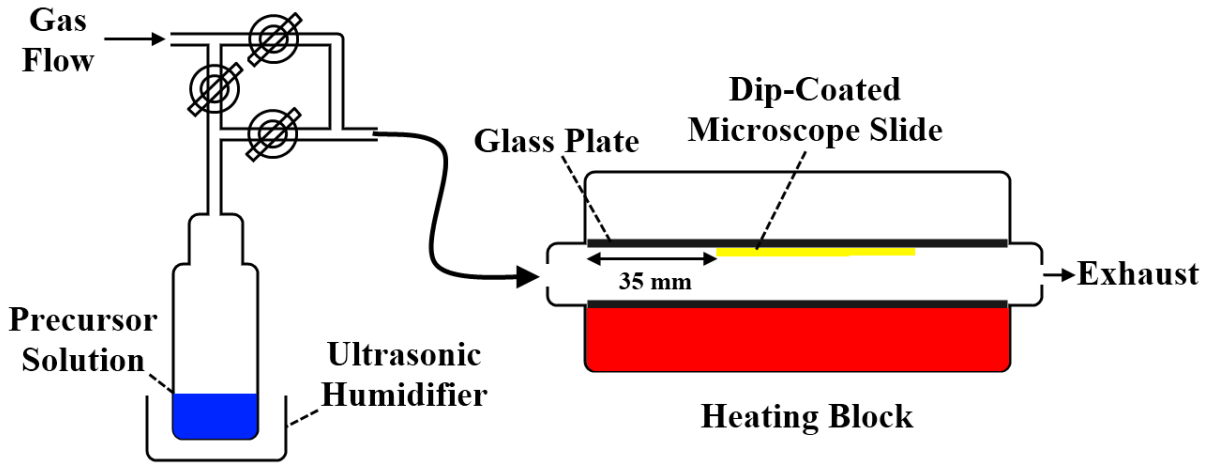

Figure 5.03. Schematic of the AACVD apparatus, shown is the position of the polymer coated microscope slides. The edge of the first slide is positioned 35 mm away from the reactor inlet, in the middle of the top plate.

The nitrogen flow carried the vapour from the flask until all liquid was gone, typically taking 30–35 min for a deposition. The heater was then turned off and allowed to cool to room temperature, the nitrogen flow was left on for a further 10 min. The cooled plates were removed and handled in air, the film was deposited on the top plate and the attached microscope slides. The reactor temperature, as measured by a thermocouple in the carbon heater block was maintained at 360°C. Each experiment provided three microscope slide portions, these were removed from the top plate using a scalpel, which was slid between the two pieces of glass (Figure 5.04). These AACVD coated glass slides were used for bacterial adherence assays.

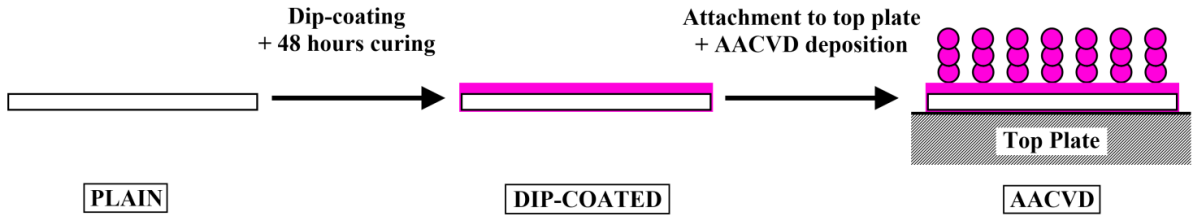

Figure 5.04. Schematic showing the film deposition process of microscope slide portions. The AACVD slide was removed from the top plate prior to microbiological testing.

5.2.5 Film Characterisation

The elastomer films were analysed as coatings on the microscope glass slide. Subsections (*ca* 1 x 1 cm) of the samples were gold-sputtered and analysed using field emission scanning electron microscopy (SEM) using a Jeol JSM-6301F operating at 5 kV. IR spectroscopy was employed over the range of 2200–4000 cm^{-1} using a Perkin Elmer FT-IR (Fourier transform infrared) Spectrum RX1 instrument. Raman measurements were made using a Renishaw 1000 spectrometer which used a 632.8 nm laser. UV–visible absorption spectra were taken using a Perkin Elmer Lambda 25 UV/VIS Spectrometer single beam instrument over a range of 300–1000 nm. Adherence tests were carried out, done by applying Scotch Home and Office masking tape to the surface followed by its removal. Scratch tests were also carried out by observing the action of a metal scalpel being dragged across a surface.

5.2.6 Surface Hydrophobicity Measurements

Water contact angle measurements were also taken using a FTA-1000 drop shape instrument, 3 μL water droplets was used to minimise any gravitational effects. The water droplet images were analysed using a digital protractor to obtain the contact angles on the surface. Points from across the slides were tested from a range of areas over the substrate plate.

5.2.7 Bacterial Strains

The bacterial strains used in this study were *Escherichia coli* (ATCC 25922) and Methicillin-resistant *Staphylococcus aureus* (eMRSA-16). Both were maintained by weekly subculture on Columbia blood agar. For experimentation, a single colony was taken from a culture plate and inoculated into 10 mL of BHI broth and cultured overnight at 37 °C in air with constant rotation (200 rpm).

5.2.8 Bacterial Attachment Assay

For determining the ability of AACVD deposited surfaces to prevent or reduce bacterial adhesion, a live/dead attachment assay was developed. All standard microbiological-safety precautions were taken during the assessment of bacterial attachment. Bacteria from overnight BHI broth cultures were

centrifuged (8000 x g, 1 min) to collect cells and the pellet resuspended in an equal amount of PBS. The OD_{600} of this cell suspension was adjusted to an absorbance of 0.05 to give an approximate titre of 1×10^7 colony-forming unit/mL. Adjusted cell suspensions were aliquoted (30 mL) into sterile Petri dishes and a single glass slide of each type (uncoated, dip-coated and AACVD coated), placed into each 30 mL of bacterial suspension. Duplicate slides of each type were used per assay. Bacteria were allowed to statically attach to each surface in suspension for 1 hour, upon which time each slide was removed and serially washed twice in 50 mL of PBS by inversion to remove any non-adherent transient bacteria. Washed slides were placed into 30 mL of BacLight Bacterial Viability Stain at ambient temperature in the dark for 15 min. BacLight Bacterial Viability Stain was prepared by adding 3 μL each of component A and component B per 10 mL of PBS.

5.2.9 Fluorescence Microscopy

Bacteria attached to glass slides (uncoated, dip-coated and CVD coated) were visualized by fluorescence microscopy using an Olympus BX51 microscope equipped with a Chroma 61000v2 D/F/R C73315 DAPI, FITC and TRITC triple bandpass fluorescence mirror unit, excited using an Olympus U-RFL-T Mercury burner and a 60x water lens. Using this fluorescence filter, live bacteria fluoresce green while membrane compromised (dead) bacteria fluoresce red. Images of the field of view were taken using a QImaging MicroPublisher 5.0RTV camera and Simple PCI (Compix Inc. Imaging systems) image capturing software. For each slide type, 5–7 images of field of view were taken at incremental points along the length of the slide. The numbers of live and dead bacteria were enumerated per field of view for each image taken.

5.3. Results and Discussion

5.3.1 AACVD of Sylgard 184

The AACVD depositions were carried out in the same way as described in Chapter 2, with microscope slides introduced to facilitate the generation of consistent films for microbiological analysis (films deposited over larger barrier layer glass substrates showed a larger variation in film properties). The AACVD depositions occurred on the top plate inside the CVD reactor, which meant the slides had to be held in place. Methods of physical attachment such as clips caused patches of uncoated substrate at the securing points. However using dip-coated glass facilitated the natural stickiness of the elastomer to hold microscope slide portions in place on the top plate. The dip-coated slides had their backs (the sides which made contact with the vacuum desiccator during curing) pressed onto the top plate, applying slight pressure while in place, a residual amount of elastomer film was enough to adhere the slides. Upon heating during the depositions, the elastomer hardened slightly and the microscope slides became stuck to the top plate, they were however able to be removed *via* separation with a scalpel.

The elastomer pre-treatment was already shown to increase the physical robustness of the superhydrophobic films deposited *via* AACVD (Chapter 2). The physical appearance of the films on the microscope slide glass did not change relative to those deposited on silica barrier layer glass (confirmed by UV–Visible spectroscopy), appearing as a hazy white film. The infra-red spectroscopy also remained consistent with the films deposited on barrier layer glass, giving no indication of major alterations caused by ion migration from the microscope slide glass. The films were imaged using SEM, the images gained showed no noticeable differences from the films deposited onto silica barrier layer glass (Figure 5.05). The surface features, deposited *via* AACVD, did show a degree of integration into the elastomer coating the substrate. This increased attachment to the underlying substrate is most likely the reason for the observed greater physical resistance of the films, when compare to depositions on plain glass.

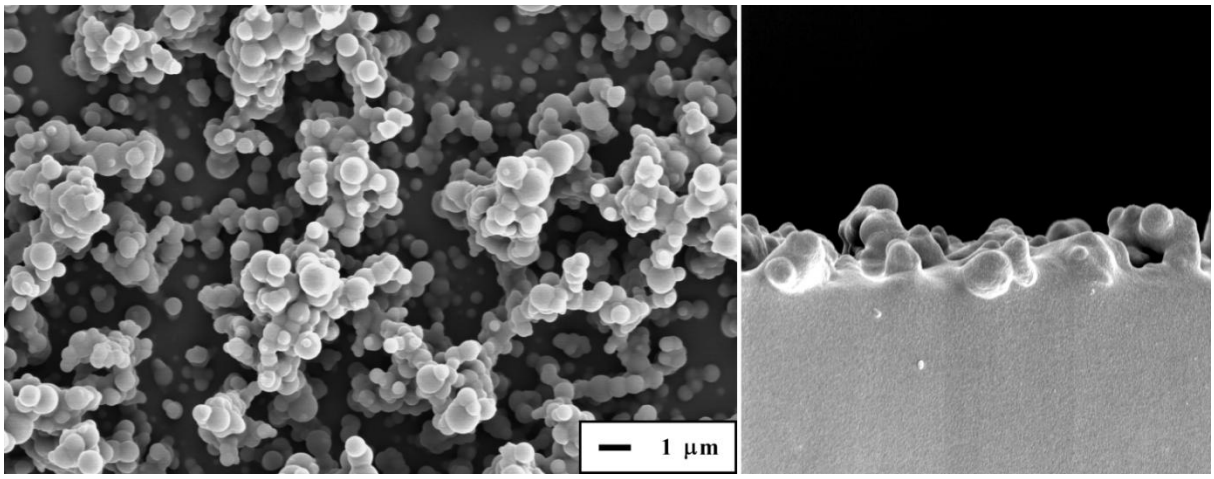

Figure 5.05. SEM images of a Sylgard 184 film deposited using AACVD using a deposition temperature of 360°C onto glass microscope slide substrates pre-treated with a dip-coated layer of the same elastomer, (left) from above (right) side-on. Partial integration of features deposited during AACVD into the elastomer coated substrate can be seen. Scale bar shown.

Water contact angle measurements of the microscope slides coated via AACVD were made prior to bacteria adherence testing (photograph of water droplet on the surface is shown in Figure 5.06). The average water contact angle achieved was 165° (with standard deviation = 1.31°), similar to the results observed on pre-coated barrier layer glass. All substrates gave consistent measurements independent of the microscope slide portion in the reactor. The consistently higher hydrophobicity was afforded by the pre-treated microscope slides. The interaction of water with the underlying substrate would be reduced due to the lower energy surface provided by the dip-coated polymer surface (water contact angle ~95°), relative to plain glass (water contact angle ~60°). Any faults in the protrusions on the surface may provide an opening for water to make contact with the surface. Therefore lessening the energy of this interaction has made the water contact angles more consistent.

Figure 5.06. Photograph showing a 10 μL water droplet on microscope slide coated with Sylgard 184 via dip-coating then AACVD.

5.3.2 Bacterial Attachment Investigation

E. coli and *S. aureus* were chosen for use in this study as they are two of the major causes of hospital acquired infections. These bacteria also demonstrate fundamental differences in cell wall structure and their use in this study will give further insight into their interaction with the surfaces. *E. coli* is a Gram-negative bacterium and *S. aureus* is a Gram-positive bacterium, and both are highly resistant to many antibiotics used in the treatment of infections.[4]

The adherence of *E. coli* to uncoated, dip-coated and AACVD coated glass was relatively low with total mean counts of only 38, 13 and 8 attached cells per field of view, respectively. The greatest level of *E. coli* adherence was to uncoated glass, while AACVD coated glass showed the least attachment (Figure 5.07). This amounted to a 79% reduction in adherence compared to uncoated glass and a 38% reduction in adherence compared to dip-coated glass. AACVD coated glass also showed the greatest proportion of dead cells (54.5%) of those that had attached. Dip-coated slides had an intermediate level of attachment and a live/dead cell ratio in between that of uncoated and AACVD coated glasses (Figure 5.07). These results demonstrate that the superhydrophobic surface of AACVD coated glass reduces the affinity of *E. coli* toward attachment, and that a large proportion of those cells that adhere to the surface cannot maintain sufficient membrane integrity and are observed as dead bacteria.

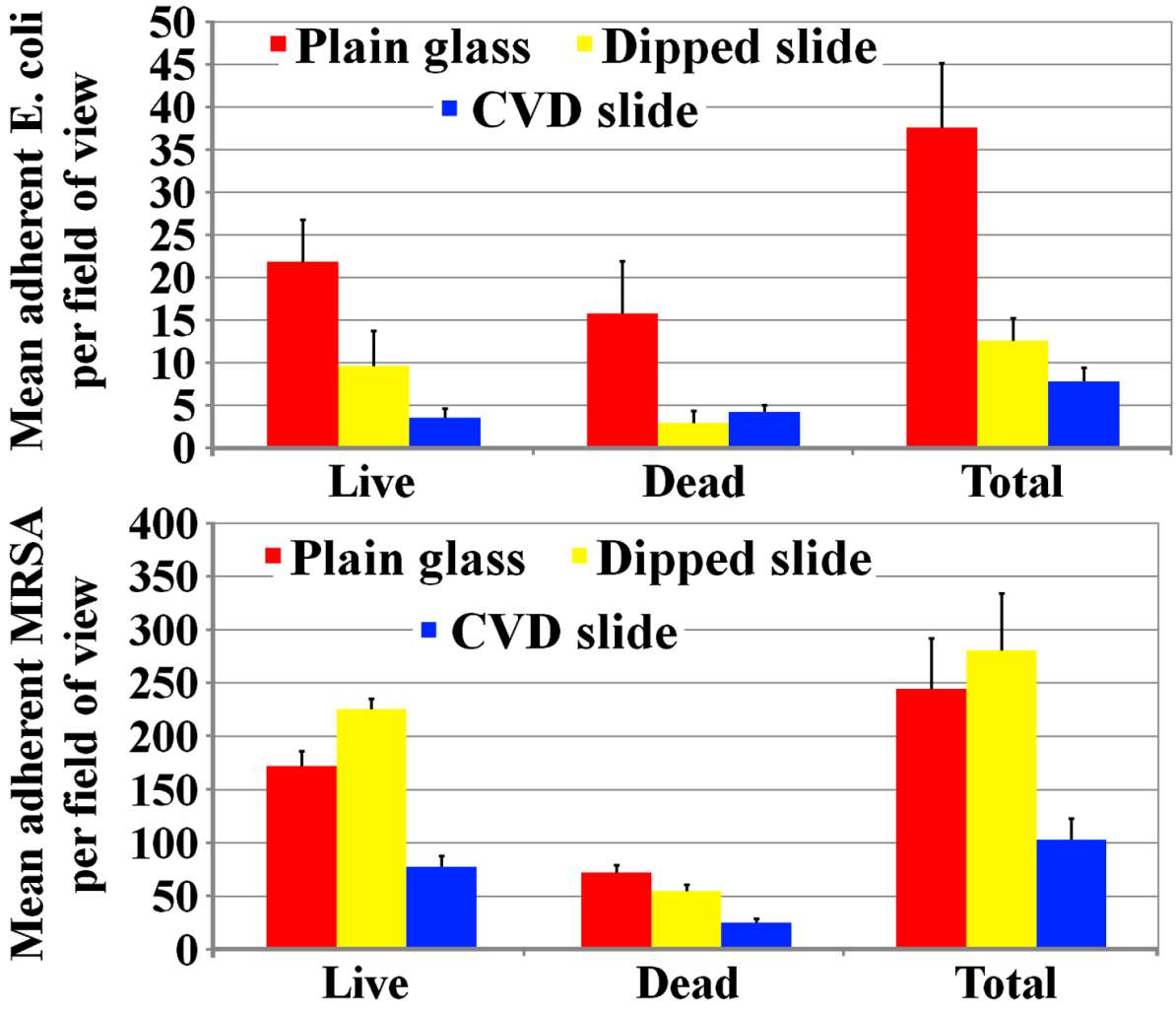

Figure 5.07. Adherence of *E. coli* and *S. Aureus* to uncoated, dip-coated and AACVD coated glass surfaces measured by fluorescence live/dead staining assay. Bars represent the mean adherent *E. coli*/*S. Aureus* and standard error of the mean per microscope field of view. Results are from 2 experiments performed in duplicate.

S. aureus gave a greater level of adherence relative to that of *E. coli* with mean counts of 245, 281 and 103 adherent cells per field of view for uncoated, dip-coated and AACVD coated glass respectively. Unlike *E. coli*, the greatest level of adherence was for dip-coated glass (Figure 5.07), while uncoated glass had the greatest proportion of dead cells (29.6%) and the highest total numbers of dead cells. However, AACVD coated glass still showed the least *S. aureus* attachment (Figure 5.07) confirming the ability of the superhydrophobic surface to reduce bacterial adhesion. The reductions of attachment to the AACVD coating amounted to 58% and 63% relative to the uncoated and dip-coated glasses, respectively. Figure 5.08 shows representative images of a section of microscope field of view demonstrating the variations in *S. Aureus* adherence observed for each surface type. Colonisation of the superhydrophobic films was restricted to the tips of the surface protrusions for both bacteria used.

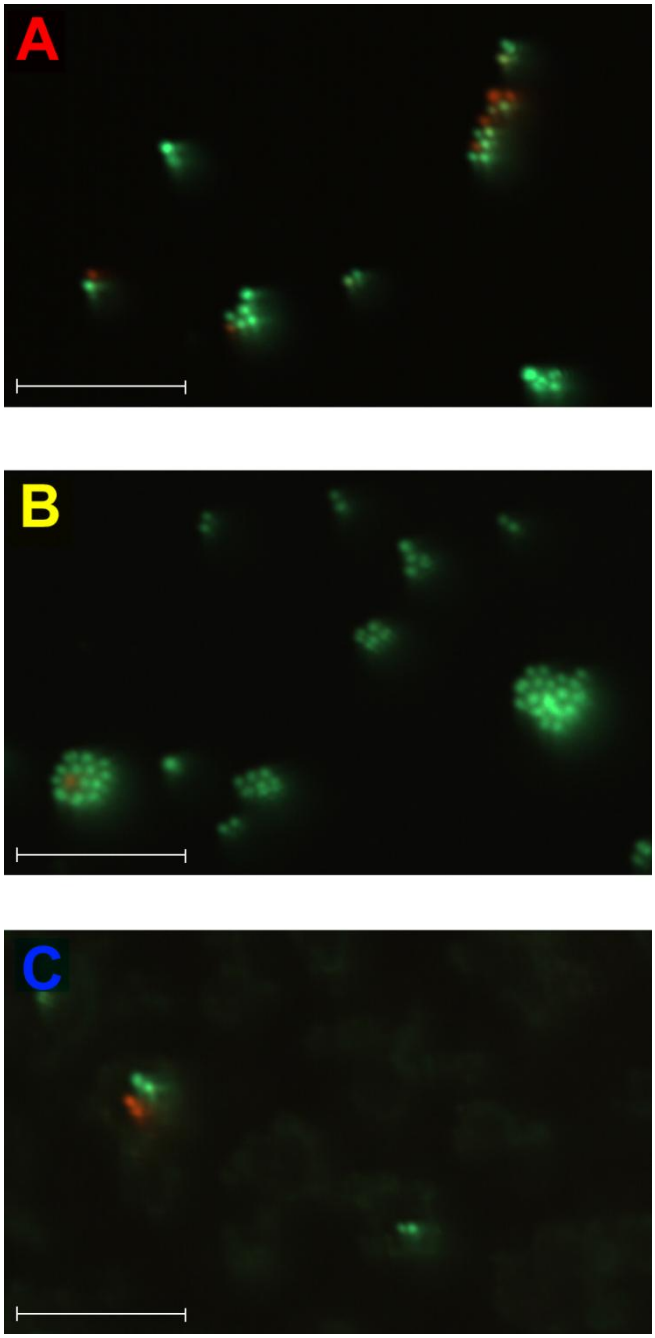

Figure 5.08. Fluorescence microscopy of *S. Aureus* attached to glass surfaces. Images are of a section of a microscope field of view showing live (green) and dead (red) *S. Aureus* cells attached to (A) uncoated glass, (B) dip-coated glass and (C) AACVD coated glass after 1 h exposure to identically populated bacterial suspensions. Bar represents 10 μm. Images are from a representative experiment.

The attachment of *E. coli* was reduced by coating the glass substrate with the elastomer. The dip-coated film lacks surface roughness thus this change was solely brought about by the composition change of the surface. The opposite was true for *S. Aureus*, which gave a slightly increased adhesion when exposed to a dip-coated glass slide. Therefore, relative to glass, *E. coli* adhesion is inhibited by a Sylgard 184 elastomer surface, and *S. Aureus* attachment is promoted by an elastomer surface. Another factor to consider is the mobility of the bacteria, *E. coli* are motile as they possess flagella and are able to actively swim away from the surface while *S. Aureus* are non-motile and could get stuck by any adhesive force of the elastomer. The slightly greater attraction of *S. Aureus* to a polymer surface rather than the plain glass surface is due to the chemical structure of the bacteria's surface. *S. Aureus* is

encased in a polysaccharide capsule, which is the bacteria's outer most layer. This layer is attracted more strongly to the elastomer material rather than to glass. *E. coli* have a similar capsule surrounding them. However these bacteria also have flagella protruding from their surface which limits contact with the polysaccharide capsule. The flagella are made up of long chain protein units, which are repelled more strongly by the elastomer surface than the glass[18/19].

The superhydrophobic surfaces formed *via* AACVD restrict the amount of contact made between the elastomer and water. The bacterial suspension is aqueous and thus most contact of the suspension is with the air trapped in the surface microstructure (Figure 5.09). The lessened surface contact results in a reduced chance of bacteria attaching to the substrate. In the case of *E. coli* the presence of attached bacteria had already been reduced by an elastomer film. The superhydrophobic film lessened the contact between the *E. coli* and the elastomer which further reduced the attachment to the surface. *S. Aureus* attachment was promoted by a flat elastomer film, relative to plain glass. However the use of the superhydrophobic substrate also resulted in a large reduction of *S. Aureus* adherence.

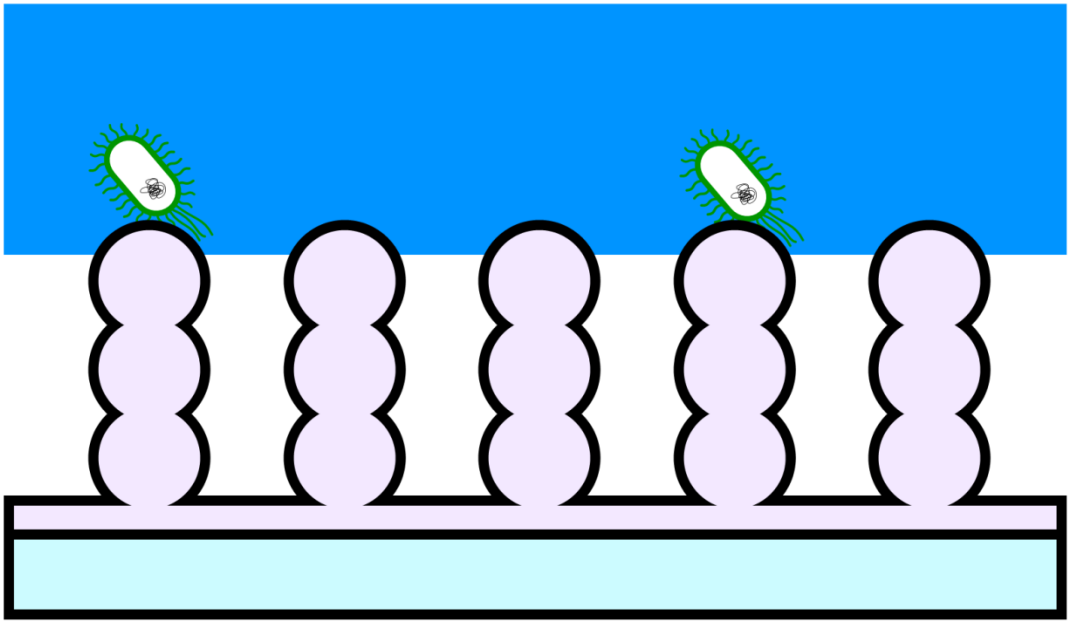

Figure 5.09. Schematic showing an aqueous bacterial suspension lying on the superhydrophobic Sylgard 184 surfaces deposited *via* AACVD, bacteria suspended in the water are only able to attach to surface protrusions.

Another factor to consider is the effect of Lotus effect self-cleaning of the surface as it was withdrawn from the bacterial suspension. A further reduction in bacterial attachment could be brought about by the movement of water, at the water-surface interface, causing detachment. This could be especially important in the phase to removing any non-adherent transient bacteria; the rinsing of the substrates causes water to move bacteria that are not strongly attached to the surface. The action of

bacterial removal can be magnified by the Lotus effect self-cleaning mechanism, which the flat surfaces did not have[20].

5.3.3 Bacterial Interaction with Superhydrophobic Surfaces

The study of the Lotus leaf and other superhydrophobic self-cleaning surfaces has been an area of extensive research. The main focus of many experiments however is the adhesion of particulate matter to the surface[7/8/21]. Particles of differing size/composition are dusted onto the surface and then rinsing with water determines the effectiveness of the self-cleaning. These experiments do not take into account the attachment of microorganisms. They however do show that the self-cleaning mechanism becomes more efficient with increased hydrophobicity. Plant surfaces with most efficient self-cleaning have multiple scales of roughness, usually large protrusions (micrometres), combined with small hairs or crystallites (nanometres)[22]. It has been shown that an increased hydrophobicity can reduce bacterial adhesion to the surface of a leaf[11].

Surface features also play a role in the ability of bacteria to attach to a surface[23]. Investigations carried out on steel substrates show a high surface roughness allowed more bacteria to colonise the surface[24]. This colonisation concentrated in the grooves of the material as this provides more surface area for the bacteria to maximise efficiency of attachment. A superhydrophobic material limits the contact of an aqueous bacterial suspension to the protrusions of the surface, allowing no contact with the grooves of the material, preventing access to the most viable place for bacterial adhesion. Any attachment of bacteria must thus come from the small fraction of area where the aqueous suspension and surface protrusions make contact. This can be seen in the fluorescence images (Figure 5.08, p138) which show the attachment of bacteria to the top of the surface feature and not in the grooves of the structure.

Surfaces constructed to mimic the dual-scale roughness of the Lotus leaf have shown that combining micro-scale and nano-scale roughness results in a higher contact angle, a lower slip angle and a lower adhesive force between the water and the surface[17/25]. Polysiloxane pillars with a nanostructure composed of wax molecules demonstrate this principle[17]. The dual-scale roughness allows for a higher proportion of water to be trapped under the water droplet, increasing hydrophobicity and also reduces the adhesive force, between the surface and water droplet, making the surface more slippery. Surfaces designed with the same principles, demonstrate similar findings[26-28].

The surface deposited in this experiment does not show an obvious dual-scale roughness (nano/microscale), however there is a large variation in particle size over the substrate (Figure 5.05), so there is some deviation from strictly one magnitude of roughness. The surface microstructure of the superhydrophobic elastomer film does draw some similarities to a Lotus leaf surface. However the incorporation of specialised nano-roughness could reduce bacterial adherence to the peaks of the

protrusions further. Although many investigations deal with the self-cleaning aspect of hydrophobic surfaces (*via* particle removal), most do not incorporate bacterial adhesion. This is a key consideration when dealing with the antimicrobial surfaces that do not include a chemical action (biocidal chemicals) on bacteria. The removal of dirt and bacteria from a surface by Lotus effect self-cleaning will only occur when water flow over the surface occurs (e.g. rinsing with water or rain). It is therefore expected that bacteria will have a period of time on the surface where attachment can be made. This investigation has aimed to replicate these conditions and has demonstrated that superhydrophobic surfaces can limit bacterial attachment. A surface aimed at self-cleaning/antimicrobial applications must have bacterial attachment carried out on it. This investigation has shown that limited contact of bacterial with the grooves limit attachment to solely the protrusions of the superhydrophobic surface. Further research in this area is required to reach a comprehensive conclusion. Additional experiments could gauge the effect of single-scale vs. dual/multi-scale roughness on the adhesion of bacteria. This is an important issue when dealing with surfaces designed for biomedical and catering industries[1].

The elastomer surfaces used in this investigation have potential for a wide scope of applications. The polymer used has been used in swell encapsulation processes, incorporating light activated antimicrobial molecules[29/30], with potential for other types of antimicrobial agents to be incorporated using this technique[31]. The AACVD deposition can be varied in order to improve durability and also transparency, and this could include varying the type of elastomer used (Chapter 2).

5.4. Conclusions

The superhydrophobic films used in this investigation were deposited *via* the AACVD of the two-part curable silicone elastomer (Sylgard 184), which was reported in Chapter 2. The polymer is hydrophobic with flat films giving a 95° water contact angle. The AACVD process facilitates a highly developed microstructure, *via* particle agglomerations during the deposition. The microscope glass substrates used were pre-coated with a thick film of the elastomer, and the resultant AACVD deposition over this gave a film with a consistently high water contact angle (averaging 165°). The slip angle of the surface was below 5°, suggesting a Cassie-Baxter wetting mechanism and potential for Lotus effect self-cleaning.[32-34]

The bacterial attachment to superhydrophobic surfaces is a vastly unexplored area, with much literature focus dedicated to removal of particulate matter in order to demonstrate the Lotus effect. This article has attempted to explore the prevention of bacterial attachment. The bacterial attachment assay involved *E. coli* and methicillin-resistant *S. aureus*. The experiments showed that after a 1 hour submersion in a bacterial suspension, the superhydrophobic elastomer films greatly reduced the attachment of both types of bacteria, relative to plain glass and dip-coated Sylgard 184 surfaces. The

investigation also detailed that while attachment was hindered by a flat polymer surface, attachment of *S. Aureus* was promoted by the elastomer surface. The main attachment areas on the superhydrophobic films were the tops of the surface protrusions. This was explained by the Cassie-Baxter wetting mechanism only allowing contact between the tops of the protrusions and the aqueous bacterial suspension, due to trapped air underneath the water in between the surface features. The elastomer surface thus has potential for application as antimicrobial surfaces that do not involve the action of chemical disinfection.

4.5. References

1. E. A. Araújo, N. J. de Andrade, L. H. M. da Silva, A. F. de Carvalho, C. A. de Sá Silva and A. M. Ramos, *Food Bioprocess Technol.*, 2010, **3**, 321.
2. A. P. A. Hendrickx, M. J. M. Bonten, M. van Luit-Asbroek, C. M. E. Schapendonk, A. H. M. Kragten and R. J. L. Willems, *Microbiology*, 2008, **154**, 3212.
3. N. Fong, A. Simmons and L. A. Poole-Warren, *Acta Biomater.*, 2010, **6**, 2554.
4. S. Noimark, C. W. Dunnill, M. Wilson and I. P. Parkin, *Chem. Soc. Rev.*, 2009, **38**, 3435.
5. A. Kafizas, S. Kellici, J. A. Darr and I. P. Parkin, *J. Photochem. Photobiol. A*, 2009, **204**, 183.
6. O. Öztürk, M. Sudagidan and U. Türkan, *J. Biomed. Mater. Res. A*, 2007, **81a**, 663.
7. C. Neinhuis and W. Barthlott, *Ann. Bot. Lond.*, 1997, **79**, 667.
8. W. Barthlott and C. Neinhuis, *Planta*, 1997, **202**, 1.
9. P. Wagner, R. Fürstner, W. Barthlott and C. Neinhuis, *J. Exp. Bot.*, 2003, **54**, 1295.
10. D. Knoll and L. Schreiber, *Microb. Ecol.*, 2000, **41**, 33.
11. L. M. Marcell and G. A. Beattie, *Mol. Plant-Microbe Interact.*, 2002, **15**, 1236.
12. B. Bhushan, *Philos. Trans. R. Soc. A*, 2009, **367**, 1445.
13. B. Liu, Y. He, Y. Fan and X. Wang, *Macromol. Rapid Commun.*, 2006, **27**, 1859.
14. X. Zhang, F. Shi, J. Niu, Y. Jiang and Z. Wang, *J. Mater. Chem.*, 2008, **18**, 621.
15. C. M. Magin, S. P. Cooper and A. B. Brennan, *Mater. Today*, 2010, **13**, 36.
16. M. Nosonovsky and B. Bhushan, *Adv. Funct. Mater.*, 2008, **18**, 843.
17. B. Bhushan, K. Koch and Y. C. Jung, *Appl. Phys. Lett.*, 2008, **93**, 093101.
18. M. Silverman and M. I. Simon, *Ann. Rev. Microbiol.*, 1977, **31**, 397.
19. K. Page, M. Wilson and I. P. Parkin, *J. Mater. Chem.*, 2009, **19**, 3819.
20. A. Solga, Z. Cerman, B. F. Striffler, M. Spaeth and W. Barthlott, *Bioinspir. Biomim.*, 2007, **2**, S126.
21. B. Bhushan, Y. C. Jung and K. Koch, *Langmuir*, 2009, **25**, 3240.
22. K. Koch, H. F. Bohn and W. Barthlott, *Langmuir*, 2009, **25**, 14116.
23. T. R. Scheuerman, A. K. Camper and M. A. Hamilton, *J. Colloid Interface Sci.*, 1998, **208**, 23.
24. E. Medilanski, K. Kaufmann, L. Y. Wick, O. Wanner and H. Harms, *Biofouling*, 2002, **18**, 193.
25. M. Nosonovsky and B. Bhushan, *J. Phys. Condens. Matter*, 2008, **20**, 225009.
26. Q. Pan, M. Wang and H. Wang, *Appl. Surf. Sci.*, 2008, **254**, 6002.
27. S. J. Pastine, D. Okawa, B. Kessler, M. Rolandi, M. Llorente, A. Zettl and J. M. J. Fréchet, *J. Am. Chem. Soc.*, 2008, **130**, 4238.

28. T. Yao, C. Wang, Q. Lin, X. Li, X. Chen, J. Wu, J. Zhang, K. Yu and B. Yang, *Nanotechnology*, 2009, **20**, 065304.
29. S. Perni, C. Piccirillo, J. Pratten, P. Prokopovich, W. Chrzanowski, I. P. Parkin and M. Wilson, *Biomaterials*, 2009, **30**, 89.
30. S. Perni, P. Prokopovich, C. Piccirillo, J. Pratten, I. P. Parkin and M. Wilson, *J. Mater. Chem.*, 2009, **19**, 2715.
31. R. M. Gant, Y. Hou, M. A. Grunlan and G. L. Cote, *J. Biomed. Mater. Res. A*, 2009, **90a**, 695.
32. C. W. H. Dunnill, Z. A. Aiken, J. Pratten, M. Wilson, D. J. Morgan and I. P. Parkin, *J. Photochem. Photobiol. A*, 2009, **207**, 244.
33. A. Kafizas, S. Kellici, J. A. Darr and I. P. Parkin, *J. Photochem. Photobiol. A*, 2009, **204**, 183.
34. C. W. Dunnill, Z. A. Aiken, J. Pratten, M. Wilson and I. P. Parkin, *Chem. Vap. Depos.*, 2010, **16**, 50.

Chapter 6

Dynamic Study of the Interaction of Water with a Surface

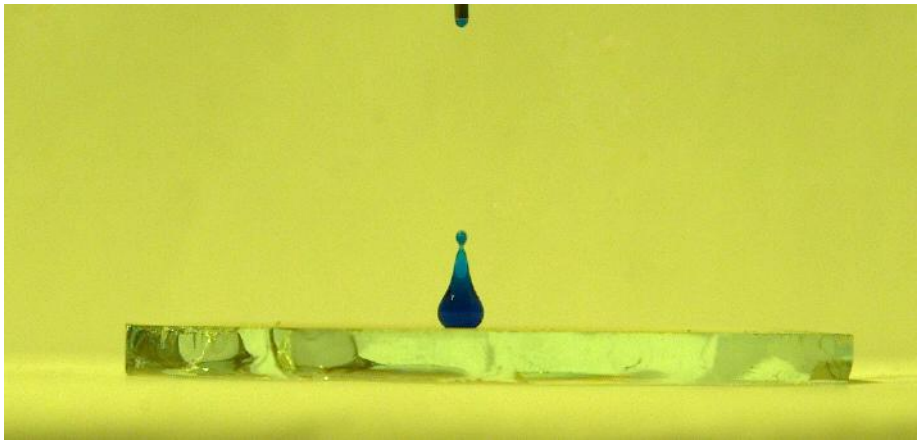

Figure 6.01. A water droplet rebounding from impact with a superhydrophobic surface.

6. Dynamic Study of the Interaction of Water with a Surface

6.1. Introduction

6.2.1 The Comparison of Water Contact Angles and Tilt Angles

The water contact angle is a hugely valuable measurement in accessing the hydrophobicity of a surface. When dealing with superhydrophobic surfaces however, there is a greater amount of error when reading large water contact angles.[1] This error can be introduced through gravitational bowing of water droplets[2], caused when using a relatively large droplet volume (Figure 6.02), and the analysis of the droplet shape by computer programs can also cause large differences in results[1] (Section 1.2.2). Given this, in order to meaningfully compare the water contact angles of two different surfaces the analysis method must be consistent, i.e. droplet volume, dispensing method and analysis method. This cannot always be achieved given the variation of options within different software packages, in addition to the difficulty with consistent contact angle image analysis.[3-7]

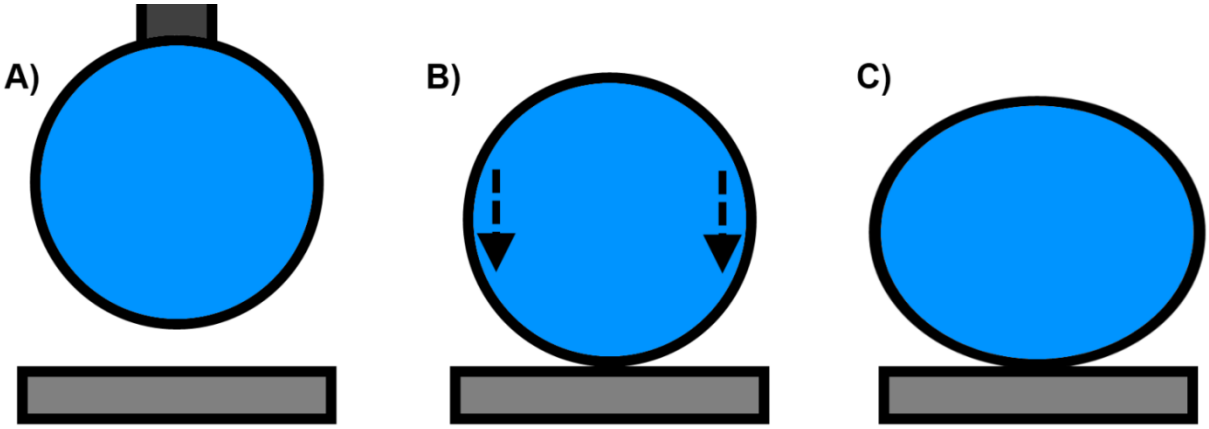

Figure 6.02. Schematic showing the dispensing of a water droplet on a superhydrophobic surface (**A**), with the edges of the droplet deforming the water droplet and increasing the apparent water contact angle (**B** > **C**). The extent of droplet bowing increases with the volume of the droplet.

Water tilt angles (the angle at which a water droplet begins to move when the surface is tilted) can also give an indication of the hydrophobicity of a surface, as low tilt angles usually relate to a low energy of interaction between water and the surface.[8] This measurement can be related to the advancing and receding water contact angles but use of these can result in similar complications as described above. The tilt angle itself is partially a gravitational effect and so is dependent on the volume of the water droplets used, with high mass/volume droplets moving before those with lower mass/volume in most cases, for the same surface[9]. With factors such as tilt method (tilting with incremental or smooth movement) which must also be considered. In order to render the tilt angle results comparable then all the above factors must also be considered, with the same droplet volume and tilting method used in each case.

6.2.2 Factors Affecting the Behaviour of Water on a Surface

There are three main factors that influence the dynamic interaction between water and a surface[10/11]:

- *Surface Hydrophobicity* – A surface with greater hydrophobicity (i.e. a surface with higher water contact angle), has a larger repulsive force toward water. This gives a greater likelihood of displaying dynamic effects such as Lotus effect self-cleaning and water bouncing.
- *Wetting Mechanism* – The amount of air under water as it lies on a surface affects the amount of frictional force felt between the surface and the water. This is reflected primarily by a difference in tilt angle, where low tilt angle surfaces are more likely to exhibit dynamic effects.
- *Surface Microstructure* – The surface microstructure can have other effects on the interaction with water other than the wetting mechanism. Water pinning (the local adhesion of water to specific points on the surface) is promoted by surfaces with microstructures with sharp edges, such as square edged columns (Figure 6.03). This effect creates additional adhesion to the surface when the water on the surface begins to move away, thus lessening the likelihood of dynamic effects. The amount of water pinning on a surface can be reduced by creating rounded surface features that allow the gradual release of water from a surface.

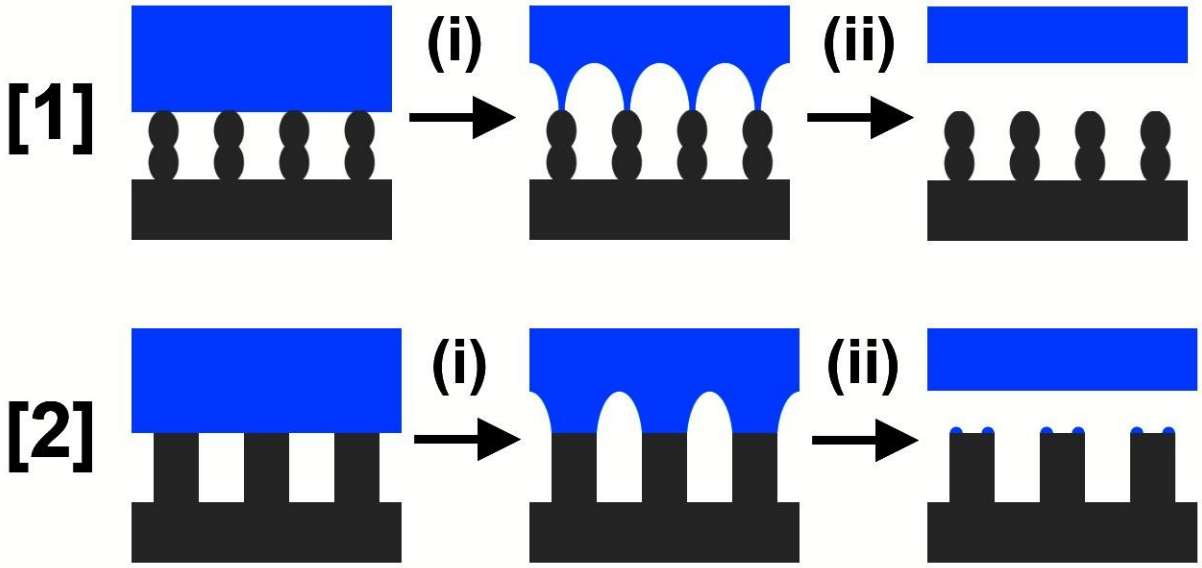

Figure 6.03. Schematic showing the removal of water from Cassie-Baxter surfaces with differing microstructure types - [1] Rounded and [2] Sharpened edges. Different stages of detachment are shown – (i) Partial - Droplet is more effectively held by pinning to surface type [2] and (ii) Full – Droplets that were pinned leave behind traces of water on the surface making the surface stickier on subsequent bounces.

6.2.3 Water Bouncing Studies

Extensive studies have been carried out into water bouncing, and this has enabled the dynamic behaviour to be well classified[12/13]. The various modes of water droplet-surface impact (deposition, splash, break-up and rebound) have been related to droplet volume, impact velocity and surface properties. In addition, by studying different liquids, changes in behaviour can be tracked and related to the physical properties of the liquid.[14/15] Other properties of droplet bouncing such as water-surface contact time, droplet morphology and bounce elasticity have also been studied.[16] The experiments used to analyse the full extent of water droplet bouncing usually require extremely high speed video cameras (capturing at > 10^4 frames per second[13]), this equipment is not only expensive but setting-up these experiments could be time consuming and would be an inefficient analysis technique for research groups who focus on superhydrophobic surface synthesis.

Water droplet movement/bouncing on a surface is highly dependent on multiple factors. The ambiguity and frailties of current methods toward cross-comparison of results, in addition to inability of static measurements not fully characterising a surfaces hydrophobicity drives the need for a dynamic analysis technique which is able to be compared with unambiguous results. In this chapter a definition of superhydrophobicity based on the ability of water to bounce on a surface is proposed, as water bouncing incorporates analysis of multiple surface properties in one measurement. These include: the surface's fundamental hydrophobicity (indication of θ), the ability to prevent penetration of surface protrusions (wetting mechanism, $\theta_{Advancing}/\theta_{Receding}$) and dynamic interaction with that surface (water pinning and self-cleaning). The method used in this chapter is focused toward facile and unequivocal results that can be replicated without the disparity caused by water contact angle measurements, while providing an indication of multiple surface properties simultaneously. It is shown that the bouncing characteristics are related to the surface microstructure. Furthermore for superhydrophobic surfaces with a similar microstructure it is shown that there is a linear relationship between number of bounces on the surface and the static water contact angle. The surface hydrophobicity measuring technique utilises the number of water bounces, a relatively simple property to measure, and this requires less expensive equipment as a relatively low capture rate is required (> 500 frames per second). The set-up is a more accessible analysis technique that provides results that can be directly compared between research groups, while ruling out error in water contact angle measurement.

6.2. Experimental Details

6.2.1 Materials

With the exception of Sylgard 184 Silicone Elastomer which was purchased from R. W. Greeff, sand paper and dispensing tips which were purchase from Onecall and PTFE sheets which were purchased

from Alfa Aesar, all chemicals used in this investigation were purchased from Sigma-Aldrich Chemical Co; including chloroform, methylene blue, TEOS, hydrochloric acid, toluene, HMDS, copper plate, copper nitrate trihydrate, potassium persulfate, sulphuric acid, methanol and ethanol.

6.2.2 Surface Materials

6.2.2.1 Pre-prepared Surfaces

Glass. Portions of silica barrier layer glass provided by Pilkington NSG, used for previous CVD depositions, were washed with water and acetone and dried at 80°C for 10 minutes. Some portions were subsequently heated in an oven at 500°C for 1 hour.

Copper. Copper plates (1 mm thick) were tested after rinsing with acetone and drying at 80°C for 10 minutes.

6.2.2.2 Titanium Dioxide

Silica barrier layer glass was used to deposit titanium dioxide films *via* atmospheric pressure CVD, from gaseous $TiCl_4$ and ethyl acetate precursors at a 500°C deposition temperature using the same method used by Hyett *et al*.[17]

6.2.2.3 Silicone Elastomer

Surfaces were deposited *via* AACVD as described in Section 2.2.5. The variation on hydrophobicity was brought about by changing the amount of precursor deposited. Films showing a high variation in water contact angle were formed by reducing the flow rate of the nitrogen carrier gas to 0.5 L/min.

6.2.2.4 Functionalised Silica Microparticles

Surfaces were deposited *via* hybrid CVD as described in Section 3.2.2. Only films deposited at 550°C were used in this study.

6.2.2.5 Functionalised Copper Hydroxide

Surfaces were deposited *via* AACVD as described in Section 4.2.3, in addition to the oxidation and functionalisation of copper sheets treated using the same method.

6.2.2.6 Polytetrafluoroethylene

PTFE sheets (1.6 mm) thick were used as received. Roughening was also carried out by action of sand paper (abrasive grade – P36 and P50) moved by hand over varying periods of time up to 1 minute.

6.2.3 Static Surface Hydrophobicity Measurement

Static water contact angles images were obtained using an FTA 1000B Automated Drop Shape Analyser using 3 μL water droplets, surface baselines and subsequent tangents at the point of droplet contact were assigned manually to prevent error caused by image analysis software. For surface where averages were taken, a number of measurements were made across the films and the average values taken (average ten measurements). Spot testing was also carried out on films with varying thickness, where one measurement was made and position of measurement marked on the reverse of the substrates.

6.2.4 Water Bouncing Measurement

The water droplet bouncing experiments were studied using a Vision Research Phantom v710 high speed camera equipped with a Nikon 24-85 mm F2.8 macro zoom lens with images captured at 3000 frames per second. Water droplets were dropped from a height of 20 mm (tip to surface) using a microsyringe fitted with a 27 gauge dispensing tip (unless otherwise stated). Droplets impacted the surface at approximately 0.34 m/s (estimated by gravimetric calculation) and the water droplets from this tip were 8 μL in size and were left to detach under their own weight (Figure 6.04). This set-up was varied to examine the effect of droplet impact velocity and volume. Methylene blue was added to the water to aid visualisation, this did not change the behaviour of the water droplets on the surface. The stage which held the substrates was made level using a spirit level, and was accurate to within 0.2°.

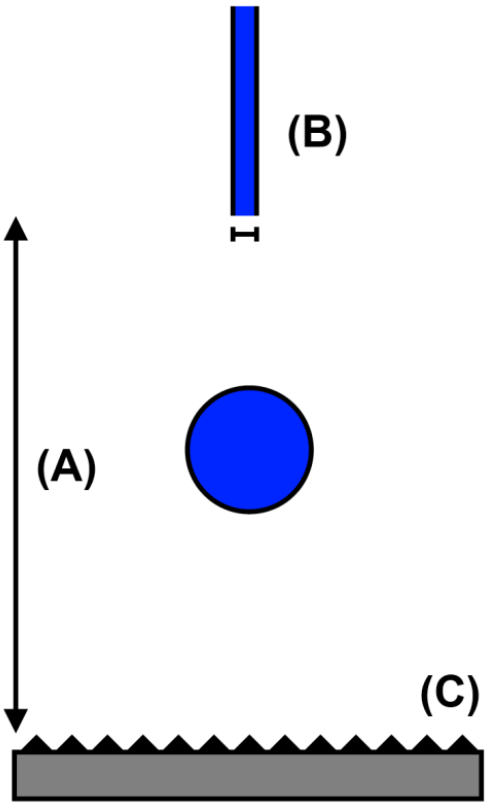

Figure 6.04. Schematic showing the water bounce experimental set-up. The variable of the experiments are (A) Drop height – this determines the velocity of droplet impact, (B) Dispensing tip – this determines the droplet volume and (C) Substrate – this dictates the nature of the water-surface interaction. The optimum set-up was (A) 20 mm and (B) 27 Gauge (internal diameter – 0.203 mm) with a level substrate (C).

A second (inexpensive) camera was used to repeat some experiments – Casio HS EX-FH25 using a capture rate of 1000 frames per second.

6.2.5 Water Droplet Rolling Observation

Motion of droplets was studied using the Vision Research Phantom v710 high speed camera equipped with a Nikon 24-85 mm F2.8 macro zoom lens with images captured at 3000 frames per second. Droplets of water (~15 μL volume) were dropped onto tilted superhydrophobic silica films (18° from horizontal, Section 6.2.2.4), coloured plastic particles used for craftwork (~1 mm^2) were suspended in the water and dispensed using a syringe. Particles were added to aided visualisation of rolling motion.

6.3. Results and Discussion

6.3.1 Water Droplet Bouncing

6.3.1.1 Effect of Water Impact Speed and Droplet Volume

The dropping height determined the velocity of impact, and the optimum height was decided as the maximum height for the droplet to suffer no fragmentation upon impacting with the surface, insuring maximum droplet momentum, and the maximum number of potential bounces was achieved. The ideal droplet volume was decided as the smallest droplet dispensable, without lateral movement becoming a factor, as small droplets would give more bounces; however smaller droplets still are more likely to be affected by minute levelling issues or air movement. The 8 μL droplet volume and 20 mm dropping height (tip to surface) was found to be optimum (Figure 6.05). The droplet could easily be replicated and fell under its own weight when dropped from a 27 gauge dispensing tip (internal diameter – 0.203 mm). Larger droplets, dispensed from wider tips (gauge 25 and below), resulted in fragmentation and required a lower drop height which subsequently reduced the maximum number of bounces achieved. Smaller water droplets (from gauge 30 dispensing tips) allowed for higher drop heights without fragmentation and also increased the maximum number of bounces observed (14 bounces were achieved on a surface with a water contact angle of 175° from a height of 20 mm). However lateral movement of droplets was also increased during bouncing even for surfaces that registered perfectly horizontal by a spirit level. This became greater at higher θ, and rendered accurate bouncing measurements difficult – for example fifteen repeat experiments were required for just one run in which the droplet remained in the field of view.

6.3.1.2 Water Bouncing on Surfaces with a Rounded Microstructure

A wide range of surfaces with relatively flat or rounded microstructures were tested possessing static water contact angles between 0-175° and included silica, copper, titanium dioxide, flat PDMS surfaces and various rough-rounded silica and PDMS polymer surfaces (Figure 6.05). A series of spot testing

experiments was also carried out on rounded elastomeric surfaces. This involved forming a surface with variable hydrophobicity across a substrate, testing water contact angles (θ) at various positions over the film and performing water dropping experiments at positions with a known θ (Figure 6.06). It was noted that water droplets did not bounce under these conditions unless static water contact angles of 151° or greater were achieved on a surface. The number of bounces on the surface was defined as the sum of instances the droplet had a defined air gap between the surface and the water droplet after initial contact. It was found that the number of bounces for surfaces with rounded microstructure (Figure 6.07) increased linearly with θ above 151° with the maximum number observed for an 8 μL droplet as twelve (Figure 6.06). It was empirically found that a simple linear relationship existed between under these conditions, with the relationship holding for a surface with rounded surface features, this is given below:

$$B = \frac{\theta - 151}{2.4}$$

Where B is the number of bounces and θ is the static water contact angle on the surface in degrees.

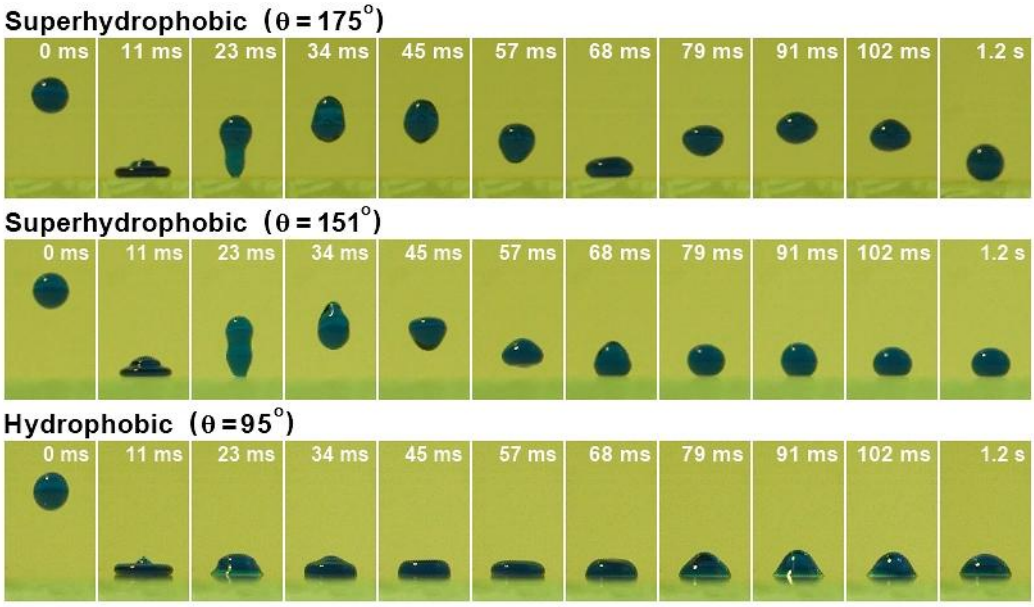

Figure 6.05. Series of photographs of an 8 μL water droplet dropped from a height of 20 mm (tip to surface) and bouncing on substrates with a range of water contact angles. The droplets velocity at point of impact was 0.34 m/s. Water droplets were coloured with methylene blue to aid visualisation; this did not alter the bouncing behaviour on the surface.

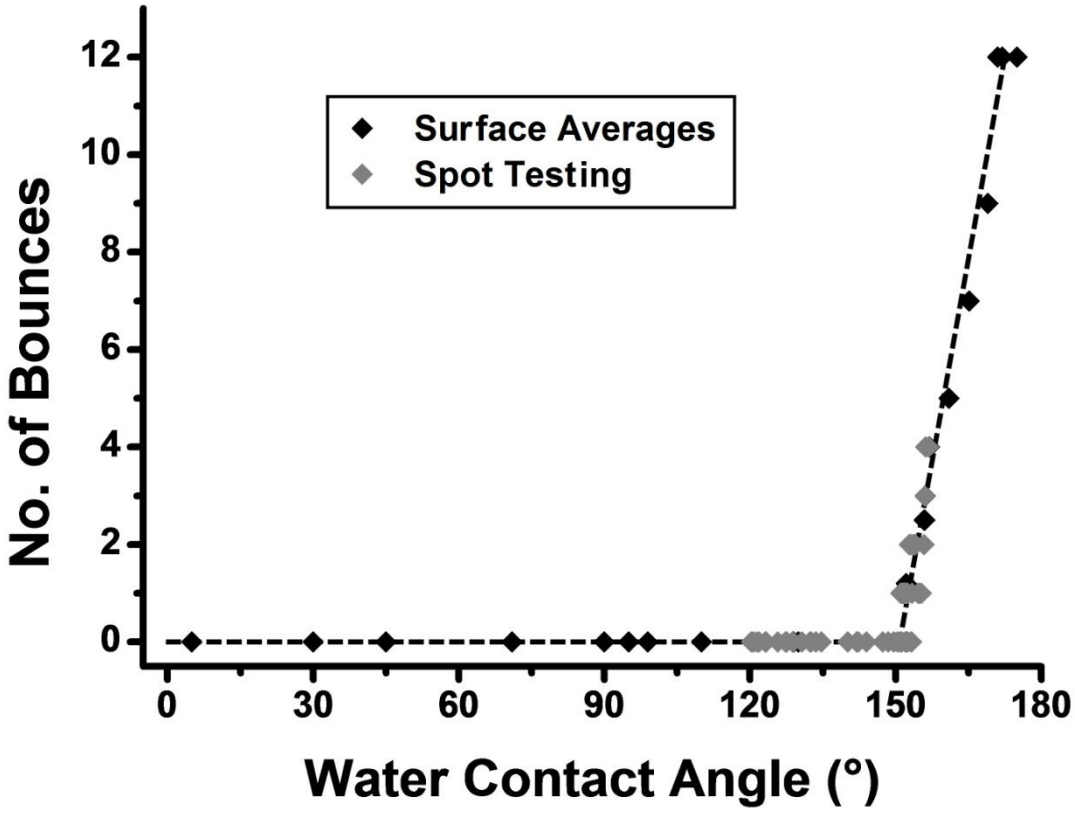

Figure 6.06. Plot showing number of bounces of a water droplet dropped from a 27 gauge dispensing tip from a height of 20 mm (tip to surface). Surfaces chosen demonstrated a range of hydrophobicities and all possessed rounded or flat microstructures. Spot testing measurements were carried out on silicone elastomer surfaces deposited *via* AACVD. Water bouncing only occurred on surfaces with water contact angle over 151°.

Water tilt angles (θ_t) on a surface provide a direct measurement of a waters adhesion to a surface - this is the angle from horizontal at which a droplet started to move on a surface. Comparing the number of bounces observed on the superhydrophobic surfaces and θ_t, gave three classes of behaviour – $\theta_t > 70°$ did not show any water bouncing, θ_t = 7-70° had B = 1-5 and surfaces with $\theta_t <$ 7° showed the largest number of bounces B = 5-12.

6.3.1.3 Varying Surface Microstructure

Surfaces with spiky/sharp ridged microstructures (PTFE roughened with sandpaper, functionalised copper hydroxide nanoneedles, Figure 6.07) required a larger static water contact angle of ≥ 156° to observe a water bounce. The sharp features can promote water pinning on their surface (Figure 6.03). The maximum number of bounces seen for a θ = 172° sharp microstructure surface was twelve under our standard conditions, indicating that for extremely high θ water pinning became less significant. This, in effect, shifted the linear relationship displayed by surfaces with rounded surface features, and so bouncing on surfaces with microstructures that promote water pinning begins at a higher θ.

However the maximum number of bounces still reached 12 at particularly high θ due to a substantial reduction in solid-liquid contact.

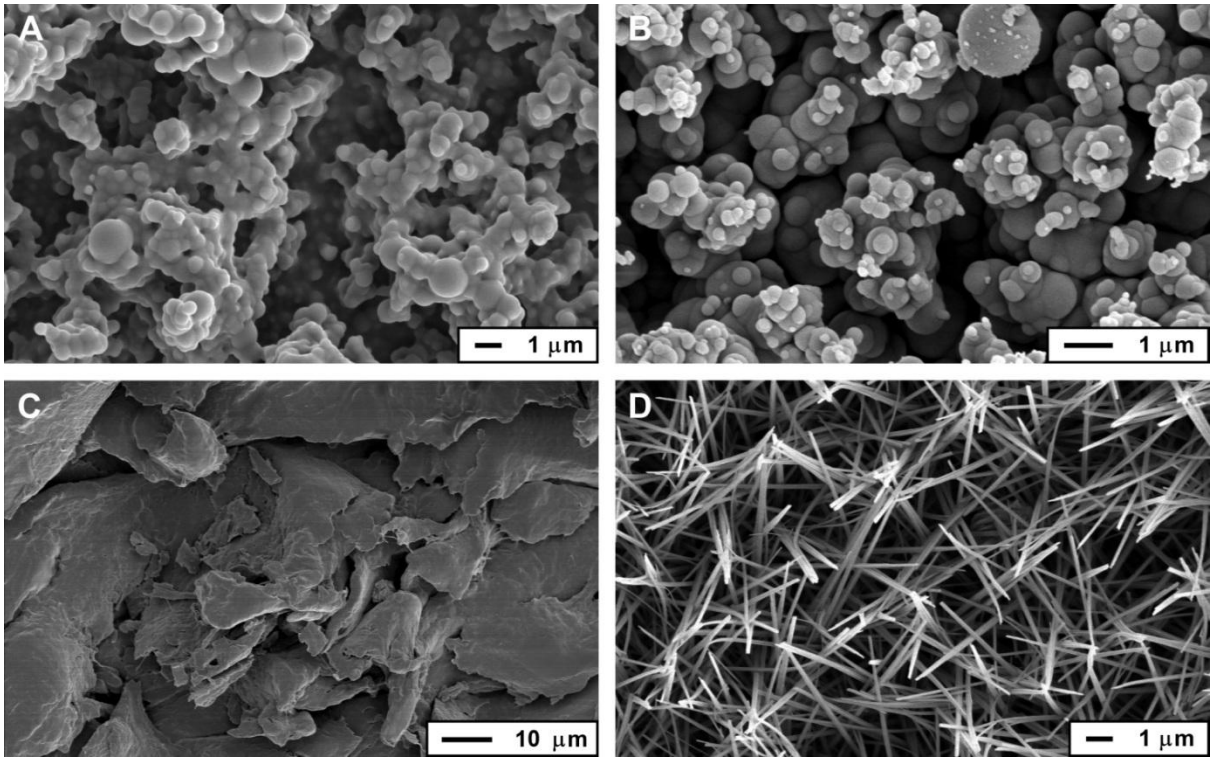

Figure 6.07. SEM images of superhydrophobic surfaces - Rounded (A) Sylgard 184 elastomer agglomerations, θ = 165° / B = 7 and (B) functionalised silica microparticles, θ = 175° / B = 12, in addition to sharp-edged (C) sandpaper roughened PTFE, θ = 158° / B = 2, and (D) thiol-functionalised copper hydroxide nano-needles, θ = 172° / B = 12. Scale bars inset.

6.3.1.4 Superhydrophobic Water Bouncing

The data shows a connection between water contact angle and the ability of water to bounce on a surface, provided the microstructure type remains consistent. Shifting of the relationship occurs when testing surfaces which possess a microstructure capable of pinning water. The areas of water pinning increase the adhesive force between surface and water, which lessens the rebound momentum of the water droplet and reduces the chance of loss of contact with the surface. Exceptionally hydrophobic surfaces which pin water can reduce the efficiency of Lotus-effect self-cleaning and even prevent water rolling as it moves over a surface, even if water contact angles are over 150°. Given this, surfaces with water contact angles over 150° can thus be deemed as non-superhydrophobic due to their lack of ability to facilitate Lotus-effect self-cleaning. The discrepancy between water contact angle and the dynamic behaviour of water on a surface (measured by water bouncing) means single static measurements (θ, $\theta_{Advancing}$, $\theta_{Receding}$ or θ_t) are insufficient in measuring superhydrophobicity for the purpose of cross field comparisons of differing surface morphology types. In addition, the disparity caused by distinct methods of water contact angle measurement (drop shape analysis) used by

different research groups, requires the implementation of the same techniques in order to allow direct comparison – even though the water contact angle may not reflect the true nature of the surface's hydrophobicity.

The water bouncing experiments discussed in this chapter examines the effect of multiple-key properties (θ, θ_t and water pinning) which denote a surface as superhydrophobic, in a single measurement. It can thus be said that a superhydrophobic surface will display a certain ability to facilitate water bouncing. As the bouncing on rounded surfaces commenced at 151° it was thus concluded that a surface capable of achieving one or more bounces (given the described parameters) can be judged to be superhydrophobic. The number of water droplet bounces increased linearly with water contact angle for surfaces with similar microstructures with this relationship shifted for surfaces with different microstructures. A new scale of superhydrophobicity has thus been established, based simply on the number of water bounces. Not only does this technique provide a universal indication of a surfaces superhydrophobicity, through analysing a combination of multiple surface features which dictate superhydrophobicity, but it also avoids the potential disparity in measuring the static water contact angle.

6.3.2 Rolling Motion of Water Droplets

The movement of water was tracked by the addition of polymer particles (insoluble in water) suspended within a droplet; methylene blue dye did not allow the visualisation of water movement. The circular rolling motion of particles could be clearly observed with particles on the outer edge moving faster (Figure 6.08). The rolling motion of water droplets suggests that Lotus effect self-cleaning can take place on the surface. The superhydrophobic state is related to Lotus effect self-cleaning[18], by studying this movement in-depth the mechanism of water travelling across a surface (sliding or rolling) can be assigned. The rolling motion associated with the Lotus-effect self-cleaning mechanism as a contributing factor of a surfaces superhydrophobicity can be confirmed.

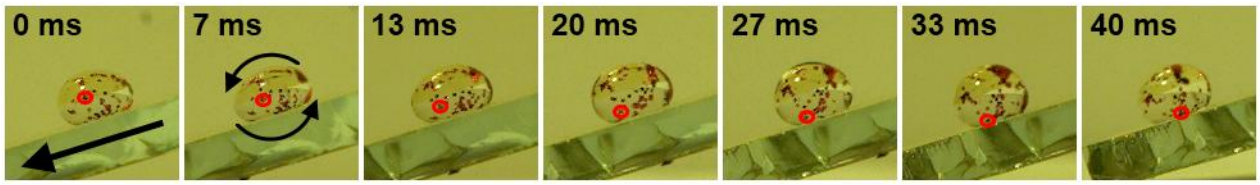

Figure 6.08. Schematic showing a water droplet (~15 μL) moving down a tilted superhydrophobic functionalised silica surface deposited *via* Hybrid CVD. The rolling motion of the droplet can be seen by tracking the movement of plastic particles suspended within the droplet – the same particle is circled in each image.

6.4. Conclusions

The question of superhydrophobicity should not be restricted to the water contact angle achieved on a surface, or even tilt angle. This chapter shows the effect of surface hydrophobicity and microstructure on the dynamic behaviour of water on a surface. Water bouncing experiments performed on hydrophobic surfaces showed that the ability of water to bounce (given specific parameters) was limited to surfaces with water contact angles greater than 151°. Surfaces that promoted water pinning, through sharp surface microstructures, did not facilitate water bouncing until water contact angles exceeded 156°. As the results correlate with the superhydrophobic contact angle (150°), it is suggested that surfaces capable of facilitating at least one bounce are superhydrophobic. Through a linear rise in number of bounces with water contact angle demonstrated by surfaces with similar microstructures a new scale of superhydrophobicity was established, through the relationship which is shifted with a change in microstructure type. The water bouncing technique is facile and unambiguous, allowing for direct comparison of a surfaces superhydrophobicity while avoiding potential disparity of different water contact angle analysis.

A technique for studying the internal movement of water droplets moving across a surface was also developed, allowing the visualisation of droplet rolling. The rolling mechanism is a key attribute of Lotus effect self-cleaning with its confirmation providing additional insight into the hydrophobicity of a surface. This chapter has confirmed the importance of dynamic studies on hydrophobic surfaces, with static measurements not being able to provide a comprehensive description of surface hydrophobicity.

6.5. References

1. X. Zhang, F. Shi, J. Niu, Y. Jiang and Z. Wang, *J. Mater. Chem.*, 2008, **18**, 621.
2. S. D. Hong, M. Y, Ha and S. Balachandar, *J. Colloid Interface Sci.*, 2009, **339**, 187.
3. M. Nosonovsky and B. Bhushan, *Microsyst. Technol.*, 2005, **11**, 535.
4. X. Zhang, F. Shi, J. Niu, Y. Jiang and Z. Wang, *J. Mater. Chem.*, 2008, **18**, 621.
5. J. W. Krumpfer and T. J. McCarthy, *Faraday Discuss.*, 2010, **146**, 103.
6. S. Wang and L. Jiang, *Adv. Mater.*, 2007, **19**, 3423.
7. H. F. Hoefnagels, D. Wu, G. de With and W. Ming, *Langmuir*, 2007, **23**, 13158.
8. K. Koch, B Bhushan, Y. C. Jung and W. Barthlott, *Soft Matter*, 2009, **5**, 1386.
9. T. Furuta, M. Sakai, T. Isobe, S. Matsushita and A. Nakajima, *Langmuir*, 2011, **27**, 7307.
10. S. Suzuki, A. Nakajima, M. Sakai, Y. Sakurada, N. Yoshida, A. Hashimoto, Y. Kameshima and K. Okada, *Chem. Lett.*, 2008, **37**, 58.
11. P. F. Hao, Z. H. Yao and X. W. Zhang, *Sci. China Phys. Mech. Astron.*, 2011, **54**, 675.
12. M. Callies and D. Quéré, *Soft Matter*, 2005, **1**, 55.
13. D. Quéré, *Nature*, 2005, **435**, T168.
14. A. L. Yarin, *Annu. Fluid Mech.*, 2006, **38**, 159.

15. A. Biance, F. Chevy, C. Clanet, G. Lagubeau and D. Quéré, *J. Fluid Mech.*, 2006, **554**, 47.
16. D. Richard, C. Clanet and D. Quéré, *Nature*, 2002, **417**, 881.
17. G. Hyett, J. A. Darr, A. Mills and I. P. Parkin, *Chem. Eur. J.*, 2010, **16**, 10546.
18. Z. Guo, W. Liu and B. Su, *J. Colloid Interface Sci.*, 2011, **353**, 335.

Chapter 7

Separation of Oil-Water Mixtures

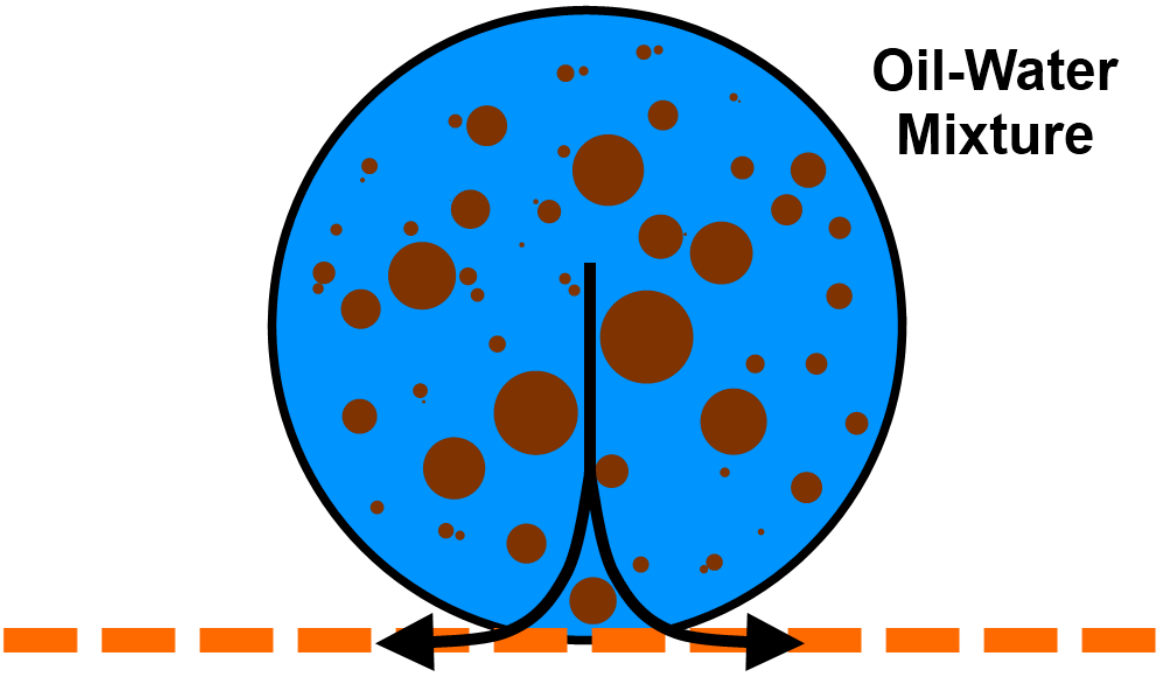

Figure 7.01. Mixed droplet of oil-water impacting a superhydrophobic mesh, the mesh strongly attracts oils. The arrow show the movement of oil onto the mesh, while retaining the ball of water sitting on top.

7. Separation of Oil-Water Mixtures

7.1. Introduction

Major incidents of ocean oil spillages have been reported in the media since the start of large scale ocean oil drilling[1]. Recent events in the Gulf of Mexico outline the need for the clean, portable and efficient methods for separating oil from water[2]. Current methods employed for the use in large scale oil spillages into water include skimming the top layer of water for removal of particulates, in addition to the use of oil absorbing materials to remove liquid substituents[3]. Inefficiencies of these methods are as follows: top layer removal techniques only remove material from the depths they reach physically, and materials used to absorb oil must be subsequently removed and later destroyed.[3]

Hydrophobic materials containing alkyl groups can also act to attract oils (oleophilic)[4]. Materials such as flat PTFE surfaces will achieve water contact angles around 100°[5], these demonstrate contact angles with hexane which are near 0°.[6] The oleophilicity of a material can be magnified in the same way as hydropilicity, and so by increasing surface roughness the contact angles with oils will decrease further (assuming a Wenzel-type interaction)[7]. This means that superhydrophobic surface constructed from alkyl containing materials have the potential for being extremely oleophilic (superoleophilic) (Figure 7.02).

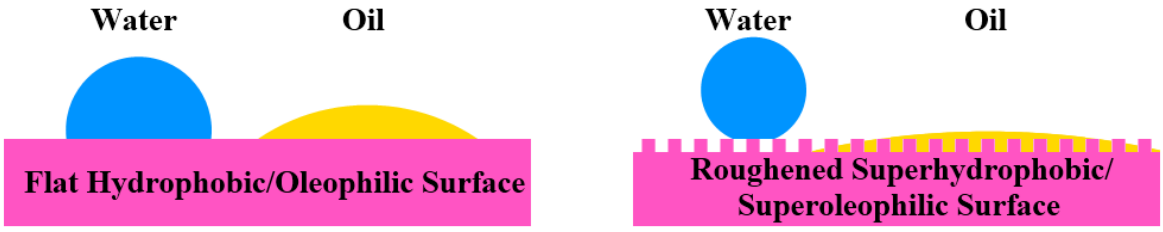

Figure 7.02. Schematic showing the interaction of water and oil with hydrophobic/oleophilic surfaces upon roughening.

The superhydrophobic/superolephilic surfaces can be extended to separating oil and water, due to the extreme difference of interaction with each liquid. Placing small amounts of an oil-water mixture on a surface with superhydrophobic/superolephilic properties would result in the sheeting of oil component across the surface, and balling-up of water within the mixture, in effect separating the mixture. If this was extended to large quantities of liquid, this would be an ineffective separation technique. There have been some recent developments in the use of superhydrophobic surfaces to separate oil and water, most examples include the use of mesh to aid separation.[8-10]

Previous chapters have focused on solely water's interaction with superhydrophobic surfaces; this chapter will deal with the design and implementation of devices to separate oil-water mixtures, using superhydrophobic meshes. The meshes are coated with Sylgard 184 polymer *via* AACVD, this

renders them extremely hydrophobic and as the Sylgard elastomer is also oleophilic, oils are attracted into the films. The porous nature of the mesh allows oil to flow through the mesh while water sits on top. The efficiency of separation strongly depends on the design of the device used, with the two most successful designs reviewed in detail. Separation efficiencies of up to 98% were achieved.

7.2. Experimental Details

7.2.1 Materials

All materials used in this investigation were purchased from Sigma-Aldrich Chemical Co; including copper gauze, Sylgard 184 silicone elastomer, chloroform and toluene.

Copper gauzes consisted of thin copper wires (of varying thickness 110, 190 and 410 μm) woven in a criss-cross pattern (Figure 7.03) to create pores (of varying dimensions 152, 251 and 853 μm respectively).

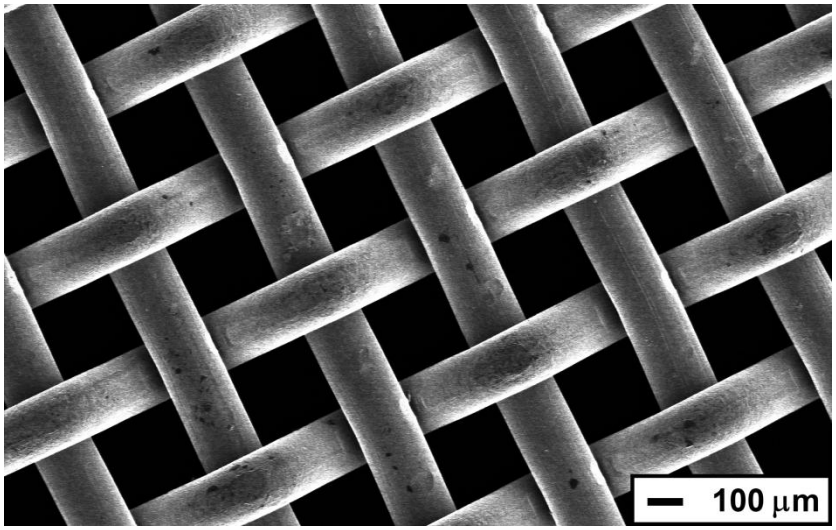

Figure 7.03. SEM image showing copper gauze (as received). Wire diameter is 190 μm and pore dimensions of 251 μm.

7.2.2 Superhydrophobic Mesh

Precursor solutions of Sylgard 184 elastomer (2 x 0.5g in 50 mL of chloroform) were used in an AACVD process to deposit elastomer onto the copper meshes.

The AACVD depositions were carried out in a cold-walled horizontal-bed CVD reactor. The reactor contained top and bottom plates (barrier layer glass), with copper mesh (of varying thicknesses) placed against the top plate for deposition to occur (dimensions: 145 x 45 mm, Figure 7.04). The bottom plate was placed on a carbon block which was used to heat the CVD reactor chamber. The mesh was position approximately 7 mm above and parallel to the bottom plate, with the complete assembly enclosed inside a quartz tube. The aerosol of the precursor solution was generated using a PIFCOHEALTH ultrasonic humidifier, the device had an operating frequency of 40 kHz and

25 W of power. The aerosol generated was moved to the reactor using a nitrogen gas flow via PTFE and glass tubing, where it entered between the top and bottom plates. Any gaseous by-products left *via* an exhaust.

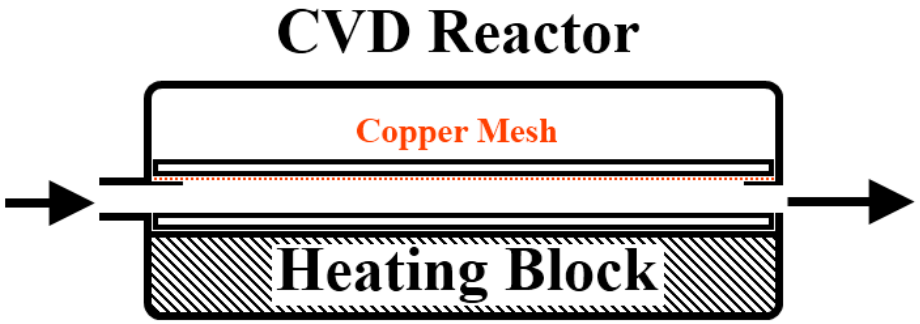

Figure 7.04. AACVD reactor containing the copper mesh during the elastomer deposition.

The reactor temperature (as measured by a thermocouple in the carbon heater block) was maintained at 360°C. The carrier gas (nitrogen) flow through the flask was continued until all liquid was depleted, this took typically 30–35 min. After all liquid was transferred to the reactor the heater was then turned off and allowed to cool to room temperature, and the nitrogen was flowed continuously. The cooled mesh was reversed and the deposition process was repeated, in order to cover both sides of the mesh. After the second deposition the cooled meshes were removed and handled in air.

7.2.3 Device Designs

For each design, mixtures of toluene and water (1 : 1 cm^3) were prepared in Pasteur pipettes, the pipettes were then vibrated using a Vortex-Genie 2, 230V (Scientific Industries). The dispersed mixtures were immediately used in the separation experiments where the mixtures were released at 1 drop/second from the pipette.

7.2.3.1 Tilted Flow Separation

The elastomer-covered meshes were trimmed to remove any uncoated sections (dimensions: 120 x 45 mm), and the meshes were curved slightly along the primary axis to facilitate the flow of water along the mesh. The trimmed meshes were positioned with a 12° tilt angle. Solvent mixtures were released at the top of the substrates, 20 mm away from the top-edge in the centre, and 20 mm above from the mesh. An organic solvent collection vessel was placed directly beneath the dropping pipette, below the mesh. Water was collected using another collection vessel place at the end of the tilted mesh (Figure 7.05). A device was constructed for each of the meshes used.

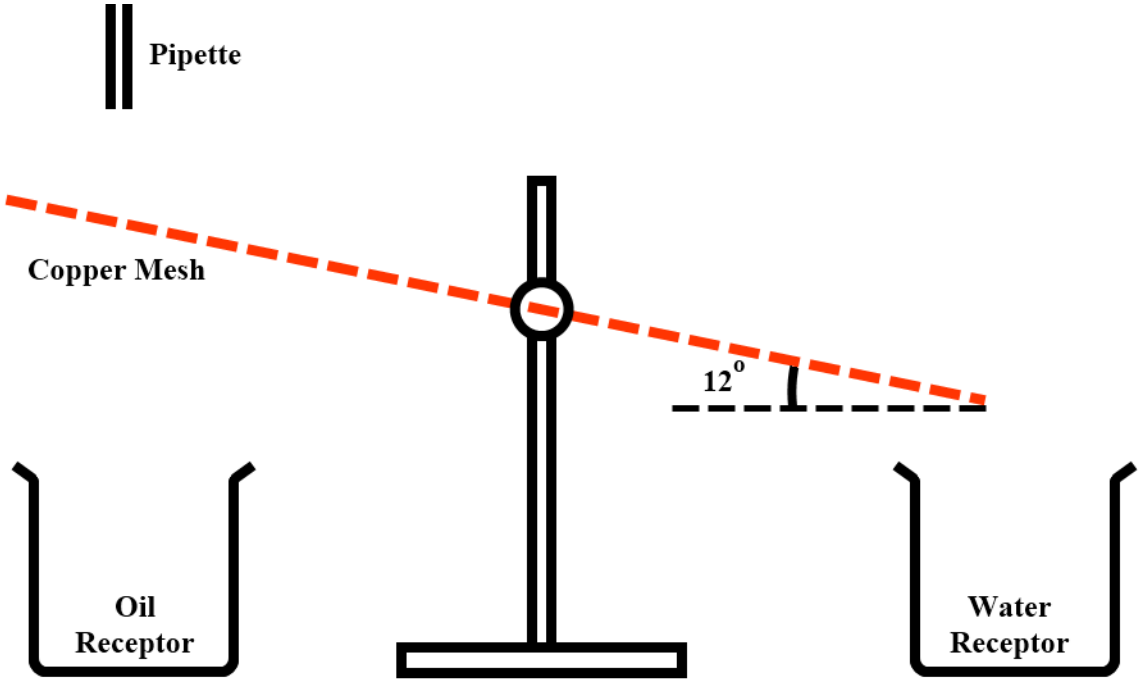

Figure 7.05. Schematic showing the tilted flow separation set-up. The pipette is 20 mm above the copper mesh and 20 mm to the right of the mesh edge. The tilted copper mesh is curved to allow directed flow down the gradient, and is secured at its edges by clamp and clamp stand.

7.2.3.2 Horizontal Dual-Layer Separation

The elastomer covered mesh was cut into portions (dimensions 45 x 45 mm). One portion was fixed inside a small beaker, while another was placed over the rim of the same beaker, the two mesh portions made contact in the centre (Figure 7.06). This beaker was place into a larger container, with the dropping pipette positioned over the centre of the copper mesh, 20 mm above it. A device was constructed for each of the meshes used.

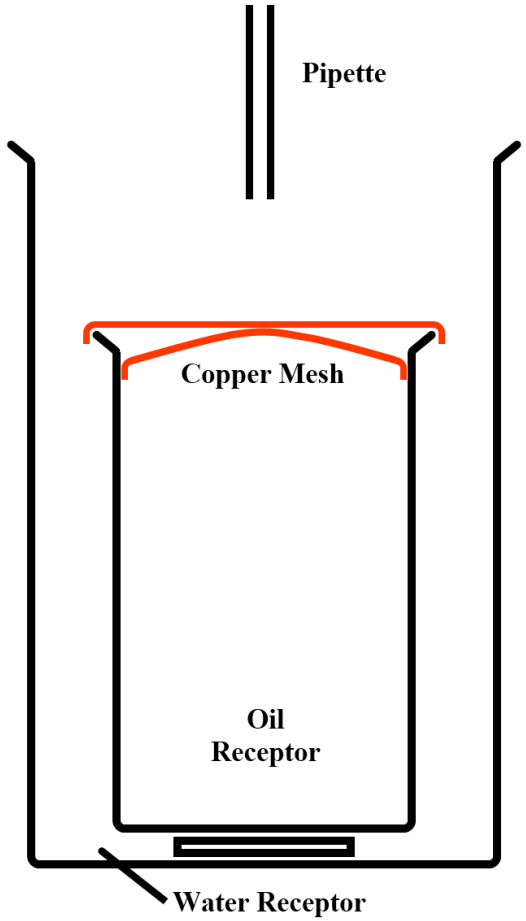

Figure 7.06. Schematic showing the horizontal dual-layer separation set-up. The pipette is 20 mm above the copper mesh.

7.2.4 Film Characterisation

The films were analysed as deposited onto the copper meshes. Subsections (ca 1 x 1 cm) of the samples were gold-sputtered and analysed using field emission scanning electron microscopy (SEM) using a Jeol JSM-6301F operating at 5 kV. Energy dispersive X-ray (EDX) analyses of carbon-sputtered samples were measured using the same machine. Raman measurements were made using a Renishaw 1000 spectrometer which used a 632.8 nm laser. Adherence tests were carried out, done by applying Scotch Home and Office masking tape to the deposited films, removed and any difference in film appearance noted. Scratch tests were also carried out by observing the action of a metal scalpel being dragged across a surface.

Water contact angle measurements were carried out using an FTA-1000 drop shape instrument, 3 μL water droplets were used to minimise any gravitational effects. The water droplet images were analysed using a digital protractor to obtain the water contact angles on the surface. A range of points across the substrates were tested, with 12 measurements made on each mesh. Water slip angles were also measured, noting the angle to the horizontal at which 3 μL water droplets moved on the surface. Many positions across the substrates were tested.

7.3. Results and Discussion

7.3.1 Mesh Properties

AACVD deposition caused all meshes to gain a white/hazy coating. Raman spectroscopy showed peaks relating to C-H stretches of the polymer side groups. Polymer protrusions were confirmed on each mesh by SEM imaging (Figure 7.07), showing highly rough microstructures on the mesh wires. The microstructure observed is similar to that achieved on flat glass substrates (Chapter 2), but additional surface roughness is provided by the curvature/pores of the copper mesh. Water contact angles (Table 7.1) reflect this additional effect with most of the measurements exceeding the average for superhydrophobic films deposited onto flat substrates (160°). The tilt angles were also relatively low, caused by the additional air underneath droplets on the surface facilitated by the mesh pores. The highest water contact angles were achieved on meshes with 251 μm wide pores. This mesh size provided additional roughness while introducing substantial air under a water droplet. Smaller mesh sizes (152 μm pore) resulted in contact angles closer to those observed on films deposited on flat substrates (160° superhydrophobic Sylgard elastomer on flat substrate). The lowest water contact angles recorded were on meshes with large pore sizes (853 μm), the large pores allowed water to sink into them reducing the apparent contact angle and reduced water's ability to move across the coated surface.

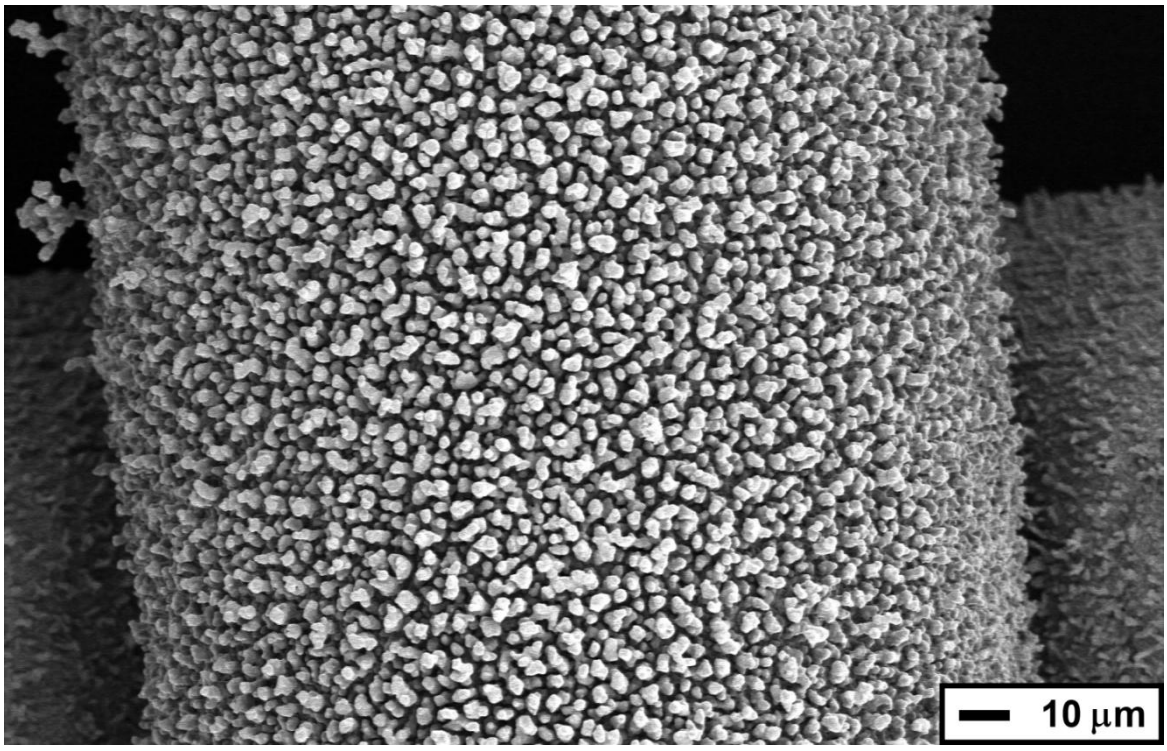

Figure 7.07. SEM image of copper mesh (pore dimension 251 μm) coated with Sylgard 184 using AACVD at a 360°C deposition temperature. The surface microstructure is similar to that deposited onto flat substrates (Chapter 2), however additional surface roughness is afforded by the structure of the mesh.

Mesh Pore Dimensions (µm)	Water Contact Angle, Uncoated (°)	Water Contact Angle, Coated (°)	Tilt Angle, Coated (°)
152	100	163	7
251	135	168	< 2
853	85	132	~ 30

Table 7.1. Water contact angle/tilt angle data for coated and uncoated copper meshes.

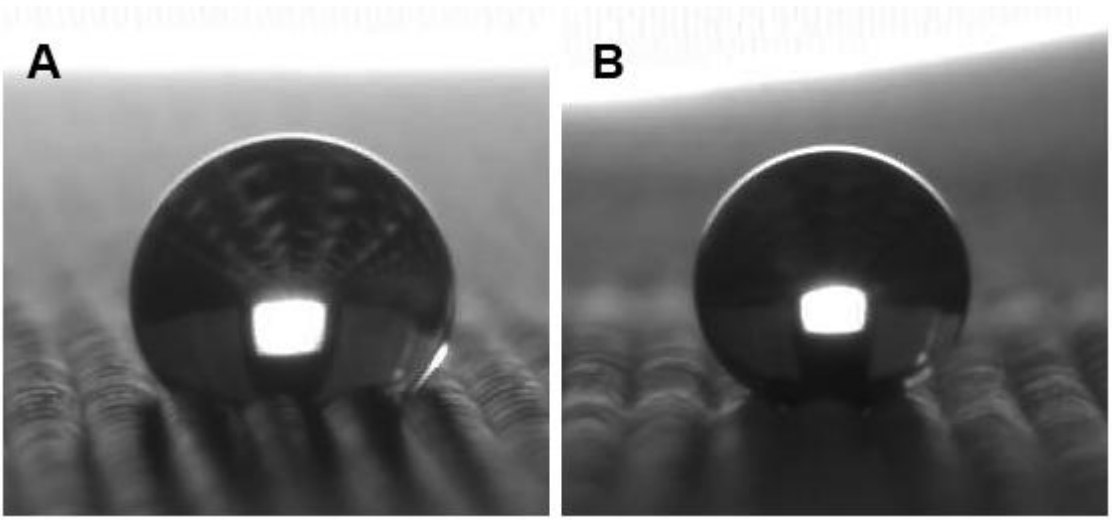

Figure 7.08. Image showing 3 mL water droplets on copper mesh with 251 µm pores – (A) untreated, θ = 135° and (B) coated with Sylgard 184 *via* AACVD, θ = 168°.

7.3.2 Tilted Flowing Separation

The expected mechanism of separation for this design was for the mixture of water to make contact with the mesh above the oil receptor. The toluene in the droplets is absorbed into the mesh and passes through it, dropping into the oil receptor. Water remaining on the mesh surface, repelled by the mesh, is directed to roll down the 12° gradient into the water receptor. The efficiency of each mesh was judged by calculating the amount of oil removed from the water-oil mixture. The 12° tilt angle gave the best results for separation; lower tilt angles resulted in slower movement of droplets, which allowed for droplets combing on the mesh surface and a greater amount of toluene was dragged into the water receptor. Higher tilt angles directed the spread of toluene into the water receptor, lowering separation efficiencies.

Meshes with 853 µm pore sizes did not act to separate the water: toluene mixtures, since drops of the mixtures would almost completely fall through the mesh into the oil receptor, with small amounts of water trapped in the pores of the mesh. Some toluene was observed to spread across the mesh. The mesh used with 152 µm pores did not let any water through into the oil receptor with all water dropped travelling into the water receptor. However there was major spreading of toluene

throughout the mesh. The toluene spreading across the mesh travelled down toward and dropped into the water receptor, with some toluene evaporating along the way. The mesh with 152 μm pores allowed 72 % of toluene through to the water receptor (Table 7.2).

Mesh Pore Dimensions (μm)	Water in Receptor (% of Starting Mass)	Toluene Impurity in Water Receptor (% of Starting Mass)
152	> 99	72
251	> 99	45
853	4	0

Table 7.2. Separation efficiencies of tilted flow set-up. Toluene impurity states the amount toluene recovered from the water receptor.

The mesh with medium pore sizes (251 μm) allowed some toluene to flow through to the oil receptor (~30 % of the toluene dropped), but spreading through the mesh also occurred. All the water dropped was recovered, and 45 % of toluene was collected in the water receptor (with the remaining toluene lost by evaporation) (Table 7.2). Although there is some reduction in toluene using this set-up, the inefficiencies caused by spreading of toluene through the mesh allowed contamination of the collected water. Reports in the literature using a similar set-up allowed for greater efficiencies of separation, but the surface chemistry of the mesh was different. Incorporation of long chain thiols results in a different interaction with toluene and possibly less spreading on the mesh surface.

7.3.3 Horizontal Dual-Layer Separation

This set-up took into account the spreading of the toluene across the meshes. Inclusion of dual-layers would allow toluene (directed by gravity) to travel directly into the oil receptor. The mechanism of separation was expected to commence with contact of the droplet mixtures with the mesh. Toluene in the droplets would be absorbed into the top layer of mesh, and then move into the lower level of mesh and be directed into the oil receptor. Water within a droplet making contact would remain on the top of the mesh, falling into the water receptor when excess water lies on top. The efficiency of each mesh was judged by calculating the amount of oil removed from the water-oil mixture. A single layer of mesh was used primarily but this resulted in a large amount of toluene spreading across the mesh and dropping into the water receptor – severely diminishing the devices efficiency.

The large-pored mesh was inefficient in separation, with almost all of the mixture droplets falling through and only partial retention of water in the mesh pores. The small-pored mesh once again did not allow water to penetrate into the oil receptor, but the spreading of toluene throughout the mesh occurred very quickly with spreading across the top mesh layer and dropping over the side of the oil receptor into the water receptor. The small pores resulted in 8 % of toluene traveling into the water

receptor, while 60 % of toluene was recovered in the oil receptor, with the rest lost to evaporation (Table 7.3).

Mesh Pore Dimensions (μm)	Water in Receptor (% of Starting Mass)	Toluene Impurity in Water Receptor (% of Starting Mass)
152	> 99	40
251	> 99	2
853	11	2

Table 7.3. Separation efficiencies of horizontal dual-layered set-up. Toluene impurity states the amount toluene recovered from the water receptor.

Mesh with medium pore sizes allowed for the most efficient separation. No water was allowed through the mesh into the oil receptor. The spreading of toluene occurred less rapidly with only 2 % of toluene traveling into the water receptor – thus providing a separation efficiency of 98 % (Table 7.3). The success of a medium pore size over large pores is readily apparent, the large pores were unable to retain water effectively and thus separation could not be achieved. Water droplets that sit on the small pored mesh possess a reduced amount of air under the water droplets (relative to the other meshes used), this decreases hydrophobicity affording the coated mesh similar properties to those observed on flat substrates. Spreading of toluene occurred more rapidly, which resulted in the contamination of the water gathered. The medium sized pores gave a reduction in toluene spread, while still supporting water to sit on top of the mesh.

7.4. Conclusions

The superhydrophobic coating on copper mesh greatly improved the hydrophobicity of the Sylgard 184 films, relative to those deposited on flat substrates. The introduction of additional air under the water droplets, caused by the pores of the mesh, facilitates higher water contact angles. The meshes were incorporated into two device designs, with the use of dual-layers of superhydrophobic mesh proving to greatly increase separation efficiencies. Separation efficiencies of up to 98 % were achieved using this design, due to the directed spreading of toluene throughout the mesh. Further improvements would focus on tuning the pore size of the mesh and varying the dimensions of the functional portions of mesh used in the horizontal dual-layer separation set-up.

7.5. References

1. A. Jernelöv, *Ambio*, 2010, **39**, 353.
2. J. R. Skalski, D. A. Coats and A. K. Fukuyama, *Environ. Manage.*, 2001, **28**, 9.
3. A. H. Hammoud and M. F. Khalil, *P. I. Mech. Eng. E - J. Pro.*, 2003, **217**, 49.

4. C. Su, *App. Surf. Sci.*, 2009, **256**, 1413.
5. Z. J. Yu, E. T. Kang, K. G. Neoh, C. Q. Cui and T. B. Lim, *J. Adhesion*, 2000, **73**, 417.
6. H. Tavana, F. Simon, K. Grundke, D. Y. Kwok, M. L. Hair and A. W. Neumann, *J. Colloid Interface Sci.*, 2005, **291**, 497.
7. S. M. M. Ramos, A. Benyagoub, B. Canut and C. Jamois, *Langmuir*, 2010, **26**, 5141.
8. T. Lim and X. Huang, *J. Hazard. Mater.*, 2006, **B137**, 820.
9. Q. Wang, Z. Cui, Y. Xiao and Q. Chen, *App. Surf. Sci.*, 2007, **253**, 9054.
10. L. Feng, Z. Zhang, Z. Mai, Y. Ma, B. Liu, L. Jiang and D. Zhu, *Angew. Chem. Int. Ed.*, 2004, **43**, 2012.

Chapter 8

Conclusions

Figure 8.01. Photograph showing water droplets sitting on a superhydrophobic Lotus leaf.[1]

8. Conclusions

8.1. The Development of New Routes to Superhydrophobic Surfaces

The aims of this of this research were to construct superhydrophobic surfaces *via* novel methods using CVD as a technique. The inherent complications of depositing superhydrophobic surfaces *via* CVD were identified in Chapter 1. Conventional CVD methods follow a molecular surface based reaction, generally resulting in the formation of flat uniform thin films, a deviation from the requirement of high surface roughness in superhydrophobic surfaces. The initial experimental chapters deal with overcoming this complication.

The deposition of polymers *via* AACVD was covered in Chapter 2. This was the first reported use of polymers to form superhydrophobic surfaces using AACVD. The need for a thermosetting polymer precursor was identified, and was rationalised through *in-situ* curing leading to the formation of polymer microparticles in the gas phase. The result was a one-step process for the deposition of a superhydrophobic surface, facilitated by the low energy of the elastomers used. Previous work in the use of polymers to generate superhydrophobic surfaces, included the action of plasma on PTFE[2], in addition to the breakdown of fluorocarbons[3] using a similar plasma route. The method discovered during this research is not only a simple one-step route, but it can also be applied to almost any substrate able to survive the 300-360°C deposition temperature.

In-situ polymer formation was also used to form silica surfaces (Chapter 3). The novel deposition of silica microparticles utilised a solution-based reaction which allowed for the acid-catalysed breakdown of TEOS precursor; this began at 450°C. This is much less than the thermal decomposition temperature of TEOS which occurs above 700°C[4], which would be required for any CVD route which used thermal vaporisation of precursors. The curing of these silica precursors gave microparticles was analogous to those observed in the previous chapter. A post-treatment to lower surface energy the microparticle surfaces rendered them exceptionally superhydrophobic.

The use of particle preformation to gain surface roughness described in these two chapters utilises the thermophoretic effect in order to deposit preformed particles. Further investigation is required into the reasons why no detectable amount of material was deposited onto the bottom plate of the CVD reactor. This research would include possible calculation and simulation of conditions inside the CVD reactor, in addition to deposition of particles of known sizes. Improvements to the outline techniques will also be attempted; these include the use of different polymers as well as microbiological testing on enhanced polymer surfaces.

The deposition of copper and copper (I) oxide films from copper (II) nitrate (Chapter 4) is an example of a conventional CVD deposition. The deposition of copper metal at 350°C was very

unexpected, as depositions of Cu(0) had only been reported at temperatures lower than this or under an atmosphere containing reducing agents[5]. The formation of copper metal was rationalised through the *in-situ* production of hydrogen through the breakdown of methanol solvent. The benefit of carrying out a deposition that follows a conventional CVD mechanism is that conformal coverage of a substrate is achieved. Conformal coverage would allow for uniform coating of pre-roughened substrates and the generation of microroughness (substrate) as well as nanoroughness (thin film) leading to magnification of the post-functionalisation surface hydrophobicities afforded by either length scale individually.

Further analysis is required in order to confirm the production of gas phase hydrogen. In addition to this the use of pre-roughened substrates will also be carried-out to form surfaces with greater hydrophobicities.

8.2. The Anti-microbial Application of Superhydrophobic Surfaces

A bacterial attachment experiment was developed in order to examine the ability of bacteria to attach to superhydrophobic surfaces (Chapter 5). The range of current examination of antimicrobial testing on these highly water-repelling surfaces rarely extends further than the removal of particulate material under the action of water[6]. The attachment assay not only tested Lotus-effect self-cleaning but also revealed preferential point of attachment. The submersion experiments revealed that positions of bacterial attachment was limited to the peaks of surface protrusions, which had not been reported previously. Further testing of bacterial adhesion on these surfaces could offer further insight into producing surface coatings aimed toward reduced surface transferred infections.

8.3. Utilising the Dynamic Interaction of Water

The work carried out during this thesis has resulted in a wide range of surfaces being synthesised, each with a specific type of interaction with water. The ability to synthesis a surface with a definite roughness and surface chemistry facilitated a large investigation into the nature of water bouncing on hydrophobic surfaces (Chapter 6). A relationship was established between water contact angle, surface roughness and number of bounces achieved. Conclusions from the investigation included a new definition for superhydrophobicity and a new scale of superhydrophobicity; which was based on the ability of a surface to facilitate water bouncing. A technique was also developed to monitor the internal motion within a water droplet moving across a surface.

The water bouncing technique was developed in order to expand the range of testing available to those who synthesis superhydrophobic surfaces. Further experimentation is required to test the results gained from the technique. Confirmative studies must be carried out to justify wider uptake of this new technique. Further work will also be carried-out which examines the boundary between 0 and 1 bounce, and also tackle the issue of ‘When is a bounce, a bounce?’.

The facets of superhydrophobic surfaces were extended to the separation of toluene and water. By considering the hydrophobic/oleophilic nature of the materials used to construct superhydrophobic surfaces, the simultaneous repulsion of water and attraction of toluene was achieved. This lead to the design and testing of devises which successfully achieved the separation of toluene and water. This was done by altering the process of the AACVD of polymers, by deposition onto mesh instead of a flat substrate. The separation experiments will be extended to a wider range of organic solvents, with further aims geared toward scaling-up the experiments to separate larger amounts of liquids.

The main goal of the project was to synthesise hydrophobic surfaces using CVD, this meant overcoming inherent complications of the technique and would require the development of novel routes. A further aim was to explore the functional properties of the synthesised surfaces. The large number of hydrophobic surfaces generated in this project was allowed primarily through understanding of the surface features required for high surface hydrophobicity. Through exploration of existing methods, general routes to forming hydrophobic surfaces were drafted. The principle established in Chapter 1 allowed for the design of exceptionally hydrophobic surface coating, these were formed using multiple techniques. Given the range of surfaces synthesised further investigation into the nature of surface hydrophobicity was made possible.

8.4. References

1. http://pgtnaturegarden.org/2011/05/water-drops-on-a-lotus-leaf/
2. S. H. Yang, C. Liu, W. Hsu and H. Chen, *Surf. Coat. Technol.*, 2009, **203**, 1379.
3. D. J. Balazs, C. Hollenstein and H. J. Mathieu, *Plasma Processes Polym.*, 2005, **2**, 104.
4. R. Gordon, *J. Non-Cryst. Solids.*, 1997, **218**, 81.
5. H. Ko, J. Jhin, D. Byun, J. Lee and D. Park, *IEEE Trans. Compon. Packag. Technol.*, 2005, **28**, 781.
6. A. Solga, Z. Cerman, B. F. Striffler, M. Spaeth and W. Barthlott, *Bioinspiration Biomimetics*, 2007, **2**, S126.

Appendices

Appendices

A.1 List of Publications

1. C. R. Crick and I. P. Parkin, 'CVD of Copper and Copper Oxide Thin Films via the in-situ Reduction of Copper (II) Nitrate — A Route to Conformal Superhydrophobic Coatings', *J. Mater. Chem.*, DOI: 10.1039/c1jm11955a.

2. C. R. Crick and I. P. Parkin, 'Superhydrophobic Silica Films on Glass Formed by Hydrolysis of an Acidic Aerosol of Tetraethylorthosilicate', *J. Mater. Chem.*, 2011, **21**, 9362.

3. C. R. Crick, S. Ismail, J. Pratten and I. P. Parkin, 'An Investigation into Bacterial Attachment to an Elastomeric Superhydrophobic Surface Prepared via Aerosol Assisted Deposition', *Thin Solid Films*, 2011, **519**, 3722.

4. C. R. Crick and I. P. Parkin, 'Aerosol Assisted Deposition of Melamine-formaldehyde Resin: Hydrophobic Thin Films from a Hydrophilic Material', *Thin Solid Films*, 2011, 519, 2181.

5. A. Kafizas, C. R. Crick, I. P. Parkin, *J. Photoch. Photobio. A*, 2010, **216**, 156.

6. C. R. Crick and I. P. Parkin, 'Superhydrophobic Polymer Films via Aerosol Assisted Deposition — Taking a Leaf Out of Nature's Book', *Thin Solid Films*, 2010, **518**, 4328.

7. C. R. Crick and I. P. Parkin, 'Preparation and Characterisation of SuperHydrophobic Surfaces', *Chem. Eur. J.*, 2010, **16**, 3568.

8. C. R. Crick and I. P. Parkin, 'A Single-step Route to Superhydrophobic Surfaces Through Aerosol Assisted Deposition of Rough Polymer Surfaces: Duplicating the Lotus Effect', *J. Mater. Chem.*, 2009, **19**, 1074.

9. C. R. Crick and I. P. Parkin, 'Water Droplet Bouncing – A Definition for Superhydrophobic Surfaces', submitted to *Chem. Comm.*, 01/08/2011.

10. C. R. Crick and I. P. Parkin, 'Advances in the Aerosol Assisted Depositions of Polymers', *J. Nanosci. Nanotechnol.*, To be presented at EuroCVD 2011.

A.2 Water Contact Angle/Water Bouncing - Full Data Set

The following data details the bouncing of water droplets on various surfaces, 8μL droplets were dropped from a height of 20 mm (dispensing tip to surface).
[*'Surface average' data provides water contact angle and water bouncing averages on each surface type (10 spots for each surface), 'spot testing' uses water droplets bouncing on a point with known water contact angle.*]

Surface Averages			
CA (°)	**No. Bounces**	**Material**	**Roughness Type**
5	0	*UV-Irradiated Titania*	Flat
30	0	*Non-Irradiated Titania*	Flat
45	0	*Glass*	Flat
71	0	*Heat Treated Glass*	Flat
90	0	*Copper Metal*	Flat
95	0	*Flat Sylgard 184 Elastomer*	Flat
99	0	*Flat Dyneon FC-2120 Fluoroelastomer*	Flat
110	0	*AACVD Coating of Dyneon FC-2120 Fluoroelastomer on Glass*	Rounded
129	0	*AACVD Coating of Sylgard 184 Elastomer on Glass*	Rounded
130	0	*AACVD Coating of Sylgard 184 Elastomer on Glass*	Rounded
152	1.2	*AACVD Coating of Sylgard 184 Elastomer on Glass*	Rounded
156	2.5	*AACVD Coating of Sylgard 184 Elastomer on Glass*	Rounded
156	2.5	*AACVD Coating of Sylgard 184 Elastomer on Glass*	Rounded
156	3	*AACVD Coating of Sylgard 184 Elastomer on Glass*	Rounded
157	4	*AACVD Coating of Sylgard 184 Elastomer on Glass*	Rounded
161	5	*AACVD Coating of Sylgard 184 Elastomer on Glass*	Rounded
165	7	*AACVD Coating of Sylgard 184 Elastomer on Glass*	Rounded
169	9	*AACVD Coating of Sylgard 184 Elastomer on Elastomer Substrate*	Rounded
171	12	*Thiol-functionalised Copper Hydroxide Nanoneedles*	Sharp (Needles)
172	12	*Fluorinatedthiol-functionalised Copper Hydroxide Nanoneedles*	Sharp (Needles)
175	12	*Trimethylsiloxane Functionalised Silica Microparticles Deposited by Hybrid CVD*	Rounded

Spot Testing			
CA (°)	**No. Bounces**	**Material**	**Roughness Type**
120.3	0	*AACVD Coating of Sylgard 184 Elastomer on Glass*	Rounded
120.8	0	*AACVD Coating of Sylgard 184 Elastomer on Glass*	Rounded
121.5	0	*AACVD Coating of Sylgard 184 Elastomer on Glass*	Rounded
121.9	0	*AACVD Coating of Sylgard 184 Elastomer on Glass*	Rounded
123.2	0	*AACVD Coating of Sylgard 184 Elastomer on Glass*	Rounded
123.3	0	*AACVD Coating of Sylgard 184 Elastomer on Glass*	Rounded
125.7	0	*AACVD Coating of Sylgard 184 Elastomer on Glass*	Rounded
127.3	0	*AACVD Coating of Sylgard 184 Elastomer on Glass*	Rounded
127.4	0	*AACVD Coating of Sylgard 184 Elastomer on Glass*	Rounded
127.6	0	*AACVD Coating of Sylgard 184 Elastomer on Glass*	Rounded
128.8	0	*AACVD Coating of Sylgard 184 Elastomer on Glass*	Rounded
128.8	0	*AACVD Coating of Sylgard 184 Elastomer on Glass*	Rounded
130.7	0	*AACVD Coating of Sylgard 184 Elastomer on Glass*	Rounded
132.4	0	*AACVD Coating of Sylgard 184 Elastomer on Glass*	Rounded
132.6	0	*AACVD Coating of Sylgard 184 Elastomer on Glass*	Rounded
133.6	0	*AACVD Coating of Sylgard 184 Elastomer on Glass*	Rounded
134.7	0	*AACVD Coating of Sylgard 184 Elastomer on Glass*	Rounded
140.2	0	*AACVD Coating of Sylgard 184 Elastomer on Glass*	Rounded
142.0	0	*AACVD Coating of Sylgard 184 Elastomer on Glass*	Rounded
142.3	0	*AACVD Coating of Sylgard 184 Elastomer on Glass*	Rounded
144.0	0	*AACVD Coating of Sylgard 184 Elastomer on Glass*	Rounded
147.4	0	*AACVD Coating of Sylgard 184 Elastomer on Glass*	Rounded
148.5	0	*AACVD Coating of Sylgard 184 Elastomer on Glass*	Rounded
149.6	0	*AACVD Coating of Sylgard 184 Elastomer on Glass*	Rounded
149.7	0	*AACVD Coating of Sylgard 184 Elastomer on Glass*	Rounded
150.4	0	*AACVD Coating of Sylgard 184 Elastomer on Glass*	Rounded
150.8	0	*AACVD Coating of Sylgard 184 Elastomer on Glass*	Rounded

151.1	1	*AACVD Coating of Sylgard 184 Elastomer on Glass*	Rounded
151.2	0	*AACVD Coating of Sylgard 184 Elastomer on Glass*	Rounded
151.3	1	*AACVD Coating of Sylgard 184 Elastomer on Glass*	Rounded
151.4	1	*AACVD Coating of Sylgard 184 Elastomer on Glass*	Rounded
151.4	1	*AACVD Coating of Sylgard 184 Elastomer on Glass*	Rounded
151.4	1	*AACVD Coating of Sylgard 184 Elastomer on Glass*	Rounded
151.4	1	*AACVD Coating of Sylgard 184 Elastomer on Glass*	Rounded
151.6	1	*AACVD Coating of Sylgard 184 Elastomer on Glass*	Rounded
151.7	1	*AACVD Coating of Sylgard 184 Elastomer on Glass*	Rounded
151.7	1	*AACVD Coating of Sylgard 184 Elastomer on Glass*	Rounded
151.7	1	*AACVD Coating of Sylgard 184 Elastomer on Glass*	Rounded
151.8	1	*AACVD Coating of Sylgard 184 Elastomer on Glass*	Rounded
151.8	1	*AACVD Coating of Sylgard 184 Elastomer on Glass*	Rounded
151.9	1	*AACVD Coating of Sylgard 184 Elastomer on Glass*	Rounded
151.9	0	*AACVD Coating of Sylgard 184 Elastomer on Glass*	Rounded
151.9	1	*AACVD Coating of Sylgard 184 Elastomer on Glass*	Rounded
152.0	1	*AACVD Coating of Sylgard 184 Elastomer on Glass*	Rounded
152.1	0	*AACVD Coating of Sylgard 184 Elastomer on Glass*	Rounded
152.1	1	*AACVD Coating of Sylgard 184 Elastomer on Glass*	Rounded
152.1	1	*AACVD Coating of Sylgard 184 Elastomer on Glass*	Rounded
152.2	1	*AACVD Coating of Sylgard 184 Elastomer on Glass*	Rounded
152.3	1	*AACVD Coating of Sylgard 184 Elastomer on Glass*	Rounded
152.4	0	*AACVD Coating of Sylgard 184 Elastomer on Glass*	Rounded
152.5	1	*AACVD Coating of Sylgard 184 Elastomer on Glass*	Rounded
152.8	0	*AACVD Coating of Sylgard 184 Elastomer on Glass*	Rounded
152.8	2	*AACVD Coating of Sylgard 184 Elastomer on Glass*	Rounded
153.0	2	*AACVD Coating of Sylgard 184 Elastomer on Glass*	Rounded
153.1	0	*AACVD Coating of Sylgard 184 Elastomer on Glass*	Rounded
153.2	0	*AACVD Coating of Sylgard 184 Elastomer on Glass*	Rounded

153.3	2	*AACVD Coating of Sylgard 184 Elastomer on Glass*	Rounded
153.4	1	*AACVD Coating of Sylgard 184 Elastomer on Glass*	Rounded
153.7	2	*AACVD Coating of Sylgard 184 Elastomer on Glass*	Rounded
153.8	2	*AACVD Coating of Sylgard 184 Elastomer on Glass*	Rounded
153.8	2	*AACVD Coating of Sylgard 184 Elastomer on Glass*	Rounded
153.9	2	*AACVD Coating of Sylgard 184 Elastomer on Glass*	Rounded
153.9	2	*AACVD Coating of Sylgard 184 Elastomer on Glass*	Rounded
154.0	2	*AACVD Coating of Sylgard 184 Elastomer on Glass*	Rounded
154.6	1	*AACVD Coating of Sylgard 184 Elastomer on Glass*	Rounded
154.7	1	*AACVD Coating of Sylgard 184 Elastomer on Glass*	Rounded
155.2	1	*AACVD Coating of Sylgard 184 Elastomer on Glass*	Rounded
155.8	2	*AACVD Coating of Sylgard 184 Elastomer on Glass*	Rounded
156.0	3	*AACVD Coating of Sylgard 184 Elastomer on Glass*	Rounded
156.2	4	*AACVD Coating of Sylgard 184 Elastomer on Glass*	Rounded
156.3	5	*AACVD Coating of Sylgard 184 Elastomer on Glass*	Rounded
156.7	4	*AACVD Coating of Sylgard 184 Elastomer on Glass*	Rounded

PTFE - Spot Testing			
CA (°)	**No. Bounces**	**Material**	**Roughness Type**
105	0	*Flat Polytetrafluoroethylene Substrate*	Flat
125.4	0	*Mechanically Roughened Polytetrafluoroethylene*	Sharp
128.3	0	*Mechanically Roughened Polytetrafluoroethylene*	Sharp
139.6	0	*Mechanically Roughened Polytetrafluoroethylene*	Sharp
143.2	0	*Mechanically Roughened Polytetrafluoroethylene*	Sharp
146.8	0	*Mechanically Roughened Polytetrafluoroethylene*	Sharp
149.7	0	*Mechanically Roughened Polytetrafluoroethylene*	Sharp
151.4	0	*Mechanically Roughened Polytetrafluoroethylene*	Sharp
152.2	0	*Mechanically Roughened Polytetrafluoroethylene*	Sharp
153.1	0	*Mechanically Roughened Polytetrafluoroethylene*	Sharp
153.1	0	*Mechanically Roughened Polytetrafluoroethylene*	Sharp
154.3	0	*Mechanically Roughened Polytetrafluoroethylene*	Sharp
155.7	0	*Mechanically Roughened Polytetrafluoroethylene*	Sharp
156	0	*Mechanically Roughened Polytetrafluoroethylene*	Sharp
156.4	1	*Mechanically Roughened Polytetrafluoroethylene*	Sharp
157	1	*Mechanically Roughened Polytetrafluoroethylene*	Sharp
157.1	2	*Mechanically Roughened Polytetrafluoroethylene*	Sharp
157.4	1	*Mechanically Roughened Polytetrafluoroethylene*	Sharp
157.9	2	*Mechanically Roughened Polytetrafluoroethylene*	Sharp
158.3	2	*Mechanically Roughened Polytetrafluoroethylene*	Sharp